UNIVERSITY OF SOUTHAMPTON

SCHOOL OF ENGINEERING SCIENCES

BIOENGINEERING SCIENCES RESEARCH GROUP

MODELLING THE MECHANICAL BEHAVIOUR OF THE INTERFACE BETWEEN PROSTHESIS AND BONE

BY

Suk Yee Leung

Thesis for the degree of Doctor of Philosophy

April 2008

UNIVERSITY OF SOUTHAMPTON

ABSTRACT

School of Engineering Sciences

Bioengineering Sciences Research Group

Doctor of Philosophy

MODELLING THE MECHANICAL BEHAVIOUR OF THE INTERFACE BETWEEN PROSTHESIS AND BONE

By Suk Yee Leung

The integrity of the cement-bone interface is vital to the long term stability of cemented arthroplasty. Although the factors affecting the strength of the cement-bone interface are well documented the behaviour and load transfer across the interface at the trabecular level has been largely neglected. In addition, modelling of the cement-bone interface has mostly been limited to evaluation at the continuum level.

In the following study, two modelling approaches have been developed for evaluation of the microstructural behaviour of the cement-bone interface. The first technique used a unit cell as a simplification of the morphology of cancellous bone. Using this method, variations in volume fraction resulting from changes in trabecular thickness and porosity size were shown to influence the resulting apparent stiffness. When cement was added to the unit cell, the stiffness became significantly greater with increasing cement penetration. The second approach used high resolution computed tomography (CT) images of the microstructure of the interface to create micro finite element (μFE) models of the interface. A cancellous bone analogue was selected and smooth surface models were created. It was shown that correlation of the volume segmented from CT images to the actual volume was vital for accurate calculation of the apparent level stiffness. The cancellous bone analogue material was then used to create analogue specimens representative of the cement-bone interface. Two non-destructive techniques, micro CT imaging and acoustic emission, were used to monitor damage evolution in the interfacial region, with the aim of validating finite element models of the interface. Initiation and progression of damage through the cement and foam was isolated and characterised by analysis of the associated AE parameters, and correlated well with the CT data. Therefore, the ability of AE as a passive tool to provide early indication of failure in situ was demonstrated. When the cement-bone analogue interface was loaded in bending, damage initiated at stress concentrations formed by irregularities in the aluminium geometry, recesses and notches formed by flow of cement into the aluminium. μFE models of the cement-bone analogue specimens were created. Linear elastic models showed regions of high stress at the failure loci. μFE models of specimens with differing degrees of cement interdigitation were created and it was demonstrated that the local load transfer across the interface was different for different penetration depths.

The combined use of experimental and computational methods has enabled evaluation of the behaviour of the cement-bone interface at the microstructural level. Further development of the models and the use of more clinically representative loading conditions will enhance the understanding of the role of interface morphology, trabecular architecture and properties on the resulting interface strength. In addition, these methods may be combined with macroscopic scale models of prosthesis/bone constructs to evaluate factors such as stem design on the interface conditions.

CONTENTS

LIST OF FIGURES

LIST OF TABLES

NOMENCLATURE

Abduction	To draw outward from the midline of the body.
Adduction	To draw inward towards the medial plane of the body.
AE	Acoustic Emission
Anterior	Toward the front plane of the body; opposite to posterior.
ASTM	American society for testing and materials
BPO	Benzoyl peroxide
BW	Body Weight
Cancellous bone	The trabecular tissue found in the middle of bone.
Cortical bone	The tissue forming the outer layer of bone.
CT	Computed Tomography
δ	Displacement
D	Bending Stiffness
Distal	A position away from the reference point.
DNA	Deoxyribonucleic acid
E	Modulus of Elasticity
Extension	A straightening movement where the relative angle between two adjacent segments increases.
F	Force matrix
FE	Finite element
FEA	Finite element analysis
Flexion	Movement at a joint that decreases the angle between the bones .
G	Shear modulus
HA	Hydroxyapatite.
High resolution FE	Finite element models constructed from high resolution images typically CT images.
I	Second moment of area
in vitro	*In glass*. In an artificial environment.
in vivo	*In the body.* Opposite to *in vitro.*
Inferior	Pertaining to the lower side.
K	Global Stiffness Matrix
Lateral	Away from the midsaggital plane.
Lavage	Cleaning or rinsing

LVDT	Linear variable differential transducer
Macrophage	Cells within tissue which engulf and remove debris
MD	Mesh density
MDA	Medical Device Agency
Medial	Toward the midsaggital plane.
μFE	Micro finite element
Micro FE	See High resolution FE
MMA	Methylmethacrylate
MRI	Magnetic resonance imaging
NICE	National Institution of Clinical Excellence
OA	Osteoarthritis. Inflammation of the joint as a result of wear of the cartilage.
OPF	Open cell polyurethane foam
Osteoporosis	A disease of the bone characterised by reduction in bone mineral density, change in microarchitecture and reduction of mechanical properties
P	Load
PCL	Posterior cruciate ligament.
PMMA	Polymethylmethacrylate
Posterior	Towards the rear of the body; opposite to anterior.
Proximal	A position closer to the reference point
PTFE	Polytetrafluoroethylene
ρ	Density
RA	Rheumatoid arthritis
R_a	Surface roughness
Resurfacing	Procedure where the surface of the femoral head is replaced
RSA	Roentgen stereophotogrammic analysis
Superior	Towards the upper surface
Synovial fluid	Thick fluid found in the cavity of synovial joints
τ	Shear stress
THA	Total Hip Arthroplasty
THR	Total Hip Replacement
TJR	Total Joint Replacement
Trabeculae	Latin for *little beam*. Any of the individual struts forming a network in cancellous bone.
UHMWPE	Ultra high molecular weight polyethylene
Vf	Volume Fraction
Voxels	Three dimensional pixels

DECLARATION OF AUTHORSHIP

I, Suk Yee Leung, declare that the thesis entitled *'Modelling the Mechanical Behaviour of the Interface between Prosthesis and Bone'* and the work presented in the thesis are both my own, and have been generated by me as the result of my own original research. I confirm that:

- this work was done wholly or mainly while in candidature for a research degree at this University;
- where any part of this thesis has previously been submitted for a degree or any other qualification at this University or any other institution, this has been clearly stated;
- where I have consulted the published work of others, this is always clearly attributed;
- where I have quoted from the work of others, the source is always given. With the exception of such quotations, this thesis is entirely my own work;

I have acknowledged all main sources of help;

- where the thesis is based on work done by myself jointly with others, I have made clear exactly what was done by others and what I have contributed myself;
- Parts of this work have been published and is detailed in Appendix A

Signed: ……..

Date:……..

ACKNOWLEDGEMENTS

Deo Gratias

During the course of this PhD, I have been very lucky to meet some truly great people that have contributed directly and indirectly towards this PhD. I'd like express to them my gratitude and appreciation for all their support through the years.

Firstly, a great big thank you to Dr Martin Browne and Dr Andrew New for their excellent supervision, guidance and friendship. Thanks for being great Boss! Thank you also to Professor Mark Taylor – I'll get up Snowdon one of these days. I wouldn't have got anywhere at all in the labs without the excellent work of all the technicians; especially Eric Bonner and Rob Barnes. Thank you to Mark Mavrogordato for allowing me use of his beautifully made AE sensors. Diolch to Gwyneth and thanks to Sonya and Dawn for all their help in all things financial. I would have been beaten by the computer if it wasn't for; Jonathon Jeffers, Elena Samsonova, Adam Briscoe, Mike Strickland and Andy Hopkins. My gratitude to the School of Engineering Sciences and DePuy for their financial support and to Pera for use of their labs.

Thank you for those in the Bioengineering office AKA *the office of fun* both past and present. For fear of forgetting any of you, I won't name any of you – you know who you are!

Thank you to my dear friends who made my time in Southampton such great fun. Thanks to Ian and Kieran for the movie nights, to Lucy (who is the best!) who has taught me that a cup of tea solves pretty much everything, to Duncan for letting me stay and for the excessive volumes of mash, to all the kickboxers at IMAO and also to my dear friends Elena, Lily, Polly, Anne, Catherine, Carolina and Sara.

Thank you to my family Mum, Dad and Tim for all your support and love over the years. Thanks also to Heather and Dave and the rest of my new family.

And lastly but by no means least, my love and gratitude to my wonderful husband, Fr. Christopher Kinch. Your patience, love, support and ability to always make me smile has helped me through all the grumpy days. You're my hero.

Chapter 1. *Introduction*

The hip is used extensively through our daily lives. The average number of steps that a person takes each year, is approximately 2 million[1]. On average, 28.9% of the day is spent on activities necessitating motions of the hip; such as walking, running, stair climbing, getting up and sitting down[2]. Damage to the hip, for example through wear of the cartilage separating the surfaces of the joint (known as osteoarthritis), can lead to severe pain and loss of mobility. Total hip replacement is a common method of treating conditions of the hip such as osteoarthritis, rheumatoid arthritis, fracture of the neck of the femur and damage resulting in loss of blood supply to the head of the femur (avascular necrosis). In 2006-2007, 65,532 hip replacement procedures were recorded by the NHS and independent healthcare clinics in England and Wales[3]. The National Institution for Clinical Excellence suggest that hip replacements should demonstrate a revision rate at 10% or less at 10 years[4]. Although effective, some prosthesis require revision surgery; 5,821 revision procedures were recorded in 2006 in England and Wales[3]. As the population increases, together with the incidence of obesity[5], more people can be expected to undergo a hip replacement operation; this and the subsequent number of revision procedures could become a burden to the health service.

Asceptic loosening is the most common cause of revision surgery although the reasons and mechanisms are not fully understood [6, 7]. Loosening is often attributed to the deterioration of one of the interfaces i.e. the interface between stem and cement or cement and bone in a cemented implant and the interface between prosthesis and bone in an uncemented implant[6, 8].

In a cemented implant, where the femoral or acetabular component is secured using bone cement, the fixation of an implant depends on the mechanical interlock formed by the penetration of cement into cancellous bone. The integrity of the cement-bone interface is vital for long term stability of joint replacements. The initial fixation of the cement bone interface can become compromised immediately postoperatively due to necrosis of the bone caused by heat from the polymerisation of cement[9], excessive reaming of the femoral canal[10], gaps or residual stresses formed by shrinkage of cement[11, 12] or local monomer toxicity[13]. Damage to the bone or excessive stresses at the cement-bone interface can lead to the formation of an intervening fibrous tissue layer. The presence of this intervening tissue has been shown to decrease the strength of the cement-bone interface leading to early migration and eventual loosening of the implant[6, 14]. Over a period of six months to two years, a successful cement-bone interface will exhibit regions of remodelling of necrotic bone near the cement-bone interface and regions of direct cement on bone contact in load bearing regions[15-17]. Under ideal conditions, the interface can remain stable for many years without any adverse biological response. However, interface failure can occur due to deterioration of cement or bone, leading to component migration and eventual loosening of the implant[6].

Improvements in cementing technique, for example, by optimising the viscosity of cement at time of insertion[11, 17-19], the cleaning the bone surface[18-20], using a distal plug in the femur[18] and pressurisation of the cement[21], increase the strength and stability of the cement-bone interface by optimising the cement-bone interlock. These have resulted in improved long term success rates for hip prostheses. In addition to cement interlock, the quality of cancellous bone (its geometry, presence of disease and mechanical properties) affects the cement-bone interface strength[22]. As a result of substantial heterogeneity, anisotropy, interspecimen variability and difficulty in preparing samples, experimentally determined mechanical properties exhibit substantial variation[23, 24]. Therefore, for the same depth of cement penetration, the strength of cement bone interface will also exhibit variation as a function of bone properties[25].

Relatively little is known about the microstructural behaviour of the cement-bone interface such as local stress distribution across the interface, whether bone or cement fails first and the affect of bone quality and architecture on the integrity of the interface. The local deformations and motions of the cement and bone at the interface are important in the understanding of the influence of mechanical loading on the loosening process[26, 27]. Due to the numerous factors that affect the morphology and properties of the cement bone interface, the microstructural behaviour

may be difficult to examine experimentally. Finite element analysis offers a powerful method of evaluation of the properties of the interface. Finite element methods have been used previously in orthopaedic biomechanics as a preclinical analysis tool to examine the stress distribution and effect on fixation in the femoral stem, cement and bone construct for various designs and orientations of implants[28]. Due to the complex geometry of cancellous bone and the cement bone interface, the cement-bone interface has often been modelled as a continuum, assuming averaged properties over a representative length or volume. However, this assumption may not be valid at the cement-bone interface as the discontinuous surface of cancellous bone can result in local stress concentrations above the material thresholds of interest (for example fatigue limit or yield stress of cement or bone)[29].

The aim of this thesis is to examine methods of modelling the behaviour of the cement-bone interface at the microstructural level and the various factors which may affect its strength. The first method involves the development of theoretical cellular models to examine the effect of varying degrees of cement penetration and trabecular architecture on the strength of the interface. The structure of cancellous bone is represented by a single unit cell which is assumed to be regular and repeating. The variation in strain for both bone and cement is evaluated for differing degrees of cement penetration, trabecular thickness and cell size. The second approach involves the development of micro finite element (μFE) models based on high resolution computed tomography (CT) images of the cement-bone interface. A cancellous bone analogue with a representative morphology is selected to eliminate problems associated with mechanical testing of bone. This work does not appear in a sequential order and is detailed in Chapter 3 and 5. μFE models of the analogue material without cement are created using a smooth surface meshing technique. The effect of threshold, mesh density and smoothing parameters on the accuracy of predicted modulus is examined and compared with experimental data. Once the factors influencing the accuracy of models were determined, analogue representations of the interface were manufactured and tested to provide details on the microstructural behaviour of the cement-bone interface for validation of the finite element models. Non destructive techniques are used to monitor and examine the initiation and progression of failure of analaogue samples subjected to four point bend loading. Early location of failure is detected and characterised using acoustic emission, (AE). CT images of the sample are collected before and after testing to visualise the progression of damage. Finally, corresponding μFE models of the interface analogue samples and further models with varying degrees of cement penetration are created using the smooth surface meshing technique. Linear elastic and elasto-plastic analysis are then performed on these models to examine the stress distribution across the interface and validated with the locations of failure observed in experimental testing.

1.1. References

1. Silva, M., E.F. Shepherd, W.O. Jackson, F.J. Dorey, and T.P. Schmalzried, *Average patient walking activity approaches 2 million cycles per year - Pedometers under-record walking activity.* Journal of Arthroplasty, 2002. **17**(6): p. 693-697.
2. Morlock, M., E. Schneider, A. Bluhm, M. Vollmer, G. Bergmann, V. Muller, and M. Honl, *Duration and frequency of every day activities in total hip patients.* Journal of Biomechanics, 2001. **34**(7): p. 873-881.
3. Dury, P., J. Morrison, C. Newell, M. Pickford, M. Roayll, M. Swanson, L. May, J. van der Meulen, and N. Silbanda, *National Joint Registry for England and Wales 4th Annual Report*. 2007, National Joint Registry: Hemel Hempstead, Hertfordshire.
4. *TA2 Hip disease - replacement prosthesis: Guidance on the selection of prosthesis for primary total hip replacement*. 2000, National Institution for Clinical Excellence: London.
5. *UK Obesity Statistics*, 2007, [cited March 2008]; Available from: http://www.annecollins.com/obesity/uk-obesity-statistics.htm.
6. Bauer, T.W. and J. Schils, *The pathology of total joint arthroplasty I. Mechanisms of implant fixation.* Skeletal Radiology, 1999. **28**(8): p. 423-432.
7. Herberts, P., H. Malchau, and G. Garellick, *The Swedish national hip arthroplasty register. Annual report 2005*. 2006, Sahlgrenska University Hospital: Gothenburg, Sweden.
8. Jasty, M., W.J. Maloney, C.R. Bragdon, D.O. OConnor, T. Haire, and W.H. Harris, *The initiation of failure in cemented femoral components of hip arthroplasties.* Journal of Bone and Joint Surgery-British Volume, 1991. **73**(4): p. 551-558.
9. Stanczyk, M. and B. Van Rietbergen, *Thermal analysis of bone cement polymerisation at the cement-bone interface.* Journal of Biomechanics, 2004. **37**: p. 1803-1810.
10. Garcia, O.G.R., F.L. Mombiela, C.J. De La Fuente, M.G. Aranguez, D.V. Escribano, and J.V. Martin, *The influence of the size and condition of the reamers on bone temperature during intramedullary reaming.* Journal of Bone and Joint Surgery-American Volume, 2004. **86A**(5): p. 994-999.
11. Lennon, A.B. and P.J. Prendergast, *Residual stress due to curing can initiate damage in porous bone cement: experimental and theoretical evidence.* Journal of Biomechanics, 2002. **35**(3): p. 311-321.
12. Race, A., A. Miller, M.T. Clarke, and K.A. Mann, *Cement-implant interface gaps explain the poor results of CMW3 for femoral stem fixation.* Acta Orthopaedica, 2005. **76**(5): p. 679-687.
13. Lu, J.X., Z.W. Huang, P. Tropiano, B.C. D'Orval, M. Remusat, J. Dejou, J.P. Proust, and D. Poitout, *Human biological reactions at the interface between bone tissue and polymethylmethacrylate cement.* Journal of Materials Science-Materials in Medicine, 2002. **13**(8): p. 803-809.
14. Radin, E., C.T. Rubin, E.L. Thrasher, L.E. Lanyon, A.M. Crugnola, A.S. Schiller, I.L. Paul, and R.M. Rose, *Changes in the Bone-Cement Interface after Total Hip Replacement.* The Journal of Bone and Joint Surgery, 1982: p. 1188-1200.
15. Charnley, J., *The bonding of prostheses to bone by cement.* The Journal of Bone and Joint Surgery British Volume, 1964. **46**: p. 518-529.
16. Charnley, J., *Low friction arthroplasty of the hip; theory and practise*. 1979, Berlin: Springer-Verlag.
17. Vernon-Roberts, B., *The initial state*, in *the bone-cement interface, Workshop Report*, L.J. Lewis and J.O. Galante, Editors. 1984, American Academy of Orthopaedic Surgery. p. 8-22.
18. Breusch, S. and H. Malchau, *What is modern cementing technique*, in *The well-cemented total hip arthroplasty theory and practise*, S. Breusch and H. Malchau, Editors. 2005, Springer. p. 146-149.

19. Herberts, P. and H. Malchau, *Long-term registration has improved the quality of hip replacement.* Acta Orthopaedica Scandinavica, 2000. **71**(2): p. 111-121.
20. Krause, W., W. Krug, and J.E. Miller, *Strength of the cement-bone interface.* Clinical Orthopaedics, 1982. **163**: p. 290-299.
21. Oates, K.M., D.L. Barrera, W.N. Tucker, C.C.H. Chau, W.D. Bugbee, and F.R. Convery, *In vivo effect of pressurisation of polymethylmethacrylate bone-cement.* The Journal of Arthroplasty, 1995. **10**(3): p. 373-381.
22. Stone, J.J.S., J.A. Rand, E.K. Chiu, J.J. Grabowski, and K.N. An, *Cement viscosity affects the bone-cement interface in total hip arthroplasty.* Journal of Orthopaedic Research, 1996. **14**(5): p. 834-837.
23. Carter, D.R. and W.C. Hayes, *The compressive behavior of bone as a two-phase Porous Structure.* The Journal of Bone and Joint Surgery, 1977. **59-A**(7): p. 954-962.
24. Keaveny, T.M. and W.C. Hayes, *A 20-year perspective on the mechanical-properties of trabecular bone.* Journal of Biomechanical Engineering-Transactions of the ASME, 1993. **115**(4): p. 534-542.
25. Graham, J., M. Ries, and L. Pruitt, *Effect of bone porosity on the mechanical integrity of the bone-cement interface.* Journal of Bone and Joint Surgery-American Volume, 2003. **85A**(10): p. 1901-1908.
26. Heaton-Adegbile, P., J. Hussell, and J. Tong, *In-vitro assessment of load transfer and strain distribution across the cement-bone interface in an artificially replaced acetabulum.* Journal of Bone and Joint Surgery British Volume, 2006. **Vol 88-B**(SUPP_III,): p. 386.
27. Mann, K., M. Miller, R. Cleary, D. Janssen, and N. Verdonschot, *Experimental micromechanics of the cement-bone interface.* Journal of Orthopaedic Research, 2008. ***In Press***.
28. Huiskes, R. and J. Stolk, *Biomechanics and preclinical testing of artificial joints: the hip*, in *Basic orthopaedic biomechanics and mechano-biology*, R. Huiskes and V. Mow, Editors. 2004, Lippincott Williams & Williams.
29. Harrigan, T.P., M. Jasty, R.W. Mann, and W.H. Harris, *Limitations of the Continuum Assumption in Cancellous Bone.* Journal of Biomechanics, 1988. **21**: p. 269.

Chapter 2. *Literature Review*

The following literature review is divided into three main sections:

Section 2.1 Biomechanics of the hip includes general background details such as the anatomy of the hip, joint contact forces, reasons for hip arthroplasty, total hip arthroplasty procedure and methods of monitoring and assessment.

Section 2.2 Bone: provides a review of the mechanical properties of bone and the methods and limitations of experimental testing

Section 2.3 Fixation: this provides a review of the literature for the behaviour and properties of the stem-cement interface and the cement-bone interface in total hip replacement.

The final Section 2.4 provides a summary of the literature review and how it relates to this thesis.

2.1. Biomechanics of the Hip

2.1.1. Anatomy of the Hip

The hip is an enarthrodial, or ball and socket, joint consisting of the femoral head and acetabulum (Figure 2.1). The femur articulates within the acetabulum to achieve multi-axial motion. In a healthy hip, the articulating surfaces are protected by a layer of articular cartilage and encapsulated by a synovial membrane containing synovial fluid; the natural lubricant of the joint. Ligaments are dense connective tissues which help to maintain and protect the joint and also to transfer load from the bone during movement. They also help to limit excessive motion[1, 2]. The synovial hip joint is held in place by a number of ligaments: the capsular, ilio-femoral, ligamentum teres, cotyloid and transverse ligaments.

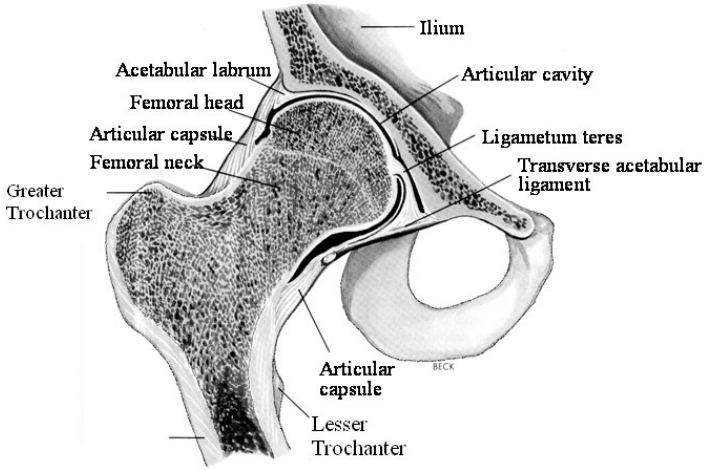

Figure 2.1: Anatomy of the Hip

The pelvic girdle consists of two coxal bones, each of which is the fusion of three smaller bones; the illium, the ishium and the pubis. The area where these bones converge forms the acetabulum or the socket of the hip joint. The pelvic bones distribute the weight of the body into the lower extremities and also act as attachment points for the muscles that articulate the hip joint. The pelvis also houses and protects some parts of the digestive and urinary tracts and the reproductive system[1].

There are seventeen muscles which produce multi-axial motion at the hip joint: flexion, extension, abduction, adduction and internal/external rotation. Flexion of the hip is the anterior motion of the femur in the sagittal plane (Figure 2.2). Extension is the opposite; the posterior movement of the femur in the saggital plane. Abduction is the lateral movement of the leg and adduction, the medial movement of the leg, both in the coronal plane. In active motion, the hip can achieve approximately 120° of flexion, 20° of extension, 45° of abduction and 45° of

adduction[3]. The majority of the muscles originate from the surface of the pelvis and insert into the femur. By working in groups, the muscles are able to achieve the primary motions of the hip joint. These are adapted and summarised in Table 2.1 from Gray's anatomy[1].

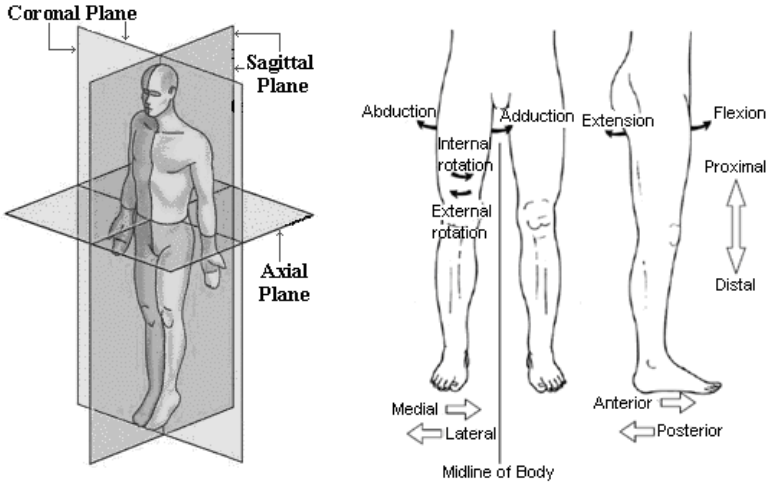

Figure 2.2: The body defined by planes; coronal, sagittal and axial[4] [Left]. Directions and motions of the hip[3] [Right]

Movement	Active Muscles	Stopped by
Flexion	Psoas, Iliacus, Rectus Femoris, Sartorius, Pectineus, Adductor Longus and Brevius and anterior fibres of Gluteus medius and minimus.	Thigh and abdomen contact.
Extension	Gluteus maximus assisted by hamstrings	Tension of the ilio-femoral ligament
Adduction	Adductor magnus, longis and brevis, Pectineus, Gracilis and lower part of Gluteus maximus	Contact with the thighs
Abduction	Gluteus medius and minimus and upper part of gluteus maximus.	Inner band of ilio – femoral ligament and pubo-femoral band
Internal Rotation	Gluteus minimus and the anterior fibres of the Gluteus medius, the Tensor fasciæ latæ and the Iliacus and Psoas major;	Outer band of ilio-femoral ligament
External Rotation	Posterior fibres of the Gluteus medius, The posterior fibers of the Glutæus medius, the Piriformis, Obturatores externus and internus, Gemelli superior and inferior, Quadratus femoris, Glutæus maximus, the Adductores longus, brevis, and magnus, the Pectineus, and the Sartorius.	Ischio-capsular ligament and hind part of capsule.

Table 2.1: Movements of the hip joint [1]

2.1.2. The Gait Cycle and Forces across the Hip

The contact forces on the hip vary during the gait cycle. A typical gait cycle and loading profile is summarised in Figure 2.3. Initial contact occurs as the heel makes contact with the ground. The foot is then in flat contact with the ground supporting almost all the body weight before the heel rises. The toe then leaves the ground marking the end of the stance phase and entering the swing phase. During the swing phase the other foot wholly supports the body. The swing phase ends with heel contact, and the cycle then repeats [5].

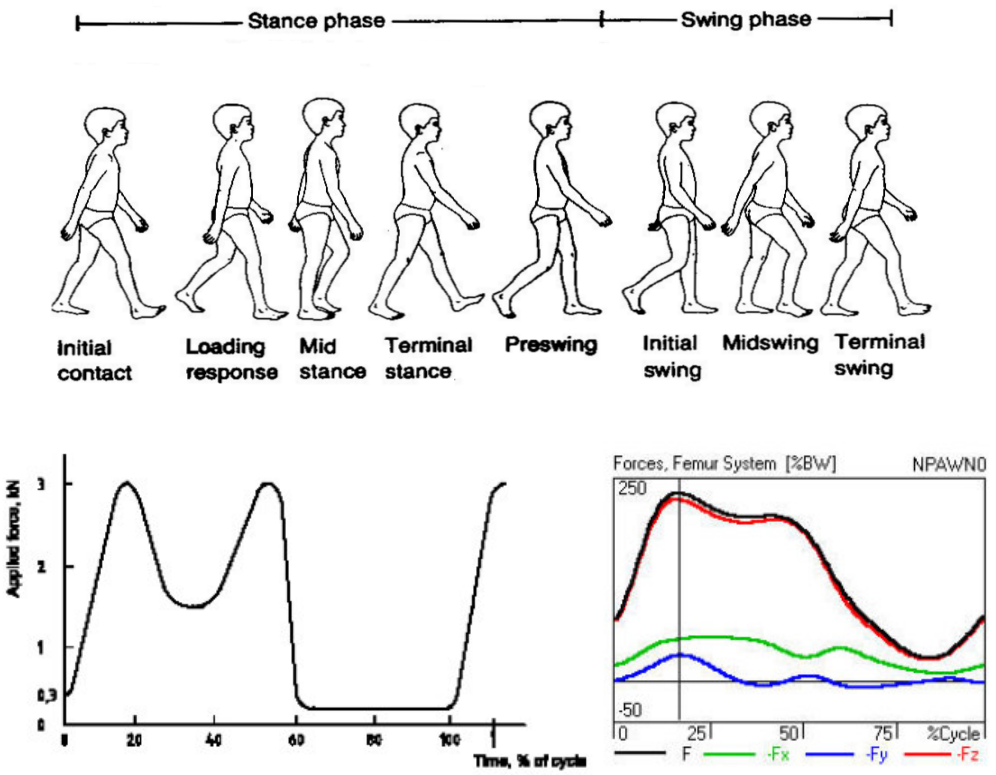

(a) ISO 14242-1:2002 loading cycle, (b) Bergmann loading cycle

Figure 2.3: The gait cycle[5] with the forces across the hip from a. ISO 14242-1:2002 and b. the Bergmann loading cycle [6]

Ideally, preclinical testing of existing and new hip prosthesis designs should include tests with environment and loading conditions representative of the hip. However, due to the complex nature of the hip joint and the difficulty in measuring muscle forces, data regarding exact forces across the hip is limited. An approximation of the loads across the hip can be extracted from the derivation of contact forces. The magnitude and direction of joint contact force through the gait cycle have been measured *in vivo* using implanted telemetric devices. Bergmann *et al*[6] implanted instrumented hip prostheses into patients and measured the contact forces for running and walking. The forces varied across the gait cycle with the first peak load corresponding to

heel strike (Figure 2.3). The average peak forces across the hip joint for patients walking at approximately 4km/h were 211-285%BW (percentage body weight) although in a previous study [7] a peak force of 409%BW was found. Jogging raised the peak force and torsional moment. During stair climbing, the peak forces seen were greater; up to 251%BW, with an increase in torque compared to walking of 23%. During the course of the study, one patient stumbled and peak forces of up to 870%BW were noted.

Loads and conditions across the hip vary with each patient and depend on lifestyle and activity levels. For example, the loading conditions across the hip for an obese bedridden person will differ greatly to those of an Olympic sprinter. These are extreme examples and the activity levels and loads across the hip are unlikely to reflect the average conditions for the current demographic of total hip arthroplasty (THA) candidates [8]. It is therefore important to assess average activity levels in the population of THA patients to understand the long-term conditions which the hip prosthesis must withstand. Morlock *et al* [9] conducted a study of the duration and frequency of everyday activities for a number of patients after THA. Activities were measured between 30 minutes after waking of the patient and 12 hours before the patient went to bed. They found that the most common activities were sitting (44.3% of the time), standing (24.2%), walking (10.2%), lying down (5.8%) and stair climbing (0.4%). This differs from the standardised testing required of hip prosthesis (Figure 2.3) which only assesses the prosthesis for a set number of cycles at an average loading profile characteristic of gait. By neglecting to include variable amplitude loading, time dependant factors such as creep of materials may be neglected in the analysis of the performance of prosthesis designs. With the current status of THA, patients are demanding restoration of function to allow for active lifestyles rather than the sole alleviation of pain as was required in early hip replacements. Therefore, more realistic and vigorous testing is required to assess new and existing prosthesis designs for durability and longevity to meet these current demands.

2.1.3. Brief History of Joint replacement

One of the earliest recorded hemi-arthroplasties was performed in 1894 by Gluck in Germany. Ivory was used to replace the femoral head and secured using a mixture of resin, powdered pumice and plaster of Paris. However, many of these procedures failed due to the high incidence of infection at that time[10]. The first total hip replacement (THR), where both surfaces were replaced with metal components, was performed in the 1930's by Phillip Wiles at Middlesex hospital. The majority of implants failed within a few years of implantation. Remarkably, one patient was reported with the implant in situ 35 years after implantation[11]. In 1940s, the Judet brothers in France developed a short metal stem with an acrylic hemispherical cap. These failed quickly due to improper biomechanical design, poor quality acrylic and overuse by patients[10].

G. K. McKee also developed a metal on metal implant in the 1940's. These implants provided initial relief of pain but were followed by rapid loosening. Failure was due to high frictional torque and high volumes of metallic wear debris. In the 1960s, Mckee, joined with J. Farrar to modify stem design and improve surgical procedures to address the issues of rapid failure [10].

Sir John Charnley[12] was unconvinced by the use of metal-on-metal bearing surfaces in THA. Inspired by a patient implanted with a squeaky Judet prosthesis, he developed the concepts of low friction arthroplasty by exploring the lubrication regime, friction and wear of bearing surfaces. In order to reproduce the squeak heard from the Judet prosthesis, he designed a load bearing pendulum system and used it to evaluate the coefficient of friction of different surfaces. Boundary layer lubrication occurs in natural joints as a result of the presence of synovial fluid. Fluid film (hydrodynamic) lubrication of stainless steel surfaces with synovial fluid was unachievable with the available machining of that time. As such, Charnley chose to use polymer materials with metal as a bearing surface. PTFE was the first attempt of a low friction bearing material. However, rapid failure within a year of implantation due to excess wear and an adverse tissue reaction to the wear debris, led to the abandonment of this material. The alternative was ultra high molecular weight polyethylene, UHMWPE which was more wear resistant than PTFE and demonstrated fluid film lubrication. In addition, to address the issues of high frictional torque, the femoral head diameter was reduced from 28mm to 22.2mm. The changes to the hip prosthesis design were highly successful and the Charnley stem still employ these key concepts today albeit with a few minor alterations resulting from clinical experience. The success of this prosthesis, in addition to problems of loosening and the concerns that metal wear debris may be carcinogenic, led to the demise and eventual withdrawal of the metal-on-metal components in the late 1960s. Metal on UHMWPE remains the most popular choice of bearing surface for THRs today. However, this was not the end of metal-on-metal components. In 1984, as a result of improvements in manufacture and further research, metal-on-metal components were re-released onto the market [13].

Charnley also introduced the widespread use of acrylic cement to secure the femoral component in place; an idea first introduced in 1953 by Haboush [14, 15]. Charnley was the first to use auto-polymerizing cement and suggest fixation of the component was maintained by interlock of the cement into bone rather than adhesion[16]. Cement was introduced to all available areas in the femur so that load was distributed over the widest possible area of bone.

In the long term wear debris from UHMWPE material can cause adverse effects in the body such as osteolysis (discussed in section 2.1.6) which can lead to degradation of the cement-prosthesis interface and eventually failure of the implant. These problems led to the introduction of cementless and hybrid (where one component is cemented and the other cementless) implants in 1980s. Instead of using cement to fix the implant, these prosthesis rely on porous or bioactive

coatings (or both) that promote and stimulate bone growth into the surface of the prosthesis. Precise reaming of the femoral canal for a tight fit to stimulate bone apposition onto the stem is required. If the strains generated during implantation are too high, femoral fractures may occur during impaction of the components [17]. These prostheses also require good bone quality for adequate ingrowth and therefore cementless and hybrid implants are more commonly used in younger patients (those under 60) where osteoporosis is less likely [13]. In addition, in patients where only the femoral head is damaged, resurfacing can be performed as a precursor to THR. The development of these alternate arthroplasty procedures has not hindered the development of cemented prosthesis. Cemented implants are still the favoured choice of procedure making up 89.5% of all THRs in Sweden from 1992 to 2005 [13].

2.1.4. Common Causes of Joint Replacement

A hip replacement is required when a patient experiences severe pain and disability accompanied by radiological changes at the hip and where non-operative treatment has failed or is futile. The common causes of hip replacement, as categorised by the Swedish arthroplasty register [13] are listed below with a brief description of the conditions.

Osteoarthritis

Osteoarthritis[18-20] is the most common cause of THR comprising of 94% of primary hip procedures in the UK in 2005, and 76.3% of THR procedures in Sweden in the period 1992-2005. Osteoarthritis is a degenerative joint disease that commonly affects middle aged and elderly people. It is the breakdown of the articular cartilage which protects joint surfaces, due to normal "wear and tear" of the joint. It can lead to bone on bone contact which may cause intense pain to the patient. Osteoarthritis is uncommon in patients under 40 and more common in women. Obesity and joint damage also increase the likelihood of early development of osteoarthritis.

Fracture

Fractures of the proximal femur or the pelvic bone cause 11.5% of the total hip procedures recorded in the Swedish arthroplasty register from 1992-2005 and 1% of total hip procedures performed in the UK. Hip fractures are commonly caused by falls in elderly patients (with an average age of 75.9) with poor bone quality due to osteoporosis.

Inflammatory Arthritis

Also known as rheumatoid arthritis, RA [18, 20]. RA is a chronic disease caused by inflammation of the synovium rather than wear of cartilage as with osteoarthritis. It can cause deterioration in the function of the joint, joint pain and joint damage and often affects multiple joints in the body. Inflammatory arthritis was the reason for 4.3% of THRs [19] and 1% of the hip replacements in

the UK in 2005. This number of hip replacement patients with inflammatory arthritis has dropped in recent years (from 7.34% in the period 1992-2000 to 2.8% in 2005 [19]) due to improved treatments by using anti-inflammatory drugs such as ibuprofen in the early stages of the disease.

Idiopathic Femoral Head Disease

Femoral head disease lead to 3% of the hip replacements in the UK and 2.9% in period 1992-2005 of the procedures recorded in the Swedish register [19] and includes avascular necrosis, ischemic necrosis and asceptic necrosis. Idiopathic/femoral head disease is due to the loss of blood supply to the femoral head leading to gross bone necrosis although the causes are not fully understood.

Other

Other causes include childhood diseases such as dysplasia (a hereditary disease where a misshapen acetabulum causes a high incidence of dislocations), tumors and secondary arthritis [19].

2.1.5. Modern Surgical Procedure for Cemented Arthroplasty

THR involves the removal of the femoral head and subchondral bone layer of the acetabulum. A metallic ball and stem is then inserted into a prepared cavity in the femur and can be secured with or without cement and the acetabular component inserted into the acetabulum. Depending on the severity of disease and the amount of pain and loss of function experienced by the patient, the surgeon will make a decision as to which surgical approach and procedure to use [21].

In a THR operation (Figure 2.4), the surgeon makes an incision approximately 10-12 inches in length[22]. Depending on the surgical approach (the exact position of the incision and direction from which the hip joint is assessed), certain muscles are detached or dissected and the hip is dislocated. The cartilage and subchondral layer of the acetabulum are removed. The acetabulum is deepened using a reamer to expose cancellous bone for anchorage of the acetabular cup to the desired anatomical position. Multiple 6-10mm anchorage holes of approximately 10mm depth are made in the roof of the acetabulum. Copious lavage is applied to ensure that blood and bone marrow are removed from the bone surface to aid cement penetration into the pores of the cancellous bone. Bone cement is mixed (section 2.3.1) and is inserted at a high viscosity into the acetabular cavity and pressurised to ensure a minimum cement mantle thickness of 2mm is maintained; a guideline suggested by Charnley [23] and maintained today [24]. An acetabular cup of at least 4mm smaller in diameter than the largest reamer used is inserted.

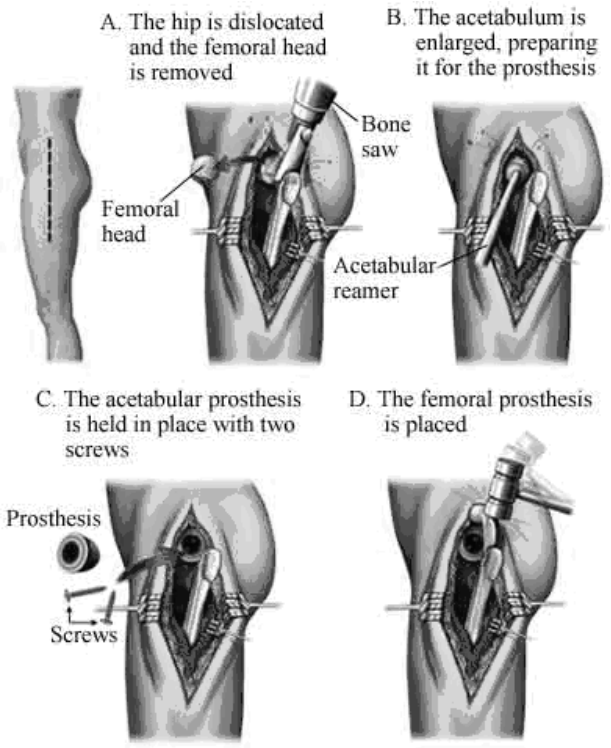

Figure 2.4: Surgical procedure for total hip arthroplasty[25]

For the femoral stem, the femoral head is resected, approximately 1.5-2mm above the lesser trochanter, level to the piriformis fossa and approximately 35° to the femoral shaft [22]. The piriformis fossa is located to facilitate correct stem alignment. A canal finder is rotated and inserted into the medullary canal to provide an initiation point for broaching. Before broaching a U-shaped section of cancellous bone parallel to the calcar is removed in order to reduce damage caused to cancellous bone by the reamers. 3-5mm of cancellous bone adjacent to the medial calcar is preserved for anchorage of the stem. Broaches are then inserted into the medullary canal which are typically 2mm greater than the stem design to produce a continuous 2mm cement mantle. A minimum of 3mm of cancellous bone maintained medially and anteriorly to allow for cement interdigitation is suggested [22]. The medullary canal is then lavaged and a cement restrictor introduced to a depth 1.5-2mm below the expected stem depth. A cement restrictor is used to plug the shaft to improve pressurisation of the cement. A clean interface for bone cement is recommended [26] for good cement interlock therefore further pulsating lavage is applied until the surface of the bone appears white. Cement is then added at a medium viscosity and applied under pressure. A femoral seal is added and cement is pressurised for 2-3mins to achieve adequate interdigitation. The femoral stem is then inserted in line with the longitudinal line of the femur. Stem alignment is important for long term stability of the femoral stem. Current guidelines for surgeons suggest that a cement mantle of 5mm at the medial calcar and a 2-3mm thickness distally is an indicator of a well cemented implant.

2.1.6. Failure Scenarios of THR

Revision is the exchange or extraction of one or all the parts of the prosthesis. As categorised by the Swedish arthroplasty; the reasons for revision are, in order of precedence: aseptic loosening, dislocation, deep infection, fracture, technical error, implant fracture and pain only [13]. Aseptic loosening is the most common cause of revision of hip arthroplasty resulting in over 74.9% of revision procedures in the Swedish arthroplasty in the period 1979-2005. Aseptic loosening is regarded as a process rather than an individual event; the theories and mechanisms proposed will be outlined in this section.

Particulate Reaction/Osteolysis: The presence of wear debris can trigger an adverse particulate reaction leading to eventual loosening of the component. The most biologically active size UHMWPE particles have been shown to be within the range 0.1-10μm in size[27]. Particles within this size range stimulate macrophages which attempt to remove the particle from the body. However, since UHMWPE is inert, the macrophage cannot remove the particle and instead the region becomes inflamed. This triggers an osteoclastic bone resorption response. This adverse biological response is known as osteolysis. If the particles lie within the interface between prosthesis and bone; bone resorption at the interface can lead to reduced implant support and as a result, increase relative interface motions leading to gross loosening of the implant [28]. Macrophage induced osteoloysis is more predominant for UHMWPE particles than metal debris possibly due to the smaller mean particle size of metal debris (40nm) produced. Although metal debris is less likely to cause osteolysis, it is not inert and has the potential to cause tissue toxity, hypersensitivity and DNA damage [29].

Stress Shielding: When the prosthesis is inserted, the resultant load is shared between the prosthesis and bone. As the prosthesis is considerably stiffer than the surrounding bone, it carries a greater portion of the load. Therefore, the bone carries a reduced load and is said to be stress shielded. This reduction in load triggers a resorptive remodelling response which can lead to degradation of the supporting bone and eventual loosening of the prosthesis. Stress shielding is influenced by material properties of the stem (the stiffness), the method of fixation and the quality and stiffness of the surrounding bone [30]. Cementless stems, which often have higher moduli, are more likely to cause stress shielding. There is some debate as to whether stress shielding is truly a failure mechanism [31] as there is no direct correlation between clinical data and stress shielding. However, the thinning of bone due to resorption can contribute and accelerate other failure processes and can cause problems if revision operation becomes necessary for other reasons.

Stress Bypass: Stress bypass causes a similar pattern of resoption to stress shielding. However, stress bypass is a result of poor proximal contact due to over reaming with a good fixation at the

distal tip in a wedge type position. The stem is positioned such that the load bypasses the proximal femur and hence triggers bone resorption in the proximal region. Due to its nature, stress bypass is almost exclusive to cementless implants.

Damage accumulation: Damage accumulation can occur in the prosthesis, interfaces, cement or supporting bone as a result of the repetitive cyclic loads that they are subjected to. Damage due to fatigue accumulates at loads significantly lower than the loads required for static failure until failure of the interface [32], prosthetic material (e.g cement mantle [33]) or failure of the supporting bone[34]. Once fixation is disrupted, increased micromotion can occur; a fibrous tissue layer may develop at the interfaces between prosthesis and bone and eventually lead to gross loosening.

Micromotion/Migration: Micromotion is the deformation within the bone-prosthesis construct. Migration is the irrecoverable movement of components in the long term and is characterised by permanent, progressive changes in the position of the prosthesis or the cement mantle or both. Migration can be described by three phases. The initial phase immediately postoperative is a rapid phase of migration due to the settling in of the prosthesis into a layer of necrotic bone [35]. This is followed by a slower continuous phase, the cause of which is unknown but which appears to be dependant upon anatomical location, fixation and implant design [35, 36]. The third phase characterised by increased migration and occurs towards the end of the prosthesis lifetime. The cause of this third phase is often attributed to wear debris induced osteolysis.

The rate of the initial migration can be indicative of whether a prosthesis is more likely to fail [37, 38]. Kobayashi *et al*[37] found that a migration rate of below 0.4mm in 2 years predicts a success rate of 95% in 10 years and as a result, concluded that implant designs exhibiting greater a migration rate than this should not be used. However, this study did not take into account prostheses designed to migrate such as the Exeter stem where some initial migration may be beneficial to the lifetime of the prosthesis [36]. Alfaro-Adrian *et al*[39] compared two differing designs of prosthesis: the Charnley Elite and the Exeter. The Exeter stem has a smooth tapered finish and is designed to subside within the cement mantle whereas the Charnley-Elite has a small collar and a 'vaquasheen' (matt) finish designed to compress the cement and inhibit implant migration. The Charnley Elite had a mean migration rate of 0.4mm at 2 years and the Exeter stem had substantially increased distal migration (1.2mm at 2 years) than the recommended rate. Based on the recommendations of Kobayashi, the Exeter stem should not be used, however clinical data shows that the Exeter has an excellent survival rate of 97% at 15 years [40]. This suggests that the recommendations regarding migration rate should take account of implant design.

Alfaro-Adrian *et al* [39] also showed that the site of initial migration has implications on how the implant functions and fails. The Exeter stem exhibited migration solely at the cement-stem

interface whereas the Charnley-Elite showed migration at both cement-bone and cement-stem interfaces. Depending on the design, the implications of interface failure may differ.

2.1.7. Overview of Clinical Assessment of THR

As the demographic of THR patients shift to include younger and more active patients, the demands on the performance and longevity of implants are increased. Charnley [23] was aware of the limitations and finite life of hip replacements designs and warned against implanting into young patients. "*Below the age of 65 the situation is very different. The younger the patient the more the surgeon must guard against allowing the patient's subjective symptoms to influence his judgement. He must turn deaf ears to exaggerated adjectives used to describe the intolerable quality of pain*." This concept of limiting THR to older patients is still maintained today. Ideally, a hip prosthesis should last the remainder of the patient's life however this can not always be achieved. The average age of the patient requiring hip replacement is reducing, life expectancy is increasing and patients are expecting to return to active lifestyles, thus demands on the longevity of hip prostheses are increased. Revision surgery is complex, time consuming and dangerous to the patient. Often the revision procedure will not be as successful in returning function or last as long as the primary operation. In addition, procedures can be costly. The economic demands on the health service and increasing frequency of hip procedure are the drivers for improving performance and longevity of hip implants [8, 13, 41].

In order to evaluate and improve the lifetime and success of hip prostheses designs, it is beneficial to monitor and further understand their failure processes. In the following section a case study of the failure of the 3M ™ Capital™ hip prosthesis and the implications from the investigation will be presented followed by a review of current clinical monitoring techniques of THRs and the characterisation of failure using these techniques.

Failure of the 3M™ Capital™ hip replacement

The importance of monitoring the performance of hip replacements is illustrated by the case study of the failure of the 3M™ Capital™ hip replacement; the aftermath of which led to the establishment of the UK's national joint register.

The 3M Capital hip replacement was marketed in the UK from 1991-1997 when 4,688 Capital hips were implanted in 79 clinical centres throughout the UK. Two designs were available the *Modular* or *Monobloc* which were *'flanged'* or *'roundback'* respectively. These components, with minor design changes, were similar to the Charnley hip prosthesis which was known for its history of clinical success [42].

At the time of introduction of the Capital hip, regulations regarding the introduction of new hip prosthesis designs did not exist. CE marking was introduced in 1995 and the Capital design was

granted a CE mark in 1995. It was thought that since the design was so similar to the Charnley prosthesis, it too would be clinically successful.

Following a poor short term performance, an investigation was launched in 1995 by the Medical Device Agency (MDA) and the implanted hips monitored through to 1998. As a result of the high incidence of loosening, a hazard notice was issued in 1998 (Medical Devices Agency Hazard Notice HN 9801) advising all patients implanted with a Capital hip to be recalled for clinical review. 3M Health Care and Department of Health commissioned The Clinical Effectiveness Unit of the Royal College of Surgeons of England to identify the causes and extent of the poor short term performance of the hip[42].

The patient's case notes, x-rays and questionnaires to both surgeons and to the patients were the key sources of information used by the study to identify risks and failure. In particular the characteristics of the patient, the surgical technique used, the type of hip replacement, quality of cement and the level of function reported by patients were recorded in order to determine the cause of the high level of failure. Function was self evaluated by patients using the Oxford hip score; a series of standardised questions used to evaluate the function, pain and activity levels of the patients. Performance of the prosthesis was defined by the revision rate and the probability that the Capital hip would not need replacement after a certain time after implantation (typically 5 years). Revision was used as an indicator of failure.

The results from the investigation suggested that the minor design changes were responsible for the poor performance of the modular flanged Capital hip. The implanted Capital stems showed debonding, cement abrasion, migration and osteolysis shortly after implantation. The modular flanged version of the capital hip performed significantly worse when compared to the monobloc round head design. The monobloc round head design had a success rate of 97.1%, 5 years after implantation compared with the moduluar flanged version with 89.2% functioning 5 years after implantation. The incidences of revision were higher for young patients and for men. The use of cement antibiotics and cement quality were also associated with a lower revision rate.

The benchmark for THRs issued by the National Institute for Clinical Excellence NICE, first in 2003, suggest that hip replacements should demonstrate a revision rate of 10% or less at 10 years. The monobloc round head design conforms to this standard whereas the moduluar flanged version did not. The conclusions of the study by the clinical effectiveness unit suggested that, had the appropriate systematic analysis of the performance of the capital hip system been in place prior to the introduction of the prosthesis, then the high incidence of failure would have been identified by 1995. Following the recommendations from this study, a national joint registry for the UK was established in 2003[8] to recognise future failings rapidly. In addition,

guidelines on the best practice in clinical care, surgical technique and monitoring of THR in the UK to reduce revision rate were detailed by the British Orthopaedic Association [26].

2.1.8. Clinical Methods to Monitor and Assess THR

Arthroplasty registers are a rich source of information regarding the monitoring of hip replacements. The first of such registers was the Swedish arthroplasty (1979) [13] followed by the Finnish (1980), Norwegian (1987), Danish (1995) and later the UK (1999). Typically these registers record information and analysis regarding the hip (and sometimes knee) procedures performed such as the type of procedure, prosthesis type, cement type, patient demographic and information regarding revisions. Using this information, improvements to the procedure can be assumed. For example, the establishment of the Swedish arthroplasty led to widespread improvements in cementing techniques [43].

Hip scores are commonly used to assess the function of the joint. The function, pain and mobility of the patient are graded via a series of questions. The Harris Hip Score [44], introduced in 1969 is commonly used. Pain, function, absence of deformity and range of motion is graded by the surgeon out of a total of 100, where 0 indicates disability and 100, perfect function. Typically, a candidate for hip replacement will have a score of 40-50 pre-surgery and 80-90 post-surgery. There are a number of alternate scores available, such as the Oxford hip score used in the Capital study. This is a patient orientated score as opposed to surgeon directed, as with the Harris score [45]. Questions such as "*During the past 4 weeks, how would you describe the pain you usually had from your hip: None, very mild, mild moderate or severe"* are posed. Measures of items such as pain are subjective and therefore hip scores cannot be used alone as a measure of the performance of THA.

Radiographs are also used to assess the performance of a total hip prosthesis. The best practice guidelines[26] state that a patient should have good quality antero-posterior and lateral radiographs before discharge from hospital. Radiographs are used to assess the performance of the hip replacement such as alignment, surgical technique, quality of the cement mantle and signs of infection. They can also be used to detect signs of loosening such as migration, defects in the cement mantle and radiolucent zones. Radiolucent zones are the result of the presence of soft tissue and can be used to indicate loosening in x-rays. Harris *et al* [46] suggested that the radiolucent line could be used as an indicator of damage at the cement-bone interface with a larger radiolucent line indicative of extensive damage or regions of gross loosening. Radiolucencies covering 50-90% of the cement-bone interface were shown to be indicative of a failed cement-bone interface. In an attempt to quantify and examine loosening in more detail and compare the performance of femoral components using radioluency as an indicator, Gruen *et al* [47] divided the femoral component into seven zones as illustrated in Figure 2.5. Looseness

was defined by any changes in mechanical integrity of the load carrying cemented femoral component such as fractured acrylic cement and radiolucent zones at the stem-cement interface or cement-bone interface. These seven regions commonly referred to as 'Gruen zones' are used by many subsequent studies to specify the regions for failure or factors affecting the cement mantle [48-52].

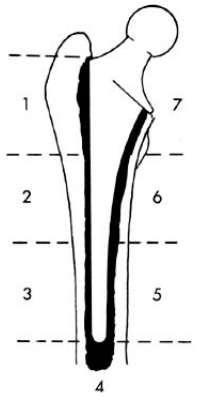

Figure 2.5: The seven sections of the femoral component used for evaluation of looseness and progressive loosening as defined by Gruen *et al* [47]

Roentgen stereophotogrammic analysis, RSA can be used to more accurately monitor the movement of the prosthesis relative to bone and detect early signs of failure [53]. Tantalum markers are inserted into the prosthesis and bone and simultaneous x-rays are taken of the joint with the patient in a calibration cage. Software is used to calculate 3D coordinates of each marker. Groups of markers define rigid bodies which represent implant and bone. These rigid bodies are compared between time points to estimate the 3D motion of the implant relative to bone. RSA offers a high degree of accuracy and can detect translations of as little as 10μm [53-55]. RSA has been applied to THR to examine migration rates of various prosthesis designs and its role in the loosening process [36, 56, 57].

Survivorship studies examine a group of patients until a set end point such as revision [48]. This allows comparison of designs of prosthesis and surgical technique. However, it can be difficult to keep track of patients unless a national follow-up scheme such as the arthroplasty registers is in existence. Retrieval analysis at revision [58] or post-mortem [32, 59] can allow examination of failed or well functioning prosthesis [60] in more detail.

Clinical analysis alone does not provide complete understanding of the failure process [61]. Prostheses are categorised as failed (by arthroplasty registers) when the patient experiences excessive pain and/or loss of function necessitating a revision procedure for alleviation of the problem. By this point, the prosthesis is at the endpoint of failure; damage processes may have initiated well before this point and information regarding the initiation of failure may be lost due

to damage of the materials, migration of the implant and changes to the bone structure due to adaptation. *In vitro* analysis allows assessment of the performance of new component designs before clinical application to prevent gross failure due to inferior designs such as with the Capital hip and to allow comparison of competing devices.

2.1.9. Overview of *in vitro* Analysis of THR: Computational Methods

The finite element (FE) method allows analysis of a structure by dividing it into simple parts called elements. The elements are linked to adjacent element by nodes. In a structural problem, the forces and displacements of these nodes are related by the stiffness matrix for each element. The stiffness term of a node is the sum of the stiffness for each element that node is connected to. These terms are collected together in the global stiffness matrix, K. The nodal forces, F can then be linked to displacements, δ through the equation:

$$(F) = [K] (\delta)$$

Equation 2.1

These equations are solved by assuming equilibrium exists; that the sum of the forces at each node must be zero unless there is an external force applied [62]. The stiffness matrix [K] is determined using the principle of minimum potential energy i.e. the displacement that sasfies the differential equations of equilibrium as well as the boundary conditions of the surface will give the minimum potential energy than any other displacement that satisfies the conditions of the bounding surface.

Finite element modelling is widely used in orthopaedic biomechanics as a preclinical analysis tool, to evaluate the biomechanics of musculoskeletal structures and to evaluate time dependant factors such as bone adaptation and fatigue. In biomechanics, FE models can be split into four main categories: static (implicit) analysis, adaptive analysis, dynamic (explicit) analysis and FE coupled with statistical methods. Static models are used to evaluate the response of the joint to static forces, typically peak forces in gait. They are used to evaluate the design and performance of prostheses by comparison of stresses, strains or micromotions at the interface between the bone and implant. Adaptive models are used to evaluate the effect of time dependant factors such as bone adaptation, fatigue of bone or bone cement, the behaviour of the prosthesis-bone interface or wear. Dynamic models are used to evaluate joints where stresses are a function of kinematics, such as at the knee. FE with statistic methods are used to identify the risk of failure and the key parameters associated with failure [61, 63].

FE models rely on clinical data to build and validate the models. Computed tomography (CT) images are often used to generate the complex geometric finite element models of bone. Meshes are generated by fitting nodes to a boundary defined by the CT images [64] or alternatively the voxels (three dimensional pixels) of the CT images can be transferred directly to finite elements.

More recently, high resolution CT images have been used to develop models to evaluate the microstructure of complex geometries such as cancellous bone [65] and even complete models of the hip [66].

At the fundamental level, the FE method finds an approximate numerical solution to boundary value problems [62]. The behaviour of biological tissues can be highly non-linear and can make the solution complex and time consuming. The quality of the solution depends on a number of factors such as the quality of the mesh, application of appropriate boundary conditions and material properties. Element distortion can introduce errors in the solution process. Discretisation of the geometry of the femur will only give an approximation of its volume. Generally a higher mesh density will give a more accurate solution, however there is an offset of accuracy with solution time or computational power required. Therefore a convergence study should be part of FEA studies to ensure the suitability of the mesh density.

FE models are only as accurate as the data used to create and validate them and as such can only be used on a comparative basis [67]. Obtaining results from clinical analysis can be quite time consuming. In addition, data regarding the stress state of the prosthesis, migration or damage processes may not be provided by clinical analysis. Instead, *in vitro* techniques can be used to analyse the performance of prosthesis.

2.1.10. Overview of *in vitro* Analysis of THR: Experimental Methods

In vitro techniques can be used to examine the stresses or strains in cement bone constructs, the migration of the prosthesis relative to cement and bone under dynamic loading and wear of the prosthesis. This section will give an overview of these techniques with particular focus on two non-destructive evaluation techniques: acoustic emission (AE) and computed tomography (CT).

Stress/strain analysis is typically applied to implant-bone constructs. Typically, deformation of the construct under load is measured and stresses are calculated using elasticity theory. Most commonly, strain gauges are attached to the surface of the bone or prosthesis [67-69] or encased in cement. For example in 1978, Oh *et al* [68] examined the strain distribution of cadeveric femurs with and without femoral components implanted. Unidirectional strain gauges were attached at various sites on the femur in the same plane and strains were examined under loading conditions representative of a single load stance. Lanyon *et al* [69] examined the stress distribution in the femur after hip replacement by attaching rosette strain gauges to the femoral component. Although this method provides direct measurements of the strain distribution in the femur, difficulties can arise in measurement due to misalignment of strain gauges and in regions of high strain gradient. Implanted telemetry can be also used to examine loads experienced by the hip (as discussed in 2.1.2). Other measurements techniques can be used to examine the femoral stresses. These include full field optical techniques such as photoelasticity, holography and

thermographic stress analysis, but are less commonly used. They are also limited to line of sight measurements and can also be time consuming [61].

In vitro techniques are also used to measure migration of implants under dynamic loading. Migration can be measure in 2D, using LVDTs to identify migration patterns with limited location and resolution of 20-200 microns, or 3D, such as RSA. Non destructive methods are often used to evaluate joint-prosthesis constructs. MRI and ultrasound are often used to diagnose and monitor THA[61]. These methods are not reviewed here.

Acoustic emission

Acoustic emission (AE) is a non destructive monitoring technique based on wave propagation. When a material experiences abrupt changes in stress or strain, or damage occurs, transient elastic waves are generated by the rapid release of energy from a localised source, usually a defect in the material. This phenomenon is known as acoustic emission and has a typical frequency range of 20KHz to 1MHz. By monitoring AE, damage initiation and propagation at multiple sites can be examined.

Factors which affect the propagation of waves through the material influence the characteristics of the resultant AE signal. These factors include material structure, environment and temperature [70]. Mechanical history also influences the generation of AE. The Kaiser effect [71], first documented in 1953, describes the phenomenon whereby a material will only emit acoustic activity after a primary load is reached. On elastic reloading of a specimen, little or no acoustic activity will be recorded until the previous maximum load is reached. When permanent damage occurs in the specimen, significant acoustic emission activity is recorded before the previous maximum load applied is reached. This is known as the Felicity effect and can be used as an indicator of permanent damage. During reapplication of the load, the Felicity ratio is defined as the ratio between the applied load at which activity is first recorded and the previous maximum applied load.

AE allows continuous monitoring of a sample and location of damage. Using two or more transducers (piezoelectric sensors) on the surface of the material, the origin of the AE and consequently the location of damage can be detected. The piezoelectric sensor transforms the acoustic wave into a voltage which is then processed and characterised. In order to eliminate background noise from mechanical and electric sources, a threshold is set below which signals are not recorded. For bone cement, this is typically 40dB[33, 72]. In order to locate damage, two or more sensors (depending on the size of the sample) must be used and the wave velocity of the material determined. To determine wave velocity, an artificial signal is induced on the surface of the material, typically by breaking a pencil lead on the surface of the material at a known location (also known as a Hsu-Neilson source) and the difference in arrival time at each

transducer is noted. Therefore by knowing the position of the transducer array, the wave velocity can be calculated.

AE has been used in orthopaedics for assessment of the integrity of implants. AE has been used to distinguish a loose and well-fixed prosthesis by attaching transducers to the skin near the greater trochanter. Signal filtering was used to remove the noise from skin friction and transducer motion. The detected AE from loose prostheses has been shown to correlate with radiolucencies at the bone-cement interface [70].

AE has also been used *in vitro* for damage monitoring of bone cement and its interfaces. Qi [73] used a wavelet analysis to study the attenuation of a signal through an artificial cement-bone construct. Several transducers were attached to rectangular specimens and pencil lead breaks performed on the surface at selected positions. The attenuation of the amplitude and energy was examined at varying distance from the source. The presence of an interface greatly increased attenuation of the signal however; the use of a couplant greatly reduced attenuation particularly at the cement-bone interface. In another study, Qi *et al* [74] used AE for three dimensional analysis of damage of notched bone cement specimens under tensile fatigue. They reported good location of events ahead of notch tip in real time and provided a fatigue failure time history. However, the accuracy of the algorithm used to locate events was subsequently brought into question as damage appeared to occur in the specimen notch where there was no material [75, 76], although the ability of their technique to detect cracking of bone cement was not challenged.

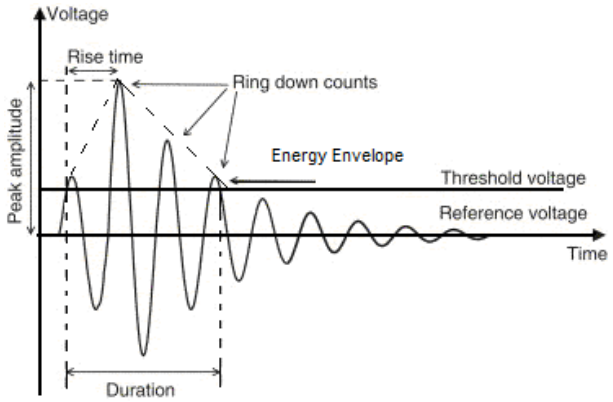

Figure 2.6: Schematic of AE hit of voltage versus time. AE parameters are indicated.[33]

Roques *et al* [72] used an alternative approach by performing a parametric analysis to monitor fatigue damage of specimens in four point bending. Parametric analysis allows the distinction of damage events from noise. A schematic of an AE hit (a signal recorded by one channel or transducer) and its associated parameters are shown in Figure 2.6. Trends and parameters associated with the cement failure process were identified and correlated to microscopic

observations of damage. The AE parameters recorded for each acoustic event or hit were maximum amplitude, duration, rise time, energy and number of threshold crossings. Duration and risetime were found to be most indicative of failure as they reflect the way energy is released in the material. Aging of the cement in Ringer's solution produced longer risetimes indicative of more plastic behaviour compared to aging in air which produced lower risetimes at higher loads. Jeffers *et al* [33] also used a parametric technique to predict failure in uniaxial tensile fatigue specimens of bone cement. Energy (in arbitary energy units eu) and duration (in μs) of events were used as predictors of failure.

Acoustic emission allows on line damage monitoring and has the ability to differentiate between failure mechanisms. It can continuously monitor a specimen in real time, for damage, without the need for interruption of tests or sectioning of a sample. However, analysis of the resulting data can be complicated. In addition, the technique requires some form of validation of damage regions.

X-ray Computed Tomography (CT)

CT imaging offers a non destructive method of three dimensional visualisation and characterisation of an object through the volumetric mapping of its x-ray attenuation (which is closely related to density). At the fundamental level, CT involves capturing a series of multiple x-ray views of an object at a range of angular orientations. X-rays are emitted from a source, pass through the object and the amount of attenuation (through scattering and absorption) of the x-ray signal is measured by a detector. Attenuation of monoenergetic x-rays is described by the Beer-Lambert Law[77].

$$I = I_0 e^{-\mu x}$$

Equation 2.2

Where I_0 = the initial x-ray intensity

I = the intensity of the x-ray after it has traversed a thickness of material, x

μ = linear absorption coefficient for the material scanned

When this equation is applied to a non-homogenous material, the equation becomes:

$$I = I_0 e^{-\int \mu(s) ds}$$

Equation 2.3

Where the line integral is taken along the direction of propagation and $\mu(s)$ is the linear absorption coefficient as a function of distance along the ray path. As the attenuation coefficient

is also generally a function of x-ray energy, the complete solution requires solution of the equation over the range of the effective x-ray spectrum.

$$\int \mu(s)ds = -\ln(I / I_o)$$

Equation 2.4

To reconstruct a three dimensional image, the series of radiographs at different angular orientations is processed so that the local value of attenuation is determined at every point of the sample volume. The most commonly used algorithm is filtered back projection in which the 2D images are filtered and each view is successively superimposed over a square grid at an angle corresponding to its acquisition angle.

CT was first developed for widespread use for medical science in the 1970s. In order to maximise effectiveness and minimise patient exposure to radiation, limited doses of low energy x-rays were used (≤125KeV). To obtain as much data as possible, large detectors (of the order of mm) were used. In the 1980s, CT was extended for use in industrial applications and as there were no constraints on radiation dose, higher energies and longer exposure times could be used and higher resolution of images could be obtained by use of smaller detectors (decline in signal related to a smaller surface area could be compensated by higher x-ray intensities and longer exposure times).

Ketchem[78] divides CT scanners into four categories as summarised in Table 2.2. Medical CT scanners are generally in the conventional category but some span the high resolution range. Industrial scanners extend from the conventional category to the ultra high resolution category. This includes bench-top micro-CT scanners that can achieve cubic voxel sizes as small as 5µm [79]. Synchrotron x-ray sources are required to achieve the resolutions defined as true microtomography and can provide a resolution of just below 1µm with a voxel size of 0.7µm. Examination of bone and stem-bone constructs span the whole range of these resolutions, however the definition of CT categories is often vague. The terms 'high resolution' and 'micro-CT' are often used interchangeably to describe resolutions below 50µm [65] or scans which resolve detail at the trabecular level.

Category	Scale of observation	Scale of resolution
Conventional	m	mm
High-resolution	dm	100µm
Ultra-High-Resolution	cm	10µm
Microtomgraphy	mm	µm

Table 2.2: Classification of computed tomography as defined by Ketchem[78]

CT imaging has been used extensively to provide data for finite element models. Three dimensional patient specific models are created by fitting boundaries to CT images [63, 80]. These models are limited to the resolution of clinical scanners although the continuum assumption is often used to neglect microstructural features and generalise the properties of cancellous bone. Higher resolution FE models (to the resolution of 10µm) can be used to examine the microstructural behaviour of bone [81-84].

Artefacts and partial volume effects can appear during tomography, obscuring details of interest and introducing errors for quantitative analysis [78, 85]. These errors include:

Beam hardening: As a polychromatic beam passes through an object, the lower energy X-rays are more easily attenuated than the higher energy x-rays, thus a beam will preferentially lose the lower end of its spectrum. This increase in mean energy is termed beam hardening. This is the most common artefact encountered in benchtop CT imaging and causes an object to appear brighter at its edges than at the centre. It can also appear as cupping or streaks across an image. Filtration and software can be used to eliminate the effects of beam hardening.

Aliasing: This appears as streaks in the end images at the corner of objects and is a result of steep intervals in projections.

Detector saturation/ photon starvation: The detector signal needs to be proportional to photon flux. If the detector is saturated, or the signal is attenuated too much, then streaks may appear on the resulting image.

Ring artefacts: These appear as full or partial circles centred on the rotational axis. They occur in third generation scanners (rotating x-ray tube and detector assembly) as a result of a shift in output from individual or sets of detectors which cause the corresponding rays to have anomalous views.

Partial volume effect: This is the blurring of material boundaries as a result of the voxels at the boundaries consisting of an aggregate value of x-ray attenuation of the two materials.

2.2. Bone

The longevity of a prosthetic implant is dependant upon its stability within its environment. Failure of the interfaces and degradation of the support from bone can lead to migration, loosening and eventual failure of the implant [86, 87]. The quality of bone (and its microstructure) can influence the quality of fixation [88, 89]. As such, it is important to understand the mechanical limitations of bone. In this section, the structure and properties of bone, adaption and post yield behaviour of the bone is discussed.

2.2.1. Structure of Bone

Bone provides mechanical support for the body as well as contributing to important physiological functions such as metabolic activities. It serves as a reservoir for essential ions such as calcium, for which bone is the main regulator. It provides attachment points for muscles and ligaments and also provides support and leverage for motion [90]. Bone consists of 65% mineral phase, 35% organic matrix, cells and water. The mineral phase is largely $Ca_{10}(PO_4)_6OH_2$ which is also known as hydroxyapatite. The mineral is largely responsible for the high stiffness of bone relative to other body tissues. The organic phase is approximately 90% type I collegen and 10% noncollagenous proteins [91].

In a long bone such as the femur, three regions can be distinguished as illustrated in Figure 2.7; the ephiphyses (the ends of the bone), the diaphysis (the central shaft) and the metaphesis (the region in between the ephiphysis and diaphysis). Two types of bone tissue make up a long bone; cortical bone and cancellous bone. Cortical bone forms the outer shell and appears as a series of lamellae. It has a porosity of 5-30% and forms approximately 80% of the total bone mass of an adult. It has an apparent density of between 1.0-2.0 gcm^{-1}. At the microscopic level, the structural unit of cortical bone is an osteon or Haversian unit. Osteons constitute two thirds of cortical bone and are separated by interstitial bone and held together by cement lines. An osteon is typically cylindrical in shape, approximately 200µm in diameter and up to 20mm long. The Haversian canal lies in the centre of the osteon and contains the nerve fibres and blood vessels which supply nutrients to the surrounding tissue. Each osteon is made of concentric layers of lamellae formed of collagen fibres impregnated with hydroxyapatite and other mineral crystals[90, 92, 93]. Cancellous bone forms the inner part of a long bone. It has a porosity of up to 90% [93] and forms 20% of the total bone mass of an adult, although the surface area is almost ten times greater than cortical bone. It has an apparent density of 0.05-1.0gcm^{-1}. At the microstructural level, cancellous bone appears as a network of rod or plate like struts otherwise known as trabeculae. The trabeculae are made of hydroxyapatite crystals embedded in a collagen-fibre matrix[94]. The pores between these trabeculae are typically of the order of 1mm in diameter and are filled with bone marrow and cells[95]. Cancellous bone does not exhibit an osteonal structure like cortical bone, instead it consists of parallel sheets of lamellae aligned with the orientation of trabeculae. The average trabecular thickness depends on anatomic site and loading environment but is generally 50-300µm[96]. The structure of cancellous bone depends on its relative density. At high densities the rods flatten out into plates forming a closed cell structure whereas at low densities, the cells are open and like a network of rods. Generally high density bone is found in regions of high loading and low density bone in regions of low loading. The relative density, defined by the density of the whole specimen, ρ^* divided by the density of the individual trabeculae ρ_s (ρ^*/ρ_s), varies from 0.05 to 0.7 [91].

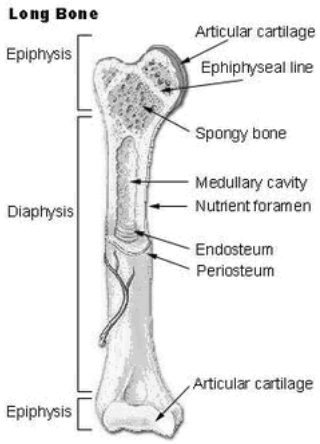

Figure 2.7: Structure of a long bone [97]

2.2.2. Development and Maintenance of Bone

Bone is heterogeneous and anisotropic. The heterogeneity arises from variations in volume fraction, architecture and tissue properties. The anisotropy varies with the anatomic site and loading conditions of that site. Bone is adaptive and responds to mechanical stimulation from its surrounding environment. In the femur, the trabeculae can be seen to develop along the principle stress trajectories in accordance with Wolff's law [91, 98]. If the load is multi-directional then cancellous bone will have no preferred orientation. There are two processes which control bone quantity: modelling and remodelling. Modelling is the adaptive response to changes in loading conditions such as increasing the thickness of the cortex in long bones and apparent density in cancellous bone in regions of high stress. Remodelling is the process of maintaining the equilibrium of bone repair and bone resorption. Equilibrium is usually maintained between deposition and removal of bone resulting in a stable bone density or geometry. If the equilibrium is disrupted, for example by a change in loading conditions, then either bone apposition or removal will dominate until equilibrium is established once again. This phenomenon is described by Wolff's law: bone is created in regions of high stress and removed in regions of low stress [99].

The exact stimulus for adaptation of bone is not fully understood although several candidates have been proposed including strain, stress and strain energy density or microdamage resulting from fatigue [100-102]. Although there is ambiguity surrounding the stimulus, it is generally accepted that there exists a 'lazy zone' about the equilibrium for which remodelling will not occur (Figure 2.8). In this zone no activity occurs. When a change in the stimulus occurs above this zone bone apposition occurs and below, bone resorption.

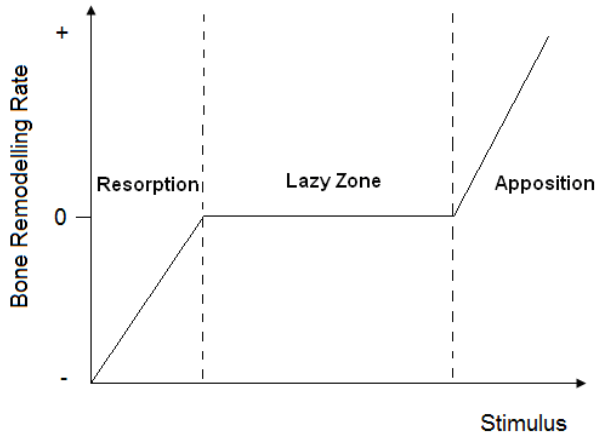

Figure 2.8: Adaptation of bone exhibiting a lazy zone or equilibrium where bone is not added or removed

The major types of cell that regulate bone growth and maintenance are osteogenic cells, osteoblasts, osteocytes and osteclasts. Osteogenic or stem cells are the primary cells from which other cells evolve. These can evolve into osteoblasts which are bone forming cells. Osteoblasts contain receptors for hormones regulating bone growth. The cells lay down bone until they surround themselves completely in bone matrix. When the cells cease to create bone they evolve into osteocytes. Osteocytes do not produce bone but maintain the cellular activities in the surrounding area. Osteoclasts found on the surface of bone, remove bone through the release of enzymes. They also contain receptors for hormones regulating bone growth.

2.2.3. Mechanical Properties of Bone

The reported mechanical properties of bone exhibit a high degree of variation due to many factors among which are its viscoelastic and anisotropic nature. The measured values of strength and modulus of bone depend on the direction of loading and the strain rate of testing as shown for cortical bone by Reilly and Burstein[103] and summarised in Table 2.3. Generally, accepted values of modulus for cortical bone lie between 16-20GPa[84].

Loading Mode	Ultimate Strength (MPa)	Elastic Modulus (GPa)
Longitudinal		17.0
Tension	133	
Compression	193	
Shear (torsion about longitudinal axis)	68	
Transverse		11.5
Tension	51	
Compression	133	
Shear		3.3

Table 2.3: Ultimate strength of adult femoral cortical bone tested at strain rates 0.02-0.05 per second[103]

The reported values in literature for elastic modulus exhibit substantial variation (as shown in Table 2.4). The reported strength of cancellous bone also exhibits variation and has been reported as low as 0.4MPa and as high as 50MPa [90, 93, 104-106]. Tensile strength for cancellous bone has been reported in the range 1-20MPa. Cancellous bone exhibits strength asymmetry (difference in compressive and tensile strength). There is some debate as to whether the tensile strength of bone is equal to, less than or higher than the compressive strength of bone. The reported values for shear strength are in the range 1-20MPa [89, 107] and shear modulus in the range 3.4-4.175GPa [89, 108].

Strain can be used as an indicator of failure. There is a strong linear correlation between the failure stress of bone and elastic modulus. This suggests that failure strain is relatively constant since the ratio of stress to modulus is strain [95].

The properties of cancellous bone can be defined at the apparent level and the tissue level. The apparent level, also known as the continuum level, considers bone as a continuous material with the average properties of a representative bone volume. This was defined by Harrigan [109] as a cube with a minimum of five trabecular lengths, which equates to approximately 5mm. The modulus of the individual trabeculae is referred to as the tissue level. The reported values of tissue level modulus vary with the experimental technique used. Tensile tests report modulus values of 0.4-3.6GPa, values from four-point bend test range from 3.81-5.72GPa [110-112] and ultrasound techniques yield values in the range of 10.4-14.8GPa [113, 114]. More recently, nanoindentation has given values between 6.9-25GPa [115-117].

Source	Year	Type of bone	Test Method	Elastic Modulus (Gpa) (±SD)
Runkle and Pugh[118]	1975	Distal femur	Buckling	8.69±3.17(dry)
Townsend et al[119]	1976	Proximal tibia	Inelastic buckling	11.38(wet)
				14.13(wet)
Williams and Lewis[120]	1982	Tibia	Compression test with 2D FEA	1.3
Ku et al[121]	1987	Frozen tibia	3-point bending	3.17+1.5
Mente and Lewis[122]	1987	Dried femur, fresh tibia	Cantilever bending with FEA	5.3±2.6
Ashman and Rho[113]	1989	Femur	Ultrasonic testing	13±1.5
Kuhn et al[112]	1989	Iliac crests	3-point bending	3.81
Mente and Lewis[123]	1989	Dried femur, fresh tibia	Cantilever bending with FEA	7.8±5.4
Ryan and Williams[124]	1989	Bovine femur	Uniaxial tension	0.76±0.39
Choi et al[111]	1990	Tibia	3-point bending	4.59
Jensen et al[125]	1991	Vertebra	FEA (3D)	3.8
Choi and Goldstein[126]	1992	Tibia	4-point bending	5.35±1.36 (wet)
Rho et al[114]	1993	Tibia	Tensile testing	10.4±3.5 (dry)
			Ultrasonic testing	14.8±1.4 (wet)
Van Rietbergen et al[127]	1995	Proximal tibia	Micro-FEA	2.23-10.1
Silva and Gibson[128]	1997	Vertebra	FEA (2D)	0.1
Hou et al[129]	1998	Vertebra	Micro-FEA	5.7
Ladd et al[130]	1998	Vertebra	Micro-FEA	6.6
Turner et al[131]	1999	Distal femur	Nanoindentation	18.14±17
			Acoustic Microscopy	17.5±1.12
Hoffler et al[115]	2000	Vertebra	Nanoindentation	8.02±1.31
		Femoral neck		10.5±1.6
Homminga et al[132]	2001	Vertebra	Micro-FEA	5
Kim et al[133]	2002	Vertebra	Idealised Model	12
Van Rietbergen et al[134]	2003	Femur	Micro-FEA	10
Bayraktar et al[135]	2004	Femur	Experimental and FEA	18±2.8
Norman et al[116]	2007	Proximal femur	Nanoindentation	14.22±1.07

Table 2.4: Reported values in literature for elastic modulus for cancellous bone

Due to the degree of variation of mechanical properties of cancellous bone, many attempts have been made to describe the strength and modulus of bone as a function of apparent density. Cancellous bone exhibits an open cellular structure. For cellular materials, mechanical properties are strongly related to apparent density. Expressions relating strength and elastic modulus can be empirically derived for cellular materials in the form of Equation 2.5.

$$\gamma = A\rho^B$$

Equation 2.5

Where γ is the material property (such as modulus or strength), ρ is the apparent density (mass/bulk volume) and *A* and *B* are constants. Galante [136] tested 71 samples of human vertebral bone and showed a linear relationship between compressive strength and apparent density. Carter and Hayes [104] tested human and bovine specimens of cortical and cancellous bone. They demonstrated a quadratic relationship of compressive strength with apparent density and a cubic relationship of apparent modulus and density. Hodgskingson and Currey [137] included testing of bovine, horse and human bone samples in order to capture the behaviour of a larger range of relative densities. They showed that that the relationship was closer to quadratic than cubic. Stone [138] found that in bovine trabecular specimens to show that shear strength was proportional to relative density to the exponent of 1.65. Rice *et al* [139] presented a statistical analysis of pooled data from several sources and concluded that a squared relationship best described both modulus and strength. Van Reitbergen [94] found from examining the varying relationships and data in literature that bone volume fraction accounted for 92% of the variation in Young's modulus, 88% of the variation of shear modulus and 76% variation in Poisson's ratio. This therefore shows that apparent density alone cannot predict the mechanical properties of bone.

An alternative approach, for generalisation of the apparent level mechanical properties of bone based on cellular theory, is to create a model of bone based on an idealised structure of cancellous bone. A repetitive structure based on unit cells is used to represent the structure of bone. Structural analysis (which can be in 2D or 3D) is then performed on this idealised structure to derive theoretical relationships between bone volume fraction and mechanical properties [91, 140, 141]. These idealised versions of bone structure can be combined with FEA to isolate and examine the effect of microstructure on the continuum properties. For example, Silva *et al* [128] and Guo *et al* [142] both examined the affect of age (thinning and loss of trabeculae) on vertebral bone using cellular models using different idealised cells. Both Silva and Guo found that microstructure strongly affected the mechanical properties. Guo *et al* also noted that trabecular loss is more detrimental to the strength of cancellous bone than thinning. This suggests that connectivity of trabeculae is also a factor in determination of mechanical properties. Kim *et al* [133] showed the importance of the structure of the unit cell in determination of mechanical properties. The study examined the effect of strut taper in an analytical cellular model of vertebral bone on the mechanical properties. Models with strut taper exhibited mechanical properties of the order 1.8-2.2 times higher than those with uniform struts. This study highlights one of the disadvantages of idealised models. Cellular models are often regular,

idealised and isotropic and therefore do not fully represent the anisotropic structure of cancellous bone.

The final approach to be discussed in the determination of the mechanical properties of bone is micro-finite element (μFE) analysis. These are FE models based on high resolution 3D images of the bone architecture. The resolutions are typically below 50μm for specimens of cancellous bone and approximately 100μm for whole bone models. A common method of creating the FE mesh from CT images is the voxel-element technique[65, 143]. Tomographic images consist of voxels (volume elements) of differing grey values which relate to the x-ray attenuation coefficient of the material within the voxel[78]. To segment the cancellous bone structure from the surrounding soft tissue a grey level threshold is selected. Each voxel with grey level above this threshold is directly converted to an eight node brick element. The number of elements in these models is often of the order of millions and model solution requires the use of multiple parallel processors [65]. An alternative approach is to create a tetrahedral mesh based on a triangular surface model of the tomographic data [144]. With this method, the surfaces can be smoothed, creating a more representative depiction of the cancellous bone surface rather than the stair-case like surface created in voxel models. For smooth surface models, an intermediate step of creating a triangular surface and optimisation of element number is necessary which may directly influence the accuracy of the resulting model.

μFE analysis has been used to characterise the anisotropic elastic properties of cancellous bone as they relate to morphology. From the characterisation of the elastic properties of a number of bone specimens, it has been found that the anisotropic behaviour of bone is a result of its architecture alone. This implies that the anisotropic elastic properties of bone can be calculated from μFE models of a bone specimen with an effective isotropic tissue modulus [145]. This has led to the focus on determining an accurate tissue modulus for accurate modelling using a combination of experimental and FE techniques [130, 145, 146]. μFE methods are effective in calculation of material properties of bone but require careful selection of resolution, isotropic tissue modulus, boundary conditions and mesh size for accurate results [146, 147]. Discretisation of the surface can introduce errors in the results of up to 20% [148]. μFE analysis is computationally expensive, with models consisting of elements of magnitude 10^6. In addition, FE models often require validation and can therefore be quite time consuming compared to theoretical models.

2.2.4. Limitations in Determining the Mechanical Properties of Bone

The structure and properties of bone vary with many factors such as age, sex, disease and species[149]. With age, particularly for women, bone can become osteoporotic. This is the thinning and loss of trabeculae leading to deterioration in quality and strength. Due to the heterogeneity of bone, it is often difficult to obtain reproducible results for characterisation of

the material properties of bone. This coupled with experimental errors, account for the large variation in the reported values of strength and modulus of bone [95]. Experimentally, the preparation of bone samples can affect the measured properties of bone. Machining of specimens can damage individual trabeculae leading to an underestimation of modulus. Chemicals and storage can also have a deleterious effect on the properties of bone [149].

A common method of determining compressive properties is the platen compressive test where a sample of bone is sandwiched between two parallel plates and compressed at a set strain rate until failure occurs. End artefacts such as non-uniform deformation of the surface of the bone or friction are primary sources of inaccuracies. Keaveny [150] showed that the end effects can result in 20-40% errors in determined values of modulus and strength. He suggested that to reduce end artefacts, the ends of the specimens could be embedded into a sample holder although this would require large specimens of bone. Constraining the ends of the sample may over constrain the specimen causing the sides to bulge and thus introducing non-uniform loading conditions across individual cells. The properties of bone are also dependant on strain rate of testing and if the specimens are tested wet or dry.

The deformation of the bone is used to calculate modulus. Deformation can be measured in a number of ways. Extensometers can be attached to the surface of the sample. However, attaching extensometers can damage the surface of bone. Errors in measurement will translate to errors in determination of modulus [150]. An alternative is to attach extensometers to the platens. Optical techniques can be used but often, due to the discontinuity of the surface, there can be a high amount of noise in the signal [151]. An alternative non destructive method is ultrasonic testing. The Young's modulus is calculated from the directly measured apparent density and the square of the velocity of the ultrasonic waves as they pass through the specimen. The advantage of this technique is that smaller samples can be used, the errors due to end effects are eliminated and the three orthogonal Young's modului and shear moduli can be easily determined from a sample. However, time dependant properties cannot be measured. Ultrasonic measurements of elastic properties are based on the propagation of a wave through a material. Due to the highly porous nature of cancellous bone, attenuation of the wave is likely to occur. As a result, errors in measurements can occur if dispersive effects are not included. Due to the porosity of the bone, low frequency waves with longer wavelengths are required to determine the elastic properties of cancellous bone [92].

2.2.5. Post Yield Behaviour of Cancellous Bone

Microdamage of individual trabeculae occurs in the femoral head *in vivo* and has been shown to accumulate with age. It has been proposed that microdamage to trabeculae could act as a

stimulus for remodelling [95]. The response of cancellous bone to damage is also important in understanding fixation of prostheses.

The post yield behaviour of bone has been determined at both the apparent and tissue level. At the apparent level, bone has a similar stress strain curve response to open cell foam. Hayes and Carter [152] tested specimens of bovine cancellous bone under uniaxial compression and examined the post yield behaviour relative to energy absorption characteristics. These tests showed the stress-strain response at the apparent level (Figure 2.9). This shows an initial linear elastic response until the yield stress (deviation from the linear elastic region) is reached. This is followed by a region of "strain softening" followed by pore collapse, where the curve appears almost horizontal. In this region, fracture and buckling of the trabeculae is responsible for the energy absorption and load dissipation in bone. Following significant deformation of the trabeculae, the cells close and stiffness increases rapidly due to densification of the material. The post yield behaviour of bone is density dependant; pore closure occurs at lower strains for higher densities of bone. Gibson and Ashby [91] with the analogy of cancellous bone to foam, stated that at low relative densities, bending of trabeculae tends to dominate failure of trabeculae whereas at higher relative densities, the trabeculae tend to fail by the formation of plastic hinges in bending.

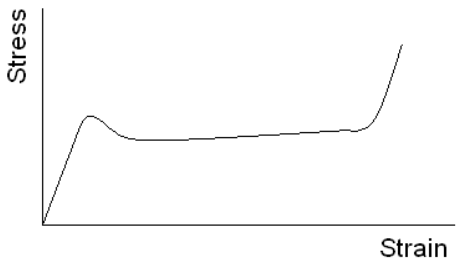

Figure 2.9: Compressive stress-strain behaviour of cancellous bone adapted from Hayes and Cater[152]

Experiments on specimens of trabecular bone have shown that when it is loaded past its yield point, it unloads to a residual strain at zero stress, reloads with a modulus equal to the initial modulus and then develops a reduced modulus (Figure 2.10). Keaveny *et al*[153] found that for strains up to 3%, the modulus reductions of human trabecular bone was in the range of 5.2-91%. These modulus reductions are not related to immediate change to bone density[154] but depend strongly on the applied strain. Reductions in strength are also associated with loading beyond the yield stress of bone.

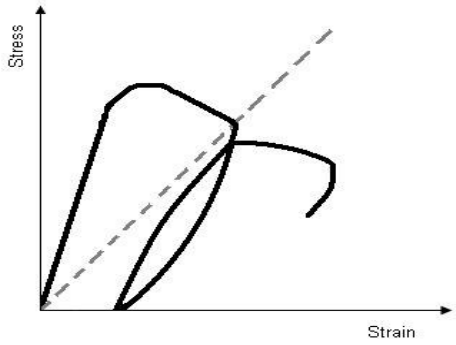

Figure 2.10: Schematic of stress-strain post yield damage behaviour of trabecular bone adapted from Keaveny[95]

At the tissue level, the reductions in modulus and strength occurring as a result of overloading have been shown to be the result of microdamage. Microdamage forms in cortical and trabecular bone during *in vivo* day to day activities. Damage to the trabeculae can also occur if an isolated overload occurs, for example a fall or trauma. Bone will heal in response to microdamage, however if more than one incidence of overload occurs with insufficient time for healing the residual strain will be greater than the first event[95]. The accumulation of damage within bone can increase the likelihood of bone fracture. Microdamage has been shown to occur preferentially in trabecular bone rather than cortical bone and more likely to appear in the form of microcracks rather than complete fracture of the trabeculae[155-157]. Fyhrie *et al* [156] examined the compressive failure behaviour of human vertebral cancellous bone to 15% strain. They noted that trabeculae orientated horizonatally with respect to the applied load were first to fracture. Vertically orientated trabeculae appeared to buckle due to the accumulation of microdamage. It was also suggested that since disconnected trabeculae are rapidly resorbed, complete fracture of trabeculae can lead to the loss of repair potential. Keyak *et al* [158] examined the complete failure of vertebral trabecular bone using uniaxial compression tests. They found that the damage of bone could be described by a tri-linear stress-strain curve. The initial behaviour exhibited a linear elastic region until a stress, *S* was reached. The material then exhibited perfectly-plastic behaviour which is then followed by a region of decreasing stress with increasing strain.

µFE analysis combined with experimental techniques has also been used to examine the damage behaviour of open cell foam [81, 82, 159]. These techniques examining post-yield behaviour are relatively new and computationally expensive and therefore research in this area is quite limited. Non-linear models are required to simulate the strain dependant behaviour of material properties and large deformations of trabeculae. Muller *et al* [81, 82] used µCT images to examine in-situ damage behaviour of whale vertebral specimens. A micro-compression device was presented which took CT images of bone samples at different stages of loading. Failure in rod-like

specimens of bone was by buckling and bending followed by collapse of overloaded trabeculae. Alonso Vazquez *et al* [159] used this in-situ imaging technique coupled with non-linear μFE analysis to predict the post-yield failure response of open cell aluminium foam. The model was able to predict post-yield behaviour up to 5% strain.

When subjected to fatigue loading, cortical bone exhibits strength and modulus degradation and accumulation of strain/creep. Creep of bone has been shown to follow a three phase response; initial rapid response, a steady state creep at constant creep rate and rapid increase in strain before fracture [95]. Qualitatively, cancellous bone exhibits similar behaviour to cortical bone [160, 161].

Investigations into the fatigue behaviour of bone are relatively limited. Michel *et al* [160] examined the fatigue behaviour of bovine trabecular bone. The stress-strain plots exhibited increasing non linearity, hysteresis and decreasing secant modulus with time. With failure defined by a 5% reduction in secant modulus, the number of cycles to failure corresponded to strain through a power law relationship. A difference in modulus degradation in low and high cycle fatigue was also noted. The modulus increased slightly for low stress rates and progressively decreases for high stress rates. In both cases, there was a rapid drop in the final stages of fatigue failure. Two types of failure were observed; brittle like failure and buckling. Similar to the monotonic compression tests of Fyhrie *et al*[156], brittle failure was more common in the trabeculae transverse to the direction of loading and buckling was more common in trabeculae parallel to the direction of loading.

Due to the complexity of the behaviour of cancellous bone in fatigue, synthetic bone models are often used to assess the performance of implants. Characterisation of these foams has shown a similar behaviour to that reported for cancellous bone [91, 162, 163].

2.3. Fixation of Cemented Implants

Regardless of whether an implant is cemented or cementless, fixation and the creation of an adequate interface are vital for long term stability of the implant [21, 92]. For cementless implants, the reamed cavity is smaller than the stem width. The implant is inserted into the femur with an interference fit in order to produce residual strains to stimulate bone apposition. If these residual stresses are too high femoral fractures may occur during impaction of the components. Porous coatings such as titanium or cobalt beads can be added to the surface of cementless implants to allow bone to grow into the void spaces of material[86]. Bioactive coatings such as hydroxyapatite (HA) can be used to stimulate bone growth on the surface of the implant. However, both porous coatings and bioactive coatings require a sufficient interference fit to provide initial stability and time for bone growth. If the initial micromotions exceed 100-500 microns then a fibrous tissue layer can form between implant and bone. This can lead to rapid

migration of the implant and eventual loosening [86, 164]. Cemented implants rely on sufficient interlock between the cement and cancellous bone. Iwaki *et al* [165] showed that with a secure initial fixation, minimum migration of the implant and absence of radiolucent lines, then lytic lesions at five years and aseptic loosening at ten years were not likely to occur. The following section describes the factors which influence the fixation of cemented implants with particular emphasis on the cement-bone interface.

2.3.1. Mechanical Properties of PMMA

Bone cement is a grouting agent used to secure orthopaedic implants. The most commonly used bone cements are acrylic polymers such as polymethylmethacrylate (PMMA). The cement consists of two parts: an acrylic polymer powder and liquid monomer. These parts are mixed shortly before required in the operating theatre and used at the correct time after mixing. For a given cement, the working time depends most strongly on the environment temperature (Figure 2.11). The powder, usually PMMA based, contains benzoyl peroxide (BPO); an initiator of radical polymerisation, a radiopacifier such as barium sulphate and antibiotics to reduce infection. The liquid component is usually methylmethacrylate (MMA) and also contains an accelerator and a stabiliser (to prevent premature polymerisation in storage). Palacos® (Heraeus Medical GmbH, Germany) cement also contains chlorophyll, making the cement green so that it is more visible to surgeons. When the two components are mixed together, polymerisation begins. The rate of polymerisation depends on the temperature at mixing. A higher temperature causes faster polymerisation. At the initiation of polymerisation, the polymer swells and partially dissolves in the monomer. The initiator is released and reacts with the accelerator to produce free-radicals. As a result of the high number of free radicals, polymer chains are generated. The viscosity of the mixture increases with reducing mobility of the monomer until the cement is cured[166]. The viscosity affects the handling characteristics of the cement. The viscosity increases with time after mixing and varies with cement type[167].

Polymerisation of the cement is exothermic with peak temperatures between 67-124°C depending on the type of cement and amount of cement considered[168]. At the cement-bone interface, temperatures measured clinically are lower, in the range of 40-46°C. Thermal necrosis of the bone surrounding the cement can occur due to high temperatures. But osteonecrosis depends on duration of exposure as well as temperature. Moritz and Henriques [169] suggested that cell necrosis occurs after 30 seconds exposure to a temperature of 55°C and after five hours after an exposure to 45°C. Over 70°C the regenerative capacity of bone is damaged. Lundskog[170] also found extensive necrosis in cortical bone subjected to temperatures over 70°C. Eriksson and Albrektsson[171] recorded tissue damage for exposures of one minute at a temperature of 47°C. However, other reports suggest that thermal necrosis is not a result of

polymerisation of cement but rather the result damage to the bone during preparation of the bone cavity. For example, Jerreris *et al*[172] suggested that osteonecrosis is a result of mechanical, vascular and chemical degradation rather than solely increased temperatures at the cement-bone interface. Initial preparation of the femoral canal using rasps can damage cells and disrupt the vascular supply. The monomer in the bone cement can also cause chemical destruction to the bone[173].

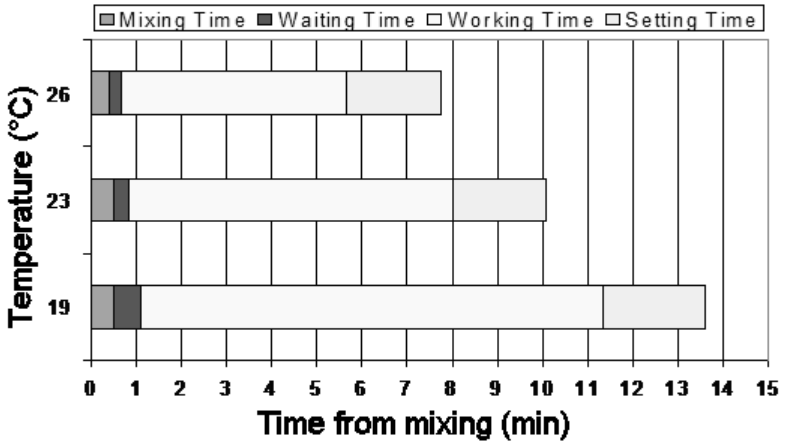

Figure 2.11: Map of polymerisation of a typical acrylic bone cement [174]

Cement shrinkage is caused by the change in density during polymerisation. Theoretically shrinkage is 6-7% as a result of the reduction of MMA[166]. In reality, this value is lower due to porosity. This is the reason that handmixed cement exhibits less shrinkage than vacuum mixed cement. *In vivo,* absorption of water often compensates for cement shrinkage. The resulting change in volume due to shrinkage induces residual stresses within the cement and gaps at the cement-bone interface which may lead to an initiation of cracks at the interface between cement and bone and within the cement itself. This damage can lead to a reduction in fatigue life[175].

The properties of cement are dependant on many factors including preparation method, mixing technique, method of testing, testing temperature, and type of cement. The cement may be mixed using different methods. These are manual or hand mixing, centrifugation mixing, vacuum mixing and combined mechanical mixing[168]. The most common method of mixing is vaccum mixing as it has been shown to produce cement with lower porosity than other methods. In addition, compared to other methods, vacuum mixing reduces monomer evaporation and exposure in the operating theatre, prevents air entrapment in the cement and increases the mechanical strength[176]. At high strain rates, bone cement is a brittle material and thus exhibits an elastic load displacement curve followed by sudden failure under tensile loading. Bone cement is a thermoelastic polymer therefore it has temperature dependant properties. It is viscoelastic and under sustained loading or fixed displacements it exhibits creep or stress relaxation. The creep rate depends on the type of cement and environment. Creep rate also

increases with strain rate, increases with temperature and reduces with the age of cement. Bone cement will creep less in compression and shear than in tension. Due to the number of variables that affect the properties of cement, the reported mechanical properties exhibit variation as summarised in Table 2.5.

Properties	Range of values
Ultimate Tensile Strength	23.6MPa to 47MPa
Tensile modulus	1583MPa to 4120MPa
Ultimate Compressive Strength	72.6-117MPa
Compressive Modulus	1940-3180MPa.
Shear Strength*	32-69MPa

* tested in accordance with ASTM D732

Table 2.5:Mechanical properties of PMMA[168]

2.3.2. The Stem-Cement Interface

In a cemented implant two interfaces exist; the stem-cement interface and the cement-bone interface. Based on retrieval of 16 femora, Jasty *et al*[32] examined the initial mechanisms of loosening. In all of the 16 specimens, the cement-bone interface remained intact whereas debonding at the stem-cement interface and fractures in the cement mantle were seen. They suggested that stem-cement debonding followed by progression of damage into the cement mantle were early indicators of loosening and damage to the cement-bone interface, indicated by radiolucency is a later event. FE analysis showed that stem-cement debonding causes higher cement stresses at the corners of the stem[177, 178]. In a study on the long term effects of stem cement debonding, Verdonschot and Huiskes[179] found that debonding at the interface elevated cement stresses by four times and promoted the formation of a pathway for wear debris. Fluid pressure has been proposed as a cause of osteolysis leading to loosening even in the absence of wear debris[180]. During the first six postoperative months, a fibrous tissue layer may form at the stem-cement interface. The fibrous tissue layer contains fluid and the addition of load onto the prosthesis produces fluid pressure at the interface between prosthesis and bone. This pressure is sufficient to cause osteocyte death and induce osteolysis. The conclusions from these studies prompted research into improving the performance of the cement mantle and examination of methods to increase the bond at the stem-cement interface.

There are a number of factors that affect the strength of the stem-cement interface. These include the cementing technique, cement shrinkage, geometry and stiffness of the implant and surface roughness of the stem. Preparation and mixing of the cement affects the quality of the cement mantle by affecting the amount of porosity present. Pre-existing flaws in the cement mantle are often the initiation sites for damage and reduce static and fatigue strength[33, 181]. Bishop *et al* [181] suggested that when a stem is implanted at body temperature, polymerisation progresses from the bone towards the stem. This induces pore formation in the cement mantle

near and at the cement-stem interface. They suggested that preheating the stem would reverse this process and reduce porosity at the interface and improve fatigue strength of the interface. However, Wang[182] showed that although pre-heating of stem reduced a six fold reduction in porosity, there was only a minor improvement in fatigue strength. Therrmal shrinkage occurs during the curing of the cement. This can induce residual stresses of up to 10MPa in the cement mantle. The residual stresses may be dissipated by stress relaxation such as creep or damage to the cement. Residual stresses of this magnitude can initiate damage at the stem-cement interface[183]. Gap formation can also occur at the stem-cement interface due to shrinkage particularly for grit blasted surfaces. The presence of gaps could increase the likelihood of debonding[184, 185]. Geometry can affect the shear strength of the interface. The geometry of the stem can introduce local stress raisers into the cement mantle which can cause crack initiation and failure at the interface[186].

Increasing the surface roughness of stems increases the shear strength of the stem-cement interface. Wang *et al*[187] examined the influence of different surface treatments on the push out strength of stems. The surfaces were polished (Ra=0.03µm±0.005), bead blasted (Ra=0.64µm±0.06), coarse grit blasted (Ra=4.65µm±0.74) and plasma sprayed with cobalt-chrome (Ra=9.593µm±2.84). The test showed push out strengths of 0.48kN for the polished surface and 9.85kN for the grit blasted surface. They found that increasing the surface roughness by a factor of 100 yielded an increase in shear strength of a factor of 20. However, there was a limit where further increases in surface roughness had no effect. Crowinshield *et al*[188] examined specimens with surface roughness ranging from 0.1-6.3µm which gave push out strengths of 200-10000KN. An upper limit to surface roughness was found where failure would occur in the cement mantle rather than at the interface. Verdonschot *et al* [189] used a combined 2D local and global FE model of a tapered stem to examine the effect of surface roughness (Figure 2.12). The 2D model represented one element of the global tapered stem model. The interface was assumed to be unbonded and frictionless contact was simulated using gap elements. The local model used varying sinusoidal surface profiles to represent the surface roughness of the stem. Roughness values (R_a) were varied between 0-30µm. The global coefficient of friction was determined from the ratio of tangential force and applied compressive force. The results of the study showed that stem-cement friction was elevated for higher surface roughness. Cement stresses and friction were also increased by the morphology of the surface profile. It was shown that increasing surface roughness reduced micromotions of the stem. However, the local model showed increased peak stress concentrations around the asperities of the surface profiles for higher surface roughness. Therefore, if stems with increased surface roughness debond, they are likely to cause elevated cement damage due to abrasion.

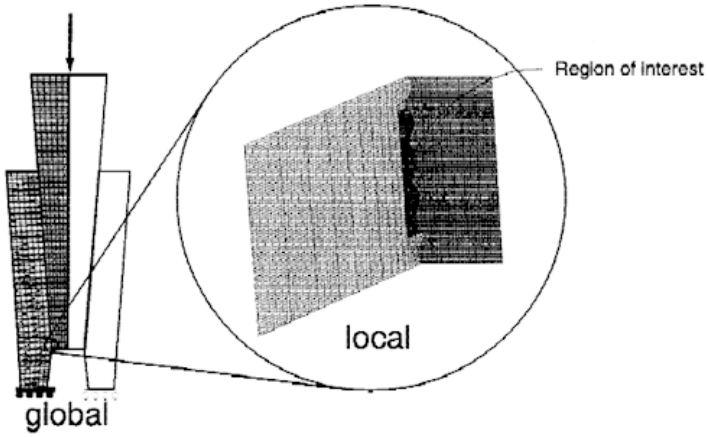

Figure 2.12: Global and local modelling of the cement-bone interface[189]

2.3.3. The Cement-Bone Interface

Although much focus of research has been in increasing the strength of the stem-cement interface, it remains a matter of debate as to whether a stronger stem-cement interface actually improves the longevity of an implant. Attempts to improve the bonding between the stem-cement interface have led to early incidences of failure due to loosening at the cement-bone interface[190, 191]. Gardiner and Hozak[190] suggested that the improved bond at the stem-cement interface transfers increased stresses to the cement-bone interface, increasing its likelihood of failure. The significance of damage to the stem-cement fixation or the cement-bone interface has been said to depend on whether the prothesis is designed to slip or not[39]. Race *et al*[192], in contrast to the earlier study by Jasty[32], show that early failure is concentrated at the cement-bone interface. Therefore research into examination of load transfer and the integrity the cement-bone interface has become increasingly important.

2.3.4. Histology of the Cement Bone Interface

Charnley[15, 23] examined the histology of the cement-bone interface by sectioning of *post-mortem* femurs from patients with clinically successful implants. In load bearing regions direct contact between cement and bone occurred. On the ends of the trabeculae, end caps of bone tissue had formed indicative of bone remodelling. Although these regions of direct contact were few in number, they were sufficient to transfer load from prosthesis to bone. In non-load bearing regions, a fibrous tissue layer had developed between cement and bone as illustrated in Figure 2.13. In the case of successful replacements, this layer was thin and non-continuous. A thick fibrous tissue layer appears as lucency on a radiograph and is indicative of loosening.

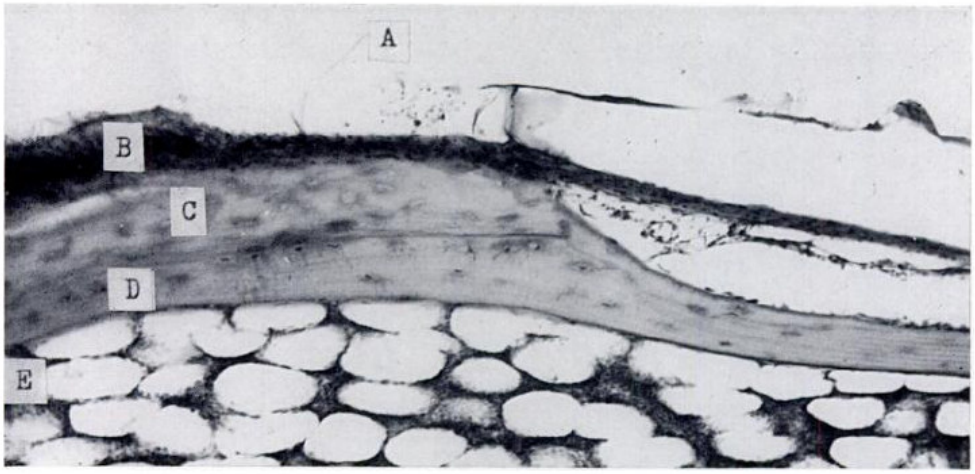

Figure 2.13: Histology of the cement-bone bond taken from Charnley[15]. A indicates site of cement. B is layer of fibrous tissue. C is dead cancellous bone. D is new lamella bone deposited on dead bone and closing the trabecular space. E shows fatty marrow with normal appearance

The histology of the interface changes with time postoperatively. Vernon-Roberts [193] characterised the histology of the cement-bone interface in stable hip prosthesis from a few weeks to 20 years after implantation from a number of macroscopic and microscopic studies. The stability was defined by four phases of the tissue reaction:

i. Up to three weeks after implantation a layer of dead bone up to 5mm in thickness was found in apposition to the cement surface. Towards the end of the three weeks osteoclasts laying down new bone were present.

ii. The reparatory phase began at four weeks. This lasted a minimum of six months and could last up to two years. Microscopy revealed a thin layer of connective tissue approximately 1.5mm thick between bone and cement. Active remodelling of tissue occurred.

iii. Stabilisation occurred between 6months to 2 years postoperatively. All necrotic and repaired bone was replaced by living lamellar bone. All architectural modelling was completed. The fibrous tissue remained or disappeared.

iv. At a minimum of two years, the prosthesis could be regarded as stable. Lamellar trabecular bone appeared in close contact with cement surrounding the prosthesis although a thin layer of tissue was normally present between the bone and cement surface.

Jasty [60] also examined thirteen *post mortem* well functioning prostheses. These were from prosthesis implanted from 40 months to 18.5 years. All specimens exhibited an intact cement-

bone interface with interdigitation of the cement into the trabecular bone. For the femora retrieved at 5 to 17.5 years, extensive remodelling of the trabeculae was seen. In the proximal metaphysic and proximal part of the diaphysis of the specimens, this was characterised by thick trabeculae running circumferentially around the cement mantle and thinner trabeculae running around the thick trabeculae, which gradually merged with the outer cortex. In the long term, evidence was seen of trabeculae growing into the undulations of the cement.

From the above histological studies, a well functioning prosthesis will exhibit an intact cement-bone interface with direct contact between cement and bone and bone apposition to the surface cement. However, the histology of the cement-bone interface in a loosened prosthesis is different. Radin *et al* [194] examined the histology of changes around the femoral component in sheep implanted with prosthesis. The sheep were made to walk on a concrete surface six weeks postoperatively to induce loosening in the implants. Radiolucency developed at the bone-cement interface as a result of bone resorption and the formation of thick fibrous tissue at twelve weeks postoperatively. This radiolucency was parallel to a decrease in torsional rigidity of the structure and histological deterioration of the interdigitation of the cement-bone interface. Tissue formation was observed as early as three weeks postoperatively. Bone remodelling occurred however there was a net loss of bone overall.

2.3.5. Properties of the Cement-Bone Interface

Since bone cement does not have any adhesive qualities, the strength of the cement-bone interface depends on the mechanical interlock between cement and cancellous bone. Improved cement interdigitation into the cancellous bone has been shown to increase the strength of the cement-bone interface [195-200]. Increased interdigitation can be achieved by pressurisation of cement, lavage of the bone surface and viscosity at time of insertion. By using proximal seals, distal plugs and lavage, an increase of up to 82% in shear strength of the cement bone interface can be seen when compared to without[201, 202]. As such, factors affecting the cement bone interface have been the focus of much research and interface properties can exhibit substantial variation as summarised in Table 2.6.

In vitro studies have shown that the cement-bone interface is stronger with increased cement penetration into the trabecular bone [89, 198, 200]. Cement penetration depths below 1-2mm have low interface strengths and are likely to show increased micromotion [198, 203]. Pressurisation directs cement flow into the trabecular spaces and overcomes bleeding pressure, allowing increased penetration of cement into cancellous bone. Oates *et al* [200] examined the effect of cement pressurisation on the strength of the interface in an *in vivo* study of goats. Pressure was maintained using a distal plug and a pneumatic gun apparatus in half the animals and digital packing in the other half. Interfaces produced with the pneumatic gun were found to be stronger

than those produced by digital packing; although there was a limit beyond which increasing pressure had no effect. In addition to pressurisation, cleaning the surface of bone also aids cement penetration. Lavage before insertion of cement removes loose cancellous bone, blood and fat from the surface of the bone. This aids penetration of the cement into the trabecular spaces and improves the contact between cement and bone [89, 198]. Krause *et al* [198] showed that pressurised interfaces with lavage exhibited greater strength than as cut, unpressurised interfaces. *In vitro* tensile and shear tests of cancellous bone from proximal tibias were performed to determine the mechanical strength of the cement-cancellous bone interlock with respect to preparation of bone surface and cementing technique. Tensile strength varied from 2.72 ± 1.42MPa for as cut specimens to 5.30 ± 2.13MPa for specimens subjected to high intensity lavage.

Although cement penetration depths above 1-2mm have shown to increase the strength of the cement-bone interface, there appears to be an upper limit to which further increasing cement depth does not produce any further benefits. For penetration depths above 5mm, the strength of the cement-bone interface does not increase significantly. This is possibly because bones which higher porosity which allow greater cement penetration generally have reduced bone strength [203]. With increased cement penetration depths, if failure of the interface occurs then the bone stock is reduced making revision arthroplasty more difficult. In addition, the increased volume of cement associated with higher penetration depths of cement can cause thermal necrosis due to the heat generated by polymerisation of the cement and chemical necrosis due to the presence of monomer [204]. Therefore, the optimum cement depthappears to be within the range 3-5mm [203, 205, 206].

The viscosity of cement changes with time after mixing until the cement cures. The change in viscosity varies with the type of cement. The viscosity at time of insertion can influence the degree of cement penetration. Stone *et al* [207] examined the effect of viscosity on the push out strength of cement-bone specimens. Femora were injected with cement (Simplex, Stryker-Orthopaedics, USA) at 4.5 minutes and at 6.5 minutes (after mixing) to simulate insertion at low viscosity and high viscosity cement respectively. The times of insertion corresponded to viscosities of $6.9\pm0.7x10^4$ centipoise and $34.2\pm1.6x10^4$ centipoise respectively. It was found that cement injected with lower viscosity exhibited greater failure strength. However, these tests did not simulate intramedullary bleeding or differing cements which can also influence the amount of cement interdigitation. Miller *et al* [208] included bleeding in their investigation and examined the tensile strength of a low viscosity cement; Osteopal (Biomet-Merk, Sweden) and a standard viscosity cement; Simplex.

Osteopal and Simplex were injected at 3.7 minutes and 4 minutes (after mixing) respectively into human femurs. The standard viscosity cement was 21% stronger than the low viscosity cement.

It was proposed that low viscosity cement was less effective at displacing bone marrow leading to less regions of bone apposition and therefore in lower interface strength. Similarly, Race *et al* [209] showed for implanted femurs with simulated venous back pressure that reduced viscosity cement showed inferior cement mantles. Although cement penetration was increased proximally, it was reduced distally. In addition, low viscosity cement showed lower bone apposition as a result of cement shrinkage.

Evidence suggests that it is not only the amount of penetration of cement that affects the strength but also the apposition of cement to bone. The presence of cement interface gaps and intervening fibrous tissue layer are indicative of a weaker interface and also may provide a pathway for the initiation of osteolysis[200]. Miller *et al*[208] showed 15% greater apposition between cement and bone with standard viscosity cement, which they related to greater interface strength.

Source	Parameters investigated	Source of bone	Cement	Mixing	Bone preparation	Pressure	Shear Strength, MPa	Tensile strength, MPa	Depth of penetration
Halawa *et al*[89] (1978)	Thickness of cancellous bone, preparation	Human femora	Simplex PRO^2	Hand mixed	Jet, pressure 0.21N/mm^2	0.15Pa for 30 secs	0.5-7.3		To the depth of cleaning
Krause *et al*[198] (1982)	Preparation and cement technique	Proximal tibia	Acrylic		Varied	Digital	1.83±2.08 - 5.36±3.10	9.55±4.06-20.68±8.9	
						0.17MPa	6.41±3.58-8.50±4.28	25.33±7.61 - 41.99±5.8	
Funk *et al* [88] (1994)	Cement modulus	Bovine	PMMA	Hand mixed			5.46±0.47-7.61±2.94		6mm
Oates *et al*[200] (1995)	Pressurisation of cement	Goat Femora	Simplex	Hand mixed	Lavage and brushing	High > 0.14MPa	3.059±0.399		
						Low < 0.14MPa	1.9±0.189		
Stone *et al*[207](1996)	Viscosity of cement	Human femora	Simplex	Centrifuged	Pulsating lavage	High (4.5mins after mixing)	4.1±1.6		Recorded as % of total cement volume
						Low (6.5mins after mixing)	3.1±0.5		
Mann *et al*[199](1997)	Cement interdigitation	Human proximal femora	Simplex	Vacuum	Lavage	Cement impactor		1.28±0.79	1.54±0.89
Reading *et al*[52](2000)	Pressure measurements	Human femora	CMW3, CMW1	Vacuum	Lavage and brushing	Digital	0.4-2.28		

Source	Parameters investigated	Source of bone	Cement	Mixing	Bone Preparation	Pressure, KPa	Shear Strength, MPa	Fracture toughness $MPa.m^{-1/2}$	Fatigue strength	Depth of Penetration
Lucksanasombool *et al*[210] (2001)	Fracture characteristics	Bovine femora	Simplex		Defatted	Hand		0.62±0.16		
Graham *et al*[211] (2003)	Bone porosity, penetration depth	Bovine tibia	Palacos	Hand mixing	Waterjet and trychloroethylene	60,120,180		0.8-1.6		1.5-6mm
Buckley *et al*[196](2003)	Fracture characteristics	Bovine proximal femora	CMW[3]	Vacuum	Defatted: trychloroethylen	72; maintained till cure		3.89		
Arola *et al*[212](2005)	Fatigue strength and push out strength	Bovine femora	Endurance			200 for 5minutes	2.7±0.6-23.6±2.4		0.8-5.1MPa	
Miller *et al*[208](2007)	Cement viscosity, cement bone apposition	Human Proximal femur	Osteopal, Simplex	Vacuum	Brush lavage	Distal plug, proximal seal	2±1.51 – 2.42 ±1.55			1.34-1.5mm

Table 2.6: Summary of literature reporting properties including cementing technique and amount of penetration

In addition to cementing technique and cement properties, the surface texture, quality and amount of cancellous bone remaining in the cortex has been found to affect the strength of the resulting interface. The surface texture of bone depends upon the tools used for reaming. Interface strength is greater with a rougher bone surface texture[212]. The porosity and trabecular orientation of cancellous bone significantly affects the fracture toughness of the interface[211]. Funk and Litsky[88] also found that the shear strength of cement-cancellous bone specimens was more dependant on the quality of the trabecular bone than the modulus of cement. Halawa *et al*[89] stated that the trabecular strength directly determines the strength of the resulting interface. From push out tests in transverse sectioned blocks from the proximal femur with retention of 2-3mm cancellous bone compared to 5mm, 2-3mm samples exhibited 100% greater strength. They stated that this was due to the increased strength of the trabecular bone nearer to cortex. However, detailed quantification of the cancellous bone and the penetration depths of the cement for these samples was not undertaken.

Although the importance of interdigitation on strength is often highlighted, it is not clear what the optimum penetration depth is or its relation to the bone microstructure and the resulting interface strength. The penetration depth of cement is sometimes reported (Table 2.6) but there is no standard definition for measurement. For example, Stone *et al* [207] examined the strength of the cement-bone interface with sectioning of an implanted femur. From photographs of the surface of each segment, the cement penetration volume of each segment was defined by multiplying the average length and area measurements by segment thickness. Mann *et al* [199] also used sectioning of a femur to investigate interface characteristics. Interdigitation depth was calculated by subtracting the distance from the cement to the periosteal surface (from photographic images of the surface) from the broach distance (determined from CT scans of the section).

Due to the substantial scatter in interface strength, penetration depth alone does not appear to fully describe the behaviour of the interface. Morphological features of the interface such as pedicle depth (cement that protrudes into the cancellous bone) and quantity of cancellous bone are often neglected. Maher *et al*[213] attempted to address this issue by introducing a parameter to quantify the morphological features defined as the random undulating parameter (RUP). Using image analysis, the outline of the cement-bone interface was determined from images of sectioned, cemented femora retrieved from autopsy. The mean cement diameter was evaluated using the recorded outlines of the interface. The deviations from the mean cement diameter was recorded at several locations and the mean of these deviations were defined as the RUP. This parameter was suggested as a measure of the interlock, the equivalent of the surface roughness of the interface. In a later study, Arola *et al* [214] proposed a parameter to estimate the apparent

volume of interdigitation in terms of the surface roughness profile. Although these parameters have been proposed, there is still no standard definition of the measurement of interdigitation.

The formation of an intervening fibrous tissue layer at the cement-bone interface can jeopardise the fixation of the cement bone interface. Waide *et al* [164] used combined experimental and FE techniques to examine the effect on cement strains of a fibrous tissue layer. A silicone layer was used in composite femurs to simulate two fibrous tissue conditions; a layer covering the whole cement mantle representing a revision condition and a layer covering the proximal part of the cement mantle, representing a primary operation with partial debonding and fibrous tissue formation. The composite femurs were implanted with two designs of hip prosthesis and subjected to simulated heel strike conditions. Strain gauges were used to measure cortical bone strains. The fibrous tissue layer was simulated in the FE model by creating an additional layer around the cement mantle. Cancellous bone was assumed to be act as a continuum with an average Young's modulus of 0.4GPa. Stress shielding was found to occur for both prosthesis designs when fibrous tissue was included. Both conditions of the fibrous tissue layer were found to increase cortical bone strains when compared to the well fixed condition. With the addition of a fibrous tissue layer, the experimentally determined strains in the cement mantle were similar to that of the well fixed condition. However, using the FE models, localised regions of peak strain were noted in the cement mantle.

At the microstructural level, failure of the cement-bone interface depends on the type of interlock that is achieved and degree of penetration of cement. The penetration of cement into the trabecular bone forms a composite at the cement-bone interface. As such, failure can occur through a number of mechanisms. Miller *et al* [208] classified fracture surfaces of cement-bone specimens into six categories as shown in Figure 2.14. The majority of specimens failed through failure type 2, across the composite region through bone and cement.

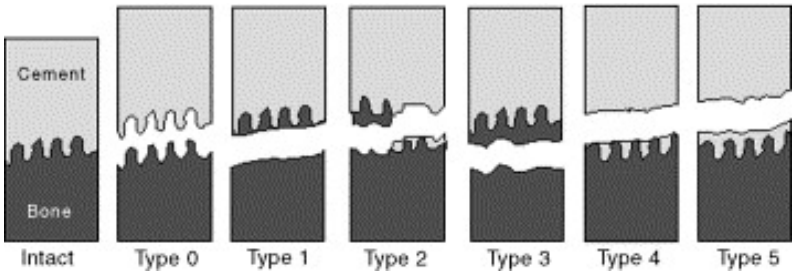

Figure 2.14: Characterisation of fracture surfaces of cement-bone interface specimens from Miller[208]

Askew *et al*[195] defined failure of the cement bone interface by the fracture of cement *pedicles*, fracture of the trabecular bone struts and the pull out of cement pedicles. Race *et al.* [192] examined the damage in the cement around femoral stems under aggressive fatigue loading

representative of stair climbing. They found that early damage was preferentially associated with the cement-bone interface in the form of microcracks. Microcracks were classified as follows (Figure 2.15);

a. Cracks in the cement between trabeculae in the composite region which did not progress into the broached area of cement
b. Cracks initiating in the spurs of trabeculae and extending into the bulk of cement
c. Cracks which form with no relation to any feature in the midmantle
d. Cracks at the stem-cement interface which appear normal to the stem
e. Void related cracks.

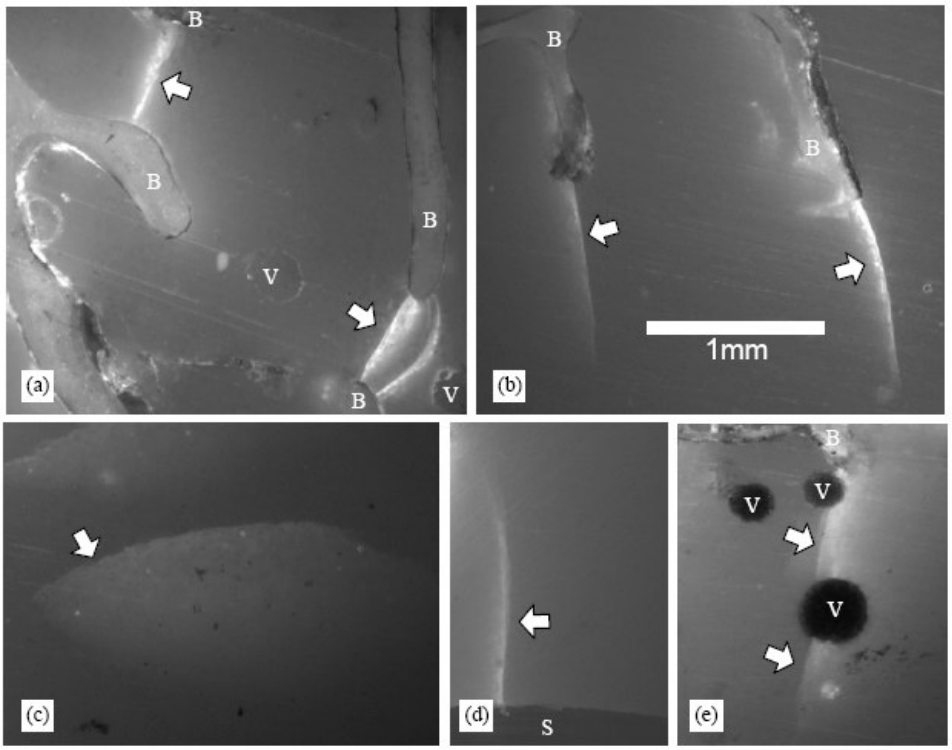

Figure 2.15: Microcracks at the cement-bone interface from Race *et al*[192]. Arrows indicate cracks, 'B' Bone, 'S' Stem and 'V' Voids. (a) cracks in interdigiated area (b) cement-bone interface (c) mid mantle (d) stem-cement interface (e) void related.

2.3.6. Cement Mantle Thickness

As well as cement interlock, the thickness of the cement mantle is thought to influence the stability of fixation and cement mantle strains. There is no clear definition in literature of what the optimum thickness of cement mantle should be. In addition, the measurement of cement mantle thickness can include or discount the regions of cement interdigitation[51, 215, 216].

Generally complete cement mantles with thicknesses above 2mm are advised. Charnley[23] suggested that a minimum thickness of 2mm should be maintained to secure fixation of the implant. In addition, Breusch and Malchau[22] advise that a stem size should be selected to guarantee a minimum cement mantle thickness of 5mm at the medial calcar and 2-3mm more distally. Fisher *et al* [217] examined the cement strains in implanted composite femurs for various cement mantle thicknesses. The composite femurs were subjected to simulated walking and standing conditions. An increase in cement mantle thickness from 2.4mm to 3.7mm, with a constant stem size caused a 49% reduction in cement strains. Kwak *et al* [218] also showed the benefit of a thicker cement mantle. The stress distributions for cement mantle thicknesses of 1-5mm were examined. The maximum tensile stress was shown to increase in the stem and decrease in the cement as the cement layer was increased. A cement mantle thickness of 3-4mm was suggested to be optimum. Ramaniraka *et al* [219] recommended a cement mantle thickness of 3-5mm based on evaluations of micromovement at the interface using 3D FE models. Clinically, cement mantle thicknesses above 2mm have shown good success rates [32, 216].

In contradiction to maintaining a continuous cement mantle, a good success rate has also been achieved in France using little or no cement mantles. This has been termed the '*French Paradox*' [220]. The technique, introduced by Marcel Kerboull involves the removal of all the cancellous bone in the medullary canal before insertion of a stem the same dimensions as the cavity resulting in a thin, discontinuous cement layer. The stem design, known as the Charnley Kerboull is polished and tapered with a neck angle of 130°. A similar approach of reaming to the same size as the stem uses the Freeman stem but not all the cancellous bone is removed [221]. Skinner *et al* [216] compared the survival and radiological outcome at ten years for the two techniques; reaming to allow for a 2mm cement layer and reaming to the same size as the prosthesis. The same stem design was implanted for both techniques. They showed a survival rate at 97.2% for the 2mm cement mantle and 98.8% for the thin cement mantle. The 'thin' technique showed greater interdigitation of cement. The reasons for these high success rates are not known but it has been suggested that the interference fit of the stem produces greater pressurisation of the cement achieving greater cement penetration (up to 3mm)[221, 222] and that the tight fit immobilises the cement-bone interface while the cement settles[216]. Another theory is that the complete removal of cancellous bone results in a stronger cement-bone interface because the cancellous bone is weaker [222]. It is clear that fixation from prosthesis to bone in a cemented implant is complex and requires further examination. Since microstructural features such as morphology affect the strength of fixation, microstructural evaluation of the interfaces is required to further understand the load transfer from prosthesis to bone.

2.4. Summary

Cemented implants are a popular choice for THA in both elderly and young patients [40]. For young patients, those below 60, the Swedish arthroplasty register [13] shows that 60.2% of primary THRs were cemented in the period 1992-2005. For patients older than 60, the share of cemented implants is 95.9%. Cemented stems have a high success rate. The polished Exeter stem exhibits a survival rate of 97% at 15 years [40]. Therefore, for elderly patients, the implants may be sufficient to last the remainder of their lives. However with younger patients, with active lifestyles, higher demands for improved longevity are placed on implant designs. With new prosthesis designs there is a need for improved preclinical tools that can assess the quality and suitability of the prosthesis.

Aseptic loosening continues to be the most frequent cause of revision of cemented implants [8]. The exact mechanisms of loosening are not fully understood but the interfaces between prosthesis and bone are thought to be initiation points for loosening. Studies have investigated the role of voids in cement [223], the stem-cement interface [32] and the cement-bone interface[192] in the failure process. The integrity of the cement-bone interface is vital to the long term stability of cemented hip arthroplasty. Previous studies of the interface have been confined to the continuum level, neglecting the effects of microstructure. Microscopic damage at the interface may eventually lead to macroscopic loosening of the implant. However, since the strength of the interface depends on the interlock of the cement with bone and since the properties of cancellous bone depend on its microstructure, the study of the behaviour of the interface at the microstructural level may help gain an understanding of the factors governing initiation of loosening. There are clearly a large number of factors that can affect the strength and longevity of the interface; thus macro-scale experimental investigations of this interface have been unable to draw any definitive conclusions on its mechanical behaviour. To gain any meaningful insight into the behaviour of this interface and the factors involved, it would be useful to analyse it at the microstructural level using a combination of experimental and computational techniques.

2.5. References

1. Gray, H. and W.H. Lewis. *Anatomy of the Human Body*. 2000 [cited; 2004, 1/2/04] Available from: http://www.bartleby.com/107/
2. *Sacroiliac Anatomy*. 2006 [cited 2006 1/6/06]; Available from: http://www.sidysfunction.com/index.htm.
3. Martini, F. and E. Bartholomew, *Essentials of Anatomy and Physiology*. 2000: Prentice Hall.
4. *Colarado comprehensive spine institution*. 2008 [cited; 2006, 1/6/06] Available from: http://www.coloradospineinstitute.com/anatomy/anatomical_planes_18.html.
5. Vaughan, C.L., B.L. Davis, and J.C. O'Connor, *The three-dimensional and cyclic nature of gait*, in *Dynamics of Human Gait*. 1992, Human Kinetics Publishers: Illinois. p. 7-14.

6. Bergmann, G., G. Deuretzbacher, M. Heller, F. Graichen, A. Rohlmann, J. Strauss, and G.N. Duda, *Hip contact forces and gait patterns from routine activities.* Journal Of Biomechanics, 2001. **34**: p. 859-871.
7. Bergmann, G., F. Graichen, and A. Rohlmann, *Hip Joint loading during walking and running measure in two patients.* Journal of Biomechanics, 1993. **28**(8): p. 969-990.
8. Gregg, P., M. Porter, T. Wilton, C. Thompson, A. Crosbie, M. Borroff, J. Timperley, P. Howard, J. Van Der Meulen, and F. Davies, *National Joint Registry for England and Wales*. 2004.
9. Morlock, M., E. Schneider, A. Bluhm, M. Vollmer, G. Bergmann, V. Muller, and M. Honl, *Duration and frequency of every day activities in total hip patients.* Journal of Biomechanics, 2001. **34**(7): p. 873-881.
10. Mow, V. and R. Huiskes, *A brief history of science and orthopaedic biomechanics*, in *Basic orthopaedic biomechanics and mechano-biology*, V. Mow and R. Huiskes, Editors. 2004, Lippincott Williams & Wilkins. p. 1-27.
11. Howse, J., *Semi-captive cups for hip replacement*, in *Joint Replacement*, R. Coombs, A. Gristina, and D. Hungerford, Editors. 1990, Orthotext. p. 135.
12. Charnley, J., *Present status of replacement therapy - principles and practice in hip replacement* Proceedings of the Royal Society of London Series B-Biological Sciences, 1976. **192**(1107): p. 191-198.
13. Herberts, P., H. Malchau, and G. Garellick, *The Swedish national hip arthroplasty register. Annual report 2005*. 2006, Sahlgrenska University Hospital: Gteborg, Sweden.
14. Haboush, E., *A new operation for arthroplasty of the hip based on biomechanics, photoelasticity, fast-setting dental acrylic and other considerations.* Bulletin of the Hospital for Joint Diseases Orthopaedic Institute, 1953. **14**(2): p. 242-277.
15. Charnley, J., *The bonding of prostheses to bone by cement.* Journal of Bone and Joint Surgery British Volume, 1964. **46**: p. 518-529.
16. Charnley, J., *Anchorage of the femoral head prosthesis to the shaft of the femur.* Journal of Bone and Joint Surgery British Volume, 1960. **42-B**(1): p. 28-30.
17. Jasty, M., R.M. Henshaw, J.C. O'Connor, and W.H. Harris, *High assembly strains and femoral fractures produced during insertion of uncemented femoral components.* The Journal of Arthroplasty, 1993. **9**(5): p. 479-487.
18. *Arthritis Research Campaign*. 2004 [cited 2004 1/10/04]; Available from: www.arc.org.uk/.
19. *The Swedish National Arthroplasty Register; Annual Report 2004*. 2005.
20. *Arthritis Foundation*. 2007 [cited 2007 1/4/07] Available from: http://www.arthritis.org/.
21. Breusch, S. and H. Malchau, *The well cemented total hip arthroplasty: theory and practise*, ed. S. Breusch and H. Malchau. 2005, Berlin: Springer.
22. Breusch, S.J. and H. Malchau, *Operative steps: Femur*, in *The Well-cemented Total Hip Arthroplasty*, S.J. Breusch and H. Malchau, Editors. 2005, Springer.
23. Charnley, J., *Low Friction Arthroplasty of the Hip; Theory and Practise*. 1979, Berlin: Springer-Verlag.
24. Breusch, S., H. Malchau, and J. Older, *Operative Steps: Acetabulum*, in *The Well-Cemented Total Hip Arthroplasty*, S. Breusch and H. Malchau, Editors. 2005, Springer.
25. Keel, J. *Hip Replacement*. 2007 [cited 2008, 2/2/08]; Available from: http://www.aurorahealthcare.org/yourhealth/healthgate/getcontent.asp?URLhealthgate=%2214822.html%22.
26. Nixon, J., *Primary total hip replacement: a guide to good practice*. 2006, British Orthopaedic Association.
27. Green, T.R., J. Fisher, M. Stone, B.M. Wroblewski, and E. Ingham, *Polyethylene particles of a 'critical size' are necessary for the induction of cytokines by macrophages in vitro.* Biomaterials, 1998. **19**(24): p. 2297-2302.
28. Ingham, E. and J. Fisher, *Biological Reactions to Wear Debris in Total Joint Replacements.* Proceedings of The Institution of Mechanical Engineers Part H- Journal of Engineering In Medicine, 2000. **214**(1): p. 21-37.

29. Brown, C., J. Fisher, and E. Ingham, *Biological effects of clinically relevant wear particles from metal-on-metal hip prostheses.* Proceedings of the Institution of Mechanical Engineers Part H-Journal of Engineering in Medicine, 2006. **220**(H2): p. 355-369.
30. Huiskes, R., H. Weinans, and B. Van Rietbergen, *The relalionship between stress shielding and bone resorption around total hip stems and the effects of flexible materials.* Clinical Orthopaedics and Related Research, 1992. **274**: p. 124-134.
31. Harris, W., *Will stress shielding limit the longevity of cemented femoral components of total hip replacement?* Clinical Orthopaedics and Related Research, 1992. **274**: p. 120-123.
32. Jasty, M., W.J. Maloney, C.R. Bragdon, D.O. OConnor, T. Haire, and W.H. Harris, *The Initiation of Failure in Cemented Femoral Components of Hip Arthroplasties.* Journal Of Bone And Joint Surgery-British Volume, 1991. **73**(4): p. 551-558.
33. Jeffers, J., M. Browne, and M. Taylor, *Damage accumulation, fatigue and creep behaviour of vacuum mixed bone cement.* Journal of Biomaterials, 2005. **26**: p. 5532-5541.
34. Taylor, M. and K. Tanner, *Fatigue failure of cancellous bone: a possible cause of implant migration and loosening.* Journal of Bone and Joint Surgery-British Volume, 1997. **79-B**(2): p. 181-182.
35. Mjoberg, B., G. Selvik, L. Hannsson, R. Rosenqvist, and R. Onnerfalt, *Mechanical loosening of total hip prostheses a radiographic and roentgen stereophotogrammetric study.* Journal of Bone and Joint Surgery British Volume, 1986. **68B**: p. 770-774.
36. Karrholm, J., H. Malchau, F. Snorrason, and P. Herberts, *Micromotion of femoral stems in total hip-arthroplasty - a randomized study of cemented, hydroxyapatite-coated, and porous-coated stems with roetgen stereophotgrammetric analysis* Journal of Bone and Joint Surgery-American Volume, 1994. **76A**(11): p. 1692-1705.
37. Kobayashi, A., W. Donnelly, G. Scott, and M. Freeman, *Early radiological observations may predict the long term survival of femoral hip prostheses.* Journal of Bone and Joint Surgery British Volume, 1997. **79-B**(4): p. 583-589.
38. Krismer, M., B. Stockl, M. Fischer, R. Bauer, P. Mayrhofer, and M. Ogon, *Early migration predicts late aseptic failure of hip sockets.* Journal of Bone and Joint Surgery British Volume, 1996. **78-B**(3): p. 422-426.
39. Alfaro-Adrian, J., H.S. Gill, and D.W. Murray, *Cement migration after THR - A comparison of Charnley Elite and Exeter femoral stems using RSA.* Journal of Bone and Joint Surgery-British Volume, 1999. **81B**(1): p. 130-134.
40. Furnes, O., L. Havelin, and B. Espehaug, *Femoral components: cemented stems for everybody?*, in *The well-cemented total hip arthroplasty*, S. Breusch and H. Malchau, Editors. 2005, Springer: Heidelberg.
41. *National Joint Registry for England and Wales: 2nd Annual Report*. 2005.
42. Fritchie, R., *An Investigation of the Performance of the 3M™ Captial™ Hip System.* 2001, The Royal College of Surgeons of England.
43. Herberts, P. and H. Malchau, *Long-term registration has improved the quality of hip replacement.* Acta Orthop Scand, 2000. **71**(2): p. 111-121.
44. Harris, W., *Traumatic arthritis of the hip after dislocation and acetabular features: treatment by mold arthroplasty. An end-result study using a new method of result evaluation.* Journal of Bone and Joint Surgery American Volume, 1969. **51**(4): p. 727-755.
45. Wylde, V., I. Learmonth, and V. Cavendish, *The Oxford hip score: the patient's perspective.* Health and Quality of Life Outcomes, 2005. **3**: p. 66.
46. Harris, W.H., *Is it advantageous to strengthen the cement-metal interface and use a collar for cemented femoral components of total hip replacements?* Clinical Orthopaedic Related Research, 1992. **285**: p. 67-72.
47. Gruen, T.A., G.M. McNeice, and H.C. Amstutz, *Modes of failure of cemented stem-type femoral components - radiographic analysis of loosening.* Clinical Orthopaedics and Related Research, 1979(141): p. 17-27.

48. Ritter, M., H. Zhou, C. Keating, E. Keating, P. Faris, J. Meding, and M. Berend, *Radiological factors influencing femoral and acetabular failure in cemented Charnley total hip arthroplasties.* The Journal of Bone and Joint Surgery (Br), 1999. **81-B**: p. 982-986.
49. Callaghan, J., J. Albright, D. Goetz, J. Olenjniczak, and R. Johnston, *Charnley total hip arthroplasty with Cement. Minimum twenty-five year follow up.* The Journal of Bone and Joint Surgery (Am), 2000. **82**(487-497): p. 487.
50. Goldberg, B., G. Al-Habbal, P. Noble, M. Paravic, T. Liebs, and H. Tullos, *Proximal and distal femoral centralizers in modern cemented hip arthroplasty.* Clinical Orthopaedics and Related Research, 1998. **349**: p. 163-173.
51. Breusch, S.J., M. Lukoschek, J. Kreutzer, D. Brocai, and T.A. Gruen, *Dependency of cement mantle thickness on femoral stem design and centralizer.* Journal of Arthroplasty, 2001. **16**(5): p. 648-657.
52. Reading, A.D., A.W. McCaskie, M.R. Barnes, and P.J. Gregg, *A comparison of 2 modern femoral cementing techniques - Analysis by cement-bone interface pressure measurements, computerized image analysis, and static mechanical testing.* Journal of Arthroplasty, 2000. **15**(4): p. 479-487.
53. Selvik, G., *Roentgen stereophotgrammetric analysis.* Acta Radiologica, 1990. **31**(2): p. 113-126.
54. Prendergast, P., *Bone Prosthesis and Implants*, in *Bone Mechanics Handbook* S. Cowin, Editor. 2001, CRC.
55. Karrholm, J., R.H.S. Gill, and E.R. Valstar, *The history and future of radiostereometric analysis.* Clinical Orthopaedics and Related Research, 2006(448): p. 10-21.
56. Franzen, H., B. Mjoberg, and R. Onnerfalt, *Early loosening of femoral components after cemented revision - a roentgen stereophotogrammetric study.* Journal of Bone and Joint Surgery-British Volume, 1992. **74**(5): p. 721-724.
57. Kiss, J., D.W. Murray, A.R. TurnerSmith, J. Bithell, and C.J. Bulstrode, *Migration of cemented femoral components after THR - Roentgen stereophotogrammetric analysis.* Journal of Bone and Joint Surgery-British Volume, 1996. **78B**(5): p. 796-801.
58. Morlock, M.M., N. Bishop, W. Ruter, G. Delling, and M. Hahn, *Biomechanical, morphological and histological analysis of early failures in hip resurfacing arthroplasty.* Proceedings of the Institution of Mechanical Engineers Part H-Journal of Engineering in Medicine, 2006. **220**: p. 333-344.
59. Hirakawa, K., J. Jacobs, R. Urban, and T. Saito, *Mechanisms of failure of total hip replacements: Lessons learned from retrieval studies.* Clinical Orthopaedics and Related Research, 2004. **420**: p. 10-17.
60. Jasty, M., W.J. Maloney, C.R. Bragdon, T. Haire, and W.H. Harris, *Histomorphological Studies of the Long-Term Skeletal Responses to Well Fixed Cemented Femoral Components.* Journal of Bone and Joint Surgery-American Volume, 1990. **72A**(8): p. 1220-1229.
61. Huiskes, R. and J. Stolk, *Biomechanics and preclinical testing of artificial joints: the hip*, in *Basic orthopaedic biomechanics and mechano-biology*, R. Huiskes and V. Mow, Editors. 2004, Lippincott Williams & Williams.
62. McHugh, P. and D. O'Mahoney. *Finite element methods: fundamentals and applications in biomedical engineering*. in *European Society of Biomechanics 2007: Finite element modelling in Biomechanics and Mechanobiology* 2007. Dublin: Trinity Centre for Bioengineering, Trinity College, Dublin
63. Prendergast, P.J., *Finite Element Models in Tissue Mechanics and Orthopaedic Implant Design.* Clinical Biomechanics, 1997. **12**(6): p. 343-366.
64. Keyak, J., J. Meagher, H. Skinner, and C. Mote, *Automated three-dimensional finite element modelling of bone: a new method.* Journal of Biomedical Engineering, 1990. **12**(5): p. 389-397.
65. Van Rietbergen, B., *Micro-FE analyses of bone: State of the art*, in *Noninvasive Assessment Of Trabecular Bone Architecture And The Competence Of Bone*, S. Majumdar and B. Bay, Editors. 2001, Kluwer Academic. p. 21-30.

66. Verhulp, E., B. Van Rietbergen, and R. Huiskes, *Comparison of micro-level and contiuum-level voxel models of the proximal femur.* Journal of Biomechanics, 2006. **39**(16): p. 2951-2957.
67. Stolk, J., N. Verdonschot, L. Cristofolini, A. Toni, and R. Huiskes, *Finite element and experimental models of cemented hip joint reconstructions can produce similar bone and cement strains in pre-clinical tests.* Journal of Biomechanics, 2002. **32**: p. 499-510.
68. Oh, I. and W. Harris, *Proximal strain distribution in the loaded femur.* The Journal of Bone and Joint Surgery (Am), 1978. **60A**: p. 75-85.
69. Lanyon, L., I. Paul, C. Rubin, E. Thrasher, R. DeLaura, R. Rose, and E. Radin, *In vivo strain measurements from bone and prosthesis following total hip replacement. An experimental study in sheep.* Journal of Bone and Joint Surgery American Volume, 1981. **63**: p. 989-1001.
70. Kohn, D., *Acoustic emission and non destructive evaluation of biomaterials and tissues.* Critical Reviews in Biomedical Engineering, 1995. **22**(3/4): p. 221-306.
71. Duesing, L. *Acoustic emission testing of composite materials*. in *Proceedings Annual Reliability and Maintainability Symposium*. 1989: IEEE.
72. Roques, A., M. Browne, J. Thompson, C. Rowland, and A. Taylor, *Investigation of fatigue crack growth in acrylic bone cement using the acoustic emission technique.* Biomaterials, 2004. **25**(5): p. 769-778.
73. Qi, G., *Attenuation of acoustic emission body waves in acrylic bone cement and synthetic bone using wavelet time-scale analysis.* Journal of Biomedical Materials Research 2000. **52**(1): p. 148-156.
74. Qi, G., J. Pujol, and Z. Fan, *3-D AE visualization of bone-cement fatigue locations.* Journal of Biomedical Materials Research, 2000. **52**(2): p. 256-260.
75. Akkus, O., *Comments on acoustic emission visualization of bone cement fatigue locations.* Journal of Biomedical Materials Research, 2002. **59**(2): p. 398-399.
76. Pujol, J. and G. Qi, *Comments on acoustic emission visualization of bone cement fatigue locations - Reply.* Journal of Biomedical Materials Research, 2002. **59**(2): p. 399-401.
77. ASTM, *E1441 Standard Guide for Computed Tomography (CT) Imaging*, in *E1441*, ASTM, Editor. 2000, ASTM International.
78. Ketcham, R. and W.D. Carlson, *Acquisition, optimization and interpretation of X-ray computed tomographic imagery: applications to the geosciences.* Computers & Geosciences, 2001. **27**: p. 381-400.
79. Ritman, E., *Micro-Computed Tomography - Current Status and Developments.* Annual Review of Biomedical Engineering, 2004. **6**: p. 185-208.
80. Keyak, J.H., J.M. Meagher, H.B. Skinner, and C.D. Mote, *Automated 3-dimensional finite-element modeling of bone - a new method.* Journal of Biomedical Engineering, 1990. **12**(5): p. 389-397.
81. Muller, R., S.C. Gerber, and W.C. Hayes, *Micro-Compression: a novel technique for the nondestructive assessment of local bone failure.* Technology and Health Care 1998. **6**: p. 433-444.
82. Muller, R., D. Jarak, M. Stauber, A. Nazarian, M. Tantillo, and S. Boyd, *Micro-mechanical evaluation of bone microstructures under load*, in *Developments in X-Ray tomography III*, U. Bonse, Editor. 2002. p. 189-200.
83. Van Rietbergen, B., *Micro-FE analysis of the bone: state of the art.* Advances in Experimental Medicine and Biology, 2001. **496**: p. 21-30.
84. Van Rietbergen, B., H. Weinans, R. Huiskes, and A. Odgaard, *A new method to determine trabecular bone elastic properties and loading using micromechanical finite-element models.* Journal of Biomechanics, 1995. **28**(1): p. 69-81.
85. Barrett, J. and N. Keat, *Artifacts in CT: Recognition and Avoidance.* Radiographics, 2004. **24**: p. 1679-1691.
86. McKoy, B., Y. An, and R. Friedman, *Factors affecting the strength of the bone-implant interface*, in *Mechanical testing bone and the bone-implant interface*, Y.H. An and R.A. Draughn, Editors. 2000, CRC Press.

87. Rose, R.M. and A.S. Litsky, *Biomechanical considerations in the loosening of hip replacements* in *Current Perspectives on Implantable Devices Vol 1*. 1989. p. 1-45.
88. Funk, M.J. and A.S. Litsky, *Effect of cement modulus on the shear properties of the bone- cement interface.* Biomaterials, 1998. **19**(17): p. 1561-1567.
89. Halawa, M., A. Lee, R. Ling, and S. Vangala, *The shear strength of trabecular bone from the femur, and some factors affecting the shear strength of the cement-bone interface.* Archives of Orthopaedic and Trauma Surgery, 1978. **92**(1): p. 19-30.
90. Cowin, S.C., *Bone Mechanics Handbook*. 2nd ed, ed. S.C. Cowin. 2001: CRC.
91. Gibson, L.J. and M.F. Ashby, *Cellular Solids: Structures and Properties*. 1988: Pegammon.
92. An, Y.H. and R.A. Draughn, *Mechanical Testing of Bone and the Bone-Implant Interface*, ed. Y.H. An and R.A. Draughn. 2000: CRC Press.
93. Carter, D.R. and M.D. Spengler, *Mechanical properties and Composition of Cortical bone.* Clinical Orthopaedics and Related Research, 1978. **135**: p. 192-217.
94. Van Rietbergen, B. and R. Huiskes, *Elastic Constants of Cancellous Bone*, in *Bone Mechanics Handbook*, S.C. Cowin, Editor. 2001, CRC.
95. Keaveny, T.M., E.F. Morgan, G.L. Niebur, and O.C. Yeh, *Biomechanics of trabecular bone.* Annual Review Of Biomedical Engineering, 2001. **3**: p. 307-333.
96. Rho, J., L. Kuhn-Spearing, and P. Zioupos, *Mechanical properties and the hierarchiacal structure of bone.* Medical Engineering & Physics, 1998. **20**: p. 92-102.
97. Young, J., A. Fritz, L. Gonghua, K. Thoburn, J. Kres, and S. Roffers. *SEER's training website: Classification of bones*. 2007 [cited 2007 1/12/07]; Available from: http://training.seer.cancer.gov/module_anatomy/unit3_4_bone_classification.html.
98. Currey, J.D., *The Mechanical Adaptations of Bone*. 1984, Princeton, NJ: Princeton University Press.
99. Webster, S.S.J., *Integrated Bone Tissue Physiology: Anatomy and Physiology*, in *Bone Mechanics Handbook*, S.C. Cowin, Editor. 2001, CRC Press.
100. Goodship, A.E. and J.L. Cunningham, *Pathophysiology of functional Adaptation of bone in Remodeling and Repair in Vivo*, in *Bone Mechanics Handbook*, S.C. Cowin, Editor. 2001, CRC.
101. Harrigan, T.P. and J.J. Hamilton, *An analytical and numerical study of the stability of bone temodeling theories - dependence on microstructural stimulus.* Journal of Biomechanics, 1992. **25**(5): p. 477-488.
102. Taylor, D. and P.J. Prendergast, *A model for fatigue crack propagation and remodelling in compact bone.* Proceedings of the Institution of Mechanical Engineers Part H- Journal of Engineering in Medicine, 1997. **211**(5): p. 369-375.
103. Reilly, D.T. and A.H. Burstein, *The elastic and ultimate properties of compact bone tissue.* Journal of Biomechanics, 1975. **8**(6): p. 393-405.
104. Carter, D.R. and W.C. Hayes, *The compressive behavior of bone as a two-phase porous structure.* The Journal of Bone and Joint Surgery, 1977. **59-A**(7): p. 954-962.
105. Keaveny, T.M. and W.C. Hayes, *A 20-year perspective on the mechanical-properties of trabecular bone.* Journal of Biomechanical Engineering-Transactions of the ASME, 1993. **115**(4): p. 534-542.
106. McCalden, R.W., J.A. McGeough, and C.M. Court-Brown, *Age-related changes in the compressive strength of cancellous bone. The relative importance of changes in density and trabecular architecture.* Journal of Bone And Joint Surgery-American Volume, 1997. **79**(3): p. 421-427.
107. Goldstein, S., *The mechanical properties of trabecular bone: dependence on anatomic location and function.* Journal of Biomechanics, 1987. **20**(11-12): p. 1055-1061.
108. Lakes, R., *Viscoelastic Properties of Cortical Bone*, in *Bone Mechanics Handbook*, S.C. Cowin, Editor. 2001, CRC Press. p. 11.1 -11.15.
109. Harrigan, T.P., M. Jasty, R.W. Mann, and W.H. Harris, *Limitations of the continuum assumption in cancellous Bone.* Journal of Biomechanics, 1988. **21**: p. 269.
110. Choi, K. and S.A. Goldstein, *A comparison of the fatigue behavior of human trabecular and cortical bone tissue.* Journal of Biomechanics, 1992. **25**(12): p. 1371-1381.

111. Choi, K., J.L. Kuhn, M.J. Ciarelli, and S.A. Goldstein, *The elastic-moduli of human subchondral, trabecular, and cortical bone tissue and the size-dependency of cortical bone modulus.* Journal of Biomechanics, 1990. **23**(11): p. 1103-1113.
112. Kuhn, J.L., S.A. Goldstein, K. Choi, M. London, L.A. Feldkamp, and L.S. Matthews, *Comparison of the trabecular and cortical tissue moduli from human iliac crests.* . Journal of Orthopaedic Research, 1989. **7**(6): p. 876-884.
113. Ashman, R.B. and J.Y. Rho, *Elastic-modulus of trabecular bone material.* Journal of Biomechanics, 1988. **21**(3): p. 177-181.
114. Rho, J.Y., R.B. Ashman, and C.H. Turner, *Young's modulus of trabecular and cortical bone material – ultrasonic and microtensile measurements.* Journal of Biomechanics, 1993. **26**(2): p. 111-119.
115. Hoffler, C.E., K.E. Moore, K. Kozloff, P.K. Zysset, M.B. Brown, and S.A. Goldstein, *Heterogeneity of bone lamellar-level elastic moduli.* Bone, 2000. **26**(6): p. 603-609.
116. Norman, J., J. Shapter, K. Short, L. Smith, and N. Fazzalari, *Micromechanical properties of human trabecular bone: A hierarchical investigation using nanoindentation.* Journal of Biomedical Materials Research Part A, 2007(In Press).
117. Zysset, P.K., X.E. Guo, C.E. Hoffler, K.E. Moore, and S.A. Goldstein, *Elastic modulus and hardness of cortical and trabecular bone lamellae measured by nanoindentation in the human femur.* Journal of Biomechanics, 1999. **32**(10): p. 1005-1012.
118. Runkle, J. and J. Pugh, *The micromechanics of cancellous bone.* Bulletin of the Hospital for Joint Diseases, 1975. **36**: p. 2-10.
119. Townsend, P.R., R.M. Rose, and E.L. Radin, *Buckling studies of single human trabeculae.* Journal of Biomechanics, 1975. **8**(3-4): p. 199-&.
120. Williams, J. and J. Lewis, *Properties and an anisotropic model of cancellous bone from the proximal tibial epiphysis.* Journal of Biomechanical Engineering, 1982. **104**: p. 50-56.
121. Ku, J., S. Goldstein, K. Choi, M. London, M. Herzig, and L. Matthews. *The mechanical properties of a single trabeculae*. in *Transactions of the Orthopaedics Research Society*. 1987.
122. Mente, P.L. and J.L. Lewis, *Young's modulus of trabecular bone tissue.* Transactions of the 33rd Orthopaedic Research Society, 1987. **12**: p. 49.
123. Mente, P.L. and J.L. Lewis, *Experimental-method for the measurement of the elastic-modulus of trabecular bone tissue* Journal of Orthopaedic Research, 1989. **7**(3): p. 456-461.
124. Ryan, S.D. and J.L. Williams, *Tensile testing of rodlike trabeculae excised from bovine femoral bone.* Journal of Biomechanics, 1989. **22**(4): p. 351-355.
125. Jensen, K.S. and L. Mosekilde, *A model of vertebral trabecular bone architecture and its mechanical properties* Bone, 1990. **11**(6): p. 417-423.
126. Choi, K. and S.A. Goldstein, *A comparison of the fatigue behavior of human trabecular and cortical bone tissue.* Journal of Biomechanics, 1992. **25**(12): p. 1371-81.
127. Vanrietbergen, B., H. Weinans, R. Huiskes, and A. Odgaard, *A new method to determine trabecularbone elastic properties and loading using micromechanical finite-element models.* Journal of Biomechanics, 1995. **28**(1): p. 69-&.
128. Silva, M.J. and L.J. Gibson, *Modeling the mechanical behavior of vertebral trabecular bone: Effects of age-related changes in microstructure.* Bone, 1997. **21**(2): p. 191-199.
129. Hou, F.J., S.M. Lang, S.J. Hoshaw, D.A. Reimann, and D.P. Fyhrie, *Human vertebral body apparent and hard tissue stiffness.* Journal of Biomechanics, 1998. **31**(11): p. 1009-1015.
130. Ladd, A.J.C., J.H. Kinney, D.L. Haupt, and S.A. Goldstein, *Finite-element modeling of trabecular bone: Comparison with mechanical testing and determination of tissue modulus.* Journal of Orthopaedic Research, 1998. **16**(5): p. 622-628.
131. Turner, C.H., J. Rho, Y. Takano, T.Y. Tsui, and G.M. Pharr, *The elastic properties of trabecular and cortical bone tissues are similar: results from two microscopic measurement techniques.* Journal of Biomechanics, 1999. **32**(4): p. 437-441.

132. Homminga, J., R. Huiskes, B. Van Rietbergen, P. Ruegsegger, and H. Weinans, *Introduction and evaluation of a gray-value voxel conversion technique.* Journal of Biomechanics, 2001. **34**(4): p. 513-517.
133. Kim, H.S. and S.T.S. Al-Hassani, *A morphological model of vertebral trabecular bone.* Journal of Biomechanics, 2002. **35**(8): p. 1101-1114.
134. Van Rietbergen, B., R. Huiskes, F. Eckstein, and P. Ruegsegger, *Trabecular bone tissue strains in the healthy and osteoporotic human femur.* Journal of Bone and Mineral Research, 2003. **18**(10): p. 1781-1788.
135. Bayraktar, H.H., E.F. Morgan, G.L. Niebur, G.E. Morris, E.K. Wong, and T.M. Keaveny, *Comparison of the elastic and yield properties of human femoral trabecular and cortical bone tissue.* Journal of Biomechanics, 2004. **37**(1): p. 27-35.
136. Galante, J.O., W. Rostker, and R.D. Ray, *Physical properties of trabecular bone.* Calcif. Tissue Res, 1970. **4**(1989): p. 236-246.
137. Hodgskinson, R. and J.D. Currey, *Young modulus, density and material properties in cancellous bone over a large density range.* Journal of Materials Science-Materials in Medicine, 1992. **3**(5): p. 377-381.
138. Stone, J.L., G.S. Beaupre, and W.C. Hayes, *Multiaxial strength characteristics of trabecular bone.* Journal of Biomechanics, 1983. **16**(9): p. 743-&.
139. Rice, J., S. Cowin, and J. Bowin, *On the dependence of the elasticity and strength of cancellous bone on apparent density.* Journal of Biomechanics, 1988. **21**(2): p. 155-168.
140. Kowalczyk, P., *Elastic properties of cancellous bone derived from finite element models of parameterized microstructure cells.* Journal of Biomechanics, 2003. **36**(7): p. 961-972.
141. Zhu, H.X., J.F. Knott, and N.J. Mills, *Analysis of the elastic properties of open-cell foams with tetrakaidecahedral cells.* Journal of the Mechanics and Physics of Solids, 1997. **45**(3): p. 319-325.
142. Guo, X.E. and C.H. Kim, *Mechanical consequence of trabecular bone loss and its treatment: A three-dimensional model simulation.* Bone, 2002. **30**(2): p. 404-411.
143. Muller, R., D. Jarak, M. Stauber, A. Nazarian, M. Tantillo, and S. Boyd, *Developments in X-Ray Tomography*, U. Bonse, Editor. 2002. p. 189-200.
144. Youssef, S., E. Maire, and R. Gaertner, *Finite element modelling of the actual structure of cellular materials determined by X-ray tomography.* Acta Materialia, 2005. **53**: p. 719-730.
145. Kabel, J., B. van Rietbergen, M. Dalstra, A. Odgaard, and R. Huiskes, *The role of an effective isotropic tissue modulus in the elastic properties of cancellous bone.* Journal of Biomechanics, 1999. **32**(7): p. 673-680.
146. Jacobs, C.R., B.R. Davis, C.J. Rieger, J.J. Francis, F. Saad, and D.P. Fyhrie, *The impact of boundary conditions and mesh size on the accuracy of cancellous bone tissue modulus determination using large-scale finite-element modelling.* Journal of Biomechanics, 1999. **32**: p. 1159-1164.
147. Kim, D.G., G.T. Christopherson, X.N. Dong, D.P. Fyhrie, and Y.N. Yeni, *The effect of microcomputed tomography scanning and reconstruction voxel size on the accuracy of stereological measurements in human cancellous bone.* Bone, 2004. **35**(6): p. 1375-1382.
148. Ladd, A.J.C. and J.H. Kinney, *Numerical errors and uncertainties in finite-element modeling of trabecular bone.* Journal of Biomechanics, 1998. **31**(10): p. 941-945.
149. Evans, F.G., *Mechanical Properties of Bone*. American Lecture Series. 1973: Thomas Books.
150. Keaveny, T.M., T.P. Pinilla, R.P. Crawford, D.L. Kopperdahl, and A. Lou, *Systematic and random errors in compression testing of trabecular bone.* Journal of Orthopaedic Research, 1997. **15**: p. 101-110.
151. Simoes, J., J. Monterio, M. Vaz, M. Taylor, and S. Blatcher. *Study with speckle interferometry of bone-implant interface conditions*. in *Proceedings of the 11th International Conference on Experimental Mechanics*. 1998. Oxford, UK.

152. Hayes, W.C. and D. Carter, *Postyield behaviour of subchondral trabecular bone.* Journal of Biomedical Materials Research Symposium, 1976. **7**: p. 537-544.
153. Keaveny, T.M., E. Wachtel, and D. Kopperdahl, *Mechanical behaviour of human trabecular bone after overloading.* Journal of Orthopaedic Research, 1999. **17**: p. 346-353.
154. Kopperdahl, D.L. and T.M. Keaveny. *Biomechanical consequences of an isolated overload in the vertebral body.* in *1999 Bioengineering Conference*. 1999. Big Sky, Montana.
155. Vashishth, D., J. Koontz, S. Qui, D. Lundin-Cannon, Y. Yeni, M. Schaffler, and D.P. Fyhrie, *In vivo diffuse damage in human vertebral trabecular bone.* Bone, 2000. **26**(2): p. 147-152.
156. Fyhrie, D.P. and M.B. Schaffler, *Failure mechanisms in human vertebral cancellous Bone.* Bone, 1994. **15**(1): p. 105-109.
157. Wachtel, E. and T.M. Keaveny, *Dependence of trabecular damage on mechanical strain.* Journal of Orthopaedic Research, 1997. **15**: p. 781-787.
158. Keyak, J.H., I.Y. Lee, D.S. Nath, and H.B. Skinner, *Postfailure compressive behavior of tibial trabecular bone - three anatomic directions.* Journal Of Biomedical Materials Research, 1996. **31**(3): p. 373-378.
159. Alonso Vazquez, A., G.H. Van Lenthe, M. Taylor, and R. Muller. *Comparison of μCT measurements and FE predictions of localised failure in a cancellous bone analogue material*. in *6th International Symposium on Computer Methods in Biomechanics and Biomedical Engineering* 2004. Madrid: FIRST Numerics.
160. Michel, M.C., X.E. Guo, L.J. Gibson, T. McMahon, and W.C. Hayes, *Compressive Fatigue Behavior of Bovine Trabecular Bone.* Journal of Biomechanics, 1993. **26**(4/5): p. 453-463.
161. Haddock, S., O. Yeh, P. Mummaneni, W. Rosenberg, and T.M. Keaveny. *Fatigue behaviour of human vertebral trabecular bone*. in *46th Annual Meeting, Orthopaedic Research Society*. 2000. Orlando, Florida.
162. Palissery, V., M. Taylor, and M. Browne, *Fatigue characterisation of a polymer foam to use as a cancellous bone analogue material in the assessment of orthopaedic devices.* Journal of Materials Science: Materials in Medicine, 2004. **15**: p. 61-67.
163. Szivek, J.A., M. Thomas, and J.B. Benjamin, *Characterization of a synthetic foam as a model for human cancellous bone.* Journal of Applied Biomaterials, 1993. **4**(3): p. 269-272.
164. Waide, V., L. Cristofolini, J. Stolk, N. Verdonschot, G.J. Boogaard, and A. Toni, *Modelling the fibrous tissue layer in cemented hip replacements: experimental and finite element methods.* Journal of Biomechanics, 2004. **37**(1): p. 13-26.
165. Iwaki, H., G. Scott, and M. Freeman, *The natural history and significance of radiolucent lines at a cemented femoral interface.* Journal of Bone and Joint Surgery British Volume, 2002. **84B**(4): p. 550-555.
166. Kuhn, K., *Properties of bone cement: What is bone cement?*, in *The well-cemented total hip arthoplasty theory and practise* S. Breusch and H. Malchau, Editors. 2005, Springer: Germany.
167. Dunne, N.J. and J.F. Orr, *Flow characteristics of curing polymethyl methacrylate bone cement.* Proceedings of the Institution of Mechanical Engineers Part H - Journal of Engineering in Medicine, 1998. **212**: p. 199-207.
168. Lewis, G., *Properties of acrylic bone cement: State of the art review.* Journal of Biomedical Materials Research, 1997. **38**(2): p. 155-182.
169. Moritz, A.R. and F.C. Henriques, *The relative importance of time and surface temperature in the causation of cutaneous burns.* Am. J. Pathology, 1947. **23**: p. 695-720.
170. Lundskog, J., *Heat and bone tissue: an experimental investigation of the thermal properties of bone and threshold levels for thermal injury.* Scand. Journal of Plastic and Reconstructive Surgery, 1972. **9**: p. 1-80.

171. Eriksson, A. and T. Albrektsson, *The effect of heat on bone regeneration: an experimental study in the rabbit using the bone growth chamber.* J. Oral Maxillofacial Surgery, 1984. **42**(705-11).
172. Jefferiss, C.D., A.J.C. Lee, and R.S.M. Ling, *Thermal aspects of self-curing polymethylmethacrylate.* Journal of Bone and Joint Surgery, 1975. **57B**: p. 511-518.
173. Talbot, J.C. and D.L. Shaw, *Effects of pre-cooling and pre-heating procedures on cement polymerisation and thermal osteonecrosis in cemented hip replacements.* Medical Engineering & Physics, 2003. **25**: p. 559-64.
174. *CMW1 Instruction Leaflet*, DePuy International.
175. Orr, J.F., N.J. Dunne, and J.C. Quinn, *Shrinkage stresses in bone cement.* Biomaterials, 2003. **24**(17): p. 2933-2940.
176. Wang, J., *Mixing: the benefit of vacuum mixing*, in *The well cemented total hip arthoplasty: theory and practise*, S. Breusch and H. Malchau, Editors. 2005, Springer: Berlin.
177. Mann, K.A., D.L. Bartel, T.M. Wright, and A.H. Burstein, *Coulomb frictional interfaces in modeling cemented total hip replacements - a more realistic model.* Journal of Biomechanics, 1995. **28**(9): p. 1067-1078.
178. Verdonshot, N. and R. Huiskes, *Mechanical effects of stem cement interface Characteristics in Total Hip Replacement.* Clinical Orthopaedics and Related Research, 1996. **329**: p. 326-336.
179. Verdonschot, N. and R. Huiskes, *The effects of cement-stem debonding in THA on the long-term failure probability of cement.* Journal of Biomechanics, 1997. **30**(8): p. 795-802.
180. Aspenberg, P. and H. Van der Vis, *Migration, particles, and fluid pressure - A discussion of causes of prosthetic loosening.* Clinical Orthopaedics and Related Research, 1998(352): p. 75-80.
181. Bishop, N.E., S. Ferguson, and S. Tepic, *Porosity reduction in bone cement at the cement-stem interface.* Journal of Bone and Joint Surgery - British Volume, 1996. **78-B**: p. 349.
182. Wang, X.A., X.Y. Liu, and G.L. Niebur, *Preparation of on-axis cylindrical trabecular bone specimens using micro-CT imaging.* Journal of Biomechanical Engineering-Transactions of the Asme, 2004. **126**(1): p. 122-125.
183. Roques, A., M. Browne, M. Taylor, A. New, and D. Baker, *Quantitative measurement of the stresses induced during polymerisation of bone cement.* Biomaterials, 2004. **25**(18): p. 4415-24.
184. Race, A., A. Miller, D.C. Ayers, R.J. Cleary, and K.A. Mann, *The influence of surface roughness on stem-cement gaps.* The Journal of Bone and Joint Surgery (Br), 2002. **84-B**(8): p. 1199-1204.
185. Muller, R.T. and N. Schurmann, *Shear Strength of the cement metal interface - an experimental study.* Archives of Orthopaedic and Trauma Surgery, 1999. **119**(3-4): p. 133-138.
186. Zarki, M., F. Saad, and M.N. Al-Ebiary, *Influence of Charnley Hip Neck-Angle Inclination on the Stresses at the Stem/Cement and Bone/Cement Interfaces.* Biomedical Materials Engineering, 2002. **12**(4): p. 411-21.
187. Wang, J.S., M. Taylor, G. Flivik, and L. Lidgren, *Factors affecting the static shear strength of the prosthetic stem-bone cement interface.* Journal of Materials Science-Materials In Medicine, 2003. **14**(1): p. 55-61.
188. Crowninshield, R.D., J.D. Jennings, and M.D. Laurent, *Cemented femoral component surface finish mechanics.* Clinical Orthopaedic Related Research, 1998. **355**: p. 90-102.
189. Verdonschot, N., E. Tanck, and R. Huiskes, *Effects of prosthesis surface roughness on the failure process of cemented hip implants after stem-cement debonding.* Journal of Biomedical Materials Research, 1998. **42**(4): p. 554-559.
190. Gardiner, R.C. and W.C. Hozack, *Failure of the cement-bone interface: A consequence of strengthening the cement-prosthesis interface?* Journal Of Bone And Joint Surgery-British Volume, 1994. **76B**: p. 49-52.

191. Della Valle, A.G., A. Zoppi, M.G.E. Peterson, and E.A. Salvati, *A rough surface finish adversely affects the survivorship of a cemented femoral stem.* Clinical Orthopaedics and Related Research, 2005(436): p. 158-163.
192. Race, A., M.A. Miller, D.C. Ayers, and K.A. Mann, *Early cement damage around a femoral stem is concentrated at the cement/bone interface.* Journal Of Biomechanics, 2003. **36**(4): p. 489-496.
193. Vernon-Roberts, B., *The initial state*, in *The Bone-Cement Interface, Workshop Report*, L.J. Lewis and J.O. Galante, Editors. 1984, American Academy of Orthopaedic Surgery. p. 8-22.
194. Radin, E., C.T. Rubin, E.L. Thrasher, L.E. Lanyon, A.M. Crugnola, A.S. Schiller, I.L. Paul, and R.M. Rose, *Changes in the bone-cement interface after total hip replacement.* The Journal of Bone and Joint Surgery, 1982: p. 1188-1200.
195. Askew, M.J., J.W. Steege, J.L. Lewis, J.R. Ranieri, and R.L. Wixson, *Effect of cement pressure and bone strength on polymethylmethacrylate fixation.* Journal of Orthopaedic Research, 1984. **1**(4): p. 412-20.
196. Buckley, P.J., J.F. Orr, I.C. Revie, S.J. Breusch, and N.J. Dunne, *Fracture characteristics of acrylic bone cement-bone composites.* Proceedings of the Institution Of Mechanical Engineers Part H- Journal Of Engineering In Medicine, 2003. **216**(6): p. 419-27.
197. Graham, J., M. Ries, and L. Pruitt. *Cement penetration depth significantly affects fracture toughness at the trabecular bone/cement interface*. in *27th Annual Meeting of the Society for Biomaterials*. 2001. Saint Paul, MN.
198. Krause, W., W. Krug, and J.E. Miller, *Strength of the cement-bone interface.* Clinical Orthopaedics, 1982. **163**: p. 290-299.
199. Mann, K.A., D.C. Ayers, F.W. Werner, R.J. Nicoletta, and M.D. Fortino, *Tensile strength of the cement-bone interface depends on the amount of bone interdigitated with PMMA cement.* Journal of Biomechanics, 1997. **30**(4): p. 339-346.
200. Oates, K.M., D.L. Barrera, W.N. Tucker, C.C.H. Chau, W.D. Bugbee, and F.R. Convery, *In vivo effect of pressurisation of polymethylmethacrylate bone-cement.* The Journal of Arthroplasty, 1995. **10**(3): p. 373-381.
201. Dunne, N.J., J.F. Orr, and D.E. Beverland, *Assessment of cement introduction and pressurization techniques.* Proceedings of the Institution of Mechanical Engineers Part H- Journal of Engineering in Medicine, 2004. **218**(H1): p. 11-25.
202. MacDonald, W., E. Swarts, and R. Beaver, *Penetration and shear strength of cement-bone interfaces in vivo.* Clinical Orthopaedics, 1993. **286**: p. 283-288.
203. Walker, P., M. Soudry, F. Ewald, and H. McVickar, *Control of cement penetration in total knee arthroplasy.* Clinical Orthopaedics and Related Research, 1988. **185**: p. 155-164.
204. Stanczyk, M. and B. Van Rietbergen, *Thermal analysis of bone cement polymerisation at the cement-bone interface.* Journal of Biomechanics, 2004. **37**: p. 1803-1810.
205. Dorr, L., J. Lindberg, M. Claude-Faugere, and H. Malluche, *Factors influencing the intrusion of methylmethacrylate into human tibiae.* Clinical Orthopaedics and Related Research, 1984. **183**: p. 147-152.
206. Kim, Y., P. Walker, and J. Deland, *A cement impactor for uniform cement penetration in the upper tibia.* Clinical Orthopaedics and Related Research, 1984. **182**: p. 206-210.
207. Stone, J.J.S., J.A. Rand, E.K. Chiu, J.J. Grabowski, and K.N. An, *Cement viscosity affects the bone-cement interface in total hip arthroplasty.* Journal of Orthopaedic Research, 1996. **14**(5): p. 834-837.
208. Miller, M., A. Race, S. Gupta, P. Higham, M. Clarke, and K. Mann, *The role of cement viscocity on cement-bone apposition and strength.* The Journal of Arthroplasty, 2007. **22**(1): p. 109-116.
209. Race, A., M. Miller, M. Clarke, K. Mann, and P. Higham, *The effect of low-viscosity cement on mantle morphology and femoral stem micromotion.* Acta Orthopaedica, 2006. **77**(4): p. 606-616.

210. Lucksanasombool, P., W.A.J. Higgs, M. Ignat, R. Higgs, and M.V. Swain, *Comparison of failure characteristics of a range of cancellous bone-bone cement composites.* Journal of Biomedical Materials Research Part A, 2003. **64A**(1): p. 93-104.
211. Graham, J., M. Ries, and L. Pruitt, *Effect of bone porosity on the mechanical integrity of the bone-cement interface.* Journal of Bone And Joint Surgery-American Volume, 2003. **85A**(10): p. 1901-1908.
212. Arola, D., K. Stoffel, and D. Yang, *Fatigue of the cement/bone interface: the surface texture of bone and loosening.* Journal of Biomedical Materials Research B Applied Biomaterials, 2006. **76**(2): p. 287-297.
213. Maher, S.A. and B.A.O. McCormack, *Quantification of interdigitation at bone cement/cancellous bone interfaces in cemented femoral reconstructions.* Proceedings of the Institution of Mechanical Engineers Part H- Journal of Engineering in Medicine, 1999. **213**(H4): p. 347-354.
214. Arola, D., D. Yang, and K. Stoffel, *The apparent volume of interdigitation: a new parameter for evaluating the influence of surface topology on mechanical interlock.* Journal of Biomedical Materials Research, 2000. **58**(5): p. 519-524.
215. Neilsson, R., E. Garling, and E.R. Valstar, *Influence of cement viscosity and cement mantle thickness on migration of the Exeter total hip prosthesis.* The Journal of Arthroplasty, 2005. **20**(4): p. 521-527.
216. Skinner, J., S. Todo, M. Taylor, J. Wang, V. Pinskerova, and G. Scott, *Should the cement mantle around the femoral component be thick or thin?* The Journal of Bone and Joint Surgery (Br), 2003. **85B**(1): p. 45-51.
217. Fisher, D., A. Tsang, N. Paydar, S. Milionis, and C. Turner, *Cement-mantle thickness affects cement strains in total hip replacement.* Journal of Biomechanics, 1997. **11-12**: p. 1173-1177.
218. Kwak, B., O. Lim, Y. Kim, and K. Rim, *An investigation of the effect of cement mantle thickness on an implant by finite element stress analysis.* International Orthopaedics, 1978. **2**(4): p. 315-319.
219. Ramaniraka, N.A., L.R. Rakoomanana, and P.F. Leyvraz, *Effects of stem stiffness, cement thickness and roughness of the cement-bone surface.* The Journal of Bone and Joint Surgery (Br), 2000. **82-B**(2): p. 297-303.
220. Langlais, F., M. Kerboull, L. Sedel, and R.S.M. Ling, *The 'French paradox'.* Journal of Bone and Joint Surgery-British Volume, 2003. **85B**(1): p. 17-20.
221. Scott, G., M. Freeman, and M. Kerboull, *Femoral components: the french paradox*, in *The Well-Cemented Total Hip Arthroplasty*, S. Breusch and H. Malchau, Editors. 2005, Springer-Link: Berlin.
222. Scheerlinck, T., J. de Mey, R. Deklerck, and P. Noble, *CT analysis of defects of the cement mantle and alignment of the stem.* The Journal of Bone and Joint Surgery (Br), 2006. **88-B**(1): p. 19-25.
223. Sinnett-Jones, P.E., M. Browne, W. Ludwig, J.Y. Buffiere, and I. Sinclair, *Microtomography assessment of failure in acrylic bone cement.* Biomaterials, 2005. **26**(33): p. 6460-6466.

Chapter 3. *Materials and Methods*

This chapter gives a general overview of the materials and methods used in this thesis. Sections 3.1 to 3.3 describe the materials and experimental techniques used to create and characterise a cement-bone analogue interface sample. This includes the non-destructive techniques used to monitor the integrity of the samples; acoustic emission and computed tomography (CT) imaging. Sections 3.4 to 3.5 describe the techniques used to model the behaviour of cancellous bone and the cement-bone interface. Two techniques are presented. Firstly, theoretical modelling of cancellous bone which uses a cubic unit cell to represent cancellous bone. Secondly, smooth surface finite element models based on high resolution CT images of the cement-bone analogue interface specimens.

3.1. Characterisation of a bone analogue material

There are a number of factors that can affect the morphology and properties of bone such as anatomical site, age, sex and health of the patient, preparation and storage, hydration of the bone during testing. Two of the most common limitations regarding in vitro testing of bone are (i) machining of the sample can introduce artefacts and (ii) the availability of fresh bone samples is limited and expensive. Therefore bone analogue materials with a similar morphology to cancellous bone are desirable alternatives for experimental studies and serve as a good benchmark for the validation of computer models.

The aim of this section is to outline the method for selection and characterisation of a bone analogue material which will be used in experimental investigations of the cement-bone interface. In addition, high resolution finite element models of both a cancellous bone-like structure and the cement-bone interface will be developed. Firstly, the specifications required for a cancellous bone analogue material are detailed. Then, the available suppliers of these analogue materials are listed along with their reported properties. Two potential materials are selected and then evaluated for their suitability using the ASTM standard F1839-01: *Rigid Polyurethane Foam for use as a Standard Material for testing Orthopaedic Devices and Instruments* and its subsidiary standards.

3.1.1. Specifications for a Bone Analogue Material

The analogue material should have a geometric structure similar to cancellous bone i.e. is highly porous and made of an interconnected series of struts. Ideally the mechanical properties should reflect the values for cancellous bone reported in literature (as summarised in Table 3.1). It should also be commercially available at a reasonable cost and easily handled so that tests may be performed easily. It was envisioned that the selected material would be used to create specimens representative of the cement-bone interface. Thus, the selected foam should allow cement flow into the pores of the foam. Gibson and Ashby [1] characterise this type of cellular material, where the pores are interconnected, as *open cell* foam.

Compressive			
Strength, MPa	2.4-35 [2-6]	E, MPa	67-13000[3-5, 7-13]
Tensile			
Strength	1-20[5]	E, MPa	349-2700[5, 13]
Shear			
Strength, MPa	1-27[4, 5, 14]	E, MPa	3.42-4.175[4, 15]
Density g/cc	0.05-1	Cell Size, mm	1-5

Table 3.1:Cancellous bone properties

3.1.2. Compression and shear test methods for testing bone analogue materials

An extensive search for cellular material suppliers was performed, the specifications and results of which are summarised in Chapter 5. The two most suitable foams selected for mechanical testing were OPF (open cell PU foam, Sawbone,) and Duocel (aluminium foam, ERG, Ca). Tests were performed for comparison of their compressive and shear properties, both relevant to the load bearing role of the cement-bone interface[16] (section 2.3.5) in order to identify which was the most suitable material for use as a cancellous bone analogue. The shear properties of OPF and Duocel aluminium foam were tested according to the ASTM standard F1839-01; Rigid Polyurethane Foam for use as a Standard Material for testing Orthopaedic Devices and Instruments, the parts of which are summarised in Figure 3.1. The compressive strength of Duocel aluminium foam was also tested to this standard.

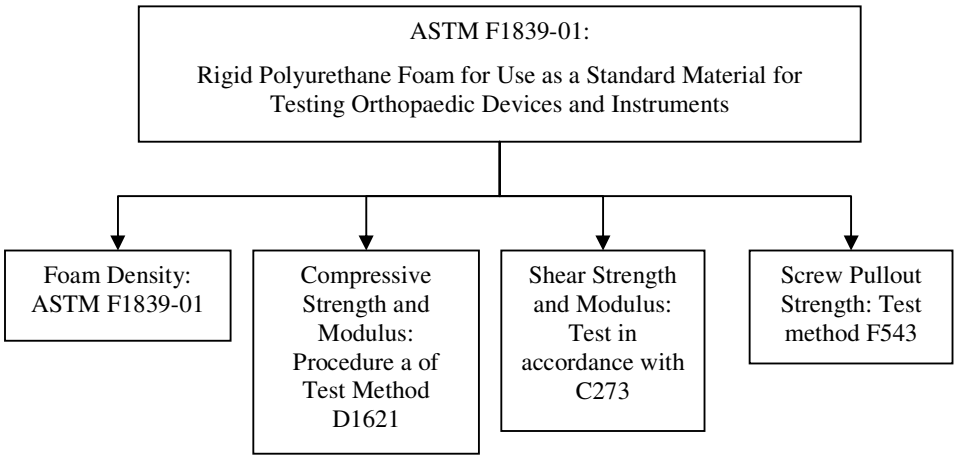

Figure 3.1: Standards for testing polyurethane foam

ASTM C273-00, which relates to shear strength testing (Figure 3.1) states that the test specimen should be rigidly supported by steel plates bonded to the facings. The thickness of the plate can vary with the strength of the sandwich but the plate length should be such that the line of action of tensile or compression force should pass diagonally through the corners of the sandwich. The loading plates should have a bending stiffness:

$$D = \frac{EI}{b}$$

Equation 3.1

of not less than 2.67MN mm^2/mm width per millimetre of core thickness.

Since the second moment of area for a rectangle is:

$$I = \frac{bd^3}{12}$$

Equation 3.2

and the Young's modulus of steel is approximately 210GN/mm^2 the minimum thickness of the shear plate, calculated from Equation 3.1, is 5.34mm. From this information and the example given in the standard the following rig (Figure 3.2) was designed for tensile shear testing of 40PPI (pores per inch) Duocel aluminium foam**.** An extensometer was used to measure the deflection of the shear plates. A schematic and photo of the shear apparatus is also shown.

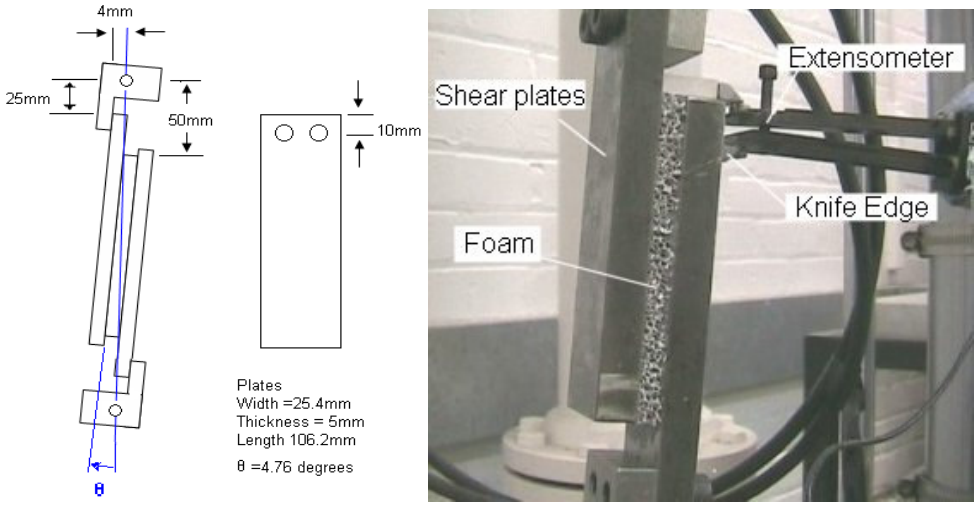

Figure 3.2: Shear Test Setup

Specimens of Duocel aluminium foam were supplied from ERG, Ca. The specimens were attached to the shear plates with epoxy adhesive (Araldite rapid, Huntsman Advanced Materials, Switzerland) and left to cure at room temperature for 24 hours. The aluminium specimens were attached with a two ply layer of glue to minimise debonding from the shear plates. Cyanoacryalate adhesive was insufficient to bond the material to the shear plates as debonding across the foam surface occurred. The OPF specimens were cut using a diamond saw with a feed rate of 9.6mm/min and at a speed of 4000rpm. One layer of epoxy adhesive was sufficient to bond the OPF specimen to the shear plates. The specimens were pulled in tension at a rate of 0.5mm/min. The displacement of the shear plates was measured using an extensometer attached to knife edges on the surface of the shear plates (Figure 3.2)

Compression testing of Ducoel foam was performed in accordance with ASTM D1621 on a computer controlled Instron 8874 servo-hydraulic machine. The apparatus consisted of two flat plates; one attached to the base of the Instron and one attached to the moving crosshead. These plates were larger than the specimen to allow uniform loading across the specimen

To ensure uniform loading across the specimen and to reduce edge effects, the platens were lowered and examined to confirm that the specimen surface was parallel to the surface of the platen before testing. The specimens were placed in the centre of the compression platens and

loaded at a crosshead speed of 2.5mm/min. Load and position was monitored by the Instron data logger at a sample rate of 0.1 KHz.

A separate test with no specimen in place was performed with the platens in contact to assess the compliance of the Instron machine. At the yield loads of the aluminium foam, the displacement associated with compliance of the Instron was less than 5% of the total cross head displacement. The results are shown in Figure 3.3.

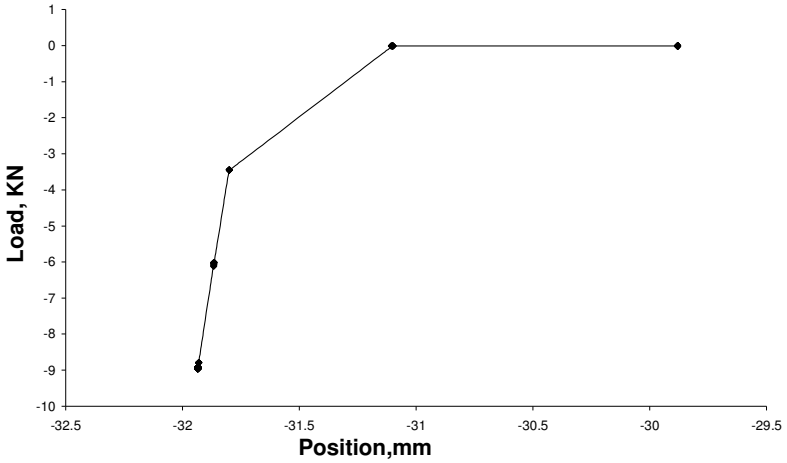

Figure 3.3: Compliance of the Instron 8874 Servo Hydraulic Machine

As stated in ASTM F1839, the required specimen dimensions for compression testing are 50.8 x 50.8 x 25.4mm. However, OPF could not be sourced in these sizes and as such was not tested.

3.2. Cement-bone Interface Analogue Testing

3.2.1. Sample Manufacture

In order to evaluate the behaviour of the cement-bone interface, cement-aluminium foam specimens representative of the cement-bone interface were constructed (Figure 3.4). A 51 x 51 x 26mm mould was manufactured from stainless steel and coated in multishield mould release (Zyvax inc, Spain). Duocel aluminium foam specimens with dimensions 50.8x 50.8 x 25.4mm were placed into the base of the mould. CMW-1 radiopaque cement (DePuy, CMW, Blackpool England) was mixed using Vacu-Mix vacuum mixing apparatus (DePuy CMW, Blackpool, England) according to the manufacturer's instructions at a room temperature of 25°C. Six minutes after initiation of mixing, the cement was applied to the top of the aluminium foam. Load was applied across the top surface of the cement compressing the cement into the pores of the aluminium. 0.038MPa uniform pressure was maintained across the top of the specimen until the cement cured. Weights were used to maintain a uniform pressure rather than the servo-hydraulic machine as the PID control of the machine was found to give undesirable small

fluctuations in load especially at low load levels even after fine tuning. The pressure across the top of the cement was maintained throughout curing to minimise the effects of shrinking of the cement and to maximise cement penetration into the pores of the foam. Cement penetration depths were measured by examining CT scans. The procedure for measuring cement penetration is detailed in Chapter 6. These conditions were maintained throughout specimen manufacture to minimise specimen variability. After the cement cured, the base of the mould was detached and the cement-foam composite removed. This was then machined into eight four point bend specimens of dimensions 10x12x50mm according to BS ISO 12108:2002 using a diamond saw (Presi Mecatome T210A, Grenoble, France) at 4000rpm and feed rate 2mm/min (the lowest achievable). The foam was examined visually before and after machining to ensure that no damage occurred to the aluminium struts. The samples were machined to ensure a minimum cement mantle thickness of 2mm and foam thickness of 4mm. The cement mantle and foam thickness were measured from CT images directly after sample manufacture.

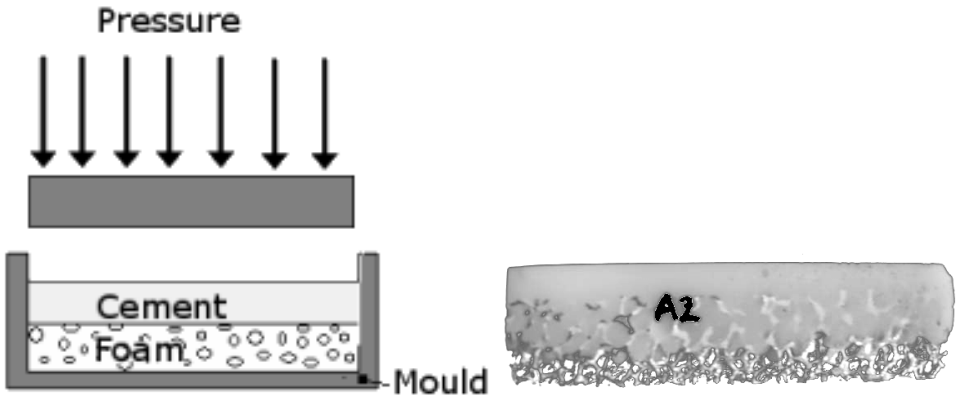

Figure 3.4: Manufacture of Interface Specimens.

3.2.2. Four Point Bend Testing of Cement-Bone Interface Analogue Specimens

As stated previously, the interface samples were machined into 10x12x50mm specimens according to BSISO 12108:2002 as shown in Figure 3.5. The depth of the sample was increased from the recommended depth (*w* in Figure 3.5) to ensure that the interface between cement and foam remained in bending during testing. The other size requirements were maintained.

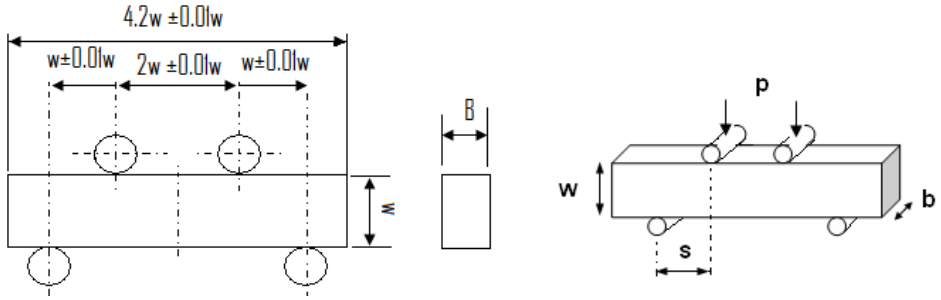

Figure 3.5: Recommended dimensions for four point bend testing reproduced from BS ISO 12108:2002 and variables for calculating stress in the four point bend sample.

The stress in the specimen can be derived from the following equations:

Stress or a beam in bending is defined by

$$\sigma = \frac{My}{I}$$

Equation 3.3

Where M is the moment and I is the second moment of area. For a beam with rectangular cross-section, the second moment of area is defined by:

$$I = \frac{bw^3}{12}$$

Equation 3.4

where b is the width of the specimen and w is the height of the specimen as shown in Figure 3.5. Moment is defined by:

$$M = \frac{Ps}{2}$$

Equation 3.5

Where P is load, and s is spacing of the rollers. By substituting Equation 3.1 into Equation 3.2, the applied stress can be defined by:

$$\sigma = \frac{3Ps}{bw^2}$$

Equation 3.6

3.3. Non Destructive Monitoring of Interface Analogues

Complimentary non destructive techniques were used to monitor and evaluate the integrity of the cement-bone interface during four point bend testing. The interface samples were imaged using high resolution computed tomography (CT) before testing at a resolution of 40µm and after

testing with a resolution of 20µm. Acoustic emission techniques were used to detect the onset of damage within the sample. Once damage was detected, testing was suspended and the specimens imaged using CT. This process was repeated until significant damage (for example crack growth across the sample or severe plastic deformation of the foam) had occurred.

3.3.1. Non Destructive Monitoring Using Acoustic Emission Techniques

Acoustic emission is a technique which has been previously used in orthopaedics for evaluation of hip prosthesis at a global level [17]. When a material experiences abrupt changes in stress or strain, or damage occurs, transient elastic waves are generated by the rapid release of energy from a localised source. This phenomenon is known as acoustic emission. The monitoring of these acoustic emissions allow passive, non destructive and real time evaluation of a material under load and allows location of regions of damage.

3.3.2. Acoustic Emission Test Set Up

A schematic of the instrumentation used to monitor acoustic emissions is shown in Figure 3.6. AMSY4 4-channel PC based acquisition system (Vallen Systeme, GmbH, Munich) with Visual AE software (Vallen Systeme, GmbH, Munich) was used to acquire and visualise the data. The sensors were attached to each end of the interface specimen with cyanoacrylate adhesive. In house 6mm diameter, broadband flat response sensors were used with a frequency range 0.2-0.8MHz. Preamplifiers were set with 40dB gain with 100KHz-1MHz filters. The threshold for activity was set at 32dB. Above this threshold the following parameters for acoustic activity were recorded (see Figure 3.6); peak amplitude, rise time, duration, ring down counts (number of threshold crossings) and energy (area bounded by the curve). In order to calibrate the speed of sound in the material, an artificial elastic wave was induced in the specimen by breaking pencil lead at various locations on the surface of the interface specimen. This is also known as a Hsu-Neilson source. A 0.5mm pencil lead was broken at the location of one sensor and the time taken for the elastic wave to reach the second sensor recorded. As the distance between the sensors is known, this allows calculation of the speed of sound in the material. Once the speed of sound in the material is determined, the location of acoustic activity above the threshold (known as a hit) can be determined. The lead break test was repeated for the other sensor and at various locations across the specimen. The lead break test also ensures that there is good acoustic contact between the specimen and sensor.

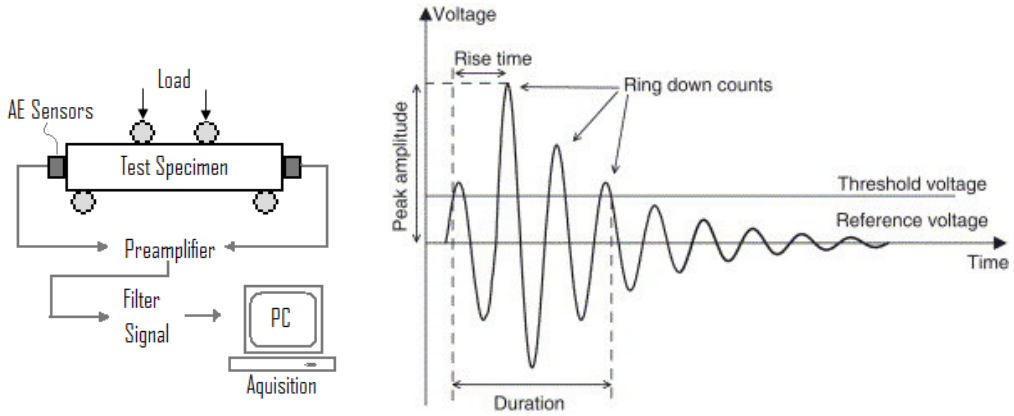

Figure 3.6: Monitoring damage using acoustic emission set up and a typical acoustic emission signal.

The four point bend specimen was incrementally loaded until acoustic emission events representative of damage were observed. These were events with high durations, energies and amplitude[18]. The Kaiser effect, first documented 1953[19] describes the phenomena whereby a material will only emit acoustic activity after a primary load is reached. On elastic reloading of a specimen, little or no acoustic activity will be recorded until the previous maximum load is reached. When damage occurs in the specimen, significant acoustic emission activity is recorded before the previous maximum load applied is reached. This is known as the Felicity effect[19] and can be used as an indicator of permanent damage. During reapplication of the load, the felicity ratio is defined as the ratio between the applied load which activity is first recorded and the previous maximum applied load. When significant damage represented by a large Felicity ratio was noted, the test was stopped and CT imaged to examine damage in the structure.

3.3.3. High Resolution Imaging using computed tomography

High resolution CT images were used to create micro finite element (μFE) models of aluminium foam and cement-bone interface specimens. It was also used to examine the integrity of cement-bone analogue specimens before and after testing. In this method, a series of radiographs of an object are taken at a number of angular projections. This series of images is reconstructed into a three dimensional volume using filtered back projection [20].

A 25 x 25 x 25mm sample of aluminium foam was imaged at a resolution of 50μm (courtesy of University of Leeds, Scanco Medical scanner, Bassdof Switzerland). These images were used to create micro FE models of aluminium foam to evaluate the sensitivity of the method of creating μFE models.

CT images of the cement-foam interface samples were collected prior and subsequent to testing at a highest resolution of 21μm to assess the integrity of the interface samples (Benchtop CT 160Xi, Xtek, UK). Scans were collected prior to testing to examine the specimen for any initial

damage and also as data to build μFE models. The initial scans for the FE models were at a lower resolution of 40μm, to minimise the size of the resulting model.

The CT scanner contained a 12 bit detector with 1216 x 1216 x 1216 voxels. A molybdenum target was used with electron gun accelerating voltage and current chosen to give the optimum contrast between cement and foam whilst maintaining sufficient x-ray penetration. Generally this was in the region of 95kV and 80μA, although these values were optimised for each scan. The scans were optimised by taking a radiograph of the sample before scanning and adjusting the parameters (typically ±5kV and ±5μA) until the maximum contrast between grey values for each material was seen without saturation of the detector i.e. so that the minimum signal did not fall below 10-20% of the detector range. A gain of 4 and exposure of 535μs was used. Images were reconstructed using CTPro (XTek).

3.4. Idealised Cellular Modelling

A three dimensional open cell cubic geometry representing cancellous bone was created in Ansys 8.1 using smaller cubic volumes (Figure 3.7). These volumes were meshed using eight node solid elements. Bone and bone cement were modelled as homogeneous, isotropic elastic continua. The material properties of bone at the tissue level were assumed uniform and equal to that of cortical bone.

	Young's modulus	**Poisson's ratio**
Bone	17GPa	0.3
Bone Cement	2GPa	0.3

Figure 3.7: Material Properties of bone and bone cement

Three geometric parameters were varied in order to examine the effect of architecture on stiffness: the thickness of trabeculae *t*, the length of the connecting trabeculae or spacing, and the length of the beams or cube size (Figure 3.8).

A compressive load of 0.1MPa was applied to the top nodes on the top face to examine the stiffness of the structure and the regions of bending. This load was relatively low to ensure the structure stayed within its linear elastic range. The nodes at the base were constrained in all directions. The cube was assumed to be part of a repeating structure, thus the nodes at the ends of the free beams were constrained parallel to the edge face. The effect of shear loading on the compressive cells was also investigated. A shear stress of 0.1MPa was applied to the top nodes as with the compressive load. To examine regions of plastic deformation in the cell without cement, the cell was loaded with a pressure of 100MPa. Where cement fully surrounds the cell, a pressure of 40MPa was applied to examine plastic deformation.

Cement was added to the unit cell to examine the effect of interdigitation. When cement was added to the unit cell, the cement was assumed to be fully bonded with the bone. The global strain of the cube was determined from the displacement of the top nodes and the original height of the specimen. Young's modulus was calculated as stress divided by strain.

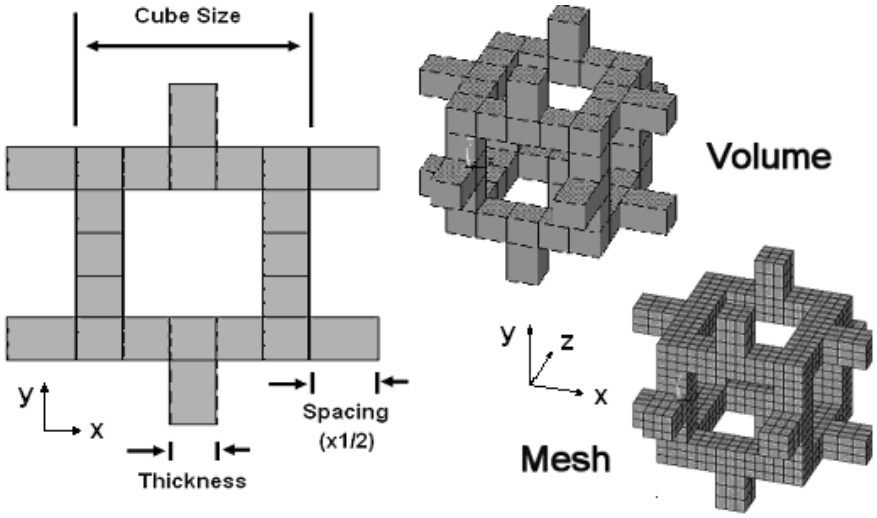

Figure 3.8:Cellular model representing open cell trabecular structure

A non linear analysis was also performed using a bi-linear isotropic hardening law to represent both materials in order to account for plastic deformation. The bilinear law describes the stress strain curve as two linear portions; the first region follows the slope of the elastic modulus. After the yield point, which is taken as the yield stress of cortical bone, 114MPa [21] and 40MPa for bone cement, the stress and strain follows a different slope; the tangent modulus. The tangent modulus was taken as 10% of the elastic modulus for both bone and cement. Pressure was incrementally increased until plastic deformation occurred.

3.5. Creation of Micro FE Models

The process of creating a smooth surface tetrahedral mesh from CT images is shown in Figure 3.9.

CT imaging – High resolution CT images of a specimen were taken and reconstructed using filtered back projection. Once the 3D image was reconstructed, it was exported as a series of 2D cross sectional images which were then read into the image visualisation software Amira 4.2 (Mercury Systems, Berlin, Germany) [22]. Images were exported as stacks of Tiff images.

Segmentation: This is the process of classifying regions of the CT image into different materials using the greyscale value. The grey value in a CT image is related to the x-ray atenuation of the material and thus the density of the material [20]. For the aluminium foam, threshold segmentation was used to differentiate the grey values of aluminium and air. A threshold of

intensity was selected where all values above are assumed to be aluminium and all values below assumed to be air. Figure 3.10 shows an example of this. Differences in architecture occur as a function of the threshold value; a low threshold results in thicker trabeculae and conversely a high threshold yields thinner trabeculae with a loss of connectivity (see Figure 3.10). Region growing techniques were used to segment the cement-foam interface samples. This is where a seed value is chosen and thresholds either side of this value are selected. This can be performed in 2D or 3D.

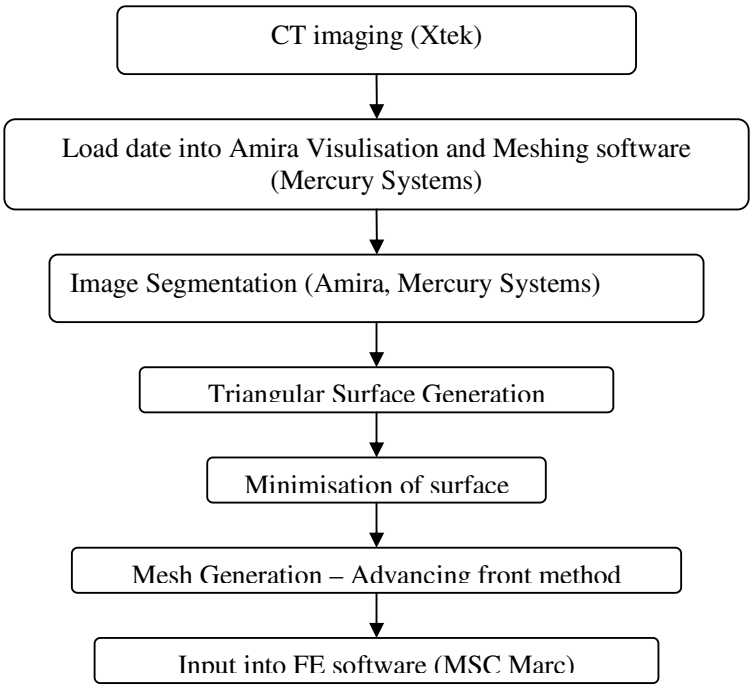

Figure 3.9: Process of building a tetrahedral mesh from CT images

Triangular surface generation: Using the marching cubes algorithm in Amira 4.2 (Mercury Systems) [22, 23], a triangular surface was created of the segmented volume. The triangular surface was then either used without further processing or smoothed using constrained or unconstrained Gaussian filters.

Minimisation of surface: An edge collapsing algorithm implemented in Amira [22] was used to reduce the number of triangles in the surface and reduce the number of resulting elements in the tetrahedral mesh. To enable mesh generation, the quality of the triangular surface was manually improved before mesh generation for example by removal of intersecting faces and improving the aspect ratio of the triangles.

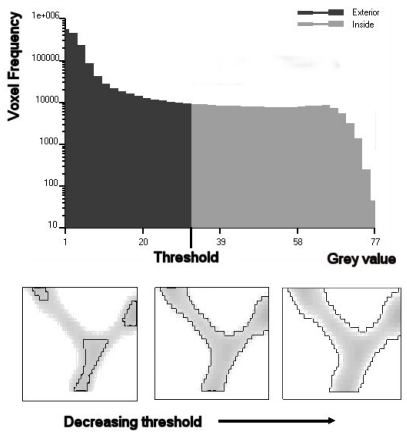

Figure 3.10:Grey level histogram and trabecular architecture changes as a function of threshold

Mesh Generation and FE model: The tetrahedral mesh was generated from the surface model using the advancing front method[13]. Using the mesh created, a three dimensional linear elastic compression analysis was performed in MARC (MSC Software Corp, London). The ends of the trabeculae opposite to the applied load were constrained in all directions. The edges of the specimen were unconstrained to match the conditions of the mechanical test rather than the continuous surface that exists in bone. In μFE models of bone the properties of the trabeculae are usually assumed to be homogenous and isotropic[14]. The tissue Young's modulus and Poisson's ratio of the aluminium were assumed to be 70GPa and 0.3 respectively. The apparent Young's modulus for the foam was obtained from the displacement due to loading. The Young's modulus and Poisson's ratio for PMMA were assumed to be 2GPa and 0.3 respectively.

3.6. References

1. Gibson, L.J. and M.F. Ashby, *Cellular Solids: Structures and Properties*. 1988: Pegammon.
2. Carter, D.R. and W.E. Caler, *Uniaxial fatigue of human cortical bone. The influence of tissue physical characteristics.* Journal of Biomechanics, 1981. **14**: p. 461-470.
3. Carter, D.R. and W.C. Hayes, *The compressive behavior of bone as a two-phase porous structure.* The Journal of Bone and Joint Surgery, 1977. **59-A**(7): p. 954-962.
4. Keaveny, T.M. and W.C. Hayes, *A 20-year perspective on the mechanical properties of trabecular bone.* Journal of Biomechanical Engineering-Transactions of the ASME, 1993. **115**(4): p. 534-542.
5. Keaveny, T.M., E.F. Morgan, G.L. Niebur, and O.C. Yeh, *Biomechanics of trabecular bone.* Annual Review of Biomedical Engineering, 2001. **3**: p. 307-333.
6. McCalden, R.W., J.A. McGeough, and C.M. Court-Brown, *Age-related changes in the compressive strength of cancellous bone. The relative importance of changes in density and trabecular architecture.* Journal of Bone and Joint Surgery-American Volume, 1997. **79**(3): p. 421-427.
7. Carter, D.R. and M.D. Spengler, *Mechanical properties and composition of cortical bone.* Clinical Orthopaedics and Related Research, 1978. **135**: p. 192-217.
8. Cowin, S.C., *Bone Mechanics Handbook*. 2nd ed, ed. S.C. Cowin. 2001: CRC.

9. Hodgskinson, R. and J.D. Currey, *Young modulus, density and material properties in cancellous bone over a large density range.* Journal of Materials Science-Materials in Medicine, 1992. **3**(5): p. 377-381.
10. Keaveny, T., E. Wachtel, C. Ford, and W. Hayes, *Differences between the tensile and compressive strengths of bovine tibial trabecular bone depends on modulus.* Journal of Biomechanics, 1994. **27**(9): p. 1137-1146.
11. Morgan, E.F. and T.M. Keaveny, *Dependence of yield strain of human trabecular bone on anatomic site.* Journal of Biomechanics, 2001. **34**(5): p. 569-577.
12. Mosekilde, L., L. Mosekilde, and C. Danielsen, *Biomechanical competence of vertebral trabecular bone in relation to ash density and age in normal individuals.* Bone, 1987. **8**(2): p. 79-85.
13. Morgan, E.F., O.C. Yeh, W.C. Chang, and T.M. Keaveny, *Nonlinear behavior of trabecular bone at small strains.* Journal of Biomechanical Engineering, 2001. **123**: p. 1-9.
14. Lakes, R., *Viscoelastic properties of cortical bone*, in *Bone Mechanics Handbook*, S.C. Cowin, Editor. 2001, CRC Press. p. 11.1 -11.15.
15. Halawa, M., A. Lee, R. Ling, and S. Vangala, *The shear strength of trabecular bone from the femur, and some factors affecting the shear strength of the cement-bone interface.* Archives of Orthopaedic and Trauma Surgery, 1978. **92**(1): p. 19-30.
16. Rose, R.M. and A.S. Litsky, *Biomechanical considerations in the loosening of hip replacements* in *Current Perspectives on Implantable Devices Vol 1*. 1989. p. 1-45.
17. Browne, M., A. Roques, and A. Taylor, *The acoustic emission technique in orthopaedics - a review.* Journal of Strain Analysis for Engineering Design, 2005. **40**(1): p. 59-79.
18. Roques, A., M. Browne, M. Taylor, A. New, and D. Baker, *Quantitative measurement of the stresses induced during polymerisation of bone cement.* Biomaterials, 2004. **25**(18): p. 4415-24.
19. Duesing, L.A., *Acoustic-Emission Testing of Composite-Materials.* Proceedings Annual Reliability and Maintainability Symposium, 1989(SYM): p. 128-134.
20. Ketcham, R. and W.D. Carlson, *Acquisition, optimization and interpretation of X-ray computed tomographic imagery: applications to the geosciences.* Computers & Geosciences, 2001. **27**: p. 381-400.
21. Black, J., *Handbook of Biomaterial Properties*, ed. G. Hastings. 1998, London: Chapman & Hall.
22. *Amira (Mercury Systems, Berlin, Germany), http://www.amiravis.com*
23. Frey, P.J., H. Borouchaki, and P.L. George, *3D Delaunay mesh generation coupled with an advancing-front approach.* Computer Methods in Applied Mechanics and Engineering, 1998. **157**(1-2): p. 115-131.

Chapter 4. *Theoretical modelling of cancellous bone and the cement-bone interface*

The integrity of the interface formed between trabecular bone and cement depends on the interdigitation of cement into the inter-trabecular spaces. In this study, the cement-bone interface has been modelled using an open cell skeletal cube to represent bone with varying amounts of cement incorporated into the "inter-trabecular" spaces in order to represent cement interdigitation. Using a simple model to represent bone allows easy examination of various factors such as bone quality, bone anisotropy and amount of cement penetration, all of which are important in determining the properties of the cement bone interface. The variations of strain in both bone and cement were examined under an arbitrary compressive load in order to understand the load transfer from cement to bone. The trabeculae and bone cement were modelled as homogenous, isotropic and elastic continua. Increased interdigitation showed improved load transfer to the bone. Increasing thickness and density of the trabeculae also showed improved load transfer. Where there was no cement interdigitation of cement into bone, there was a markedly higher strain in both cement and bone.

Presented at the 5th World Congress of Biomechanics, Munich, Germany, 29th July – 4th August 2006

4.1. Introduction

Due to the heterogenous and anisotropic nature of bone as well as the difficulty in obtaining repeatable samples, it is often difficult to obtain experimentally reproducible results for the mechanical properties of bone. Therefore, it is difficult to isolate and examine the influence of individual parameters such as trabecular thickness or porosity. The use of a simple cellular model to represent bone facilitates examination of individual factors such as bone geometry and its influence on apparent level properties.

A number of different idealised unit cell geometries modelling the behaviour of trabeular bone have been proposed in the literature. These can be polygons varying from cubic[1] to tetrakaihedron[2] structures or voronoi (random) cells[3]. A unit cell can be used for dimensional analysis to determine relationships linking mechanical properties to the relative density of the cell. In addition, these cells can form part of a repeating structure to examine the effect of trabecular loss[4] and the effectiveness of remodelling algorithms[5].

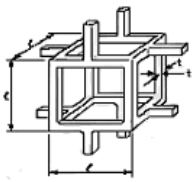

Figure 4.1: Model of open cell foam[1]

Gibson[1] derived a relationship linking relative density to stiffness using dimensional analysis. Dimensional analysis assumes that cells in foams of different relative densities are geometrically similar. The cubic geometry is constructed from a number of connected beams of length *l* and thickness *t* (Figure 4.1). The relative density and second moment of area can be related to *t* and *l* through:

$$\frac{\rho^*}{\rho s} \propto \left(\frac{t}{l}\right)^2$$

$$I \propto t^4$$

In the linear elastic regime, under uniaxial stress the cell deforms primarily through bending. Using standard beam theory from Timoshenko and Goodier 1970[6], the deflection of a beam is defined by:

$$\delta = \frac{Fl^3}{E_s I}$$

Equation 4.1

where F is the applied force, l is the length of the beam, E_s is the Young's modulus of the solid and I is the second moment of area of the beam. When uni-axial load is applied to the top of the cell within the linear elastic range, the edges of the beam will deflect, proportionally to Fl^3/E_sI. Force is related to stress, σ and length by $F \alpha \sigma l^2$. Young's modulus is defined by stress divided by strain, therefore using the above equations E^*, the Young's modulus of the cell, can be defined as

$$E^* = \frac{C_1 E_s I}{l^4}$$

Equation 4.2

where C_1 includes the geometric constants of proportionality. From experimental data, this constant is approximately 1. This can be rearranged as:

$$\frac{E^*}{Es} = C_1 \left(\frac{\rho^*}{\rho s} \right)^2$$

Equation 4.3

Where (ρ^*/ρ_s) is relative density and C_1 is a constant. The constant is determined from experimental data. The relative density of bone typically lies between 0.05 – 0.3. This equation can be applied to regions of cancellous bone where the structure is roughly equiaxed such as in the femoral head region.

The first aim of this study was to recreate the simple cubic cellular model proposed by Gibson using the FE method. The effect of changing geometry on the modulus and damage behaviour was examined. Although Gibson's model was not designed to be a geometric representation of a cellular structure, it can be used to isolate and examine the effect of individual parameters such as the trabecular thickness and pore size on the global stiffness. The effect of geometric anisotropy on compressive stiffness can be easily examined using this model although Equation 4.3 will no longer be valid.

To the author's knowledge, these techniques have not been extended for examination of the microstructural behaviour of the cement-bone interface. The stability of the cement-bone interface is vital to maintaining long term stability of a cemented prosthesis. A well established cement-bone interface can remain intact for many years without signs of any adverse biological response. However, the interface may become compromised eventually leading to progressive interface failure and eventual loosening of the implant. The amount of cement interdigitated into the trabecular spaces is thought to improve the strength of the interface and therefore improve the stability of the implant[7-9]. The microstructural properties of the cement-bone interface are poorly understood. Little is known about the local stress distribution across the interface and the affect of bone quality, architecture and cement penetration depth. The local deformations and

motions of the cement and bone at the interface are important in the understanding of the influence of mechanical loading on the loosening process[10, 11].

In FE models of stem-bone constructs, the cement-bone interface is often assumed to act as a continuum. This assumes averaged properties over a representative length. However, the continuum assumption is questionable at the cement-bone interface. Harrigan *et al* [12] examined the limitations of the continuum assumption in cancellous bone. For cancellous bone, if the quantity of interest such as stress, strain or density varies by more than 20-30% over a distance of three to five trabeculae, then the assumption is not valid. The continuum assumption is only valid when the quantities of interest do not vary substantially at the microstructural level. It was stated that there is insufficient data regarding the microstructure of the interface to be able to apply the continuum assumption. Therefore, since the behaviour at the microstructural level is not accurately known, the continuum assumption is not valid for the cement-bone interface and further approaches to evaluating the cement-bone interface are required. In the present work, the cellular model described above will be extended to modelling the behaviour of the cement-bone interface. Various degrees of cement volumes will be added to varying unit cell geometries to examine the load transfer across the interface.

4.2. Materials and Methods

An idealised unit cell based on the geometry of Gibson's model was created in Ansys 8.1. Loading and boundary conditions of the FE models are detailed in Section 3.4. To investigate the effects of geometric variables on cell mechanics, the geometric variables of the unit cell; thickness, spacing and cube size were varied as summarised in Figure 4.2.

Trabecular thickness, *t* (μm)	Cube size, *l* (mm)	Spacing, *s* (mm)	Volume fraction, %
120	1	0.3	10.52
140	1	0.3	12.48
160	1	0.3	14.65
180	1	0.3	17.06
200	1	0.3	19.73
200	1.2	0.4	14.90
200	1.4	0.5	11.89
200	1.6	0.6	9.86
200	1.8	0.7	8.40
200	2	0.8	7.30
200	1	0.5	14.90
200	1	0.4	11.89
200	1	0.3	9.86
200	1	0.2	8.40
200	1	0.1	7.30

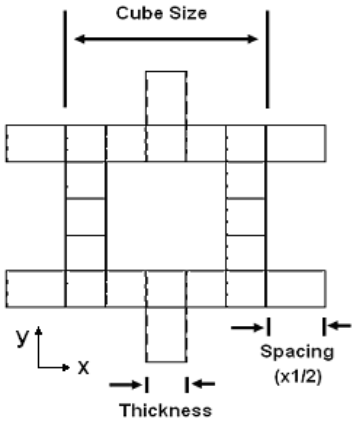

Figure 4.2: Variation of geometric properties

The effect of anisotropy was also investigated. Cube size was varied in one direction between 1-2mm whilst the other directions were held constant at 1mm. For example, when anisotropy in the x-direction was examined, the cube size in the direction would be set to 1.2, 1.4, 1.6, 1.8 and 2mm whilst cube size in the y and z direction was set to 1mm. Compressive loading was always applied in the y-direction. Spacing was set to half the cube length.

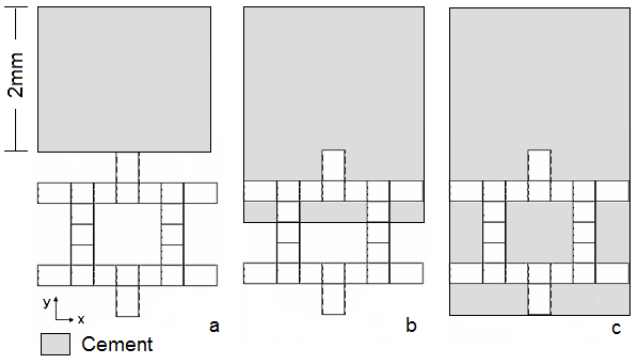

Figure 4.3: 2D projections of models of the unit cell with cement mantle of 2mm. a no interdigitation, b. partial cement penetration, c. full cement interdigitation

Three cases of cement interdigitation were then examined with variation of unit cell geometry:

a. No cement interdigitation. A 2mm cement layer was created above the bone cell geometry. The compressive load was added to the top nodes of the cement layer. Cement was assumed to be fully bonded to the bone

b. Partial cement penetration. In addition to the 2mm cement layer, cement was added to the trabecular spaces approximately midway through the geometry.

c. Full cement interdigitation. Cement was included in all intra-trabecular spaces to form a composite material.

4.3. Results

A mesh convergence test was performed to optimise the number of linear elements employed in each model for the unit cell alone. The number of elements across the struts was set at 2, 3, 4 and 5 for a set model with trabecular thickness 180µm, a cell size of 0.001mm and spacing of 0.003mm. The optimum number of elements for each strut was found to be 3. This mesh density gave a modulus within 4% of the modulus determined from the model with 5 elements across each strut (Figure 4.4).

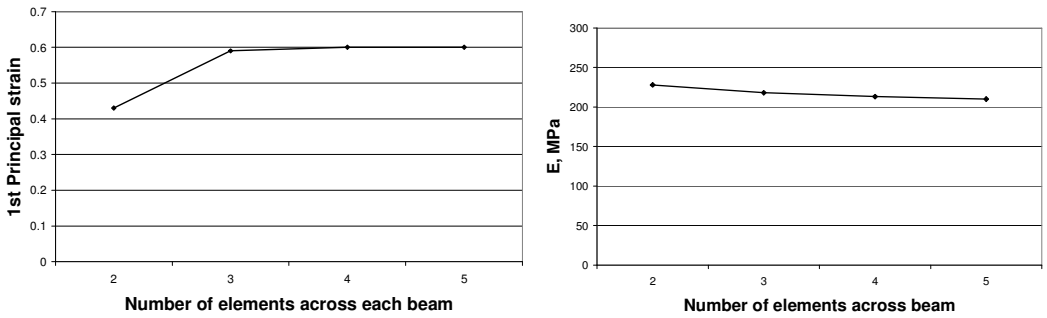

Figure 4.4: Convergence test for number of elements across each beam in the unit cell; 1st principal strain (left), apparent modulus (right)

4.3.1. Unit cell geometry: no cement

Relative density is related to volume fraction which is in turn directly related to the geometric variables; thickness, spacing and cube size. Dimensional analysis shows modulus to be proportional to the square of relative density (Equation 4.3). Therefore, modulus is plotted with the square of volume fraction to examine the effect of changing geometry (Figure 4.5).

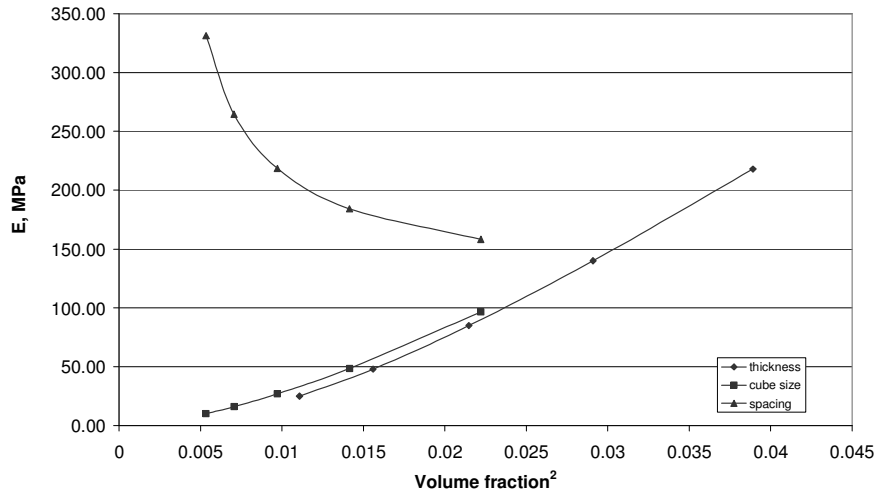

Figure 4.5:Modulus with the square of volume fraction for change in thickness, cube size and spacing of the unit cell

Of the geometric variables, increasing trabecular thickness gave the most significant change in modulus. When the thickness was changed from 120µm to 200µm, modulus changed from 25MPa to 218MPa. For an increase in cube size from 1.2 to 2mm, there is a 92% decrease in modulus from 193MPa. For an increase in spacing from 0.1mm to 0.5mm, there is a 64% decrease in modulus from 883MPa. When thickness is reduced, the regions of elastic deformation remain the same but more deformation occurs within the thinner beams (Figure 4.6).

Geometric anisotropy in the direction normal to loading was investigated. The strains resulting from elastic deformation are shown in Figure 4.7. With low anisotropy for example in Figure 4.7a, the regions of deformation are similar to an equiaxed structure. As more anisotropy occurs, increased deformation occurs in the beams transverse and parallel to the direction of loading. Where anisotropy occurs in the direction of loading, the main regions of elastic deformation occur as a result of bending of the struts. With increasing anisotropy, the strain in the beams parallel to the direction of loading are reduced.

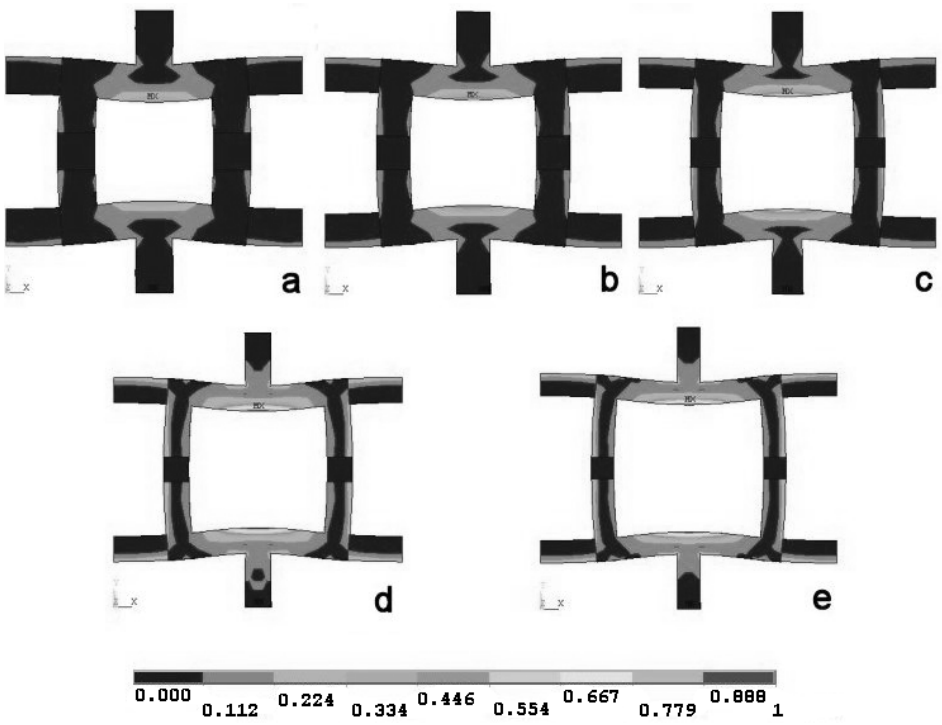

Thickness: a 200µm, b 180µm, c 160µm, d 140µm and e 120µm.

Maximum strain was 3.12×10^{-5}

Figure 4.6: Normalised first principal strain for cells with decreasing thickness.

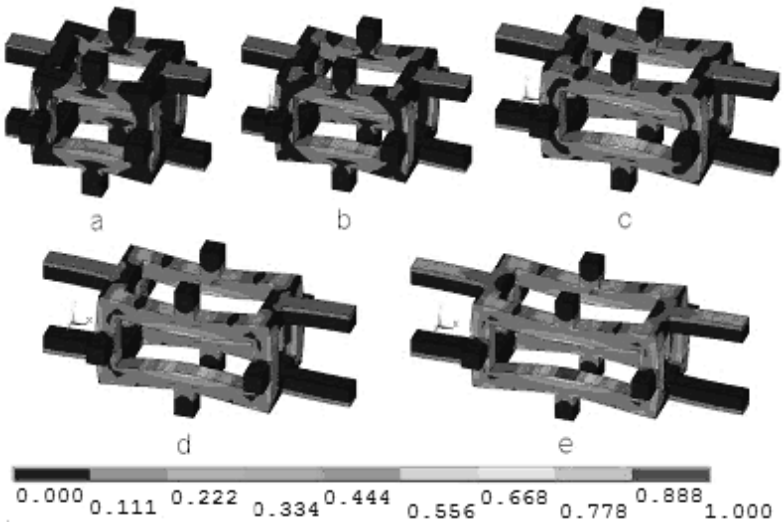

Maximum strain was 3.47 x 10^{-5}

Figure 4.7: Normalised first principal strains on cell with increasing anisotropy normal to applied load.

4.3.2. Cement-Bone Interface

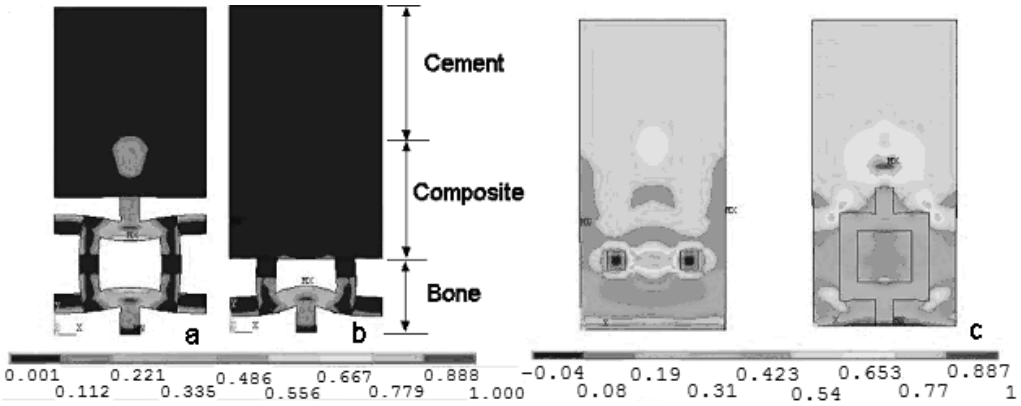

a. No interdigitation b. partial cement interdigitation c. full interdigitation
Maximum strain was, for a and b; 0.004 and 2.48 x 10 $^{-5}$ for c

Figure 4.8:Normalised first principal strains for models with varying cement interdigitation. Maximum strain was 2.48 x 10 $^{-5}$ for a and b and

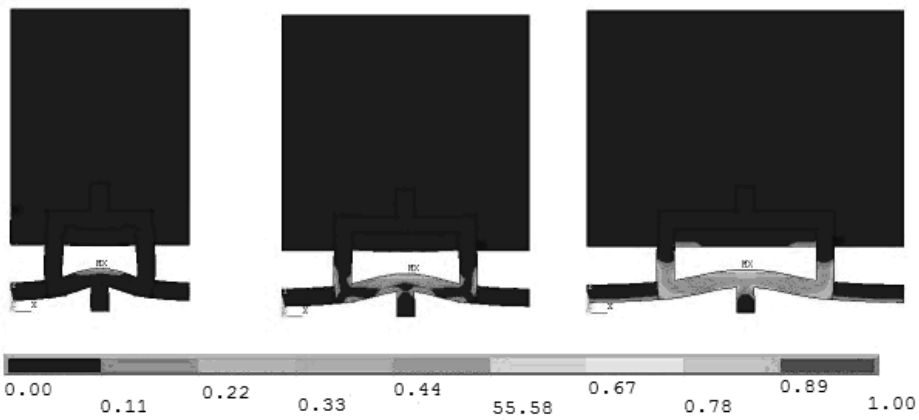

Maximum strain was 0.002

Figure 4.9: Normalised first principal strain for partial cement interdigitation with varying anisotropy in the direction normal to loading

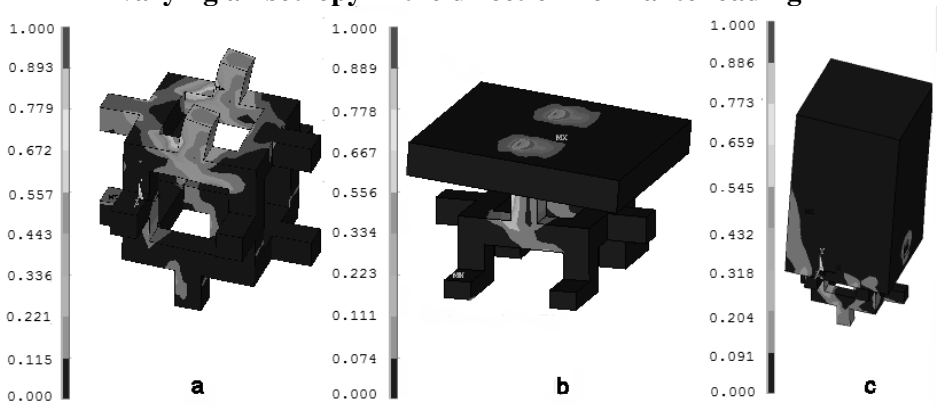

Maximum strain a. 0.013 b. 2.934 c. .3970

Figure 4.10: First principal strain of cellular model under shear loading a. cell only, b. section of no interdigitation model, c. partial cement interdigitation

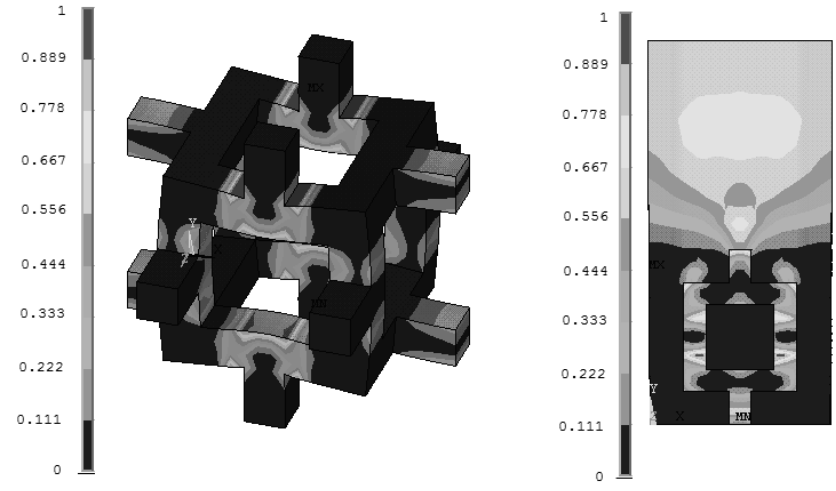

Maximum strain: 0.214 (left), 0.009 (right)

Figure 4.11: Plastic strain for cell only (left) and full interdigitation (right) model

As more cement was added, the global stiffness further increased as expected for a denser structure. In the case where cement was semi interdigitated into the trabecular pore, a composite region was formed. In this region, the deformation of the bone was reduced and the strain was transferred to the cement in the composite region. Where a composite region existed, the strains in the cement layer were lower than for the case without interdigitation. The bone below the composite region deforms by bending similar to the cell without cement.

Where full cement interdigitation into the cell was modelled, stiffness was increased by an order of magnitude. For a variation in thickness of beams from 120-200µm, global stiffness increased from 2.18-2.34 GPa. For a change in cube size of 1.2-2mm and a decrease in spacing from 0.5-0.1mm, stiffness changed from 2.28GPa to 2.182GPa and from 2.273 to 2.443GPa respectively. With variations in geometry, the stiffness stays within in a relatively small range. This shows that the composite is less sensitive to variations in geometry than the cellular material alone

When anisotropy was modelled with partial cement interdigitation, the structure deformed similarly to the equiaxed models (Figure 4.8). The strains in the cement are higher in the composite region and do not extend to the bulk cement region. This increased strain in the composite also occurs for anisotropy in the direction of loading.

In a cemented prosthesis, the load across the cement-bone interface is primarily shear. The strains for the cellular model with and without cement are shown in Figure 4.10. When the unit cell is subject to shear loading, the top trabeculae deform by bending, rather than bending of the whole cell as for compressive loads. When cement is added but not interdigitated, the cement mantle appears to pivot at the point where the cement is bonded to bone. This is due to the limitations of the linear-elastic model. In this situation, the cement would not remain bonded to the bone. In addition, the trabecula below the cement mantle would deform or break. When cement is partially interdigitated, strains are reduced by an order of magnitude compared to when cement is not interdigitated. However, strains are higher than for the cellular model alone.

When plasticity was included in the model, the regions of maximum plastic strain under compressive loading were found at the meeting point of the trabeculae directly beneath the region of load and in the trabeculae normal to the direction of load (Figure 4.11). When the cell is fully surrounded in cement, strain across the whole model is reduced in comparison to the cell only. The regions of maximum strain in the cell only model become the regions of lowest strain. The trabeculae now deform in the direction parallel to loading. The strain in the cement in the composite region is comparatively low compared to the bulk cement region.

With full interdigitation, the bone and bone cement become a composite material. The stiffness of a fibre–reinforced composite can be described by the rule of mixtures:

$$E = E_m V_m + E_f V_f$$

Equation 4.4

Where E_m is the stiffness of the matrix, E_f is the stiffness of the fibre, V_m is the volume fraction of the matrix and V_f is the volume fraction of the fibre. This can be used as an approximation of the stiffness of the bone-bone cement composite. The modulus calculated from the FE models are compared to the modulus predicted by the rule of mixtures in Figure 4.12.

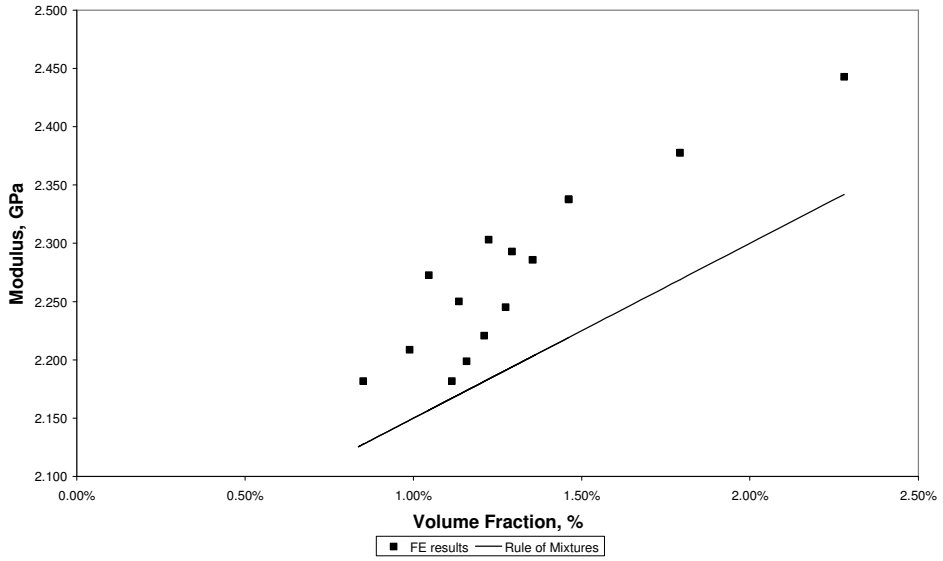

Figure 4.12: Comparison of modulus determined from FE model and modulus determined from the rule of mixtures

The rule of mixtures is used to predict the maximum stress in a uni-directional fibre reinforced composite. For these models, the moduli calculated using the rule of mixtures underpredicts the moduli calculated using FE analysis. The unit cell forms part of a network and as such the struts are more constrained than the fibres in a fibre reinforced composite. As a result, the cellular structure reinforces the composite, producing a stiffer structure than predicted. A similar effect where the modulus is greater than the modulus predicted using the rule of mixtures has also been shown for a wire mesh in an aluminium alloy [13].

4.4. Discussion

For the cellular model only without cement, variation in strut thickness followed by cube size had the most influence on the determined global modulus. Reduction in trabecular thickness and increasing porosity of cancellous bone occur with age and are typical signs of osteoporosis [14]. Silva *et al*[15], using a two dimensional cellular model, reported a reduction of 80% in Young's modulus and ultimate strength due to a 15% bone loss. For this study, a decrease in cube size of 0.8mm, which relates to a 7.6% reduction in volume fraction equates to a 90% reduction in stiffness. However, for osteoportic bone the tissue modulus may change as a result of

osteoporis. McNamara *et al*[16] examined the tissue level stiffness of osteoporotic rat femurs. It was shown that while overall bone mass and bone mineral density were decreased, the tissue level properties of the trabeculae were increased by 40-90%.

Consistent with dimensional analysis, it has been shown that a strong relationship between volume fraction and modulus exist. For differing strut thicknesses and cube sizes, there is a significant variance in the determined apparent modulus. In dimensional analysis, variations in architecture are accounted for through a constant C (Equation 4.3). With changes in the spacing, the relationship between modulus and the square of volume fraction is different (Figure 4.5). The spacing for a single cell does not influence deflection under a uniaxial compressive load and this is reflected by the small variation in global strain with spacing. The effective global area for which load is distributed increases with spacing, therefore large changes in the calculated Young's modulus are seen. With increased spacing, the cube is no longer equiaxed and Equation 4.3 becomes invalid. For more detailed analysis of the tissue level strains, a more representative structure of cancellous bone is required.

Fyhrie and Schaffler [17] found that under a compressive load, damage was found in trabeculae transverse to the direction of loading. This was seen in the equiaxed cellular model of bone. However, when the cells are elongated in the direction normal to loading (see Figure 4.7), elastic deformation also occurs in the beams parallel to the direction of loading.

Information regarding the behaviour of cancellous bone in the literature is limited to experimentally determined strength and modulus. The shear properties for cancellous bone are lower in comparison to tensile properties[18, 19]. The FE model has shown that in shear loading, regions of high strain exist at the junction of the struts. This may result in the shear failure of protruding trabeculae.

Generally, greater penetration is believed to be beneficial to the strength of the cement bone interface. This study supports this statement, as it has been shown that the determined stiffness increases significantly with increased cement penetration. The addition of cement increases the stiffness of the structure. In the case where no cement interdigitation occurs, compressive load is transferred to the cement directly above the region of contact. The trabecula below the cement layer deforms due to bending similar to the cell without cement. Race *et al*[21] found that under simulated stair climbing, microcracks preferentially formed at the cement-bone interface and that some cracks formed at the spurs of the trabecular bone and extend into the bulk region of cement. This is consistent with the pattern of plastic strain shown in Figure 4.11. This situation can arise by increased deformation at the contact point between cement and bone as a result of poor interlock. In the case where the whole cell is embedded in cement, stiffness increases significantly. The bone no longer deforms due to bending. The stiffness is less sensitive to

changes in geometry; which may suggest that for patients with osteoporosis cemented arthroplasty may be the preferred choice as the likelihood of trabecular fracture within the composite region is decreased. In this composite region, failure should not result from mechanical overload; instead damage may be caused by other factors such as damage accumulation at defects due to fatigue. Excessive penetration of cement into cancellous bone may be detrimental to the interface in the long term. In arthroplasty, it suggested that cancellous bone should be retained so that there is sufficient bone stock remaining for future procedures. It is important not to remove all the cancellous bone, as this will leave a smooth inner cortex and diminish the ability for the cement to bond to the bone. Jansson *et al* [22] examined the stress transfer across the cement bone interface with increasing cement thickness. Their results show that for increased cement penetration, the interface stresses are increased. They suggest that as a result of the stiffening of the cancellous bone due to increased cement penetration, the cancellous bone no longer acts as a soft interposing layer between cortical bone and cement. The study concludes that in order to maintain the philosophy of retaining as much cancellous bone as possible during arthroplasty, that cement penetration should be minimised to the depth necessary to achieve initial fixation.

Clinically, varying degrees of cement penetration can occur. While generally greater cement interdigitation is thought to increase the strength of the interface, there is an upper limit to which further increasing cement penetration does not produce any further benefits. Generally an optimum cement mantle of 3-5mm is suggested[8, 20]. The behaviour of the cement-bone interface at the microstructural level with varying degrees of cement penetration has not been documented. If poor cementing technique is used with insufficient pressurisation of the cement, no cement interdigitation or only partial filling of the pores may occur. Complete filling of the trabecular pores can occur with pressurised cement. Filling of the cement to the cortex of the bone can occur where large amounts of trabecular bone are removed as for the thin cement mantle technique (see section 2.3.6).

Load transfer across the cement-bone interface is primarily in shear. The unit cell model has shown that protruding trabeculae will deform by bending with maximum strain at the junction between trabeculae. When cement is bonded to the trabeculae but not interdigitated, high strains can be seen in the cement mantle above the region of contact and at the junction of the trabeculae. If strains are sufficiently high, the protruding trabeculae may break. Clinically, as the bond at the cement-bone interface is damaged, this can lead to increased micromotion and eventual loosening [23]. Where the cell is fully encased in cement, the strains are reduced by an order of magnitude compared to the model without interdigitation of the cement. When bone is encased in cement, it looses its ability to remodel [24], therefore the increased stiffness as a result

of the formation of the composite should be maintained. However, should loosening occur with increased cement penetration, the bone stock available for revision arthroplasty is reduced.

As this model is a geometric representation of cancellous bone, it has limitations in its accuracy. The unit cell uses rectangular beams and as such the edges introduce stress concentrations into the cement. This would not occur in cancellous bone as the trabeculae have smooth surfaces. The strut shape at the connections between beams is also a limitation because trabeculae are usually thicker at ends. In addition, the unit cell is assumed to be regular and repeating. In cancellous bone, the cells adapt to the mechanical environment and as such will not be regular and exhibit anisotropy.

The loads across the cement-bone interface at the microstructural level are not known and as such arbitrary loads were selected. Therefore plots of stress have not been presented and the strain values only used for comparative purposes.

Boundary conditions were applied with the assumption that the unit cell formed part of a regular and repeating structure. Cement was assumed to be fully bonded to the bone. The fully bonded condition is only really valid at the continuum level between cement and cancellous bone. Cement gaps can occur at the interface where the cement is not fully apposed to bone [25]. For this case, contact between the surfaces should be modelled. For the linear elastic model with cement that is not interdigitated into the cell, the cement mantle appears to pivot around the protruding trabeculae (Figure 4.10). It is unlikely that this would occur as damage to the trabeculae or debonding is likely to occur before this. As such, a non linear approach with contact is likely to give more representative results. Residual stresses may also be present in cement as a result of shrinkage during cure. These residual stresses have not been included in this study.

4.5. Conclusions

A unit cell model representative of cancellous bone was used to examine the effect of geometry on apparent level properties. For the model of cancellous bone alone, trabecular thickness and cell size, which are related to volume fraction of the cell, were found to have the greatest influence on the determined apparent modulus. When cement is interdigitated into the unit cell, the structure forms a significantly stiffer material but becomes less sensitive to changes in volume fraction of the cell. When the cell is fully embedded in the cement, the trabeculae are constrained and no longer deform by bending. For more detailed evaluation of the tissue level model, a more accurate geometry of bone is required.

4.6. References

1. Gibson, L.J. and M.F. Ashby, *Cellular Solids: Structures and Properties*. 1988: Pegammon.
2. Zhu, H.X., J.F. Knott, and N.J. Mills, *Analysis of the elastic properties of open-cell foams with tetrakaidecahedral cells.* Journal of the Mechanics and Physics of Solids, 1997. 45(3): p. 319-325.
3. Silva, M.J. and L.J. Gibson, *The effects of non-periodic microstructure and defects on the compression strength of two dimensional cellular solids.* International Journal of Mechanical Science, 1997. 39(5): p. 549-563.
4. Guo, X.E. and C.H. Kim, *Mechanical consequence of trabecular bone loss and its treatment: A three-dimensional model simulation.* Bone, 2002. 30(2): p. 404-411.
5. Huiskes, R., R. Ruimerman, G.H. van Lenthe, and J.D. Janssen, *Effects of mechanical forces on maintenance and adaptation of form in trabecular bone.* Nature, 2000. 405(6787): p. 704-706.
6. Timoshenko, S.P. and J.N. Goodier, *Theory of Elasticity*. 3rd ed. 1970: McGraw-Hill.
7. Askew, M.J., J.W. Steege, J.L. Lewis, J.R. Ranieri, and R.L. Wixson, *Effect of cement pressure and bone strength on polymethylmethacrylate fixation.* Journal of Orthopaedic Research, 1984. 1(4): p. 412-20.
8. Krause, W., W. Krug, and J.E. Miller, *Strength of the cement-bone interface.* Clinical Orthopaedics, 1982. 163: p. 290-299.
9. Oates, K.M., D.L. Barrera, W.N. Tucker, C.C.H. Chau, W.D. Bugbee, and F.R. Convery, *In vivo effect of pressurisation of polymethylmethacrylate bone-cement.* The Journal of Arthroplasty, 1995. 10(3): p. 373-381.
10. Heaton-Adegbile, P., J. Hussell, and J. Tong, *In-vitro assessment of load transfer and strain distribution across the cement-bone interface in an artificially replaced acetabulum.* Journal of Bone and Joint Surgery British Volume, 2006. Vol 88-B(SUPP_III,): p. 386.
11. Mann, K., M. Miller, R. Cleary, D. Janssen, and N. Verdonschot, *Experimental micromechanics of the cement-bone interface.* Journal of Orthopaedic Research, 2008. *In Press*.
12. Harrigan, T.P., M. Jasty, R.W. Mann, and W.H. Harris, *Limitations of the continuum assumption in cancellous Bone.* Journal of Biomechanics, 1988. 21: p. 269.
13. Ganesh, V. and M. Gupta, *Exceeding average rule of mixtures stiffness in composite materials with interconnected fibres as reinforcement.* Materials Science and Technology, 2001. 17(11): p. 1465-1471(7).
14. Keaveny, T.M. and O.C. Yeh, *Architecture and trabecular bone - Toward an improved understanding of the biomechanical effects of age, sex and osteoporosis.* J. Musculoskel Neuron Interact, 2002. 2(3): p. 205-208.
15. Silva, M.J. and L.J. Gibson, *Modeling the mechanical behavior of vertebral trabecular bone: Effects of age-related changes in microstructure.* Bone, 1997. 21(2): p. 191-199.
16. McNamara, L., P. Prendergast, and M. Schaffler, *Bone tissue material properties are altered during osteoporosis.* Journal of Musculoskeletal Neuronal Interactions, 2005. 4(4): p. 342-343.
17. Fyhrie, D.P. and M.B. Schaffler, *Failure mechanisms in human vertebral cancellous bone.* Bone, 1994. 15(1): p. 105-109.
18. Keaveny, T.M., E.F. Morgan, G.L. Niebur, and O.C. Yeh, *Biomechanics of trabecular bone.* Annual Review of Biomedical Engineering, 2001. 3: p. 307-333.
19. Stone, J.L., G.S. Beaupre, and W.C. Hayes, *Multiaxial strength characteristics of trabecular bone.* Journal of Biomechanics, 1983. 16(9): p. 743-&.
20. Walker, P., M. Soudry, F. Ewald, and H. McVickar, *Control of cement penetration in total knee arthroplasy.* Clinical Orthopaedics and Related Research, 1988. 185: p. 155-164.

21. Race, A., M.A. Miller, D.C. Ayers, and K.A. Mann, *Early cement damage around a femoral stem is concentrated at the cement/bone interface.* Journal of Biomechanics, 2003. 36(4): p. 489-496.
22. Jansson, V., B. Heimkes, and M. Zimmer, *Stress transfer at the femoral bone/bone cement interface as a function of the cement thickness.* Archives of Orthopaedic and Trauma Surgery, 1993. 122(2): p. 65-68.
23. McKoy, B., Y. An, and R. Friedman, *Factors affecting the strength of the bone-implant interface*, in *Mechanical testing bone and the bone-implant interface*, Y.H. An and R.A. Draughn, Editors. 2000, CRC Press.
24. Dorr, L., J. Lindberg, M. Claude-Faugere, and H. Malluche, *Factors influencing the intrusion of methylmethacrylate into human tibiae.* Clinical Orthopaedics and Related Research, 1984. 183: p. 147-152.
25. Race, A., A. Miller, M.T. Clarke, and K.A. Mann, *Cement-implant interface gaps explain the poor results of CMW3 for femoral stem fixation.* Acta Orhopaedica, 2005. 76(5): p. 679-687.

Chapter 5. Micro Finite element modelling of a cancellous bone analogue

In this section, the results for selection of a bone analogue material are presented. Following this, the accuracy of smooth surface meshing of the analogue material is investigated. Using μCT scans of the selected bone analogue material, smooth surface micro finite element models were created. The effect of image processing before creation of the mesh on the accuracy of a linear elastic FE model was investigated. Threshold, mesh density and surface smoothing parameters used in mesh generation were varied and the mechanical properties predicted by the resulting meshes compared to experimental results. It was shown that correct selection of threshold was vital to maintaining accuracy

Accepted for publication in *Proceedings of the Institution of Mechanical Engineers: Part H.* Presented at the Summer workshop of the European Society of Biomechanics: Finite element Modelling in Biomechanics and Mechanobiology, Dublin, Ireland, 26th-28th August 2007

5.1. Introduction

The academic literature reports significant variations in the mechanical properties of cancellous bone[1-3]. The mechanical properties vary with species, site, sex, age, specimen and disease. Preparation, machining artefacts, whether the sample is tested wet or dry, strain rate and direction of testing are also factors which can affect the determined mechanical properties. In the literature review, it was stated that an FE model can only be as accurate as the data used to create and validate it. Since the reported mechanical properties of cancellous bone vary considerably, to facilitate validation of μFE models, an analogue material was chosen to eliminate specimen variability and the problems related to handling and testing of cancellous bone. The selection of a bone analogue material is detailed in the first section of this chapter.

In FE models of THA, cancellous bone is often assumed to be a continuum, thus neglecting its cellular structure. Harrigan [4] states that if the continuum properties of bone vary by less than 20-30% over a distance of three to five trabeculae then cancellous bone can be treated as a continuum. However, this assumption may not be valid at the bone implant interface due to the discontinuities on the surface of cancellous bone. Therefore, there is a need to examine the microstructural behaviour of the cement-bone interface. However, in order to develop microstructural finite element models of the cement-bone interface, the accuracy of FE models of cancellous bone must first be examined.

μFE models of cancellous bone based on computed tomography (CT) images have been previously used to evaluate local tissue strains and stresses and local damage at the trabecular level [5, 6], to examine fracture at the local level in trabecular bone [7, 8] and for dynamic assessment of failure initiation and propagation in bone under load [9, 10]. A common method of building meshes from CT data is the voxel-element technique. Tomographic images consist of voxels (volume elements) of differing grey values which relate to the x-ray attenuation coefficient of the material[11]. To segment the cancellous bone structure from the surrounding soft tissue, a grey level threshold is selected, above which all voxels are directly converted to eight node brick elements. The number of elements in these models is often of the order of millions and the solution of these models require the use of multiple parallel processors [12]. With voxel-element models, the accuracy at the surface of the trabeculae may be compromised due to the stress concentrations caused by the stair-case like surface produced by the brick elements. To improve accuracy, higher resolution CT can be used, however this rapidly increases the size and computational time of the model. An alternative approach is to create a tetrahedral mesh based on a triangular surface model of the tomographic data [13]. With this method, the surfaces can be smoothed, creating a more representative depiction of the cancellous bone surface rather than that of the voxel models. For smooth surface models, an intermediate

step of creating a triangular surface and optimisation of element number is necessary which may directly influence the accuracy of the resulting model.

The second section of this chapter examines the sensitivity of a FE model to segmentation (threshold value), mesh density and smoothing of surfaces. FE models of a cancellous bone analogue material were created from μCT data using the smooth surface method. The predicted apparent Young's modulus from compression test simulations were compared to experimentally determined apparent Young's modulus values. The present work highlights shortcomings in current thresholding methods that could lead to inaccuracies in property assignment in FE models.

5.2. Selection of a Bone Analogue Material

An extensive search for cellular materials was performed, the results of which are summarised in Table 5.1. The manufacturer's reported properties of the foam are compared to reported cancellous bone properties in Table 5.2.

	Product Name	**Product**
Metal foam suppliers		
Alulight International (Austria)	Alulight	Closed Cell Aluminium Foam
ERG Materials and Aerospace Corporation (Ca, USA)	Duocel	Open Cell aluminium foam
Goodfellow (Cambridge, UK)		Aluminium, reticulated vitreous carbon RVC, nickel, stainless steel, alumina, silicon carbide foams (open/closed cell not specified)
Incofoam (UK)	Incofoam	Open Cell Nickel Foam
Zimmer (USA)	Trabecular Metal™	Trabecular metal (used as a bone scaffold): Tantalum Foam
Polymer Foams suppliers		
IMPAG (UK)	AIREX	Closed cell PVC foam
Sawbones (Sweden)	Sawbone	Open and Closed cell PU foam
Epoxies,etc (USA)		Two part mix PU foam (closed cell)

Table 5.1: Suppliers of foam

Closed cell foams were discounted as they would not allow for cement penetration into the pore spaces. Examples of open cell foam are shown in Figure 5.1. Silicon Carbide and RVC were not used because of their low Young's modulus compared to the reported values for cancellous bone. The manufactured thickness of nickel foam was too low. In addition, an available supplier of tantalum foam could not be found. The remaining suitable foams were the open cell polyurethane foam (OPF) manufactured by Sawbone and Duocel aluminium foam (ERG, Ca.).

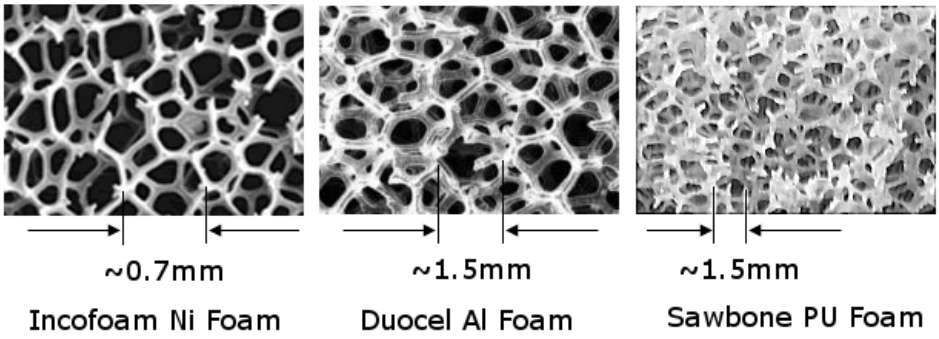

Figure 5.1: Three examples of open cell foam: nickel, aluminium and polyurethane

The maximum size that Duocel aluminium foam can be manufactured is 45 x 50 x 20mm. It possesses a structure of dodecahedron shaped cells (12-14 side polyhedra) connected by 5-6 solid continuous metal ligaments made of the aluminium alloy 6101-T6 [14]. The matrix of cells and ligaments is regular and uniform throughout the structure (Figure 5.1) with cell size (ranging from 1.5-2.5mm) dependent upon its relative density. The available porosity ranges from 5-40 PPI (pores per inch). 40 PPI foam which has been previously used in literature to represent cancellous bone, has an average cell diameter of 1.5mm. The lead time for Duocel aluminium foam (to the UK) is approximately one month.

OPF was designed for use as a cancellous bone analogue and for cement injection and modelling. It has an open cell structure with a relative density of 95% and an average cell size of 1.5-2mm. It has a low compressive strength and is limited in size to 75 x 150 x 19mm. Above this volume, the cellular structure tends to collapse during manufacture.

The two most suitable open cell foams, OPF and Duocel, were selected for mechanical testing. The methods for testing their shear and compressive properties are detailed in Chapter 3. OPF could not be sourced in the recommended sizes detailed by ASTM F1839 (thickness is limited to 20mm) and as such was not tested. Compressive properties were taken for this material from the manufacturer's datasheet [14].

	Open/ closed cell	Compressive		Tensile		Shear		Density g/cc	Cell size	Sizes,mm	Available suppliers?	Cost
		Strength, MPa	E, MPa	Strength, MPa	E, GPa	Strength, MPa	E, MPa					
Cancellous bone	Open	3-35 [1, 2, 15-17]	70-13000 [23, 24, 112, 115, 117, 156, 237-239]	1-20[16]	350-2700[16, 18]	1-27 [2, 16, 19]	3-5[19, 20]	0.05-1	1-5mm[16]	N/A	NA	N/A
AIREX c70.55: Polymer	Closed	0.9	58	1.3	0.045	0.8	22	0.06			Yes	
Alulight	Closed	3	5000-14000				500	0.5			Yes	£25/kg
Duocel aluminium	Open	2.17	93.08	1.24	0.07584	1.31	199.95	3-12% nominal	1.5mm-2.54mm	Made to order	Yes – ERG (Ca)	$2-5 (US) per inch^3
Duocel RVC	Open	0.28-1.2	31-62	0.17-1.02		0.69	30.3			Made to order	Yes – ERG (Ca)	$1-3 (US) per inch^3
Duocel Silicon Carbide	Open	1.38	2.76								Yes – ERG (Ca)	$7-15 (US) per inch^3
Trabecular Meta™ (Tantalum foam)	Open	60	3000	63					550 µm		Not commercially available	N/A
Incofoam™ Nickel Foam	Closed			1.5				300-600g/m2	450-800µm	1.5 x 5x 1000	Yes	
Sawbone	Open	0.11	6.2					0.09	1.5-2.5mm	75x150x 19	Yes	€36 per block
		0.28	18.6					0.12	1.5-2.5mm	75x151x 20	Yes	€65 per block
Aluminium foam	Closed			130-195				0.2	2,4,6,18 pores/cm	150x150 x6.35	Yes - Goodfellow	$205 (US) per block
Alumina foam	Closed	2200-2600		330000-400000	330		3.9		26 pores/cm	150x150 x6.36	Yes – Goodfellow	$235 (US) per block
Nickel Foam	Closed			400-600	199.5			0.45	20 pores/cm	150x150 x6.37	Yes- Goodfellow	$286 (US) per block
Stainless steel	Closed		190-210	460-800				0.55	24 pores/cm	150*150x 6.35	Yes - Goodfellow	$516 (US) per block

Table 5.2: Materials properties and availability

5.3. Results of Mechanical testing for OPF and Duocel: Shear testing

Shear stress was calculated from

$$\tau = \frac{P}{Lb}$$

Equation 5.1

where τ = core shear stress (MPa), P=load on specimen (N), L = length of specimen (mm) and b = width of specimen (mm).

Ultimate shear strength was calculated using P_{max} where P_{max} is the maximum load and shear yield strength was calculated at P_y where P_y equals the yield load. Yield load was calculated at 2% strain according to ASTM C273.

The shear modulus was

$$G = \frac{St}{Lb}$$

Equation 5.2

where G = shear modulus, MPa, S= ΔP/ΔU, slope of the initial portion of the graph, N/mm (where u is the displacement of the loading plates) and t is the thickness of the core in mm.

The average apparent density for Duocel, calculated by mass divided by apparent volume, was 260.8±5.8 kgm^{-3}.

The shear modulus could not be calculated for one sample because the initial portion of the graph was not linear. This sample was only used for calculating ultimate strength. The shear modulus was calculated from the linear portions of the stress/strain plots. Non-linear portions at the beginning of the stress/strain plot were neglected. Ultimate shear strength of Duocel was 2.17±0.275MPa, yield strength was 2.10±0.215MPa and shear modulus was 62.8±3.06MPa.

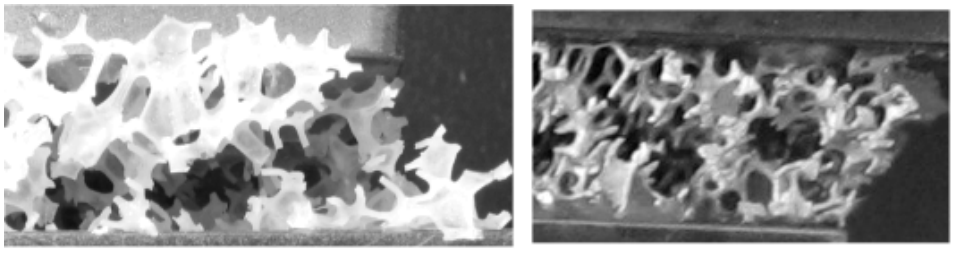

Figure 5.2: Comparison of Failure of OPF (left) and Duocel aluminium foam

There was significant plastic deformation of the aluminium foam: this can be seen by the permanent damage of the cells in the direction of loading, shown in Figure 5.2. The ultimate strength and modulus of Duocel were considerably higher than for OPF as shown in Figure 5.3.

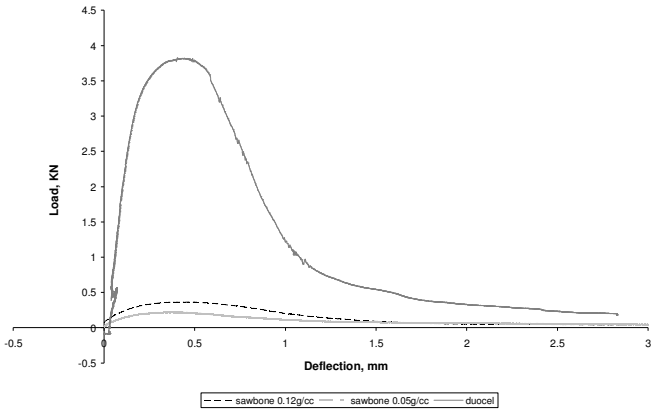

Figure 5.3: Comparison of load displacement curves of Duocel and OPF under shear

The peak load for the OPF samples with density 0.09g/cc was 0.234±0.03KN. The ultimate shear strength was 0.115±0.013MPa and yield strength was 0.0773±0.01MPa. The shear modulus was 0.00246±0.0005MPa. Comparison of the determined shear properties to those reported in literature are shown in Figure 5.4.

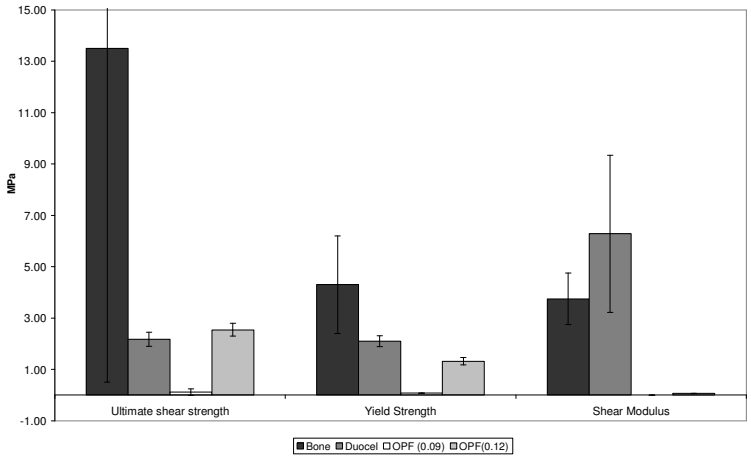

Figure 5.4: Comparison of shear properties

OPF with density 0.09g/cc was more difficult to machine that the 0.12g/cc density OPF. The material was very brittle and tended to break up when machined. With the limited thickness, machining the correct sample size was difficult as the corners of the sample were easily damaged during handling. The samples were examined for damage by eye before testing.

The strength of the 0.12g/cc OPF was higher than the lower density OPF. The average peak load for OPF samples with density 0.12g/cc was 0.378± 0.04KN, the average ultimate shear strength was 2.54±0.25MPa, the average yield strength was 1.32±0.15MPa and the average shear modulus was 0.059±0.008MPa.

5.4. Results of Mechanical testing for OPF and Duocel: Compression testing

The compressive strength and modulus were determined from the load deflection curves according to ASTM D1612.

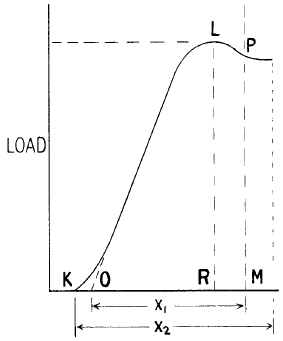

Figure 5.5: A typical load - deflection curve taken from ASTM D1621-04a

To calculate the compressive strength and modulus from the load deflection curve, the following points must be identified (Figure 5.5):

- O– This is the zero-strain point, the linear region of the load deflection is extended to the zero load line.
- M – This is the point, taken from point O of 10% deformation of the sample.

L is the point of yield, R is the related deformation. The distance O-R is the percent core deformation or strain at the yield point.

Five samples of aluminium foam were tested in compression; the load displacement curves are shown in Figure 5.6. The results for sample 1 are not shown because the test was interrupted giving a non-linear response.

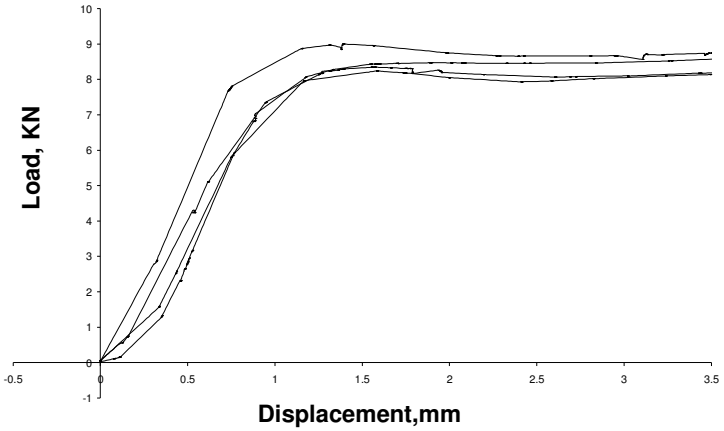

Figure 5.6: Compression test results

The results show a 'toe in' region at the beginning of the compression curves. This occurs when testing a cellular material and is a result of the collapse and fracture of the struts at the surfaces of the specimen come into contact with the platens.

The compressive strength was calculated by dividing the yield load by the initial horizontal cross-sectional area of the specimen. The mean compressive strength was 3.26±0.15MPa and mean compressive modulus was 102±7.96MPa.

The manufacturer ERG, did not provide the properties for the 10-12% density foam however the values for 8% nominal density foam are reported on the manufacturer's website [21]. These are compared to the experimental results in Table 5.3.

	10-12% Nominal Density	**8% Nominal Density (Manufacturers values)**
Compressive Strength	3.26MPa	2.17MPa
Modulus of Elasticity (Compressive)	102.3MPa	93.08MPa
Shear Strength	2.11MPa	1.31MPa
Shear Modulus	62.8MPa	199.95MPa

Table 5.3: Experimental results compared with manufacturer's values

5.4.1. Determination of Cancellous Bone Analogue

From the specifications detailed in materials and methods, two materials, OPF and Duocel were selected for mechanical testing. From mechanical testing, the Duocel aluminium foam exhibits closer mechanical properties to cancellous bone than OPF. The reported compressive strength of cancellous bone is in the range of 3-10MPa. The Duocel foam has a compressive strength of 3.26 ±0.115MPa whereas the reported strength of OPF is 0.11MPa and 0.28MPa for 0.09g/cc and 0.12g/cc density foam respectively. The shear modulus of Duocel is considerably higher than the reported values for cancellous bone (62MPa compared with 3.4-4MPa for bone) but the shear strength is lower (2.1MPa compared to 4-6MPa). The standard deviations of the strength and modulus of the foams are low compared to cancellous bone, which makes results from mechanical testing more reproducible than if cancellous bone itself were used. This is important when validating finite element models with experimental methods.

In terms of handling and availability the aluminium foam is the preferred choice. The samples were supplied ready machined to any shape and are not limited in size for the envisioned applications. The lead time for the material is approximately a month. ERG supply materials ready machined due to damage that can occur to cells and loss in strength and modulus when machining. However, Ashby[22] recommends that damage can be minimised to metal foam by

cutting with a diamond saw as opposed to a bandsaw which gives a ragged surface and can reduce Young's modulus by 15%. The OPF was difficult to machine without damage to the foam occurring, but is more readily available (lead time was approximately one week) and cheaper. However the size was limited to the standard block size of 75x150x19mm. The OPF was only tested in shear due to this limitation in size. The values of shear modulus and shear strength for both densities were lower than the reported values for cancellous bone. The cost for a 75x150x20mm sample of 0.012g/cc dense OPF was €65. The equivalent cost of Duocel for the same sample size would be €18-44.

The range of cell size reported in the literature for cancellous bone is 1-5mm. The cell size for Duocel and OPF fall within this range. A larger cell size resulting in reduced relative density, such as that found in osteoporotic bone will exhibit reduced mechanical properties. Cell size will also affect the geometry and interlock of the cement-bone interface[23].

For metallic foams, if the specimen to cell size ratio is below seven, the compressive strength and modulus may be reduced. These size effects are the result of measuring the strength of the interconnected ligaments rather than the bulk material properties[22]. Andrews *et al* [24] examined the effect of specimen thickness on the shear strength of a closed cell aluminium foam. The size effects became negligible when the thickness was twice that of the cell size. Ashby[22] states that shear tests on long slender specimens bonded to two stiff plates and loading across the diagonal of the specimen (as in ASTM C273) can constrain the cell walls producing a stiffening effect. However, these boundary effects are negligible if the ratio of specimen to cell size ratio is greater than three. These conditions were maintained for OPF and Duocel.

Cancellous bone fails in a brittle manner. Figure 5.2 shows the different failure surfaces of the two foams. OPF exhibits brittle fracture; the cells maintain their original structure whereas the cells in Duocel foam undergo large plastic deformation in the direction of loading before fracture. Under compressive loading, plastic bending and buckling were found to be the dominant deformation mechanisms. This agrees with the study by Zhou [25] who examined the deformation mechanisms of open cell aluminium foam.

Based on the experimental study described above, Duocel aluminium foam was chosen as the cancellous bone analogue because the determined mechanical properties were closer to the range of values reported in literature. In addition, handling, cost and availability of size were superior.

5.5. µFE models of Duocel aluminium foam

5.5.1. Methods

CT images of one 25 x 25 x 25mm specimen of Duocel aluminium foam were obtained, with an isotropic spatial resolution of 50µm using a Scanco Medical scanner (Bassdof, Switzerland). Smooth surface meshes were created of the images using the method detailed in Chapter 4. Amira 4.0 (Mercury Systems, Berlin, Germany) was used to create the tetrahedral meshes. Threshold, mesh density and smoothing using Gaussian filters implemented in Amira were varied for each mesh. Three categories of smoothing were implemented in Amira during triangulation of the surface; none, constrained (voxel centres defined by segmentation are maintained) and unconstrained (voxel centers can be moved) as shown in Figure 5.7. Six values of threshold were used to create models with similar mesh densities. Constrained smoothing was used. A convergence test was performed to find the optimum mesh density. Each mesh was used to produce a linear elastic model with material properties for bulk aluminium. Apparent modulus was determined from the displacement due to a known applied load. Models were solved on a 2.41GHz machine with an AMD 250 Operon™ Processor with 8GB RAM running Microsoft Windows XP Professional 64Bit.

Figure 5.7 Variation of Gaussian smoothing filters on triangular surface

5.5.2. Results: Variation of Threshold

The compressive modulus of Duocel foam was determined from 5 specimens as 102 ±7.9 MPa as detailed in section 5.4. The volume fraction of the sample, determined by gravimetry, was 9.26%.

Due to the partial volume effect, a voxel may contain an aggregate grey level of both materials, particularly at boundaries of materials. One method of segmentation is to select the threshold at the midpoint of the grey levels for 'aluminium' and 'air'. The grey values for each material were determined in regions that definitely belonged to the material (i.e. the centre of the struts). By taking 10 measurements for each material over 4 slices, the determined grey values for aluminium and air were 65±3 and 1±1. The average midpoint grey value was determined as 33.

The deviation of volume fraction of the segmented volume, due to the selection of threshold is shown in Table 5.4.

Threshold	Volume fraction, %	Difference to true volume fraction, %
31	9.36	1
32	9.08	1.8
33	8.81	4.8

Table 5.4: Deviation of volume fraction due to selection of threshold

Meshes were created with similar mesh density for each threshold value. The calculated moduli as a function of threshold are shown in Figure 5.8.

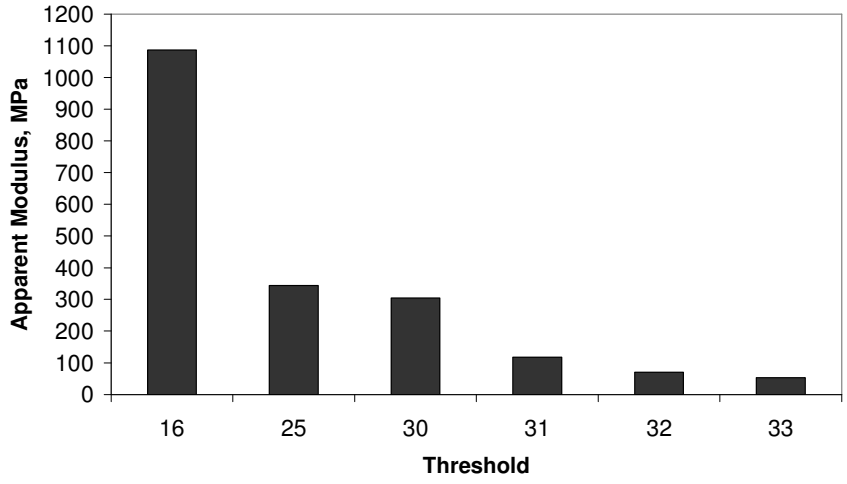

Figure 5.8: The reduction of modulus with threshold; the effect of changing the threshold is to change the thickness of the foam struts.

5.5.3. Results: Mesh Density

Surface simplification was used to vary mesh density. Mesh density was defined as the number of elements N_{ELM} divided by the number of voxels defining the segmented volume i.e. the volume fraction V_f multiplied by the number of voxels of the solid cubic volume, V_s ($MD = \frac{N_{ELM}}{V_f V_s}$). Threshold was constant. Figure 5.9 shows the convergence of modulus with mesh density.

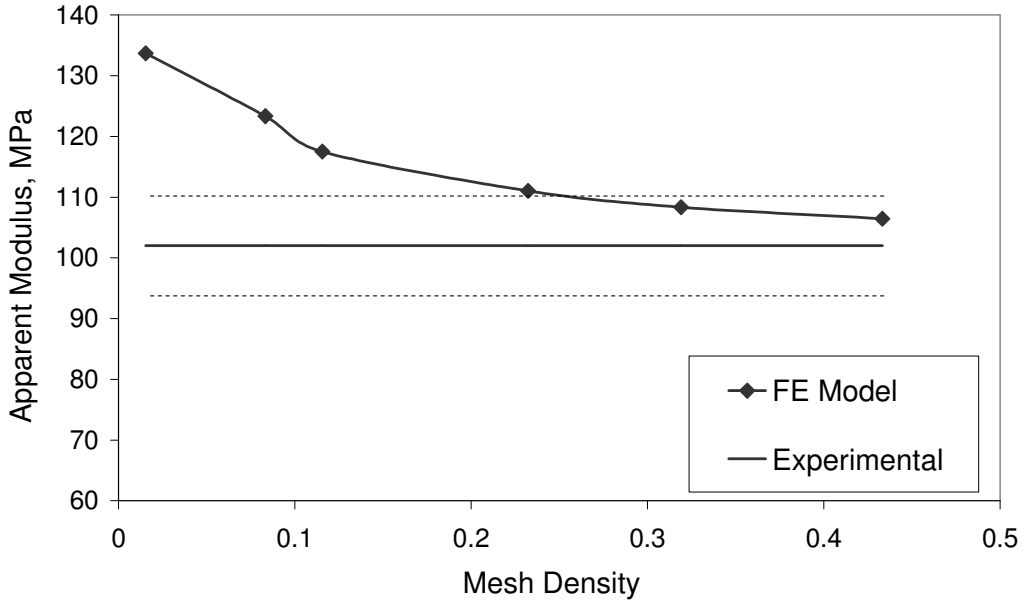

Figure 5.9: Convergence of modulus with mesh density to the experimentally determined modulus at a set threshold. Dotted lines indicate standard deviation.

5.5.4. Results: Smoothing

Triangulation of the surface resulted in a reduction of volume of material defined by segmentation of 0.93±0.00%, 11.06±0.01%, 17.8±0.020%, for no smoothing, constrained and unconstrained smoothing respectively. The results for modulus at a set threshold of 31were 400 MPa, 351 MPa and 98.9 MPa for no smoothing, constrained and unconstrained smoothing respectively. With smoothing, connectivity was reduced.

5.6. Discussion

Optimisation of mesh size, reduction of CPU time required for model solution and creation of smooth surfaces which better represent the true surface of the trabeculae are some of the benefits of smooth surface meshing of complex geometries such as cancellous bone. In this chapter, the effect of varying threshold value, mesh density and surface smoothing on the accuracy of mechanical properties determined using smooth surface tetrahedral meshing have been investigated. The apparent modulus was determined from an FE model and compared to the experimentally determined apparent modulus.

The volume of the surface produced is defined by selection of threshold. Hara [26] highlighted the importance of threshold for voxel-element meshes and showed that a 0.5% variation in threshold can lead to a 9% difference in stiffness. For selection of threshold, boundaries are

difficult to distinguish visually, due to the partial volume effect. Selecting the midpoint of grey value between two materials assumes that each voxel contains half of each phase. However, the mesh with this value does not give the closest approximation to the experimentally determined value. This is due to the loss of volume that occurs during mesh generation and highlights the need to correlate mesh volume to the volume of the sample although it may be difficult to achieve in some instances, such as with cancellous bone.

The use of smooth surface tetrahedral meshing allows optimisation of mesh density, greatly reducing the CPU time for model solution in comparison to voxel based models. CPU time for a model with optimum mesh density (for this sample) was approximately 700 seconds. Convergence to within 6% of the experimental value for modulus was seen at a mesh density of 0.4.

There are limitations to this study. Firstly, the mesh quality is not evaluated. Due to the complex geometry, distorted elements can be generated during triangulation of the structure. These can be manually corrected, but the magnitude of this resulting error has not been quantified. When a low mesh density is used, accuracy in thin struts may be compromised due to distorted elements. If an insufficient number of elements span a trabecula, stress concentrations due to the surface geometry can also occur as in Figure 5.10. Previous studies have shown that a minimum of four elements across each strut must be maintained for accuracy of local stresses. When examining the mesh with the optimum mesh density of 0.4, this is maintained.

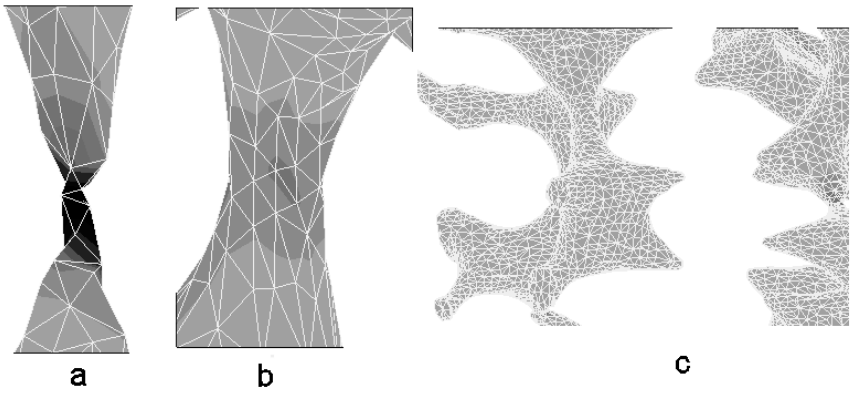

Figure 5.10: Accuracy of mesh; a. stress concentrations due to an insufficient number of elements (darker regions indicate higher stress), b. a well meshed strut c. loss of connectivity due to smoothing.

Secondly, the implementation of smoothing of the surface can lead to large losses in connectivity of the struts. This directly affects the local stresses but also has not been quantified. It may be beneficial to quantify geometric parameters other than volumetric parameters such as strut

thickness and connectivity. Lastly, the finite element model is limited to a linear elastic analysis with tetrahedral elements. Micro-plasticity in individual aluminium struts can occur well before the onset of bulk plastic yielding [25]. This again affects the accuracy of local stresses in the FE model.

This work has highlighted the importance of correlating volume of the created mesh to maintain accuracy when calculating global mechanical properties of a cancellous bone analogue. Threshold and mesh density must be optimised for accuracy. Smoothing should be controlled to maintain accuracy at the local level.

5.7. References

1. Carter, D.R. and W.C. Hayes, *The compressive behavior of bone as a two-phase porous structure.* The Journal of Bone and Joint Surgery, 1977. 59-A(7): p. 954-962.
2. Keaveny, T.M. and W.C. Hayes, *A 20-year perspective on the mechanical-properties of trabecular bone.* Journal of Biomechanical Engineering-Transactions of the ASME, 1993. 115(4): p. 534-542.
3. Stone, J.L., G.S. Beaupre, and W.C. Hayes, *Multiaxial strength characteristics of trabecular bone.* Journal of Biomechanics, 1983. 16(9): p. 743-&.
4. Harrigan, T.P., M. Jasty, R.W. Mann, and W.H. Harris, *Limitations of the continuum assumption in cancellous Bone.* Journal of Biomechanics, 1988. 21: p. 269.
5. Huiskes, R., R. Ruimerman, G.H. van Lenthe, and J.D. Janssen, *Effects of mechanical forces on maintenance and adaptation of form in trabecular bone.* Nature, 2000. 405(6787): p. 704-706.
6. Van Rietbergen, B., H. Weinans, R. Huiskes, and A. Odgaard, *A new method to determine trabecular bone elastic properties and loading using micromechanical finite-element models.* Journal of Biomechanics, 1995. 28(1): p. 69-81.
7. Pistoia, W., B. Van Rietbergen, E.M. Lochmuller, C.A. Lill, F. Eckstein, and P. Ruegsegger, *Estimation of distal radius failure load with micro-finite element analysis models based on three-dimensional peripheral quantitative computed tomography images.* Bone, 2002. 30(6): p. 842-848.
8. Niebur, G.L., M.J. Feldstein, J.C. Yuen, T.J. Chen, and T.M. Keaveny, *High-resolution finite element models with tissue strength asymmetry accurately predict failure of trabecular bone.* Journal of Biomechanics, 2000. 33(12): p. 1575-1583.
9. Alonso Vazquez, A., G.H. Van Lenthe, M. Taylor, and R. Muller. *Comparison of μCT measurements and FE predictions of localised failure in a cancellous bone analogue material*. in *6th International Symposium on Computer Methods in Biomechanics and Biomedical Engineering* 2004. Madrid: FIRST Numerics.
10. Muller, R., S.C. Gerber, and W.C. Hayes, *Micro-Compression: a novel technique for the nondestructive assessment of local bone failure.* Technology and Health Care 1998. 6: p. 433-444.
11. Ketcham, R. and W.D. Carlson, *Acquisition, optimization and interpretation of X-ray computed tomographic imagery: applications to the geosciences.* Computers & Geosciences, 2001. 27: p. 381-400.
12. Van Rietbergen, B., *Micro-FE analyses of bone: State of the art*, in *Noninvasive Assessment Of Trabecular Bone Architecture And The Competence Of Bone*, S. Majumdar and B. Bay, Editors. 2001, Kluwer Academic. p. 21-30.
13. Youssef, S., E. Maire, and R. Gaertner, *Finite element modelling of the actual structure of cellular materials determined by X-ray tomography.* Acta Materialia, 2005. 53: p. 719-730.
14. *ERG Materials and Aerospace Corporation: Data Sheet for Duocel Aluminium.* [cited 2005; Manufacturers data sheet]. Available from: http://www.ergaerospace.com/duocel_foam.htm.
15. Carter, D.R. and M.D. Spengler, *Mechanical properties and composition of cortical bone.* Clinical Orthopaedics and Related Research, 1978. 135: p. 192-217.
16. Keaveny, T.M., E.F. Morgan, G.L. Niebur, and O.C. Yeh, *Biomechanics of trabecular bone.* Annual Review Of Biomedical Engineering, 2001. 3: p. 307-333.
17. McCalden, R.W., J.A. McGeough, and C.M. Court-Brown, *Age-related changes in the compressive strength of cancellous bone. The Relative Importance of Changes in Density and Trabecular Architecture.* Journal of Bone And Joint Surgery-American Volume, 1997. 79(3): p. 421-427.
18. Morgan, E.F. and T.M. Keaveny, *Dependence of yield strain of human trabecular bone on anatomic site.* Journal of Biomechanics, 2001. 34(5): p. 569-577.

19. Lakes, R., *Viscoelastic properties of cortical bone*, in *Bone Mechanics Handbook*, S.C. Cowin, Editor. 2001, CRC Press. p. 11.1 -11.15.
20. Halawa, M., A. Lee, R. Ling, and S. Vangala, *The shear strength of trabecular bone from the femur, and some factors affecting the shear strength of the cement-bone interface.* Archives of Orthopaedic and Trauma Surgery, 1978. 92(1): p. 19-30.
21. *ERG Materials and Aerospace Corporation*. 2005 [cited 2005, 1/6/2005]; Available from: http://www.ergaerospace.com/.
22. Ashby, M.F., T. Evans, N.J. Fleck, L.J. Gibson, J.W. Hutchinson, and H.N.G. Wadley, *Metal foams; a design guide*. 2000: Butterworth Heinemann.
23. Krause, W., W. Krug, and J.E. Miller, *Strength of the cement-bone interface.* Clinical Orthopaedics, 1982. 163: p. 290-299.
24. Andrews, E.W., G. Gioux, P. Onck, and L.J. Gibson, *Size effects in ductile cellular solids. Part II: experimental results.* International Journal Of Mechanical Sciences, 2001. 43(3): p. 701-713.
25. Zhou, J., P. Shrotriya, and W.O. Soboyejo, *Mechanisms and mechanics of compressive deformation in open- cell Al foams.* Mechanics of Materials, 2004. 36(8): p. 781-797.
26. Hara, T., E. Tanck, J. Homminga, and R. Huiskes, *The influence of microcomputed tomography threshold variations on the assessment of structural and mechanical trabecular bone properties.* Bone, 2002. 31(1): p. 107-109.

Chapter 6. *Non-destructive Evaluation of the Integrity of the Cement-bone Interface*

The integrity of the cement-bone interface is related to features such as the degree of the interlock of the cement with bone and the strength and properties of cancellous bone. Previous studies have considered this interface at the continuum level, neglecting the effects of trabecular microstructure. The load transfer from cement to bone is poorly understood and as such, study at the microstructural level may provide an understanding of the factors governing initiation of loosening. Local stress concentrations may arise in the cement as a result of the discontinuous geometry of the cement-bone interface. Damage can initiate and propagate at various locations through the specimen and as such it is difficult to evaluate damage without sectioning of the sample. Non destructive testing offers a method to examine initiation and progression of failure without sectioning of the sample. In this chapter, two complimentary non destructive methods, acoustic emission (AE) and computed tomography (CT) have been used to monitor the initiation and progression of damage of an analogue cement-bone interface sample under four point bending. Early failure was detected, localised and characterised using AE. CT images of the sample before and after loading were used to visualise damage in 3D. Damage initiated in the cement at the interface between foam and composite formed by cement and foam. Damage was found to be related to stress raising microstructural features in the cement. These were caused by irregularities in the geometry of the bone analogue and recesses and notches formed by the flow of cement. This method was developed for validation of μFE models of the cement-bone interface.

Presented at the Annual congress of the International Society of Technology in Arthroplasty (ISTA), Paris, France, 4th-6th October 2007

6.1. Introduction

Traditionally, the cement-bone interface has been studied at the global level assuming that the bone acts as a continuum, neglecting microstructural effects. There are a number of factors that can affect the strength and longevity of the cement-bone interface such as cementing technique [1, 2] and quality of bone[3]. Macro-scale investigations of this interface have been unable to draw any definitive conclusions on its mechanical behaviour [4]. To gain meaningful insight into the behaviour of this interface and the factors involved, it would be useful to analyse it at the microstructural level.

Non-destructive monitoring techniques such as acoustic emission (AE) and computed tomography (CT) may be useful methods for evaluating the initiation and progression of failure at the microstructural level. Acoustic emission is a technique which has been previously used in orthopaedics for evaluation of the implanted hip prosthesis and its constituent parts at a global level [5]. When a material experiences abrupt changes in stress or strain, or damage occurs, transient elastic waves are generated by the rapid release of energy from a localised source, usually a defect in the material. This phenomenon is known as acoustic emission. The monitoring of these acoustic emissions allows a passive and real time method of locating and characterising damage within a material under load. The literature indicates that the nature of the AE signal can be correlated to failure processes [6, 7]. To date, this has either been postulated or based on the results of post-test analysis (e.g sectioning). Micro computed tomography (μCT) is a non destructive, three dimensional imaging technique. A series of radiographs of an object are taken at a number of angular projections. These images are reconstructed into a three dimensional volume using filtered back projection[8]. Studies have used μCT images (below 50μm) to evaluate the behaviour of cancellous bone[8], however μCT studies evaluating the micromechanics of the cement-bone interface are limited[9].

The present study examines the initiation and progression of failure of cement-bone analogue constructs subjected to four point bending. AE is used to provide time resolved and limited spatially resolved information on the damage processes while μCT provides high spatial resolution to enable visualisation of damage at the microstructural level. The combined use of these techniques enables verification of damage evolution, together with validation of the AE data obtained, during testing. Successful correlation of the AE data with observed failure mechanisms would be very useful for in situ monitoring of orthopaedic constructs using AE alone. In particular, μCT images of damage progression will be used in the present study to develop more accurate μFE models of the interface, allowing more in depth analysis of the behaviour of the interface.

6.2. Materials and Methods

6.2.1. Specimen Preparation

Mechanical testing using cancellous bone specimens can be quite problematic as the mechanical properties of cancellous bone can vary with species, site of acquisition, age, sex and preparation (the use of chemicals) and storage[10, 11]. In addition, damage to individual trabeculae as a result of machining may compromise the accuracy of mechanical testing for example by reducing apparent modulus[12]. Therefore, to avoid problems with specimen variability and the consequent effect on results, Duocel aluminium foam (ERG, Oakland California, USA) was chosen as a cancellous bone analogue (as characterised in Chapter 5).

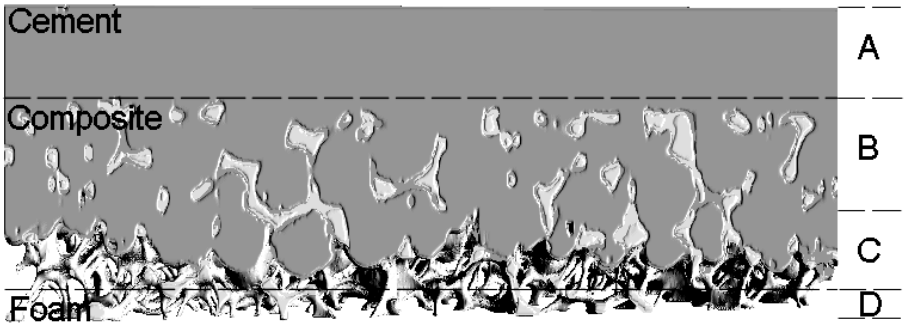

Figure 6.1: Cement-bone interface sample. A is the cement mantle, B is the composite region, C is the composite foam interface and D is aluminium foam.

Cement-aluminium foam specimens representing the cement-bone interface were manufactured. CMW1 (DePuy bone cement, CMW Ltd, Blackpool, UK) was vacuum mixed according to the manufacturer's instructions at a room temperature of 25°C. Six minutes after the initiation of mixing, the cement was applied to the top of the aluminium foam. A uniform pressure of 0.038MPa was applied across the top surface of a metal plate and the cement was compressed into the pores of the aluminium. This pressure was maintained across the top of the specimen until the cement had cured. This procedure was applied for all specimens manufactured in order to minimise specimen variability. The penetration of cement into the pores of the aluminium foam formed a composite, and the sample could be defined by two interfaces: the interface between the cement and between the composite and composite and aluminium foam. The depth of cement penetration was measured from CT scans after sample preparation according to parameters A-D (see Figure 6.1). Region A was the cement mantle, region B was a composite region of cement and foam, region C was cement, foam and air (from the minimum cement penetration to the maximum) and region D was aluminium foam. Samples were machined into eight four point bend specimens of dimensions 13x12x52mm with a cement mantle thickness of 2mm and foam thickness of 4mm. The foam struts were examined visually before and after

machining to ensure that no damage had occurred. Seven samples with an average cement penetration depth of 5mm were tested. Two other samples were manufactured with varying cement morphologies (penetration of ~2mm and no cement mantle) for FE modelling (see chapter 7) but due to time constraints were not tested.

6.2.2. Test Setup

Static four point bend testing was performed according to BS ISO 12108:2002. The neutral axis lay within the cement region so that the interface between foam and composite experienced tension. Shims were placed beneath the rollers to distribute the load across the aluminium in order to minimise local deformation of the aluminium. Load was applied incrementally using an Instron 8874 (Instron Ltd,High Wycomebe, UK) servohydraulic testing machine. Testing was suspended when AE characteristic of damage had occurred [5, 7, 13] and the specimen was µCT imaged to inspect for damage.

6.2.3. Acoustic Emission

AE sensors were used to monitor the sample as it was incrementally loaded. The reader is referred to Chapter 3 for more details on the set up of AE used.

6.2.4. Micro Computed Tomography

µCT images were collected (Benchtop CT 160Xi, Xtek, UK) prior to testing and at various points during testing, usually when AE had identified damage occurring via the Felicity effect. Initial scans of the whole sample had a resolution of 40µm. These scans were at a lower resolution than subsequent scans for ease of transfer of CT scans to FE models. Scanning of each sample after mechanical testing was undertaken at a resolution of 20µm to assess the integrity of the interface samples. Each slice of the scans were examined for damage after testing. Damage was visualised using Amira 4.0 visualisation software (Mercury Computer Systems Inc, Berlin, Germany).

The use of these complimentary techniques enabled detection of when and where damage occurred and the identification of AE parameters associated with particular types of damage via the correlation of CT and AE.

6.3. Results

The average cement mantle thickness was 3.6±0.86mm the average composite region thickness was 4.52±0.695, the average cement-foam interface thickness was 3.46±0.68mm and the average foam thickness was 1.84±0.97mm. The variation in dimensions of these regions for each sample is presented in Figure 6.2.

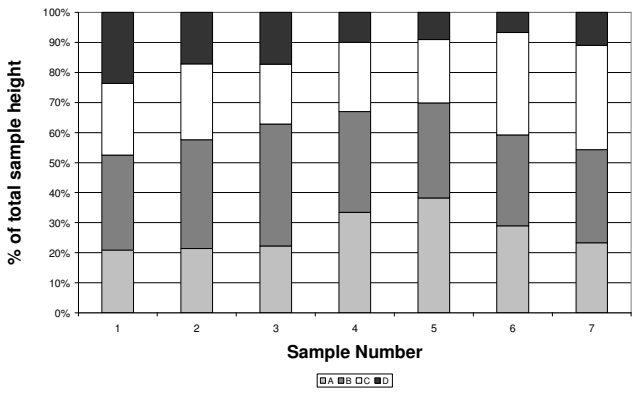

Figure 6.2: Percentage of regions of each of the cement-bone interface samples. A is the cement mantle, B is the composite region, C is the composite foam interface and D is the foam region.

Failure of the cement-bone interface under four point bending was defined by three stages:

- Buckling of the aluminium at the rollers and microcracking of the cement (damage not visible by CT) in the composite region.
- Failure of the composite region (cracking of the cement with crack lengths >0.5mm) but without cracking into the cement mantle. (as shown later in Figure 6.5)
- Progression of damage through the composite region. Cracking seen in the cement layer. Damage to aluminium struts in the path of the crack which were previously bridging the crack (see Figure 6.9).

The AE parameters associated with these stages of damage, correlated with CT images of the sample are summarised in Table 6.1. Microcracking is defined as damage smaller than the resolution that the CT scans could detect. This is defined by a minimum length of two voxels or 40µm.

Material	Amplitude, dB	Duration, µs	Energy, eu	Risetime, µs
Aluminium	60-100	800-1400	750-2000	70-130
Cement (crack initiation >0.5mm - 1mm)	75-95	1000-2000	500-2500	11-30
Cement (crack progression >1mm)	>60	100-500	400-500	10-40

Table 6.1: AE parameters associated with damage

6.3.1. Deformation of aluminium

As stated in the methods, shims were used to minimise the deformation of foam around the rollers. However, damage of the foam at the rollers still occurred before damage to the interface. Yield of aluminium was observed at a nominal stress of 6.31MPa and buckling of the foam (collapse of cells) at 7.58MPa. This was observed visually (Figure 6.3) and as a fluctuation in the position of the actuator (as a result of the control of the servo-hydraulic machine attempting to maintain a constant load). This process was captured by AE and enabled the characterisation of the foam failure. The buckling of the foam produced a high number of AE events indicative of permanent damage i.e. events with high amplitude, long durations and high energies (Table 6.1). However, it can be seen that the combination of risetime and duration is a promising method for isolating the three types of damage events. The high risetime is indicative of plastic deformation of the material; this allowed damage events associated with the aluminium foam to be distinguished from those of the cement.

The energy, duration and amplitude of AE events for the interfacial region exhibited two peaks with which time corresponded to damage events. This is illustrated for the amplitude in Figure 6.3. The first peak results from deformation of aluminium, the second peak corresponds to cement damage.

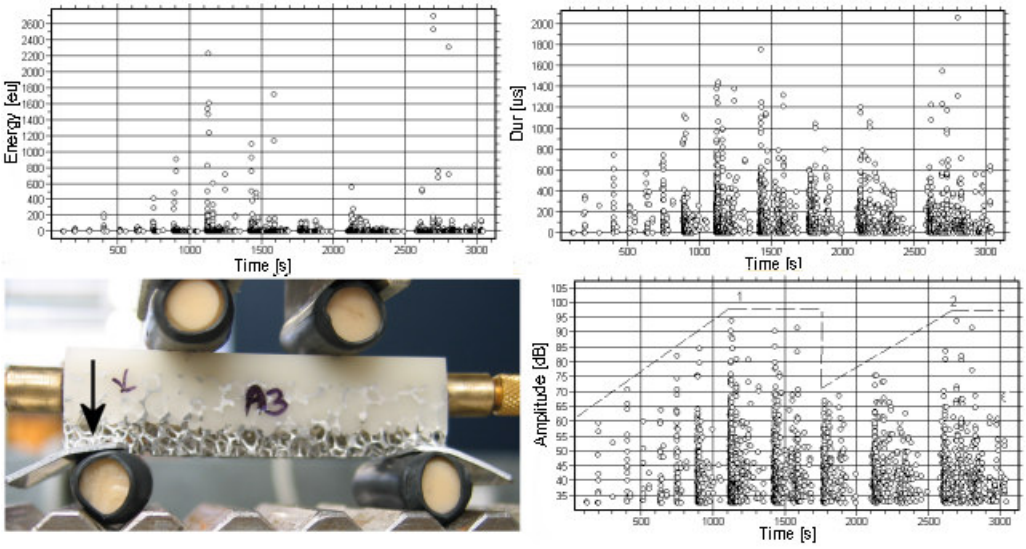

Figure 6.3: AE events; clockwise, energy, duration and amplitude resulting from four point bending of an interface sample. Bottom left shows damage of aluminium at the rollers, indicated by the arrow

6.3.2. Early indication of damage

Excellent correlation of damage location was observed for the AE signals and the μCT images. Damage was never seen in the CT images without corresponded located AE events. However, on some occasions, AE was detected without corresponding damage seen in the CT image. In the first instance this is most obviously attributable to the damage indicated by AE falling below the resolution of the CT imaging. An example of this is shown in Figure 6.4. This sample was loaded to an initial nominal stress of 6.94MPa, where some AE events were located but parameters representative of permanent damage were not seen i.e. the Felicity effect was not seen, amplitudes were low (below 70dB) and event energies and durations were low (of the order 10^2eu and below 1000μs respectively). Testing was suspended and the sample imaged with μCT, but no damage was visible in this sample. On further loading to a nominal stress of 8.21MPa, two events were located, one with an amplitude of 80dB and one with an amplitude of 45dB. The 80dB events had high rise times and duration, indicative of plastic deformation e.g. buckling and collapse of an aluminium strut. The events with amplitude of 45dB had much shorter rise times and medium duration, indicative of a more brittle event, possibly microcracking. No damage was found in the scan following this test. Testing was resumed and the sample was further loaded to a nominal stress of 10MPa where AE events indicative of damage were located in the same location. The Felicity ratio was high (approximately 0.89), maximum energies reached 4700 eu, durations reached up to 2000μs, maximum amplitude was 94dB. CT imaging of the sample revealed damage with lengths of the order of 0.5mm at the locations 26-29mm, 32mm, 36-39mm and 42.5-43.18mm from sensor 1 (see Figure 6.5). This correlated with the regions of located events in both the initial test (Figure 6.4) and subsequent test, thus showing early detection of failure below the threshold level of detection of the μCT imaging (~20μm) using AE. Located AE events without corresponding damage in the CT image were most often seen below a nominal stress of 7.5MPa with 2 to 3 hits at a given location. However, any located events with the characteristic parameters described in Table 6.1 were matched to damage in the CT image to within approximately ± 0.5mm.

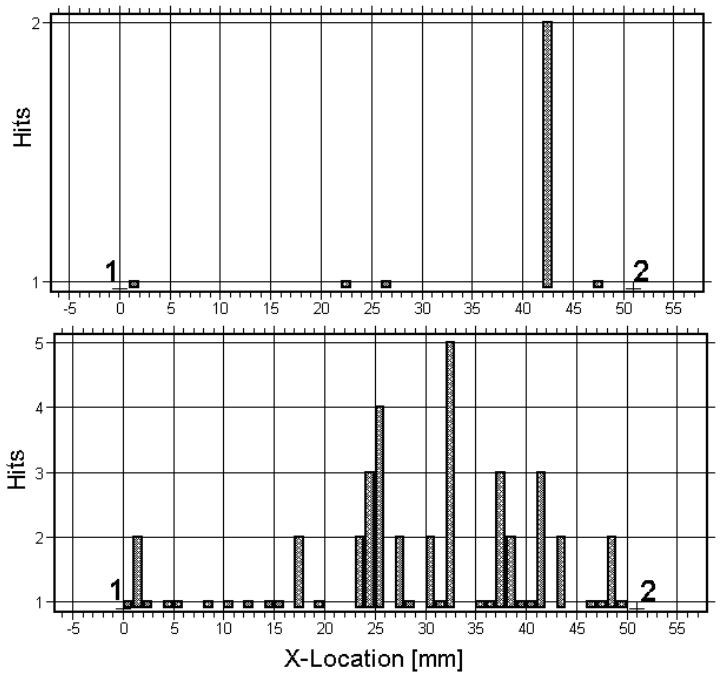

Figure 6.4: Early location of damage using AE: Left; after first loading to 6.94MPa where no damage was seen in CT images, Right; After loading sample to 10MPa, damage seen in CT images corresponding to locations on AE. The location of AE sensors is indicated by crosses marked 1 and 2 on the x-axis.

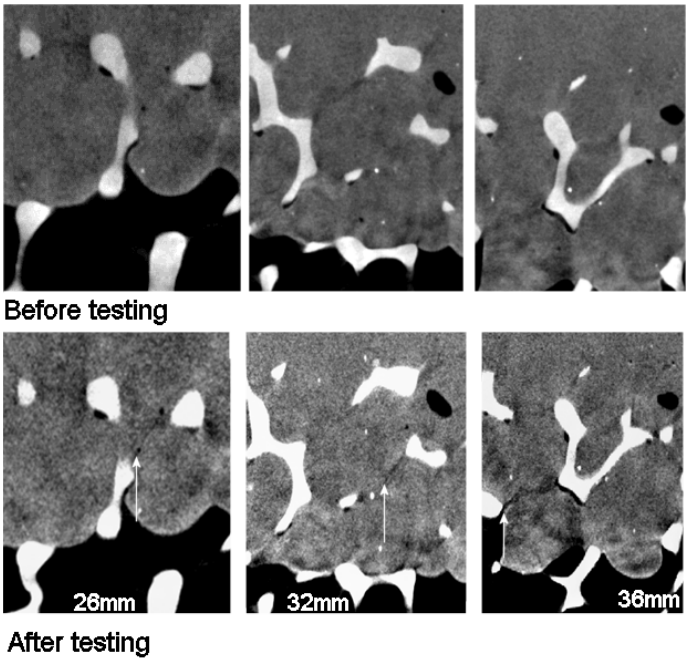

Figure 6.5: CT images of damage (of the magnitude 0.5mm) corresponding to located AE events, from the front face of the interface specimen. Damage is indicated by arrows with x-location from sensor one indicated.

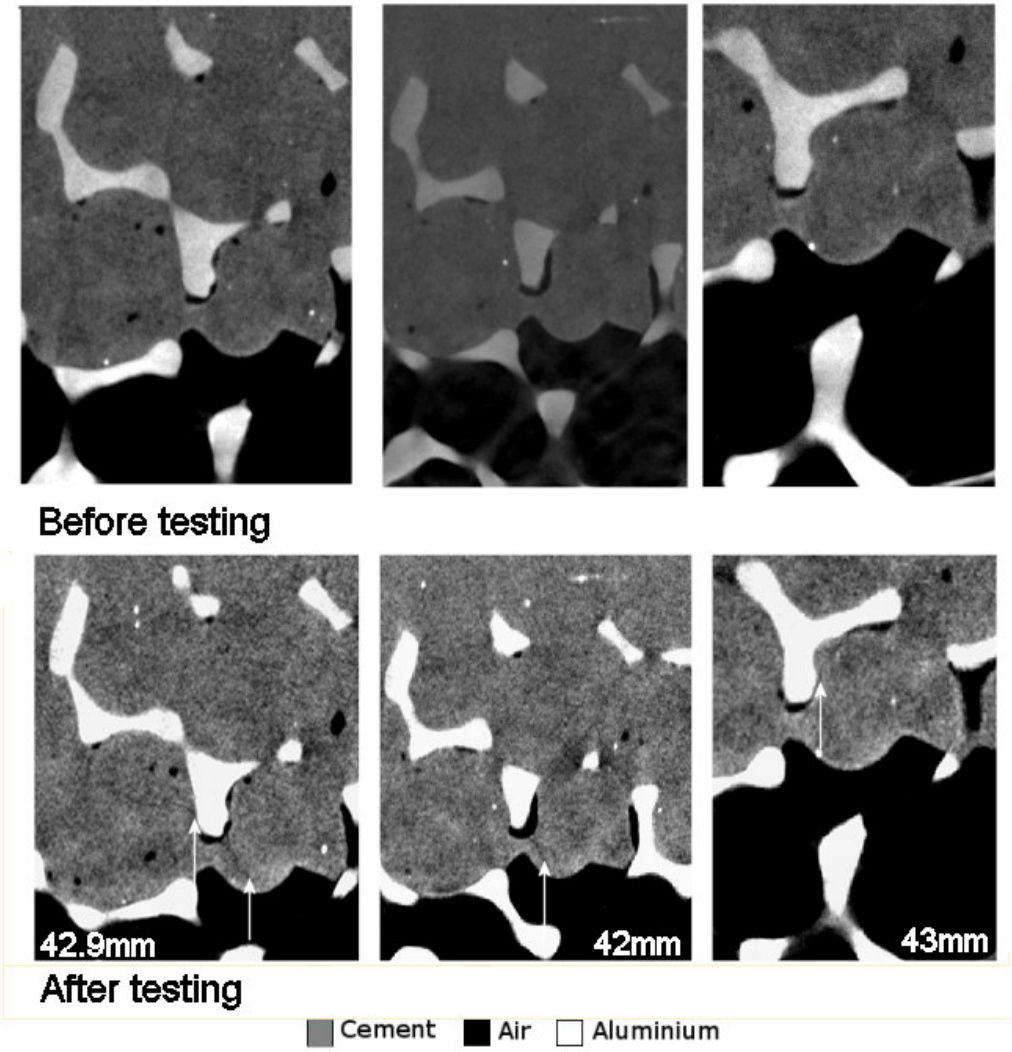

Figure 6.6 Continued.

The damage from the CT images shown in Figure 6.5 corresponded to the located events indicated by the AE in Figure 6.4. The located damage near sensors 1 and 2 (at locations 0 and 50mm) correlated with damage to the aluminium foam near the rollers. These events could be differented from cement damage by their longer risetimes.

6.3.3. Damage in composite region

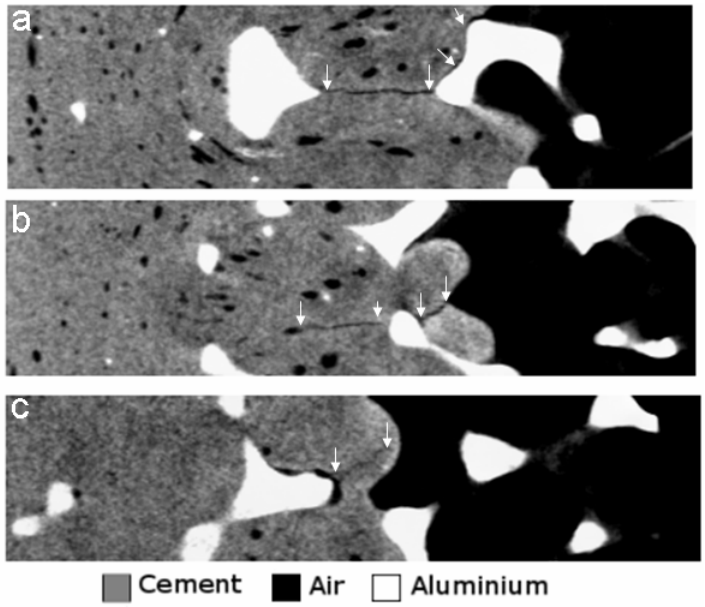

Figure 6.6: Examples of damage resulting from stress raisers (arrowed); from top to bottom a. aluminium geometric irregularities, b. notch as result of cement flow, c. recess as a result of cement flow.

Initiation of failure of the cement-foam specimens occurred at a nominal stress of 7.58MPa. Stress raisers such as geometric irregularities in the aluminium foam, notches and recesses formed as a result of cement flow into the foam were found to influence the initiation site of failure (Figure 6.6). Due to the orientation of the specimen with respect to the loading direction, initiation of failure always occurred at the aluminium composite interface. Failure did not initiate in the cement mantle. As the crack propagates through the composite region, the damage path deviates around the aluminium struts, as a result of the higher strength of the aluminium and interfacial weakness.

6.3.4. Characterisation of damage using acoustic emissions

Energy versus duration plots of the AE signals can give an indication as to the extent of the damage within the specimen. An example of this is shown in Figure 6.7. The test shown was stopped at different stages and examined for damage. At a nominal stress of 5.05MPa, with only low energy ($<10^2$eu) and duration (<1000µs) acoustic events detected, no damage to the cement was discernable in the CT scans. As loading continued to 13.3MPa and events with energies above 10^3eu and durations above 2000µs were recorded, damage was seen within the composite region in the form of cracks 0.6mm-5mm in length. With additional loading to 20.2MPa, energies reached 10^4eu and durations of 4000µs. These values were representative of critical damage progression into the cement mantle before final failure of the specimen.

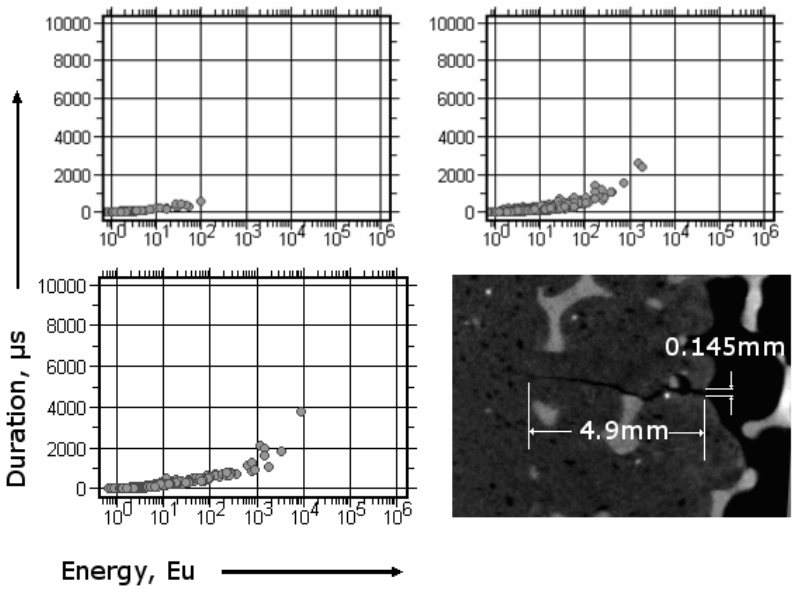

Figure 6.7: The energy and duration of AE events of the interface specimen at different stages of failure: from top left clockwise; no damage observed, initiation of damage in composite region and progression of damage into the cement mantle before ultimate failure.

6.3.5. Damage Propogation into the Cement Mantle

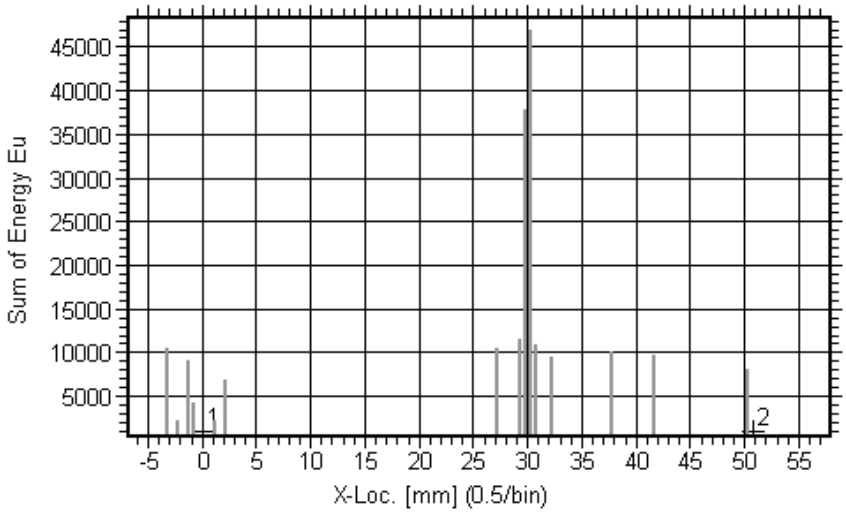

Figure 6.8: Location of damage of sample with sum of energy of events with amplitude above 60dB. Damage in sample is seen at 27 - 32mm.

The damage located by AE as indicated in Figure 6.8 correlates to the damage visualised in Figure 6.9. The damage located near sensor 1 and sensor 2 corresponded to damage to the aluminium foam in the rollers.

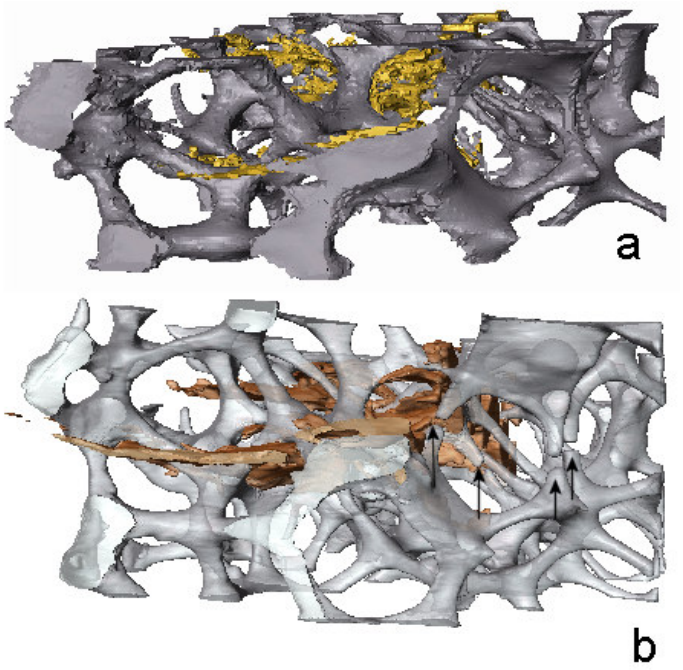

Figure 6.9: 3D visualisation of damage in interface specimen. Cement has been removed for clarity, cement layer would be present on right hand side. a. Cement damage across the composite indicated in yellow b. Aluminium strut damage as crack progresses into cement mantle indicated by arrows.

On further loading, damage that had initiated in the composite region progressed into the cement mantle. This was exhibited in one sample which was loaded four times with a maximum nominal stress of 20MPa. Evidence of crack bridging was seen in the CT images. When the specimen was loaded to 20MPa, a crack developed across the composite region (Figure 6.9a) without damage to the aluminium struts in its path. On further loading (to 14.5MPa), damage progressed into the cement region and damage to the aluminium struts in the crack path was seen (Figure 6.1b).

The Felicity effect was seen in all damaged specimens. A lower Felicity ratio (the load which acoustic activity is detected compared to the previously applied maximum load) was indicative of more damage.

6.4. Discussion

Damage of representative cement-bone interface specimens under four point bending has been characterised and visualised using non-destructive techniques. Previous studies examining the behaviour of the cement-bone interface have assumed that bone acts as a continuum i.e. has a generalised behaviour over a representative length (for cancellous bone typically 3-5 trabeculae[14]). These studies have characterised the strength of the cement-bone interface using a singular measure such as fracture toughness or shear strength and indicated factors which may

influence the reported strength such as degree of cement penetration[15, 16]. However, many of these studies have neglected to include microstructural detail such as the location of microdamage and whether initiation of damage was in cement or bone. Some studies have implied the need for closer examination of the interface; for example, Miller *et al* [1] characterised the failure of the cement-bone interface by seven categories: failure due to debonding, at the composite-bone interface, failure through the composite region, failure in bone, failure in the cement-bone composite interface and failure in the cement mantle. Microstructural details such as cement gaps (where the cement was not apposed to the bone surface) were also identified. Race *et al*[17] characterised microstructural failure in further detail by microscopic analysis of sectioned cadaveric femurs subjected to aggressive fatigue loading. However, identification of damage was limited to the sectioned regions. The monitoring and visualisation techniques employed in this study allowed regions of damage to be identified in real time and subsequent imaging to be focused on regions of suspected damage. Acoustic emission was able to locate the region of damage, and when it occurs, which could then be imaged with high resolution CT. In future, this method could eliminate the need for scanning large regions of the sample where damage is probably not present.

Excellent correlation of located AE events to the regions of damage was seen from the µCT images to within an estimated of ±0.5mm. The excellent time resolution of AE allowed monitoring of the propagation of damage as it occured. The minimum resolution of CT images used in this study (20µm) was sufficient to show damage of approximately 40-50µm. Previous studies have shown that AE is capable of detecting damage as small as 25µm[18]. Taylor *et al*[13] examined damage in CFRP using AE. They identified particular signals and suggested that for events of around 46dB, there was microcracking present in the epoxy polymer matrix. In this study, AE events representative of damage (above 60dB) were recorded before damage was discernable by CT imaging which may be evidence of microcracking in the cement. Further loading of the interface sample showed development of visible damage in the located regions. Since AE is a continuous monitoring system, testing does not need to be suspended to examine damage. This highlights an advantage over using CT images, where the removal of load may cause crack closure, which cannot be visually detected on the CT images.

Located visible damage (approximately 50µm) in size exhibited amplitudes of up to 70dB, energies of 10^3eu and durations of 2000µs. Critical damage, e.g. cracks traversing the specimen across the composite layer and into the cement mantle, with crack lengths of the order of 1-5mm were associated with event amplitudes up to 90dB, energies up to 10^4 and durations up to 4500µs. This is similar to the energy and duration values reported for CMW-1 specimens undergoing fatigue reported by Jeffers *et al* [6]. However the magnitude of signals associated with damage to aluminium and cement were similar and therefore, other parameters, specifically

the risetime of the signal is required to distinguish damage of cement from damage of aluminium.

The majority of damage occurred in the composite region, although some damage was seen to progress into the cement layer under higher stresses. Damage always initiated at the interface between aluminium and composite due to the loading configuration employed. Damage initiated in regions of high stress generated by irregularities in the aluminium geometry, recesses in the cement and notches formed by the cement flow into the aluminium pores (see Figure 6.6). Typically damage occurred as a result of a combination of the effects of these stress raisers. No microcracks were associated with pores within the cement mantle. This is consistent with the findings of Race *et al*[17] where microcracks were found to be preferentially associated with the cement-bone interface and only a small portion related to voids.

A number of limitations were associated with the experimental set up employed in this study. Shear loading is more common than tensile loading of the cement-bone interface. Shear loading was not employed in this study due to the difficulty in characterising failure due to the rapid rupture of cells in shear loading. Although shear is the predominant load state across the cement-bone interface *in vivo*, tensile loading does occur at the shoulder of the prosthesis. Cantilever bending is a recognised failure mode of the prosthesis[19] and is a result of medial migration of the proximal part of the stem due to failure of the stem-cement or cement-bone interface with maintained good fixation of the distal end in the cement.

The damage process may differ *in vivo* as the cement flow (degree of penetration of cement) may be hindered by bleeding pressure and may affect apposition of the cement to the bone surface[1]. Clinically, cement shrinkage may occur, leaving cement gaps which may change the failure process of the interface [20]. In addition, it has been shown *in vitro* that pre-heating of the stem can change the direction of cement shrinkage[21]. To manufacture the analogue specimens the cement was injected onto the aluminium foam and pressure was maintained until cure of the cement. This method reduces the amount of cement shrinkage that would occur clinically.

Damage in the composite region propagated around the aluminium struts and as a result, the damage traversed in different directions. This may be a limitation of the work, since only two AE sensors could be used given the size of sample required to ensure good resolution of the μCT images. The use of further sensors on larger samples would have enabled more confidence in the detection of damage progression in three dimensions. This would also limit the effects of signal attenuation via the highly attenuating cement media.

Finite element analysis is a useful tool for parametric multifactorial analysis and may be implemented to examine the microstructural behaviour of the interface. However, to allow for accurate simulation, FE analysis requires appropriate input data, as well as details of failure

behaviour of the interface for accurate modelling of the interface. Using the complimentary techniques presented here, the behaviour of the interface and the regions of damage could be located and matched to validate FE studies.

6.5. Conclusions

This study has shown in a cement-bone analogue interface in bending, that damage initiates at stress concentrations formed by irregularities in the aluminium geometry and in recesses and notches formed by flow of cement into the aluminium. Pores in the cement mantle were not associated with any visible damage.

This study has demonstrated the ability of AE to provide early indication of failure. Initiation and progression of damage through cement and foam has been isolated and characterised by analysing the associated AE parameters.

The method presented in this chapter allows 3D location and visualisation of damage within a cement-bone interface analogue specimen. As the samples were imaged before and after testing, it provides ideal data for creation and validation of an FE model for further examination of the cement-bone interface behaviour.

6.6. References

1. Miller, M., A. Race, S. Gupta, P. Higham, M. Clarke, and K. Mann, *The role of cement viscocity on cement-bone apposition and strength.* The Journal of Arthroplasty, 2007. **22**(1): p. 109-116.
2. Oates, K.M., D.L. Barrera, W.N. Tucker, C.C.H. Chau, W.D. Bugbee, and F.R. Convery, *In vivo effect of pressurisation of polymethylmethacrylate bone-cement.* The Journal of Arthroplasty, 1995. **10**(3): p. 373-381.
3. Graham, J., M. Ries, and L. Pruitt, *Effect of bone porosity on the mechanical integrity of the bone-cement interface.* Journal of Bone and Joint Surgery-American Volume, 2003. **85A**(10): p. 1901-1908.
4. MacDonald, W., E. Swarts, and R. Beaver, *Penetration and shear strength of cement-bone interfaces in vivo.* Clinical Orthopaedics, 1993. **286**: p. 283-288.
5. Browne, M., A. Roques, and A. Taylor, *The acoustic emission technique in orthopaedics - a review.* Journal of Strain Analysis for Engineering Design, 2005. **40**(1): p. 59-79.
6. Jeffers, J., M. Browne, and M. Taylor, *Damage accumulation, fatigue and creep behaviour of vacuum mixed bone cement.* Journal of Biomaterials, 2005. **26**: p. 5532-5541.
7. Roques, A., M. Browne, J. Thompson, C. Rowland, and A. Taylor, *Investigation of fatigue crack growth in acrylic bone cement using the acoustic emission technique.* Biomaterials, 2004. **25**(5): p. 769-778.
8. Van Rietbergen, B., *Micro-FE analyses of bone: State of the art*, in *Noninvasive Assessment of trabecular bone architecture and the competence of bone*, S. Majumdar and B. Bay, Editors. 2001, Kluwer Academic. p. 21-30.
9. Mann, K.A. and N. Verdonschot. *Stress localization at the cement-bone interface; a mechanistic micro-FEA approach*. in *52nd Annual Meeting of the Orthopaedic Research Society*. 2006. Chicago.
10. Evans, F.G., *Mechanical Properties of Bone*. American Lecture Series. 1973: Thomas Books.
11. Yeh, O. and T. Keaveny, *Biomechanical effects of intraspecimen variations in trabecular architecture: a three-dimensional finite element study.* Bone, 1999. **25**(2): p. 223-228.
12. Van Rietbergen, B., H. Weinans, R. Huiskes, and A. Odgaard, *A new method to determine trabecular bone elastic properties and loading using micromechanical finite-element models.* Journal of Biomechanics, 1995. **28**(1): p. 69-81.
13. Taylor, A., S. Gross, C. Rowland, and P. Gregson. *Monitoring failure mechanisms in CFRP orthapaedic imaplants during fatigue testing*. in *24th European Conference on Acoustic Emission Testing, EWGAE*. 2000. Paris, France.
14. Harrigan, T.P., M. Jasty, R.W. Mann, and W.H. Harris, *Limitations of the continuum assumption in cancellous Bone.* Journal of Biomechanics, 1988. **21**: p. 269.
15. Graham, J., M. Ries, and L. Pruitt. *Cement penetration depth significantly affects fracture toughness at the trabecular bone/cement Interface*. in *27th Annual Meeting of the Society for Biomaterials*. 2001. Saint Paul, MN.
16. Ramaniraka, N.A., L.R. Rakoomanana, and P.F. Leyvraz, *Effects of stem stiffness, cement thickness and roughness of the cement-bone surface.* The Journal of Bone and Joint Surgery (Br), 2000. **82-B**(2): p. 297-303.
17. Race, A., M.A. Miller, D.C. Ayers, and K.A. Mann, *Early cement damage around a femoral stem is concentrated at the cement/bone interface.* Journal of Biomechanics, 2003. **36**(4): p. 489-496.
18. Rajachar, R., D. Chow, C. Curtis, N. Weissman, and D. Kohn, *Use of acoustic emission to characterize focal and diffuse microdamage in bone*, in *Acoustic Emissions: Standards and Technology Update*, S. Vahaviolos, Editor. 1999, American Society for Testing and Materials, West Conshohocken, Pennsylvania. p. 3-19.

19. Gruen, T.A., G.M. McNeice, and H.C. Amstutz, *Modes of failure of cemented stem-type femoral components - radiographic analysis of loosening*. Clinical Orthopaedics and Related Research, 1979(141): p. 17-27.
20. Race, A., A. Miller, M.T. Clarke, and K.A. Mann, *Cement-implant interface gaps explain the poor results of CMW3 for femoral stem fixation.* Acta Orhopaedica, 2005. **76**(5): p. 679-687.
21. Bishop, N.E., S. Ferguson, and S. Tepic, *Porosity reduction in bone cement at the cement-stem interface.* Journal of Bone and Joint Surgery - British Volume, 1996. **78-B**: p. 349.

Chapter 7. *Finite Element Modelling of a Cement-Bone Interface Analogue*

Modelling of the cement-bone interface has been largely limited to evaluation at the continuum level, meaning that the stress distribution across the interface is smoothed. Due to the complex geometry of cancellous bone and the interlock of cement and bone, local stresses may be sufficiently high to initiate damage and subsequent failure of the interface. Very little information exists on the factors that affect interface stability such as the optimum cement mantle thickness and interdigitation. While it is difficult to determine these factors experimentally, μFE analysis presents a viable alternative to achieve this end. In this study, smooth surface meshing techniques have been applied to create μFE models of the specimens tested in Chapter 6. Linear elastic models of the specimen were created and subjected to loading conditions representative of four point bending. The model shows that there are localised high stresses in the composite formed by cement and bone consistent with the regions of damage seen experimentally. In addition, models of varying cement penetration were created to examine the change in load transfer as a function of interdigitation depth.

Presented at the 54th Annual Meeting of the Orthopaedic Research Society, 2008, San Francisco, California

7.1. Introduction

The behaviour at the microstructural level of the cement-bone interface is not well understood [1-4]. In Chapter 4, a theoretical cellular model was proposed to examine the effect of differing depths of cement penetration on the stiffness of the interface. However, this model was limited because its generic repeated structure and rectangular beams did not accurately represent the smooth adapted structure of cancellous bone at the local level. In FE models, the cement-bone interface is often assumed to be a continuum therefore the stress distribution across the interface is smoothed. By including the microstructural detail, local stress concentrations may be resolved which may indicate regions where failure may occur.

Examination of the microstructural behaviour of the cement-bone interface using µFE methods has been limited. Mann and Verdonschot[5] created a µFE model of a small 3x3x3.5mm section of the cement-bone interface from a cemented femur construct. The study showed that loading of the interface resulted in localisation of stress/strain above fatigue limits, particularly in the cement regions. Although the results were consistent to experimental observations reported by Kim *et al*[6], there was no direct comparison to experimental data to validate the models.

In this chapter, smooth surface µFE models of the cement-bone analogue specimens described in Chapter 6 are presented. The objective of the work was to develop µFE element models of the cement-bone analogue samples tested in Chapter 6 to examine the load transfer at the microstructural level. To begin with, a convergence test on a section of the sample was performed to determine the optimum mesh density. Following this, a linear elastic model of a greater volume of the specimen was developed in order to determine the load transfer across the interface and to attempt to correlate regions of high stress and strain with the regions of failure of the sample determined in Chapter 6. Two further models were created with different cement penetration depths to examine the effect of interdigitation on load transfer. Due to the complexity of the geometry of the cement-bone analogue sample, the peak or average stresses may not give a correct indication of the integrity or failure region of the interface model. Critical peak stresses can occur at singularities in the stress field. In addition, high peak stresses may be dissipated by localised cement failure (such as damage formation/ creep) so that critical damage may occur in other regions[7]. Therefore, in addition to the average stresses and contour plots of the stress distribution in the µFE interface models, the volumes of cement over certain thresholds (the yield stress of cement and aluminium foam) is also reported. This methodology also facilitates a comparison of the load transfer in models with different cement interdigitation depths. Finally, an elasto-plastic analysis was performed to examine the change in load transfer across the interface as a result of plastic damage.

7.2. Materials and methods

7.2.1. Convergence test

To determine the optimum mesh density for modelling of the cement-bone interface, a mesh convergence test was performed on a section of an analogue sample. A volume measuring 11.7x 12.3 x 1.2mm was segmented from a 40μm resolution CT image of the sample before testing. The volume was segmented using region growing techniques implemented in Amira 4.0 software (Mercury Systems). In the experimental tests detailed in Chapter 6, damage was not seen around pores in the cement layer region of the interface samples. Therefore, pores in the cement layer were not included in the mesh to reduce the size of the resulting model. Recesses in the cement (in the composite region) as a result of cement flow into the aluminium were included. It was shown in Chapter 5 that the resulting segmented volume of the foam has implications on the accuracy of results. Therefore, the segmented volume of the aluminium foam was matched to the manufacturers[8] reported value of volume fraction (10%) (by changing the threshold of segmentation) before generation of the triangular surface. The list of nodes and elements generated by Amira was transferred to an input file for MSC Marc using the code detailed in Appendix II. Six tetrahedral meshes of varying densities were created for convergence testing. Mesh density was calculated using the same method detailed in Section 5.3.5. Elastic moduli of 70GPa and 2GPa were used for aluminium and cement respectively. A Poisson's ratio of 0.3 was used for both aluminium and cement. The cement elements were fully bonded to the aluminium elements where they were in contact. The free ends of the aluminium foam, parallel to the top of the cement layer were constrained in all directions. An arbitrary displacement of 2mm was applied to the top most nodes of the cement layer. The resultant force of the nodes was calculated for each mesh. In addition to the resulting force, the stress distribution across the interface was examined. The sample was divided into three regions; the cement, composite and foam. The composite region was defined as any region where both cement and foam elements were present and is illustrated in Figure 7.1 (regions B and C). The average element location was calculated from the average location of the nodes and sorted into each region using the code detailed in Appendix II. The von Mises stress distribution was then calculated using the subroutine also detailed in Appendix II.

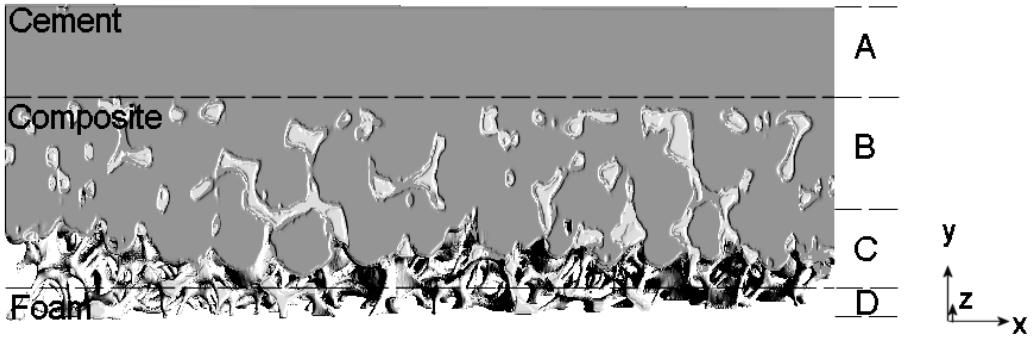

Figure 7.1: The three regions of the cement-bone interface analogue; cement, interdigitated region forming a composite and foam

7.2.2. Whole Model of Interface Analogue Specimen

A μFE model of a sample tested in Chapter 6 was created from a 40μm CT image taken before experimental testing of the sample. The region of interest, between the outer rollers, was segmented using region growing methods. This sample (henceforth referred to as sample 1) had a cement layer thickness of 4.41mm (A in Figure 7.1), a minimum interdigitation depth into the foam of 4.41mm (B) and maximum (B+C) of 7.46mm and a foam region (D) of 1.31mm. Threshold segmentation could not be performed due to the similar grey values of the cement and foam so instead, the volume was segmented using two dimensional region growing techniques implemented in Amira. A tetrahedral mesh was created using the advancing front method implemented in Amira (see Chapter 3). Two million was the maximum number of elements that could be read into Msc MARC on an 8GB RAM machine running Microsoft Windows 64Bit. The cement was fully bonded to the aluminium foam. The segmented volume fraction of foam was correlated to the manufacturer's value of 10%. The material properties were the same as for the convergence models. The nodes at the location of the lower rollers were constrained in the y direction. The nodes along the base of the right hand side were also constrained in the x direction and an additional node was constrained in the z direction. A pressure of 1MPa was applied to the nodes in the location of the top rollers. In the experiments in Chapter 6, damage was seen in the interface sample at this load. A linear elastic analysis was performed in MSC Marc to evaluate the load transfer across the interface. The stress distribution of the interface samples was examined using the same method described in section 7.2.1.

7.2.3. Variation in Cement Penetration Depth

Two samples with differing cement interdigitation depths to the sample tested were manufactured with the same technique detailed in Chapter 6. These samples were not tested experimentally due to time constraints. The differing cement interdigitation depths are detailed in Table 7.1. Using the same method detailed in Section 7.2.2, μFE models of the specimens

were created. The mesh densities, calculated using the definition introduced in Section 5.3.5, of the models are shown in Table 7.1. Contour plots of von Mises stress and the stress distribution were obtained. The percentage of volume in each region above the yield stress of cement (25MPa)[9] and the yield stress of aluminium alloy 6106-T6 (193MPa)[10] was also determined.

Sample	Cement Layer thickness, A (mm)	Minimum Interdigitation, B (mm)	Maximum Interdigitation, B+C (mm)	Foam only, D (mm)	Mesh Density
1	4.407	4.429	7.461	1.317	0.0343
2	4.335	2.2167	4.620	4.826	0.0253
3	0	9.2434	10.715	5.3988	0.0213

Table 7.1: Dimensions of Cement-Bone Analogue Samples

7.2.4. Plastic behaviour

When sample 1 was tested in four point bending, a large region of deformation of the foam was seen at the rollers. This damage to the foam may change the load transfer at the interface particularly local stresses and strains. In order to simulate this deformation and examine the change in load transfer across the interface, an elasto-plastic non linear analysis was performed on sample 1. Both aluminium and cement were assumed to be elastic-perfectly plastic. The mesh detailed in Section 7.2.2 was used. Aluminium and cement were assumed to be fully bonded. The stress distribution and plastic strain were obtained.

7.3. Results

7.3.1. Convergence test

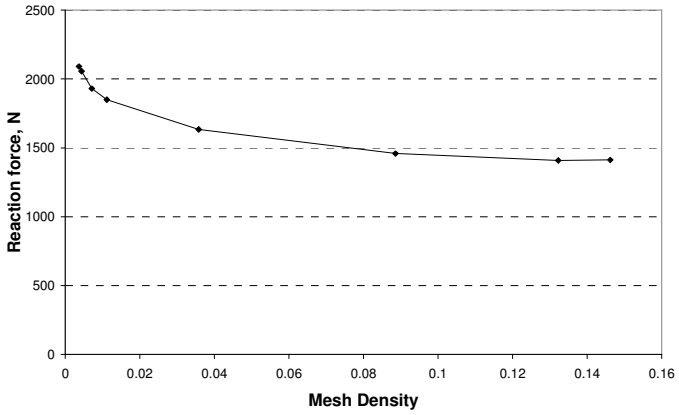

Figure 7.2: Convergence test for μFE model of the cement-bone interface analogue

The convergence of reaction force with mesh density is shown in Figure 7.2. Convergence of the resultant force to within 4 % of 1408N occurred at a mesh density of 0.08. The whole

models had a mesh density of 0.02 to 0.03. At a mesh density of 0.03 the resultant force is within 16% of the converged resultant force of 1408N.

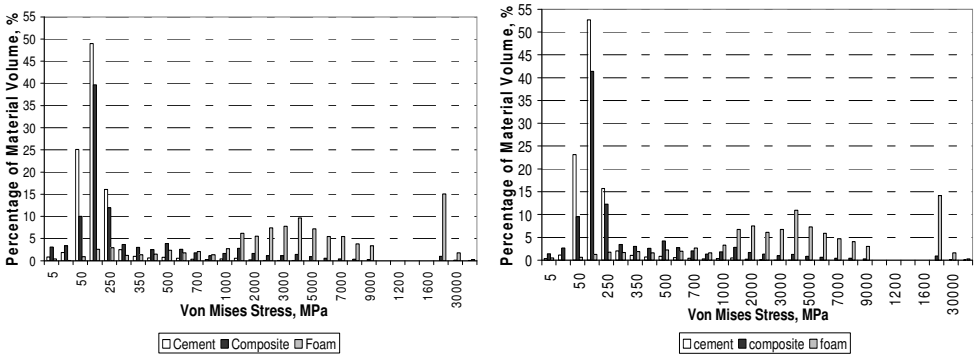

Figure 7.3: Distribution of Von Mises stress for model with mesh density 0.15 and 0.09

Figure 7.3 shows the distribution of von Mises stresses for two mesh densities 0.09 and 0.15. Both mesh densities exhibit similar stress distribution patterns. The majority of volume of cement is stressed lower than the aluminium foam. The composite region spans both. The stresses are very high as the area of applied stress was small and the applied displacement was arbitary.

7.3.2. Results for Whole Model of the Interface Analogue Specimen

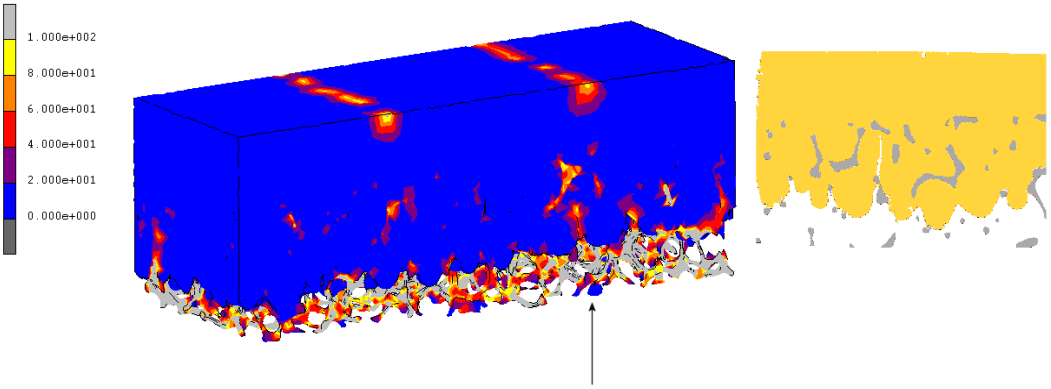

Figure 7.4: Von Mises stress for whole model of interface specimen (Left). Arrow indicates the location where failure occurred experimentally. Crack in specimen from experimental tests (Right)

There are regions of high local stress in the composite region where notches are formed as a result of the flow of the cement and at the boundary between cement and aluminium. This is consistent with the locations of damage seen in the CT images of the samples. Figure 7.4 shows (as indicated by the arrow) the region where a crack initiated and propagated when tested experimentally. There are also regions in the cement layer above the yield stress of cement in the location of the rollers. The stress distribution is shown in Section 7.3.3.

7.3.3. Models with variation in cement depth

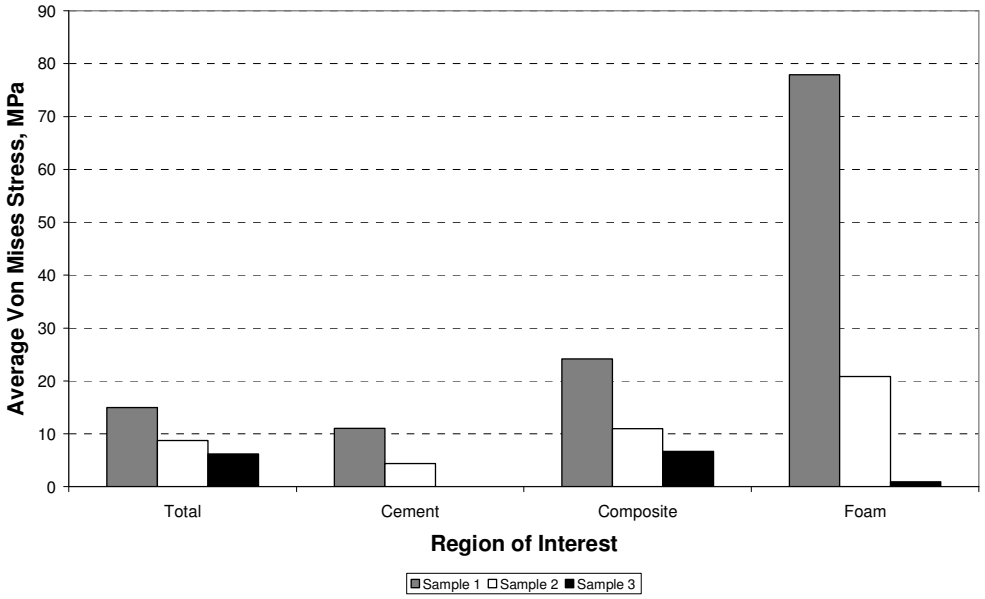

Figure 7.5: Variation in average von Mises stress of differing cement depths for the different regions of the samples.

The average von Mises stresses for models with differing amounts of cement interdigitation are shown in Figure 7.5. The average stresses are lowest for the model without a cement layer (sample 3).

The contour plots in Figure 7.6 shows that the load transfer across the interfaces varies for different interdigitation depths. Sample 1 shows regions of high stress at the asperities of cement, formed by the flow of the cement into the foam, at the interface between aluminium foam and the composite region. There are no high stress concentrations in the cement layer apart from at the nodes simulating the location of the rollers. Sample 2, which has less cement penetration than sample 1, has regions of high stress in the aluminium foam at the interface between foam and composite and also at asperities of cement at the foam-composite interface. Sample 3, which does not have a cement layer, shows a poorer load transfer to the aluminium foam beneath the interface. Stress concentrations are seen in the composite region at the boundaries between cement and aluminium foam.

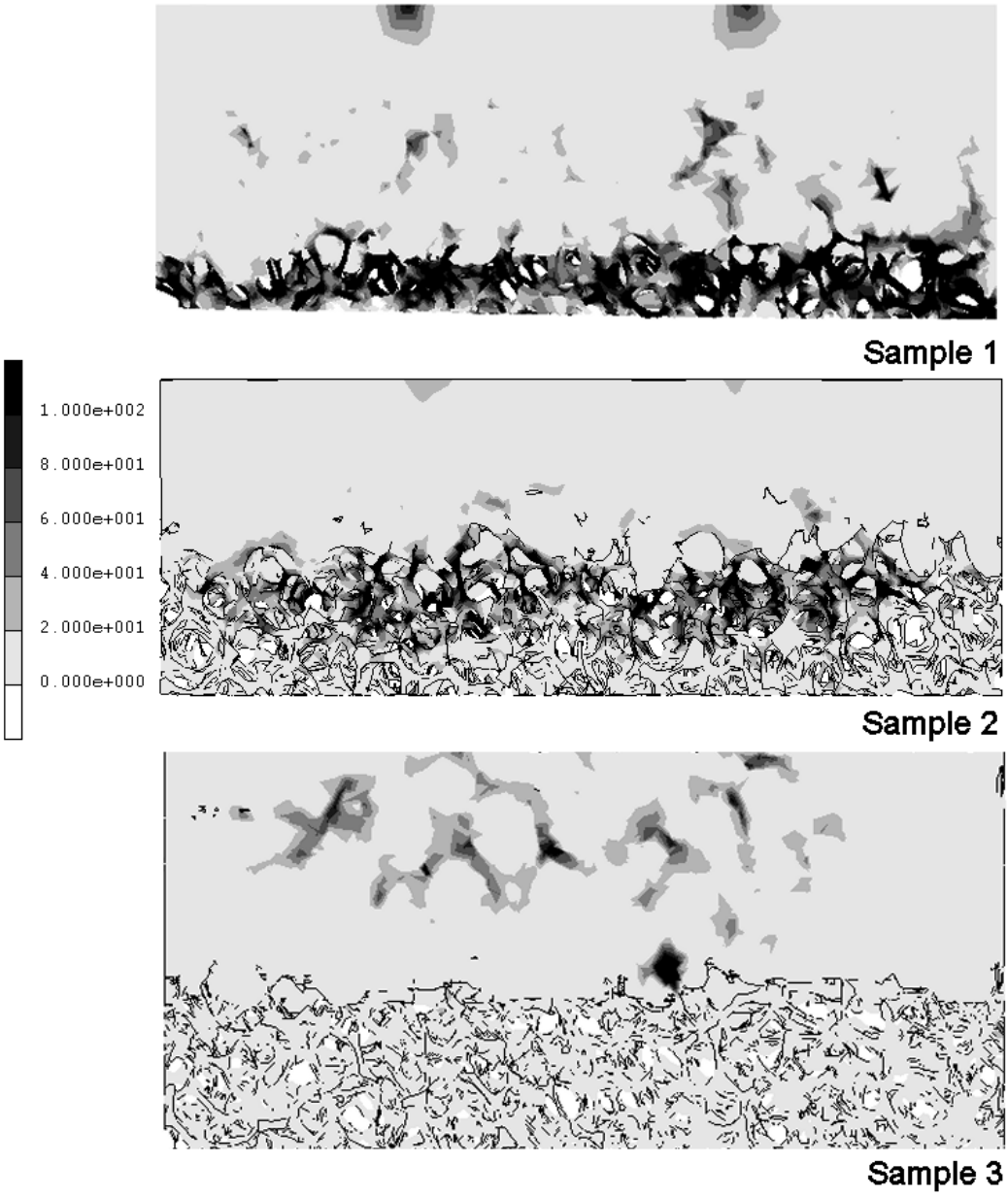

Figure 7.6: Contour plot of von Mises stress for samples with varying degrees of cement penetration

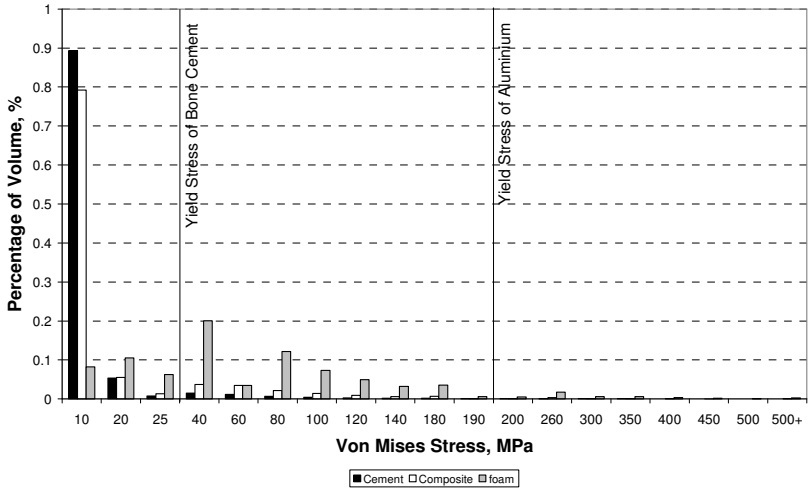

Figure 7.7: Distribution of von Mises stress for μFE model with maximum cement interdigitation of 7.4mm (Sample 1).

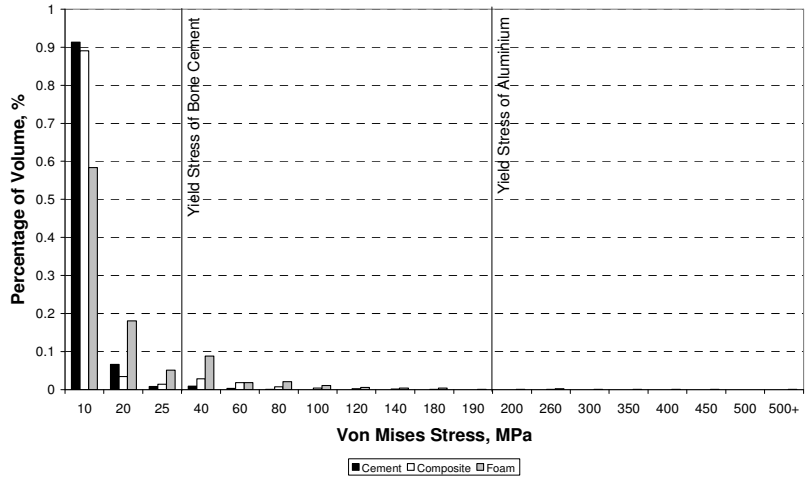

Figure 7.8: Distribution of von Mises stress for μFE model with maximum cement interdigitation of 4.6mm (sample 2).

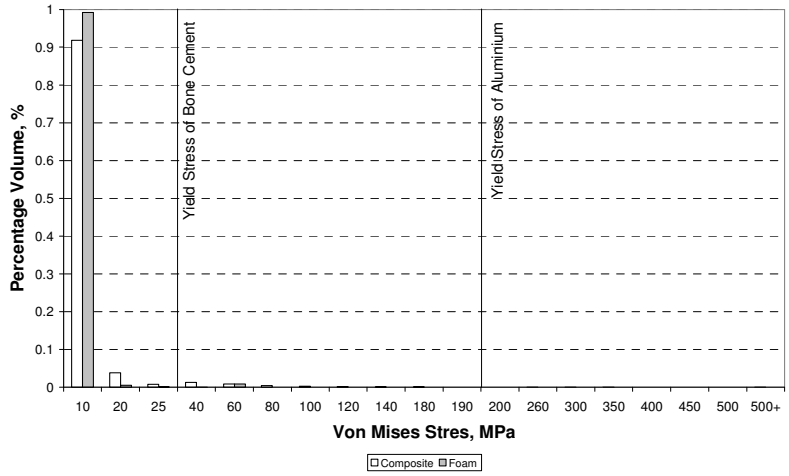

Figure 7.9: Distribution of von Mises stress for μFE model with no cement layer and maximum cement interdigitation of 10.7mm (sample 3)

The volume of cement, composite and foam, at a given stress in the range 0-500MPa according to regions is shown in Figure 7.7 to Figure 7.9. The yield stress of cement and aluminium are indicated on the Figures. The models with cement interdigitation have a similar stress distribution (Figure 7.7 and Figure 7.8). The majority of the cement layer is below the yield stress of cement. For sample 1, a higher percentage of the composite region is above the yield stress of cement (see Table 7.2). The model with the greatest volume above the yield stress of cement and aluminium is sample 1(Figure 7.7). The contour plot of the model without a cement layer shows that the load is transferred to the aluminium foam within the composite; forming local stress concentrations in the cement. However, the percentage of volume above the yield stress of cement is very low compared to the models that included a cement layer. The percentage of volume above the yield stress of cement and bone for each region is shown in Table 7.2.

Sample Number	Percentage of cement volume above 25MPa, %	Percentage of composite volume above 25MPa, %	Percentage of composite volume above yield stress of 190MPa, %	Percentage of aluminium volume above 190MPa, %
1	4.544	13.902	0.913	4.268
2	1.265	7.565	0.075	0.413
3	NA	3.528	0.001	0.173
1 (Elasto-plastic)	3.230	4.116	1.345	0.270

Table 7.2: Percentage volumes above the yield stresses of cement (25MPa) and aluminium foam (190MPa)

7.3.4. Elasto-Plastic Analysis of the Cement-Bone Analogue

Figure 7.10: Contour plot of von Mises stress for elasto-plastic analysis

The von Mises stress distribution for the elasto-plastic analysis differs from the linear elastic analysis as shown in Figure 7.6. Stress concentrations above the yield strain of cement are present in the composite region at the boundaries between cement and foam and also in the cement layer where the load is applied. There are less stress concentrations in the composite

region at the boundary between cement and aluminium and lower stresses in the aluminium foam. However, stress concentrations remain in the location where the specimen failed. Plastic deformation occurred in the foam in the region where the nodes were constrained i.e the black regions of foam in Figure 7.10.

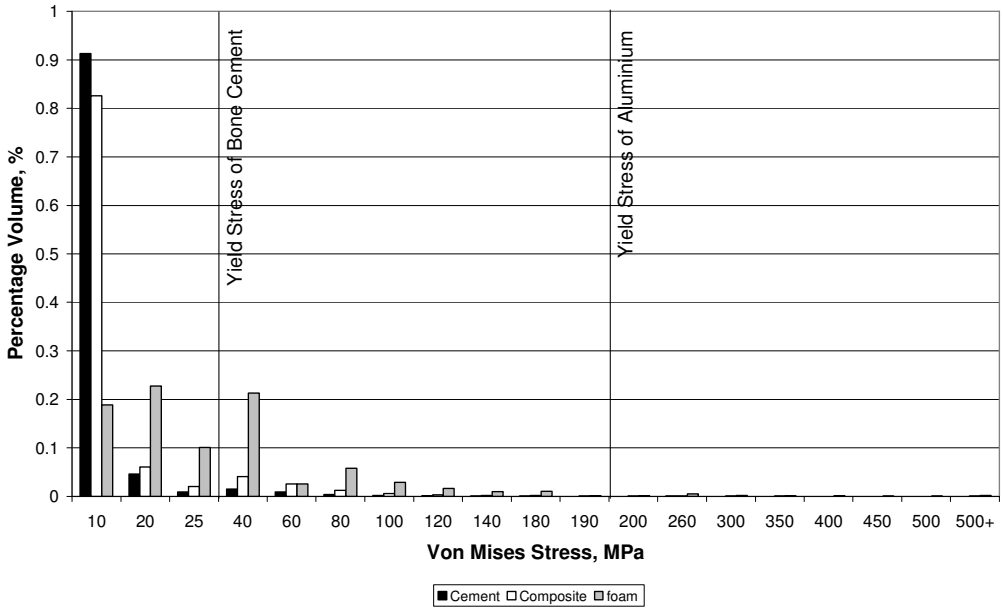

Figure 7.11 Von Mises stress distribution for elasto-plastic analysis of a cement-bone analogue sample

The stress distribution of the regions for the elastic plastic model is shown in Figure 7.11. The distribution of stresses for this model differs from the linear elastic model with the same mesh (Figure 7.7). The percentage of volume above the respective material yield limits are listed in Table 7.2.

7.4. Discussion

The optimum mesh density for convergence of the resultant force within 4% of the converged force was 0.08 but this mesh density would have required 4.2 million elements for the whole specimen. For the models of the whole specimens, the maximum number of elements was limited to two million. Therefore the accuracy of the whole models was also limited by the achievable mesh density of 0.02-0.03.

Tetrahedral smooth surface meshes of the interface samples were created in order to determine whether a linear elastic model was able to predict the region of failure. The linear elastic μFE model of the whole specimen showed regions of high stress in the composite region, at the recesses of the cement caused by cement flow into the cells of the foam. The percentage of the composite volume above the yield stress of cement was higher than the percentage of the cement

region suggesting that failure would occur in the composite region. This is consistent with the location of microcracks seen experimentally[4]. At the location where the specimen failed, there was a region of high stress as a result of a notch in the cement formed by the flow of cement into the aluminium. However, there were also regions of peak stress in the composite where failure was not seen. The regions of peak stress occurred in the cement layer in the region where load was applied and in the composite region at the boundary between aluminium and cement. This is not consistent with the experimental data where there was no sign of cracking in the cement layer and at the interface between foam and composite. Damage mechanisms were not included in the analysis. The damage of foam, such as bending and buckling of the struts and cell collapse may change the local stress transfer at the foam-composite interface. Damage accumulation and creep of the cement were also not modelled. High localised stress may be dissipated by localised cement failure such as microcracking or creep[4, 6]. As a result, stresses will be distributed away from high stress regions and critical damage may occur in a different location to that of the peak stress predicted by the linear elastic model. The boundary conditions at the interface between the cement and bone are not well understood[5]. As there is no adhesive bond between cement and bone, sliding of the materials can occur at the cement-bone interface. Histological examination of the cement-bone interface has also shown that a small gap can often occur between cement and bone as a result of cement shrinkage[11, 12]. Therefore, modelling the materials as deformable contact bodies with friction may give a more accurate model of the local behaviour. However an alternative experimental approach such as digital image correlation[2], which can examine the local displacements of the material under load, is required to validate the boundary conditions.

For the elasto-plastic analysis, the percentage of volume above the yield stress of cement was lower in the cement region and higher in the composite region when compared to the linear elastic model. The percentage of volume above the yield stress of aluminium is 0.27% for the composite and 4.116% for the aluminium which is lower than the linear elastic model. This suggests that the plastic deformation of the foam dissipates the stress in the aluminium foam. Although stress concentrations were present in the composite region at the location of failure, they were also present in the location of the simulated rollers. This suggests that further non linear behaviour should be modelled to predict the location of behaviour.

Most studies show that increased cement interdigitation results in a stronger cement-bone interface[12-14]. However other studies have shown that interface stresses increase with increasing cement penetration[15]. Clinically, large volumes of cement can cause thermal necrosis of the bone. This is a concern particularly for resurfacing implants[16] as the damage to the bone may contribute to femoral neck fractures. Good success rates have been documented for total hip prosthesis with thin or no cement mantles[17]. Studies examining the strength of the cement-bone

interface have reported penetration depths of 1-6mm. Reported cement mantle thicknesses vary between 0 and 6mm. In this study, cement layers of 4.3-4.7mm were used with maximum interdigitation values of 4 to 7mm. These values were towards the higher end of reported values so that acoustic emission sensors could be placed on the surface of the analogue samples during testing. This study has shown that as higher stresses were associated with greater depths of cement penetration in the models with a cement layer. Stress or strain of the right magnitude will stimulate remodelling of the bone leading to cement bone apposition at the cement-composite interface[3, 18]. If the stresses are too high, an intervening fibrous tissue layer will form between the bone and cement[19]. Sample 1 has twice the cement interdigitation depth of sample 2 and exhibits a higher percentage of volume of cement and aluminium above their respective yield limits. This may be due to the stiffening of the composite resulting in a diminished capability for even transfer of the load. From the contour plots (Figure 7.6), sample 2 shows a greater load transfer to the aluminium foam directly beneath the cement and to composite region, reducing the stresses in the cement layer. This suggests that there is an optimum cement interdigitation depth for the load transfer from cement to bone.

The thickness of the cement mantle is thought to influence the stability of the implant[20-23]. Thin cement mantles have shown a good success rate[24] although the difference in load transfer across the cement are not well understood. One theory suggests that "canal-filling" systems result in more areas of thin and deficient cement but is supported by stronger cortical bone[25]. This is demonstrated using FE analysis where a canal filling stem supported by cancellous bone exhibited increased crack formation compared to the same stem with cortical bone support[26]. With the thin cementing technique, cancellous bone is sometimes retained and there exists an interlock between cement and bone[27]. This situation is modelled in sample 3 to examine the microstructural load transfer across the cement-bone interface. The percentage of volume above the yield stress of aluminium was very low compared to the models with a cement layer. This suggests that failure is likely to occur in the cement in the composite region. The majority of the volume is below the yield stress of cement. This is opposed to studies that show thin cement mantles exhibit higher strains[22, 23, 28]. The canal filling prosthesis relies on an interference fit to transfer load to the cortex. The model was limited as it did not include residual stresses resulting from the fit of the prosthesis or contact conditions between the stem, cement and bone. In addition, the volume of cancellous bone is high compared to the available cancellous bone after reaming. The addition of these factors may change the pattern of load transfer however, this requires further investigation.

The role of porosity in cement with regard to loosening, such as whether damage initiates at pores, stops damage or does neither, is not fully understood. Ling *et al* [29] argued that porosity in the cement mantle is irrelevant as there is no strong clinical evidence that supports the theory

that fatigue failure initiates in pores in the cement mantle. Porosity in the cement layer was not included in the present model of the cement-bone interface because no evidence of damage was seen around pores in the cement layers in the experimental tests. In addition, neglecting porosity in the cement layer, the size of the mesh of the model was reduced.

The limitations to this study include the use of a bone analogue material. The aluminium foam has a higher modulus than bone and does not exhibit anisotropy. Mann and Verdonschot[5] showed that a reduced bone modulus reduced the percentage of cement volume over the fatigue limits of cement and bone at the cement-bone interface. This study was also limited to static loading conditions and did not simulate any remodelling of the bone or damage accumulation in the cement.

7.5. Conclusions

For the first time, a μFE model representative of the cement-bone interface microstucture with validation with non destructive evaluation techniques has been developed. This has allowed investigation into the load transfer across the interface in order to determine regions of high stress and possible locations of damage and the influence of cement penetration depth on load transfer.

This study has shown that a smooth surface tetrahedral μFE model of the cement-bone interface model exhibits local stress concentrations in the composite region of the cement-bone interface consistent with the location of damage of the specimens loaded experimentally. However, further work comparing experimental data to μFE models is required to determine the appropriate boundary conditions.

This study has also shown that the load transfer across the interface varies with the cement penetration depth. For an interdigitation depth of 2-4mm, the load is transferred across the composite region and to the aluminium foam layer. When this interdigitation is doubled, the foam in the composite layer is stiffened resulting in stress concentrations in the regions where the foam is constrained. The cement layer stresses are also reduced for the 2-4mm interdigitated region. When the cement mantle is removed, the percentage of volume below the yield stresses of respective materials is greatly reduced. Correlation of these findings to experimental data is required.

7.6. References

1. Maher, S.A. and B.A.O. McCormack, *Quantification of interdigitation at bone cement/cancellous bone interfaces in cemented femoral reconstructions.* Proceedings of the Institution of Mechanical Engineers Part H- Journal of Engineering in Medicine, 1999. **213**(H4): p. 347-354.
2. Mann, K., M. Miller, R. Cleary, D. Janssen, and N. Verdonschot, *Experimental micromechanics of the cement-bone interface.* Journal of Orthopaedic Research, 2008. ***In Press***.
3. Miller, M., A. Race, S. Gupta, P. Higham, M. Clarke, and K. Mann, *The role of cement viscocity on cement-bone apposition and strength.* The Journal of Arthroplasty, 2007. **22**(1): p. 109-116.
4. Race, A., M.A. Miller, D.C. Ayers, and K.A. Mann, *Early cement damage around a femoral stem is concentrated at the cement/bone interface.* Journal of Biomechanics, 2003. **36**(4): p. 489-496.
5. Mann, K.A. and N. Verdonschot. *Stress localization at the cement-bone interface; a mechanistic micro-FEA approach*. in *52nd Annual Meeting of the Orthopaedic Research Society*. 2006. Chicago.
6. Kim, D., M.A. Miller, and K.A. Mann, *Creep dominates tensile fatigue damage of the cement-bone interface.* Journal Of Orthopaedic Research, 2004. **22**(3): p. 633-640.
7. Lennon, A.B. and P.J. Prendergast, *Evaluation of cement stresses in finite element analyses of cemented orthopaedic implants.* Journal of Biomechanical Engineering-Transactions of the ASME, 2001. **123**(6): p. 623-628.
8. *ERG Materials and Aerospace Corporation: Data Sheet for Duocel Aluminium.* [cited 2005; Manufacturers data sheet]. Available from: http://www.ergaerospace.com/duocel_foam.htm.
9. Lewis, G., *Properties of acrylic bone cement: State of the art review.* Journal of Biomedical Materials Research, 1997. **38**(2): p. 155-182.
10. *Matweb: Material Property Data*. 2007 [cited 2007 4/3/2007]; Available from: www.matweb.com.
11. Race, A., A. Miller, D.C. Ayers, R.J. Cleary, and K.A. Mann, *The influence of surface roughness on stem-cement gaps.* The Journal of Bone and Joint Surgery (Br), 2002. **84-B**(8): p. 1199-1204.
12. Oates, K.M., D.L. Barrera, W.N. Tucker, C.C.H. Chau, W.D. Bugbee, and F.R. Convery, *In vivo effect of pressurisation of polymethylmethacrylate bone-cement.* The Journal of Arthroplasty, 1995. **10**(3): p. 373-381.
13. Askew, M.J., J.W. Steege, J.L. Lewis, J.R. Ranieri, and R.L. Wixson, *Effect of cement pressure and bone strength on polymethylmethacrylate fixation.* Journal of Orthopaedic Research, 1984. **1**(4): p. 412-20.
14. Mann, K.A., D.C. Ayers, F.W. Werner, R.J. Nicoletta, and M.D. Fortino, *Tensile strength of the cement-bone interface depends on the amount of bone interdigitated with PMMA cement.* Journal of Biomechanics, 1997. **30**(4): p. 339-346.
15. Jansson, V., B. Heimkes, and M. Zimmer, *Stress transfer at the femoral bone/bone cement interface as a function of the cement thickness.* Archives of Orthopaedic and Trauma Surgery, 1993. **122**(2): p. 65-68.
16. Little, J., H. Gray, D. Murray, D. Beard, and H. Gill, *Thermal effects of cement mantle thickness for hip resurfacing.* Journal of Arthroplasty, 2008. **23**(3): p. 454-458.
17. Langlais, F., M. Kerboull, L. Sedel, and R.S.M. Ling, *The 'French paradox'.* Journal of Bone and Joint Surgery-British Volume, 2003. **85B**(1): p. 17-20.
18. Huiskes, R., H. Weinans, and B. Van Rietbergen, *The relationship between stress shielding and bone resorption around total hip stems and the effects of flexible materials.* Clinical Orthopaedics and Related Research, 1992. **274**: p. 124-134.

19. Radin, E., C.T. Rubin, E.L. Thrasher, L.E. Lanyon, A.M. Crugnola, A.S. Schiller, I.L. Paul, and R.M. Rose, *Changes in the bone-cement interface after total hip replacement.* The Journal of Bone and Joint Surgery, 1982: p. 1188-1200.
20. Ebramzadeh, E., A. Sarmiento, H.A. McKellop, A. Llinas, and W. Gogan, *The cement mantle in total hip-arthroplasty analysis of long-term radiographic results* Journal of Bone and Joint Surgery-American Volume, 1994. **76A**(1): p. 77-87.
21. Kawate, K., W.J. Maloney, C.R. Bragdon, S.A. Biggs, M. Jasty, and W.H. Harris, *Importance of a thin cement mantle - Autopsy studies of eight hips.* Clinical Orthopaedics and Related Research, 1998(355): p. 70-76.
22. Fisher, D., A. Tsang, N. Paydar, S. Milionis, and C. Turner, *Cement-mantle thickness affects cement strains in total hip replacement.* Journal of Biomechanics, 1997. **11-12**: p. 1173-1177.
23. Ramaniraka, N.A., L.R. Rakoomanana, and P.F. Leyvraz, *Effects of stem stiffness, cement thickness and roughness of the cement-bone surface.* The Journal of Bone and Joint Surgery (Br), 2000. **82-B**(2): p. 297-303.
24. Skinner, J., S. Todo, M. Taylor, J. Wang, V. Pinskerova, and G. Scott, *Should the cement mantle around the femoral component be thick or thin?* The Journal of Bone and Joint Surgery (Br), 2003. **85B**(1): p. 45-51.
25. Scheelinck, T., D. Janssen, and N. Verdonschot, *Thin cement mantles surrounding femoral hip implants might not be deleterious in all cases.* Clinical Biomechanics, 2008. **23**(4): p. 500-501.
26. Janssen, D., J. van Aken, T. Scheerlinkck, and N. Verdonschot. *The 'French Paradox' exposed: A finite element analysis of cement philosophy on implant stability and crack formation in the cement mantle*. in *The 19th Annual Symposium of the International Society for technology in arthroplasty*. 2006. New York.
27. Scott, G., M. Freeman, and M. Kerboull, *Femoral components: the french paradox*, in *The Well-Cemented Total Hip Arthroplasty*, S. Breusch and H. Malchau, Editors. 2005, Springer-Link: Berlin.
28. Kwak, B., O. Lim, Y. Kim, and K. Rim, *An investigation of the effect of cement mantle thickness on an implant by finite element stress analysis.* International Orthopaedics, 1978. **2**(4): p. 315-319.
29. Ling, R. and A. Lee, *Porosity reduction in acrylic cement is clinically irrelevant.* Clinical Orthopaedics and Related Research, 1998. **355**: p. 249-253.

Chapter 8. *Summary and Conclusions*

The establishment of a stable cement-bone interface is vital to the long term success of cemented arthroplasty[1, 2]. The microstructural behaviour of this interface is complex due to the changes in morphology and properties that can arise from the differing cement penetration depths and the substantial heterogeneity, anisotropy and variability of the morphology and quality of the interlocking cancellous bone[3]. As a result of this variation, the properties of the cement-bone interface are difficult to isolate and examine experimentally. The motivation behind this work was to develop modelling techniques to examine the microstructural behaviour of the cement-bone interface. Two techniques, previously applied to modelling of cancellous bone structure, were extended to the behaviour of the cement-bone interface. These were:

i. Representation of the behaviour of trabecular bone by the use of an idealised unit cell to represent the structure of bone[4].

ii. Finite element models of trabecular architecture based on high resolution CT images of bone[5-7].

The first technique uses a simplification of the morphology of cancellous bone and has not been previously used to model the cement-bone interface. The variation in morphology of the unit cell and the effect of cement addition formed the basis of the investigations described in Chapter

4. It was shown that the factors which affect the volume fraction of the unit cell, such as the trabecular thickness, influence the resulting apparent stiffness. This is consistent with dimensional analysis[4] and reported power law relationships between Young's modulus and relative density derived from experimental testing of cancellous bone specimens [8-11]. The addition of cement into the unit cell resulted in an increase in the stiffness of the cell with increasing cement penetration. When the unit cell was fully embedded in cement, there was a significant increase in stiffness compared to the unit cell. The resulting composite was less sensitive to changes in morphology than the unit cell alone. This suggests that for patients with poorer quality or osteoporotic bone, increased cement penetration may be beneficial. Walker *et al*[8] suggested that for osteoporotic bone cement penetration should be increased to 5mm, from the suggested optimum of 3-4mm. However, there is a limit to which increasing cement penetration does not produce any further increase in strength[9]. In addition, should loosening occur, the amount of bone stock available for future revision arthroplasty is reduced.

The use of a cellular model to represent cancellous bone has limitations. The geometry of the unit cell is formed of rectangular beams and is not representative of the smooth surfaces of trabecular bone. In addition, the cell is regular and repeating which does not represent the adapted structure of cancellous bone. As such for more detail on the load transfer across the cement-bone interface, a more accurate representation of the geometry of bone was required.

High resolution μFE modelling was the second technique applied to evaluate the cement-bone interface. μFE modelling has been previously used for determination of elastic constants and damage behaviour of small volumes of cancellous bone[10-12]. To eliminate the problems associated with specimen preparation and variability, Duocel aluminium foam was selected as a cancellous bone analogue material. The selection and testing of this foam is detailed in Chapter 5. Duocel aluminium foam exhibits a similar structure and mechanical properties to those reported in literature for cancellous bone. Before modelling the cement-bone interface, the accuracy of μFE models of foam was evaluated and compared to experimental compression tests. Smooth surface tetrahedral meshes were created of a volume of Duocel aluminium foam to investigate the effect of segmentation (threshold), mesh density and smoothing parameters on the μFE-predicted apparent modulus of the foam. The threshold was found to have the most significant effect on the variation on the determined apparent modulus. Hara *et al*[10] demonstrated with a voxel-element model of trabecular bone that a 0.5% variation in threshold can lead to a 9% difference in stiffness. For smooth surface meshing of Duocel foam this effect was shown to be magnified, with differences of 200% to the experimentally determined apparent modulus with a change in increment of 0.4% of threshold. This sensitivity of threshold is due to the dependence of apparent modulus on the volume fraction of the resulting mesh and highlights the importance of correlating the mesh volume to the volume of the sample.

Since the micro-mechanical behaviour of the cement-bone interface is not well documented, experimental data regarding the behaviour of the cement-bone interface was required for validation of FE models. Chapter 6 describes the manufacture and testing in four point bending of cement-bone analogue samples were created. The test methods, which included AE and CT imaging, allowed 3D location and visualisation of damage within cement-bone interface analogue specimens. The samples were imaged before and after testing allowing visualisation of initiation and progression of damage. AE was used to monitor damage evolution in the sample; when AE parameters representative of damage were observed, testing was suspended and CT images were taken of the samples to visualise the stages of damage. The ability of AE as a passive tool to provide early indication of failure in situ was demonstrated; initiation and progression of damage through the cement and foam was isolated and characterised by analysis of the associated AE parameters. When the cement-bone analogue interface was loaded in bending, damage initiated at stress concentrations formed by irregularities in the aluminium geometry, recesses and notches formed by flow of cement into the aluminium. Pores in the cement mantle were not associated with any visible damage.

Finally Chapter 7 considered μFE modelling of the cement-bone analogue specimens and the effect of cement penetration depth on the load transfer across the interfaces. μFE models were created of a specimen with varying levels of cement penetration. Linear elastic analyses of a simulated four point bend test were performed for these models. The FE model correlated well with an experimental model, showing regions of high stress in the failure location i.e. at a notch formed by the flow of cement into the aluminium foam. However, there were also regions of high stress in the cement mantle where the rollers were in contact with the cement mantle where damage was not seen in the experimental tests. This may be due to the time dependent behaviour of the cement causing stress redistribution; this effect was not included in the model. The stress distribution across the cement-bone analogue sample was examined using a stressed volume approach. This method has been previously used to examine cement stresses in an implanted synthetic femur[13]. It was shown that the load transfer is different for different cement penetrations depths. For a greater amount of cement penetration there was a greater percentage of volume above the respective yield strengths of cement and bone suggesting that a greater load is transferred to the bone. However high stresses at the interface between composite and bone can lead to formation of an intervening fibrous tissue layer suggesting that there is an optimum penetration depth.

Thin cement mantles (below 1mm) have been shown to have a good success rate[14]. The exact reason for the high success rate is not known but theories suggest that use of a larger “canal thinning” prosthesis resulting in a thin and discontinuous cement mantle is supported by the cortex rather than weaker cancellous bone. The amount of cancellous bone remaining is thought

to influence the load transfer but has not been previously examined[15-17]. A μFE model of a specimen without a cement mantle was created. The stress distribution of the model showed that there was a reduction in load transfer to the foam and that the majority of the volume was below the yield stress of cement. The stress at the interface between composite and foam was reduced therefore reducing the likelihood of the formation of a fibrous tissue layer.

Smooth surface μFE models representative of cement-bone analogue specimens have been developed. Previous FE models of the interface have been limited by the lack of clinical or experimental data regarding the behaviour of the interface. A novel approach has been adopted in this study, which compares regions of high stress in the μFE models of the sample to locations of failure determined using non-destructive evaluation techniques. The fully bonded, linear elastic models have shown areas of high stress which correlate with the regions of failure. Further modelling of non-linear behaviour such as contact, creep and plastic damage may further improve the predictive capabilities of the model. In addition, further advances in CT technology and non-destructive methods will enable validation of boundary conditions. In the future, these models of the microstructure may be extended to combined continuum and local FE models to evaluate different prosthesis designs and the load transfer across the interfaces.

8.1. Further work

8.1.1. Modelling Damage of Cancellous Bone Analogue Materials

μFE techniques combined with compression tests were applied to a cancellous bone analogue material to assess the factors affecting the accuracy of the calculation of apparent modulus. However, one major limitation of this study was that, providing the correct volume fraction was maintained, the loss of connectivity resulting from smoothing of the surfaces during meshing did not appear to change the value of apparent modulus. Therefore, to ensure accurate modelling of stresses and strains at the level of the individual struts for both plastic and elastic behaviour, an alternative approach is required. One possibility is the use of in-situ CT measurements of the analogue material under load and the use of 3D digital image correlation (DIC) to track the local deformation of the aluminium struts. A recent study by Mann *et al*[18] has used 2D image correlation techniques to examine local deformations of the cement-bone interface in tension and compression. The study showed that the majority of displacement occurred at the contact interface between cement and bone. However, the morphology and quality of trabecular bone and the amount of interdigitation were not quantified. Preliminary investigations into using DIC methods to examine damage of aluminium foam and to validate FE models have been included in Appendix III.

8.1.2. Modelling of the cement-bone interface

There are further analyses that can be conducted based on the computational modelling and non-destructive techniques employed in this investigation; these can be divided into two broad areas:

i. Further investigations of the cement bone interface at the microstructural level are necessary to examine the effect of different boundary conditions. In addition, fracture mechanics approaches may be employed to gain an understanding of the interfacial failure process at this level.

ii. As an extension to this work, the model may then be used for preclinical analysis of prosthesis designs at the implanted construct level. The potential for this would clearly be related to computational resources available and efficiency of the model.

Firstly, due to time constraints, the specimens with varying penetration depths were not tested. Testing of these samples would provide further data for comparison of the FE models and behaviour of the cement-bone interface with regard to penetration depth. The predictive capabilities of the current μFE models were limited by the material and boundary conditions applied. It has been suggested that a contact or frictional interface between cement and bone would more appropriate due to the evidence of gap formation between the cement and bone[19].

However in this study, the cement was assumed to be fully bonded in order to reduce the computational time of the resulting model. The whole specimen was modelled because although the applied loads are known, the actual load transfer at the local level across the interface due to the complex morphology, may be a combination of shear, tension and compression. A smaller section of the interface specimen was not modelled because the local boundary conditions were not known. With further developments in the capabilities of experimental techniques to determine the correct boundary conditions, smaller sections of the interface samples could be modelled, allowing further modelling of non-linear behaviour. The current investigation was also limited to the tensile behaviour of the cement-bone interface. Clinically, the load transferred across the cement-bone interface is a combination of shear, compression and tension[20, 21]. Future efforts could focus on different loading modes and the resulting change in damage behaviour.

As Buckley *et al*[22] noted, very little literature exists on the fracture mechanics of the bone cement/bone interface. The majority of work in this area has investigated the fracture behaviour of acrylic bone cement only, focussing on fracture toughness testing. Buckley *et al* examined the fracture toughness of the cement/bovine bone interface using double torsion testing and linear elastic fracture mechanics. Mann *et al* [23] attempted to account for plasticity when modelling the bone/cement interface using a non-linear fracture mechanics approach. The authors were successful at estimating failure loads on a global scale for an experimental model that included tension and shear, but the models were unsuccessful in predicting the energy to failure and the shape of the post-yield response. There is therefore an opportunity to enhance the understanding of this interface by the development of more sophisticated micromechanical fracture models [24]

The methods employed in this study have not been extended to evaluating the effect of prosthesis design on the load transfer across the cement/bone interface. This has been mainly due to computational restraints. Both cellular modelling and μFE techniques could be extended to evaluation of the prosthesis but have advantages and limitations. The cellular model could be used in mixed macroscopic and local scale models to examine more complex behaviour such as fatigue and adaption of bone. Due to its simplicity and repeatable structure, this model could be easily adapted for use in a substructuring analysis. Substructuring is a technique where a group of elements is condensed to form a super-element, thus reducing computational time and allowing the solution of very large problems[25]. However, since the morphology of the cell is not fully representative of cancellous bone, the solution will be limited to comparative purposes only. The μFE model could also be used in a similar way, using smaller volumes. The quality of the solution may be better compared to the cellular model although computational times would be much greater making analysis of fatigue and adaption of bone more problematic.

8.2. References

1. Charnley, J., *The bonding of prostheses to bone by cement.* Journal of Bone and Joint Surgery British Volume, 1964. **46**: p. 518-529.
2. Radin, E., C.T. Rubin, E.L. Thrasher, L.E. Lanyon, A.M. Crugnola, A.S. Schiller, I.L. Paul, and R.M. Rose, *Changes in the bone-cement interface after total hip replacement.* The Journal of Bone and Joint Surgery, 1982: p. 1188-1200.
3. Graham, J., M. Ries, and L. Pruitt, *Effect of bone porosity on the mechanical integrity of the bone-cement interface.* Journal Of Bone And Joint Surgery-American Volume, 2003. **85A**(10): p. 1901-1908.
4. Gibson, L.J. and M.F. Ashby, *Cellular Solids: Structures and Properties*. 1988: Pegammon.
5. Alonso Vazquez, A., G.H. Van Lenthe, M. Taylor, and R. Muller. *Comparison of μCT Measurements and FE Predictions of Localised Failure in a Cancellous bone Analogue Material*. in *6th International Symposium on Computer Methods in Biomechanics and Biomedical Engineering* 2004. Madrid: FIRST Numerics.
6. Niebur, G.L., M.J. Feldstein, J.C. Yuen, T.J. Chen, and T.M. Keaveny, *High-resolution finite element models with tissue strength asymmetry accurately predict failure of trabecular bone.* Journal of Biomechanics, 2000. **33**(12): p. 1575-1583.
7. Van Rietbergen, B., *Micro-FE analyses of bone: State of the art*, in *Noninvasive assessment of trabecular bone architecture and the competence of bone*, S. Majumdar and B. Bay, Editors. 2001, Kluwer Academic. p. 21-30.
8. Walker, P., M. Soudry, F. Ewald, and H. McVickar, *Control of cement penetration in total knee arthroplasy.* Clinical Orthopaedics and Related Research, 1988. **185**: p. 155-164.
9. Krause, W., W. Krug, and J.E. Miller, *Strength of the cement-bone interface.* Clinical Orthopaedics, 1982. **163**: p. 290-299.
10. Hara, T., E. Tanck, J. Homminga, and R. Huiskes, *The influence of microcomputed tomography threshold variations on the assessment of structural and mechanical trabecular bone properties.* Bone, 2002. **31**(1): p. 107-109.
11. Van Rietbergen, B., *Micro-FE analysis of the bone: state of the art.* Advances in Experimental Medicine and Biology, 2001. **496**: p. 21-30.
12. Van Rietbergen, B., S. Majumdar, W. Pistoia, D.C. Newitt, M. Kothari, A. Laib, and P. Ruegsegger, *Assessment of cancellous bone mechanical properties from micro-FE models based on micro-CT, pQCT and MR images.* Technology and Health Care, 1998. **6**: p. 413-420.
13. Lennon, A.B. and P.J. Prendergast, *Evaluation of cement stresses in finite element analyses of cemented orthopaedic implants.* Journal of Biomechanical Engineering-Transactions of the ASME, 2001. **123**(6): p. 623-628.
14. Langlais, F., M. Kerboull, L. Sedel, and R.S.M. Ling, *The 'French paradox'.* Journal of Bone and Joint Surgery-British Volume, 2003. **85B**(1): p. 17-20.
15. Cristofolini, L., P. Erani, P. Savigni, T. Grupp, O. Thies, and M. Viceconti, *Increased long-term failure risk associated with excessively thin cement mantle in cemented hip arthroplasty: A comparative in vitro study.* Clinical Biomechanics, 2007. **22**(4): p. 410-421.
16. Scheelinck, T., D. Janssen, and N. Verdonschot, *Thin cement mantles surrounding femoral hip implants might not be deleterious in all cases.* Clinical Biomechanics, 2008. **23**(4): p. 500-501.
17. Cristofolini, L., P. Erani, P. Savigni, T. Grupp, O. Thies, and M. Viceconti, *Reply.* Clinical Biomechanics, 2008. **23**(4): p. 501-503.
18. Mann, K., M. Miller, R. Cleary, D. Janssen, and N. Verdonschot, *Experimental micromechanics of the cement-bone interface.* Journal of Orthopaedic Research, 2008. ***In Press***.

19. Mann, K.A. and N. Verdonschot. *Stress localization at the cement-bone interface; a mechanistic micro-FEA approach*. in *52nd Annual Meeting of the Orthopaedic Research Society*. 2006. Chicago.
20. Rose, R.M. and A.S. Litsky, *Biomechanical considerations in the loosening of hip replacements* in *Current Perspectives on Implantable Devices Vol 1*. 1989. p. 1-45.
21. Mann, K.A., R. Morcarski, L.A. Damron, M.J. Allen, and D.C. Ayers, *Mixed-mode failure response of the cement-bone interface.* Journal Of Orthopaedic Research, 2001. **19**: p. 1153-1161.
22. Buckley, P.J., J.F. Orr, I.C. Revie, S.J. Breusch, and N.J. Dunne, *Fracture characteristics of acrylic bone cement-bone Composites.* Proceedings of the Institution of Mechanical Engineers Part H- Journal of Engineering in Medicine, 2003. **216**(6): p. 419-27.
23. Mann, K.A. and L.A. Damron, *Predicting the failure response of cement-bone constructs using a non-linear fracture mechanics approach.* Journal of Biomechanical Engineering-Transactions of the Asme, 2002. **124**(4): p. 462-470.
24. Broek, D., *Elementary Engineering Fracture Mechanics,*. 1991, Boston: Kluwer Academic Publishers.
25. Ansys, *Release 11.0 Documentation for Ansys*. 2007: Canonsburg, Pa.

APPENDIX I: PUBLICATIONS

Journal Publications

Leung, SY, Browne, M, New A, *Smooth surface micro finite element modelling of a cancellous bone analogue material,*(2008), Proceedings of the Institution of Mechanical Engineers, Part H: Journal of Engineering in Medicine, 222(1), 144-149

Conference Publications

Leung SY, Browne M, New A., (2008), *The Use of Complimentary Non Destructive Imaging Techniques to Validate Micro FE Models of the Cement-Bone Interface* at the 54th Annual Meeting of the Orthopaedic Research Society, San Francisco, USA

Leung SY, New A, Browne M, (2007), *Use of complimentary non-destructive evaluation methods to evaluate the integrity of the bone-cement interface,* Annual congress of the International Society of Technology in Arthroplasty (ISTA), Paris, France

Leung SY, New A, Browne M, (2007), '*Smooth surface microfinite element modelling of a cancellous bone analogue material'*, The 2007 Summer workshop of the European Society of Biomechanics, Dublin, Ireland

Leung SY, New A, Browne M, (2006), '*Modelling the mechanics of the cement-bone interface',* The 5th World Congress of Biomechanics, Munich, Germany

APPENDIX II: CODES USED TO GENERATE AND RUN FE MODELS

Code used to Convert Amira output file to MSC MARC input file

```
Program Convert
C
C       Convert Amira file (ASCII .inp file) to Msc.MARC .dat input
C       Requires the element, node and materials to be listed and saved in working dir
C       Defines element sets for cement and bone
C       Written by J. Jeffers (2006).  Modified by S. Leung (2006)
        implicit real*8(a-h,o-z)
        open(unit=40,file='MARC_input.dat', status='unknown')
        write(*,*) 'hello'
        call header()
        call connectivity(numel)
        close(40)
        stop
        end
CC
CC      Open new input and write header
CC
        subroutine header()
        implicit real*8(a-h,o-z)
        character(90) line
        open(unit=10, file='amira_data.inp', status='unknown')
        do i=1,3
                read(10,*) line
        enddo
        read(10,*) num_nodes, numel
        close(10)
        write(40,0001) 'title,AMIRA_convert'
        write(40,0002) 'extended'
        write(40,0003) 'sizing,1000000,',numel,',',num_nodes
        write(40,0004) 'elements,134'
        write(40,0006) 'setname,20'
        write(40,0005) 'end'
0001    format(1a19)
0002    format(1a8)
0003    format(1a15,1i7,1a1,1i6)
0004    format(1a12)
0005    format(1a3)
0006    format(1a10)
        end
CC
CC      Element Connectivity
CC
        subroutine connectivity(numel)
        implicit real*8(a-h,o-z)
        dimension inode(4)
        character(90) line
        character(3) line1
        open(unit=10, file='amira_data.inp', status='unknown')
        iele=1
        node=1
        do i=1,3
                read(10,*) line
        enddo
        read(10,*) num_nodes, numel
        write(40,1003) 'coordinates'
        write(40,1002)3,num_nodes,0,1
        do while(node.le.num_nodes)
                read(10,*) node,(cord(k),k=1,3)
                do i=1,3
                        cord(i)=cord(i)
                enddo
                write(40,1001) node+1,(cord(k),k=1,3)
                if(node.eq.num_nodes-1)goto 2000
```

```
        enddo
2000    continue
        write(40,0004) 'connectivity'
        write(40,0006) 0,0,1
        iii=1
        jjj=1
        num1=0
        num2=0
        write (*,*) numel
        do while (iele.le.numel)
                read(10,*) iele,mat,line1,(inode(k),k=1,4)
                if(mat.eq.1) then
                        mat1(iii)=iele
                        iii=iii+1
                        num1=num1+1
                endif
                do j=1,4
                        inode(j)=inode(j)+1
                enddo
                write(40,0006) iele+1,134,(inode(k),k=1,4)
                if(iele.eq.numel-1) goto 1000
        enddo
1000    continue
        if(num1.gt.0)then
                write(40,2066) 'define          element         set     cement'

                if(num1.le.13)then
                        write(40,*) (mat1(i),i=1,num1)
                else
                        ilines=int(num1/13)
                        do l=1,ilines
                        if(l.eq.1) m=1
                        if(m+12.eq.num1)goto 2700
                        write(40,2009) (mat1(i),i=m,m+12),'c'
                        m=m+13
2700                    continue
                        enddo
c                       if (mod(in_mat(i),9).eq.0) goto 2600
                        write(40,2010) (mat1(k),k=m,num1)
c 2600                  continue
                endif
        endif
        do while (iele.le.numel)
                read(10,*) iele,mat,line1,(inode(k),k=1,4)
                        if(mat.eq.2) then
                        mat2(jjj)=iele
                        jjj=jjj+1
                        num2=num2+1
                endif
                do j=1,4
                        inode(j)=inode(j)+1
                enddo
                write(40,0006) iele+1,134,(inode(k),k=1,4)
                if(iele.eq.numel-1) goto 1010

        enddo
1010    continue

C       for mat2
        if(num2.gt.0)then
                write(40,2066) 'define          element         set     bone'
                if(num2.le.13)then
                        write(40,*) (mat2(i),i=1,num2)
                else
                        ilines=int(num2/13)
                        do l=1,ilines
                        if(l.eq.1) m=1
                        if(m+12.eq.num2)goto 2701
                        write(40,2009) (mat2(i),i=m,m+12),'c'
                        m=m+13
2701                    continue
                        enddo
                        write(40,2010) (mat2(k),k=m,num2)
                endif
        endif
```

```
      write(40,2007) 'no print'
      write(40,2008) 'end option'
      write(*,*) 'finished'

      close(10)
1001  format(1i10,3f20.10)
1002  format(4i10)
1003  format(1a11)
0004  format(1a12)
0005  format(1i8,3i7,1i4,2i7,7i6)
0006  format(6i10)
2007  format(1a8)
2008  format(1a10)
2009  format(13i8,1a8)
2010  format(13i8)
2066  format(1a66)
      return
      end
```

File Splitter to determine element locations by regions; cement, composite and foam

```
/* File splitter for Suk
 *
 * Author: Elena Samsonova <elena@soton.ac.uk>
 */

#include <iostream>
#include <fstream>
#include <sstream>
#include <string>
#include <string.h>
#include <stdlib.h>
#include <math.h>
#include <time.h>

using namespace std;

typedef struct _node_t {
  int id;
  float x, y, z;
  } node_t;

// function for qsort:
// compare nodes by their node IDs
int comp_nodes (const void *e1, const void *e2)
{
  node_t *n1 = (node_t *) e1;
  node_t *n2 = (node_t *) e2;
  if (n1->id > n2->id) return  1;
  if (n1->id < n2->id) return -1;
  return 0;
}

// The first non-comment line of an Amira file lists 5 numbers:
// node_cnt element_cnt 0 0 0
static void get_cnt (ifstream &in, unsigned int *node_cnt, unsigned int *elm_cnt)
{
  // skip comments
  while (in.peek() == '#') {
    in.ignore (INT_MAX, '\n');
    if (in.bad() || in.eof()) return;
    }

  in >> *node_cnt >> *elm_cnt; in.ignore(INT_MAX, '\n');
}

inline bool more (char *p, char *msg, int id)
{
  if (!(*p)) {
    if (msg) cerr << "Error reading " << msg <<" "<< id << ". Skipping." << endl;
    return false;
    }
  return true;
}

inline char *skip_space (char *p)
{
  while (*p == ' ' || *p == '\t') p++;
  return p;
}

inline char *skip_text (char *p)
{
  while (*p && !isspace(*p)) p++;
  return p;
}

// Nodes are shown one per line, in the format:
```

```
// id x y z
bool load_nodes (node_t *n, int node_cnt, ifstream &in)
{
  cout << "Loading " << node_cnt << " nodes... ";

  // load the nodes into the array
  for (int i=0; i<node_cnt; i++) {
    if (in.bad() || in.eof()) return false;
    if (in.peek() == '#') { in.ignore (INT_MAX, '\n'); i--; continue; }
    char line[256], *p;
    in.getline (line, 256, '\n');
    p = line;
    // We do laboreous parsing rather than a simple in >> >> >>
    // in order to avoid that an invalid record messes up the rest.
    // parse node ID
    p = skip_space(p); if (!more (p, NULL, i)) { i--; continue; } // empty line
    n[i].id = atoi (p);
    p = skip_text(p); if (!more (p, "node", n[i].id)) continue;

    // parse coordinates, expect 3
    p = skip_space(p); if (!more (p, "node", n[i].id)) continue;
    n[i].x = (float) atof (p);
    p = skip_text(p); if (!more (p, "node", n[i].id)) continue;

    p = skip_space(p); if (!more (p, "node", n[i].id)) continue;
    n[i].y = (float) atof (p);
    p = skip_text(p); if (!more (p, "node", n[i].id)) continue;

    p = skip_space(p); if (!more (p, "node", n[i].id)) continue;
    n[i].z = (float) atof (p);

    if ((i+1) % 100000 == 0) cout << i+1 <<"... ";
    }
  cout << node_cnt << " done" << endl;

  // sort the array by node ID
  qsort ((void*) n, node_cnt, sizeof (node_t), comp_nodes);
  return true;
}

// Elements are shown one per line in the format:
// id material "tet" n1 n2 n3 n4
// where "tet" means "tetrahedral" with four node ids to follow
// Sort the element IDs into the three files according to the threshold:
// take the average of the x-coordinates of the nodes.
//                    avg >= cement_low    ---->  cement
//   avg < cement_low && avg >= composit_low  ----> composit
//   avg < composit_low                       ----> foam
void sort_elements (ifstream &in, node_t *nodes, unsigned int node_cnt, unsigned int elm_cnt,
                    float cement_low, float composit_low,
                    ofstream &cement, ofstream &composit, ofstream &foam)
{
  cout << "Processing " << elm_cnt << " elements... ";
  cement  << "#Cement layer with the average x-coordinate above " << cement_low << endl;
  composit<< "#Composit layer with the average x-coordinate between " << composit_low
          << " and " << cement_low << endl;
  foam    << "#Foam layer with the average x-coordinate below " << composit_low << endl;

  // create string streams to temporarily store the element IDs
  // the first line of each output file should contain its element count
  ostringstream strcement, strcomposit, strfoam;
  unsigned int cement_cnt = 0, composit_cnt = 0, foam_cnt = 0;

  unsigned int cnt = 1;
  while (!in.bad() && !in.eof()) {
    // skip comments
    if (in.peek() == '#') { in.ignore (INT_MAX, '\n'); continue; }

    // read in the element
    int id, mat, n[4];
    char type[8], line[256], *p;
    in.getline (line, 256, '\n');
    p = line;
    // We do laboreous parsing rather than a simple in >> >> >>
    // in order to avoid that an invalid record messes up the rest.
```

```
  // parse element ID
  p = skip_space(p); if (!more (p, NULL, cnt)) continue; // empty line
  id = atoi (p);
  p = skip_text(p); if (!more (p, "element", id)) continue;

  // skip material id
  p = skip_space(p); if (!more (p, "element", id)) continue;
  p = skip_text(p); if (!more (p, "element", id)) continue;

  // skip element type
  p = skip_space(p); if (!more (p, "element", id)) continue;
  p = skip_text(p); if (!more (p, "element", id)) continue;

  // parse node IDs, expect 4
  bool err = false;
  for (int i=0; i<4; i++) {
    p = skip_space(p); if (!more (p, "element", id)) { err = true; break; }
    n[i] = atoi (p);
    p = skip_text(p); if (i<3 && !more (p, "element", id)) { err = true; break; }
    }
  if (err) continue;

  // calculate the avg x
  float avg = 0;
  node_t t = {0,0,0,0}; // temporary node for bsearch
  for (int i=0; i<4; i++) {
    t.id = n[i];
    node_t *n = (node_t*) bsearch ((void*) &t, (void*) nodes, node_cnt, sizeof (node_t),
                                   comp_nodes);
    if (!n) {
      cerr << "Warning: cannot find node "<< i+1 <<" with ID "<< t.id
           << " from element " << id << endl;
      continue;
      }
    avg += n->x;
    }
  avg /= 4.0;

  // write the element to the correct file
  if (                  avg >= cement_low  ) { strcement   << id+1 << endl; cement_cnt++;  }
  if (avg < cement_low && avg >= composit_low) { strcomposit << id+1 << endl; composit_cnt++;}
  if (avg < composit_low                     ) { strfoam     << id+1 << endl; foam_cnt++;    }

  if (cnt % 100000 == 0) cout << cnt <<"... ";
  cnt++;
 }

 cement  <<"#Element count:"<<endl<< cement_cnt  <<endl<<"#Elements:"<<endl<< strcement.str();
 composit<<"#Element count:"<<endl<< composit_cnt<<endl<<"#Elements:"<<endl<< strcomposit.str();
 foam    <<"#Element count:"<<endl<< foam_cnt    <<endl<<"#Elements:"<<endl<< strfoam.str();
 cout << cnt-1 << " done" << endl;
 if (cnt-1 != elm_cnt)
   cerr << "Warning: " << elm_cnt <<" elements expected, "<< cnt <<" found." << endl;
}

static void msg()
{
 switch (rand() % 11) {
   default: cout << "Come on now! Let me have it!! 8-)" << endl; break;
   }
}

int main ()
{
 bool done = false;
 srand ((unsigned int) time(NULL));

 while (!done) {
   // open an input file
   char infile[1064] = "";
   cout << "Enter the name of the input file: ";
   while (!*infile) cin.getline (infile, 1064, '\n');

   ifstream in (infile);
   if (in.bad() || in.peek() == EOF) {
```

```
  cerr << "Cannot read \"" << infile << "\": file does not exist or is empty." << endl
       << "Press any key to quit :-( ";
  cin.get (infile[0]);
  return 1;
  }

// open the three output files
char cement_file[1128], composit_file[1128], foam_file[1128];
strcpy (cement_file, infile); strcpy (composit_file, infile); strcpy (foam_file, infile);
char *dot = strrchr (infile, '.');
if (dot) { // cut off the extension if any
  *strrchr (cement_file,   '.') = '\0';
  *strrchr (composit_file, '.') = '\0';
  *strrchr (foam_file,     '.') = '\0';
  }
strcat (cement_file,   "_cement.dat");
strcat (composit_file, "_composit.dat");
strcat (foam_file,     "_foam.dat");

ofstream cement (cement_file), composit (composit_file), foam (foam_file);
if (cement.bad() || composit.bad() || foam.bad()) {
  cerr << "Cannot open files for writing. Giving up." << endl
       << "Press any key to quit :-( ";
  cin.get (infile[0]);
  return 2;
  }

// load the nodes
unsigned int node_cnt, elm_cnt;
get_cnt (in, &node_cnt, &elm_cnt);
if (node_cnt <= 0) {
  cerr << "Cannot allocate " << node_cnt << " bytes of memory!" << endl
       << "Press any key to quit :-( ";
  cin.get (infile[0]);
  return 4;
  }
node_t *nodes = (node_t*) calloc (node_cnt, sizeof (node_t));
if (!nodes) {
  cerr << "Cannot allocate memory for the nodes. Quitting." << endl
       << "Press any key to quit :-( ";
  cin.get (infile[0]);
  return 3;
  }

if (!load_nodes(nodes, node_cnt, in)) {
  cerr << "Failed to load the nodes." << endl
       << "Press any key to quit :-( ";
  cin.get (infile[0]);
  return 5;
  }

// get the thresholds for splitting
float cement_low, composit_low;
bool done_thr = false;
do {
  cout << "What is the cement/composit threshold? ";
  cin >> cement_low;
  cout << "What is the composit/foam threshold? ";
  cin >> composit_low;
  if (cement_low < composit_low)
    cerr << "The cement/composit threshold must be higher than composit/foam." << endl
         << "Please try again." << endl;
  else done_thr = true;
  }
while (!done_thr);

// read the elements and immediately output them into the right files
sort_elements (in, nodes, node_cnt, elm_cnt, cement_low, composit_low,
               cement, composit, foam);

// clean up
msg();
in.close();
cement.close(); composit.close(); foam.close();
free (nodes);
```

```
  cout << endl << "Done with this model. Shall we do another? (y/n) ";
  char yes;
  do {
    cin >> yes;
         if (yes == 'n' || yes == 'N') { done = true; }
    else { if (yes != 'y' && yes != 'Y') cout << "What's that? Enter y/Y/n/N: "; }
    }
  while (yes != 'y' && yes != 'Y' && yes != 'n' && yes != 'N');
  }
 cout << endl << "Bye-bye! Press any key to quit.";
 char yes; cin.get (yes);
 return 0;
}
```

Subroutine Histogram

```
=
ccccccccccccccccccccccccccccccccccccccc
cc Histogram.f                                          c
ccccccccccccccccccccccccccccccccccccccc
ccccccccccccccccccccccccccccccccccccccccccccccccccccccccccccccccccccccccccccccccccccccccccccc
cc This subroutine returns the volumes of elements at different von Mises stresses          cc
cc defined by the threshold values set in the file bins                                      cc
cc S Leung (2008)                                                                            cc
ccccccccccccccccccccccccccccccccccccccccccccccccccccccccccccccccccccccccccccccccccccccccccccc

ccccccccccccccccccccccccccccccccccccccccccccccccccccccccc
c INPUT FILES required:                                          c
c cement.dat ; list of elements in cement region                 c
c composit.dat ; list of elements in composite region            c
c foam.dat ; list of elements in the foam region                 c
c bins.dat  ; list of threshold values for stress                c
ccccccccccccccccccccccccccccccccccccccccccccccccccccccccc

CC Beginning of subroutine ELEVAR which gives an output of element quantities c

              SUBROUTINE ELEVAR(N,NN,KC,GSTRAN,GSTRES,STRESS,PSTRAN,
              1 CSTRAN,VSTRAN,CAUCHY,EPLAS,EQUIVC,SWELL,KRTYP,PRANG,DT,
              2 GSV,NGENS,NGEN1,NSTATS,NSTASS,THERM)

              IMPLICIT REAL *8 (A-H, O-Z)

              DIMENSION GSTRAN(NGENS),GSTRES(NGENS),
              1 STRESS(NGEN1),PSTRAN(NGEN1),CSTRAN(NGEN1),VSTRAN(NGEN1),
              2 CAUCHY(NGEN1),DT(NSTATS),GSV(1),THERM(NGEN1),KRTYP(4),
              3 PRANG(3,2)

cc common blocks
              include 'concom'
              include 'matdat'
              include 'dimen'

cc dimension arrays -
              dimension strain(50000), ps(3), str(3,3), vonmises(100000)
              dimension compstress(1000000), cemstress(1000000), foamstress(1000000)
              dimension cemel(50000), compel(50000), foamel(50000)
              dimension volume(10000), bins(10)
              character(200) dummy

cc open the files to read in element lists generated in histogram.exe

              if(iflag_2.eq.0) then
cc open the files for reading elements
                     open(unit=82, file='cement.dat', status='unknown')
              do i=1,2
              read(82,*) dummy
              enddo
              do i=1,1
              read(82,*) numcem
              enddo
              do i=1,1
              read (82,*) dummy
              enddo
              do i=1,numcem
              read(82,*) cemel(i)
              enddo
              write(*,*) 'read in cement data'
              write(*,*) 'number of cem elements=', numcem

              close(82)

c read in composite data
              open(unit=90, file='composit.dat',status='unknown')
              do i=1,2
              read(90,*) dummy
              enddo
              do i=1,1
```

```
            read(90,*) numcomp
            enddo
            do i=1,1
            read (90,*) dummy
            enddo
            do j=1,numcomp
            read(90,*) compel(j)
            enddo
            write(*,*) 'read in composite data'
            write(*,*) 'num of comp elements =', numcomp

            close(90)
                        open(unit=70, file='foam.dat',status='unknown')
            do i=1,2
            read(70,*) dummy
            enddo
            do i=1,1
            read(70,*) numfoam
            enddo
            do i=1,1
            read (70,*) dummy
            enddo
            do k=1,numfoam
            read(70,*) foamel(k)
            enddo
c check
            write(*,*) 'read in foam data'
            write(*,*) 'num of foam elements =', numfoam
            close(70)

c read in bin widths for the histogram
                        open(unit=92, file='bins.dat',status='unknown')
            do ii=1,10
            read(92,*) bins(ii)
            enddo


c open files for readout
                        open(unit=50, file='results.dat',status='unknown')
                        open(unit=60, file='volume.dat',status='unknown')
            iflag_2=1
c end if iflag=0
            endif

            if (inc.ge.1) then
cc the following finds the von Mises stress for each element
cc VM is a subroutine accessed at the end of ELEVAR
cc vonmises(k) is an array with all the stresses in

            if (n.le.numel) then
            call princv(ps,str,stress,ndi,nshear,0,0,0,0)
            vm=vonmis(stress,ngens1)
            vonmises(k)=vm
            totstress=totstress+vm
            if(vonmises(k).gt.mx) then
                        mx=vonmises(k)
            endif

cc ELMVAR calls volumes for each element
            CALL ELMVAR(69,n,NN,KC,VAR)
            volume(n)=var
            write(70,*) n, volume(n)
cc for total volume
            totalvol=totalvol+volume(n)

c examine elements of interest in CEMENT
            do i=1,numcem
                        if(n.eq.cemel(i)) then
c total cement volume
                        totalcemvol=totalcemvol+var
c cemstress(k) is the array of stresses on cement elements
                        cemstress(k)=vm
                        sumcemstress=vm+sumcemstress
c calculate max cement stress
            if (cemstress(k).gt.cemx) then
```

```
                cemx=cemstress(k)
        endif

c histogram bit sorts the vols out with stress
                if (cemstress(k).le.bins(1)) then
                vol1=vol1+var
                elseif(cemstress(k).gt.bins(1).and.
     1          cemstress(k).le.bins(2)) then
                vol2=vol2+var
                elseif(cemstress(k).gt.bins(2).and.
     1          cemstress(k).le.bins(3)) then
                vol3=vol3+var
                elseif(cemstress(k).gt.bins(3).and.
     1          cemstress(k).le.bins(4)) then
                vol4=vol4+var
                elseif(cemstress(k).gt.bins(4).and.
     1          cemstress(k).le.bins(5)) then
                vol5=vol5+var
                elseif(cemstress(k).gt.bins(5).and.
     1          cemstress(k).le.bins(6)) then
                vol6=vol6+var
                elseif(cemstress(k).gt.bins(6).and.
     1          cemstress(k).le.bins(7)) then
                vol7=vol7+var
                elseif(cemstress(k).gt.bins(7).and.
     1          cemstress(k).le.bins(8)) then
                vol8=vol8+var
                elseif(cemstress(k).gt.bins(8).and.
     1          cemstress(k).le.bins(9)) then
                vol9=vol9+var
                elseif(cemstress(k).gt.bins(9).and.
     1          cemstress(k).le.bins(10)) then
                vol10=vol10+var
                elseif(cemstress(k).gt.bins(10)) then
                vol11=vol11+var
                endif
c endif n.eq.cemel(i)
                endif
        enddo
c examine elements of interest in COMPOSIT
        do i=1,numcomp
                if(n.eq.compel(i)) then
c total cement volume
                totalcompvol=totalcompvol+var
c compstress(k) is the array of stresses on cement elements
                compstress(k)=vm
                sumcompstress=sumcompstress+vm
c caluclate max comp stress
        if (compstress(k).gt.compx) then
                compx=compstress(k)
        endif

c histogram bit sorts the vols out with stress
                if (compstress(k).le.bins(1)) then
                cvol1=cvol1+var
                elseif(compstress(k).gt.bins(1).and.
     1          compstress(k).le.bins(2)) then
                cvol2=cvol2+var
                elseif(compstress(k).gt.bins(2).and.
     1          compstress(k).le.bins(3)) then
                cvol3=cvol3+var
                elseif(compstress(k).gt.bins(3).and.
     1          compstress(k).le.bins(4)) then
                cvol4=cvol4+var
                elseif(compstress(k).gt.bins(4).and.
     1          compstress(k).le.bins(5)) then
                cvol5=cvol5+var
                elseif(compstress(k).gt.bins(5).and.
     1          compstress(k).le.bins(6)) then
                cvol6=cvol6+var
                elseif(compstress(k).gt.bins(6).and.
     1          compstress(k).le.bins(7)) then
                cvol7=cvol7+var
                elseif(compstress(k).gt.bins(7).and.
     1          compstress(k).le.bins(8)) then
```

```
                        cvol8=cvol8+var
                        elseif(compstress(k).gt.bins(8).and.
     1                  compstress(k).le.bins(9)) then
                        cvol9=cvol9+var
                        elseif(compstress(k).gt.bins(9).and.
     1                  compstress(k).le.bins(10)) then
                        cvol10=cvol10+var
                        elseif(compstress(k).gt.bins(10)) then
                        cvol11=cvol11+var
                        endif

c endif n.eq.compel(i)
                        endif
               enddo

c examine elements of interest in FOAM
               do i=1,numfoam
                        if(n.eq.foamel(i)) then
c total cement volume
                        totalfoamvol=totalfoamvol+var
c compstress(k) is the array of stresses on cement elements
                        foamstress(k)=vm
                        sumfoamstress=sumfoamstress+vm

c calculate max comp stress
                        if (foamstress(k).gt.fmx) then
                        fmx=foamstress(k)
               endif

c histogram bit sorts the vols out with stress
                        if (foamstress(k).le.bins(1)) then
                        fvol1=fvol1+var
                        elseif(foamstress(k).gt.bins(1).and.
     1                  foamstress(k).le.bins(2)) then
                        fvol2=fvol2+var
                        elseif(foamstress(k).gt.bins(2).and.
     1                  foamstress(k).le.bins(3)) then
                        fvol3=fvol3+var
                        elseif(foamstress(k).gt.bins(3).and.
     1                  foamstress(k).le.bins(4)) then
                        fvol4=fvol4+var
                        elseif(foamstress(k).gt.bins(4).and.
     1                  foamstress(k).le.bins(5)) then
                        fvol5=fvol5+var
                        elseif(foamstress(k).gt.bins(5).and.
     1                  foamstress(k).le.bins(6)) then
                        fvol6=fvol6+var
                        elseif(foamstress(k).gt.bins(6).and.
     1                  foamstress(k).le.bins(7)) then
                        fvol7=fvol7+var
                        elseif(foamstress(k).gt.bins(7).and.
     1                  foamstress(k).le.bins(8)) then
                        fvol8=fvol8+var
                        elseif(foamstress(k).gt.bins(8).and.
     1                  foamstress(k).le.bins(9)) then
                        fvol9=fvol9+var
                        elseif(foamstress(k).gt.bins(9).and.
     1                  foamstress(k).le.bins(10)) then
                        fvol10=fvol10+var
                        elseif(foamstress(k).gt.bins(10)) then
                        fvol11=fvol11+var
                        endif


                        endif
c endif n.eq.foamel(i)

c                       endif
               enddo

cc write out the volumes for each stress level
               if(n.eq.numel)then
               write(60,*) 'cement results'
               write(60,*) bins(1), vol1
               write(60,*) bins(2), vol2
```

```
            write(60,*) bins(3), vol3
            write(60,*) bins(4), vol4
            write(60,*) bins(5), vol5
            write(60,*) bins(6), vol6
            write(60,*) bins(7), vol7
            write(60,*) bins(8), vol8
            write(60,*) bins(9), vol9
            write(60,*) bins(10), vol10
            write(60,*) bins(11), vol11
            write(50,*) 'total cem vol is', totalcemvol

            write(60,*) 'composite results'
            write(60,*) bins(1), cvol1
            write(60,*) bins(2), cvol2
            write(60,*) bins(3), cvol3
            write(60,*) bins(4), cvol4
            write(60,*) bins(5), cvol5
            write(60,*) bins(6), cvol6
            write(60,*) bins(7), cvol7
            write(60,*) bins(8), cvol8
            write(60,*) bins(9), cvol9
            write(60,*) bins(10), cvol10
            write(60,*) bins(11), cvol11
            write(50,*) 'total comp vol is', totalcompvol

            write(60,*) 'foam results'
            write(60,*) bins(1), fvol1
            write(60,*) bins(2), fvol2
            write(60,*) bins(3), fvol3
            write(60,*) bins(4), fvol4
            write(60,*) bins(5), fvol5
            write(60,*) bins(6), fvol6
            write(60,*) bins(7), fvol7
            write(60,*) bins(8), fvol8
            write(60,*) bins(9), fvol9
            write(60,*) bins(10), fvol10
            write(60,*) bins(11), fvol11
            write(50,*) 'total foam vol is', totalfoamvol

            write(50,*) 'total strss is', totstress
            write(50,*) 'total volume is', totalvol
            write(50,*) 'max stress is', mx
            write(50,*) 'sum cement stress is', sumcemstress
            write(50,*) 'sum comp stress is', sumcompstress
            write(50,*) 'sum foam stress is', sumfoamstress
c average stresses
            avestress=totstress/numel
            avecem=sumcemstress/numcem
            avecomp=sumcompstress/numcomp
            avefoam=sumfoamstress/numfoam

            write(50,*) 'Average stress values'
            write(50,*) 'for all eles', avestress
            write(50,*) 'cement', avecem
            write(50,*) 'composite', avecomp
            write(50,*) 'foam', avefoam

            write(50,*) 'max stress values'
            write(50,*) 'cement', cemx
            write(50,*) 'composite', compx
            write(50,*) 'foam', fmx

            write(50,*) 'number of elements', numel

            write(50,*) 'number of cement', numcem
            write(50,*) 'number of comp', numcomp
            write(50,*) 'number of foam', numfoam


            endif

cc endif n.le.numel
            endif
cc a note to finish
            if(n.eq.numel) then
```

```
            write(*,*) 'finished'
            endif
cc end inc.eq.1
            endif

c1001  format(1i5)
            RETURN
            END

ccccccccccccccccccccccccccccccccccccccccccccccccc
c FUNCTION VON MISES                                                    c
ccccccccccccccccccccccccccccccccccccccccccccccccc

            real*8 function vonmis(stress,ngens1)

            implicit real*8 (a-h,o-z)
            dimension stress(ngens1)

            if (ngens1.eq.3) then
                  vonmis=sqrt(0.5*((stress(1)-stress(2))**2+
            1     stress(2)**2+stress(1)**2+ 6*stress(3)**2))
            elseif (ngens1.eq.4) then
                  vonmis=sqrt(0.5*((stress(1)-stress(2))**2+
            1     (stress(2)-stress(3))**2+(stress(3)-stress(1))**2+
            2     6*(stress(4)**2)))
            else
                  vonmis=sqrt(0.5*((stress(1)-stress(2))**2+
            1     (stress(2)-stress(3))**2+(stress(3)-stress(1))**2+
            2     6*(stress(4)**2+stress(5)**2+stress(6)**2)))
            endif

            return
            end
```

APPENDIX III: PRELIMINARY RESULTS FOR DIGITAL IMAGE CORRELATION OF ALUMINIUM FOAM

Examining the sensitivity of the μFE model to pre-processing steps by using the apparent modulus does not give an indication of the accuracy of the local stresses i.e. the stresses on the surface of the struts. This section explores the modelling of non-linear damage behaviour of the bone analogue material and shows preliminary results for 3D digital image correlation (DIC) of deformation of the foam with the FE model.

Modelling Damage of Duocel aluminium foam

The local stresses and strains do not affect the apparent modulus in μFE models of aluminium foam. This was demonstrated in Chapter 4 by an accurate prediction of apparent modulus, with the correct volume of aluminium, but with large loss of connectivity of the struts. In this section, damage is modelled in the μFE model. A micro-compressive device is used to examine deformation of the aluminium, allowing in-situ CT scans to be taken before and during loading. Using the scans, 3D digital image correlation (DIC), is performed and correlated with the μFE model.

Methods

An 11x7x11mm sample of aluminium foam was machined using a diamond saw. Using the method for creating a smooth surface μFE mesh, a model of the sample was created from a 14μm resolution CT scan of the unloaded sample. The resulting volume from selection of threshold was correlated with the true volume of the sample. Material properties of aluminium were used assuming the material behaved as a linear elastic-perfectly plastic material. The yield stress was assumed to be 193MPa. A micro-compression device was designed and manufactured in order to take *in situ* CT scans of the sample under load. This is shown in **Error! Reference source not found.**. A micrometer head is situated at the top of the device to apply a known displacement to the top compression plate. This displacement was correlated with the load measured by the load cell situated at the base of the device and with the distance between plates measured at the beginning of the CT scan. An outer Perspex tube is used to contain the device. A bearing is situated between the micrometer head and the top compression plate to remove unwanted torsion. The base plate sits on top of a ball bearing to allow the base

plate to tilt and aid alignment of the specimen. 7.6% strain was applied to the surface of the sample. Due to the relaxation of load with time, the displacement of plates was removed before scanning. Therefore only plastic strain was measured with the CT scans under load. Volumetric DIC was performed by LaVision (Oxford, UK) using image stacks of the sample before and after loading.

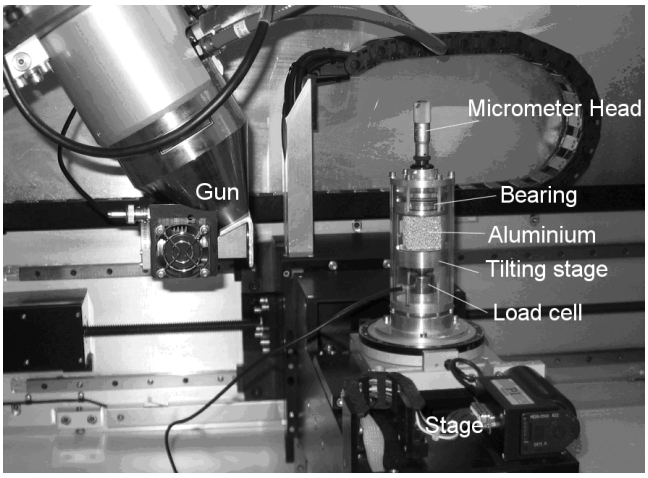

Figure A.8.1: Micro-compression device in the CT scanner

Results

The CT data was exported as a series of images normal to the direction of loading, before and after loading. To extract the aluminium from air, a low pass filter was applied to the images (as shown in FigureA.8.2). The analysis showed that there was little deformation in the x and y direction, i.e. the directions normal to the direction of loading. The majority of the displacement was in the z-direction. This is shown for some planes through the sample in FigureA.8.4.

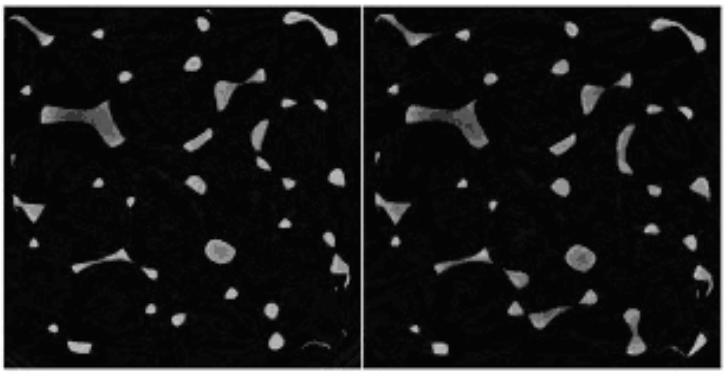

FigureA.8.2: CT images of aluminium with Low Pass filter to remove background

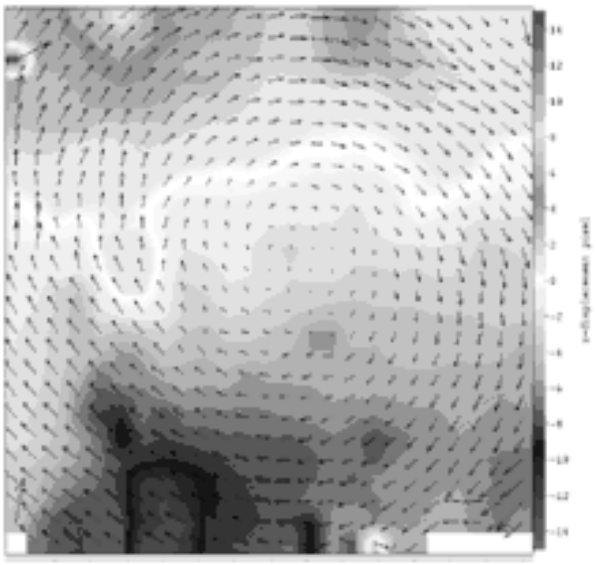

Figure A.8.3: 3D cross-correlation with 64x64x64 voxels and 50% overlap. Arrows indicate deformation vector (1 vector every 32 pixels)

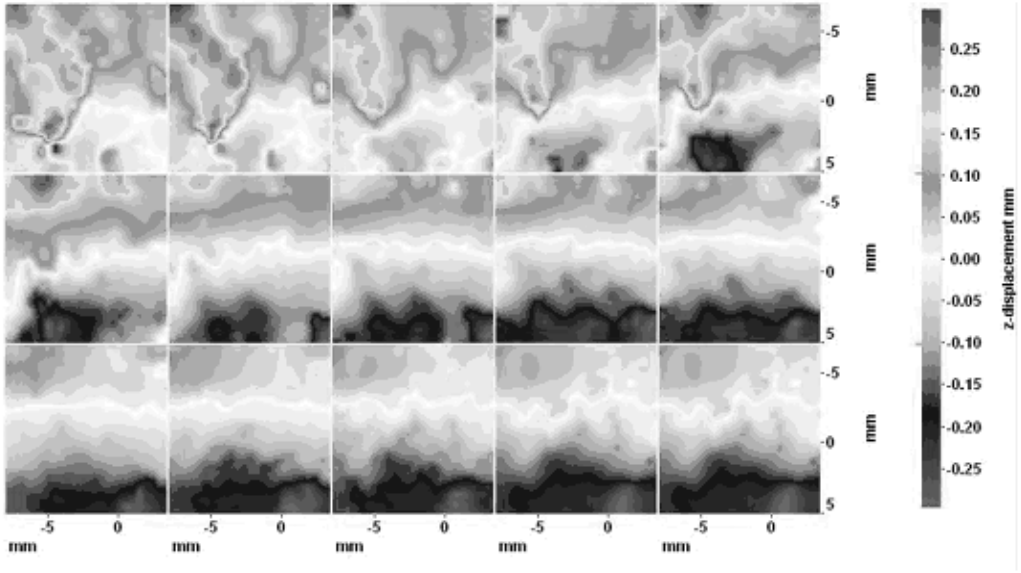

FigureA.8.4: Displacement of the sample in the direction of loading after removal of false vectors and rotation

There is evidence of shearing (tilting) of the sample from the z-displacement of 6 pixels at the top and -10 pixels at the bottom of the sample in Figure A.8.3. The vector size is 0.47mm. The sample is deformed axisymetrically in the z-plane as shown in FigureA.8.4.

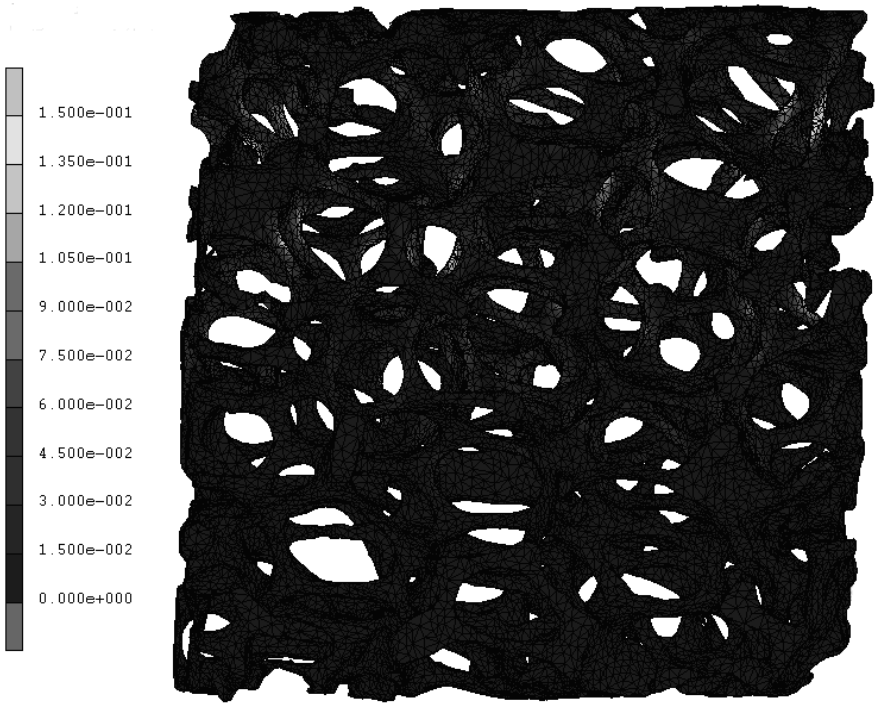

FigureA.8.5: Plastic Strain for aluminium sample

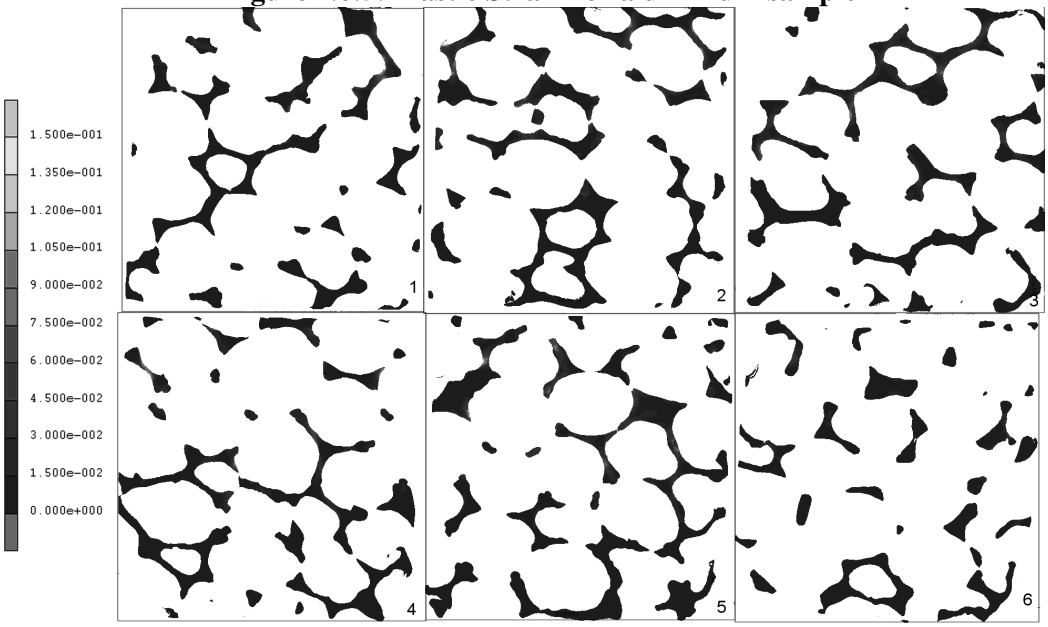

FigureA.8.6: Equivalent plastic strain on cutting planes for µFE model

The equivalent plastic strain for the µFE model of the aluminium sample is shown in FigureA.8.6. The equivalent plastic strain for aluminium is shown for six cutting planes normal to the direction of loading, through the aluminium sample in FigureA.8.6. From these images, there is no indication of axisymetric loading in the direction of loading.

Discussion

Digital image correlation allows 3D mapping of the deformation from computed tomography scans. The low pass filter used to segment the aluminium does not completely remove the background. This is evident from the streaking on FigureA.8.2. The results showed that there was little deformation in the x and y direction i.e. perpendicular to the direction of loading. This corresponds to the loading conditions of the mechanical tests where loading was applied in unidirectionally.

The DIC results also showed a shearing or tilting of the specimen. This could be due to the tilting of the bottom compression plate to correct for alignment of the specimen. This could be because the sides of the specimen were not completely parallel.

The µFE model shows plastic strain concentrations in individual struts. FigureA.8.5 shows there is higher plastic strain in the individual stuts nearer to the nodes with applied displacement. This corresponds to the study of deformation mechanisms of Duocel aluminium foam by Zhou *et al* [1] where plastic deformation was seen to initiate on struts that were adjacent to the loading surface.

The µFE model used boundary conditions where the bottom nodes were constrained in all direction and an applied displacement applied to the top nodes of the specimen. As such axisymetric loading is not seen in the plots for plastic strain.

The study here has its limitations. Errors can occur with DIC unless the process is performed under idea conditions i.e. scan conditions must be identical, the grey scale differences must be the same and the DIC can misposition cells. Due to time constraints, these conditions could not be ensured and therefore the work has not been included in the main body of the thesis.

References

1. Zhou, J., P. Shrotriya, and W.O. Soboyejo, Mechanisms and mechanics of compressive deformation in open- cell Al foams. Mechanics Of Materials, 2004. 36(8): p. 781-797.